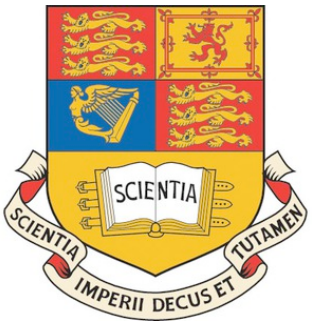
Multimodal Multispectral Optical Endoscopic Imaging for Biomedical Applications

Kevin Rongsheng Koh

Department of Computing and Institute of Biomedical Engineering

Imperial College London



Thesis submitted for the degree of Doctor of Philosophy and the Diploma of Imperial College London

For Mum and Dad

Abstract

Optical imaging is an emerging field of clinical diagnostics that can address the growing medical need for early cancer detection and diagnosis. Various human cancers are amenable to better prognosis and patient survival if found and treated during early disease onset. Besides providing wide-field, macroscopic diagnostic information similar to existing clinical imaging techniques, optical imaging modalities have the added advantage of microscopic, high resolution cellular-level imaging from *in vivo* tissues in real time. This comprehensive imaging approach to cancer detection and the possibility of performing an 'optical biopsy' without tissue removal has led to growing interest in the field with numerous techniques under investigation. Three optical techniques are discussed in this thesis, namely multispectral fluorescence imaging (MFI), hyperspectral reflectance imaging (HRI) and fluorescence confocal endomicroscopy (FCE). MFI and HRI are novel endoscopic imaging-based extensions of single point detection techniques, such as laser induced fluorescence spectroscopy and diffuse reflectance spectroscopy. This results in the acquisition of spectral data in an intuitive imaging format that allows for quantitative evaluation of tissue disease states. We demonstrate MFI and HRI on fluorophores, tissue phantoms and *ex vivo* tissues and present the results as an RGB colour image for more intuitive assessment. This follows dimensionality reduction of the acquired spectral data with a fixed-reference isomap diagnostic algorithm to extract only the most meaningful data parameters. FCE is a probe-based point imaging technique offering confocal detection *in vivo* with almost histology-grade images. We perform FCE imaging on chemotherapy-treated *in vitro* human ovarian cancer cells, *ex vivo* human cancer tissues and photosensitiser-treated *in vivo* murine tumours to show the enhanced detection capabilities of the technique. Finally, the three modalities are applied in combination to demonstrate an optical viewfinder approach as a possible minimally-invasive imaging method for early cancer detection and diagnosis.

Acknowledgements

I would like to express my sincere gratitude to various people without whom this thesis would not have been written. First and foremost I would like to acknowledge my supervisors, Professor Guang-Zhong Yang and Dr Daniel Elson, for giving me the opportunity to pursue this PhD. Special thanks especially to Dan for helping with the proofreading of this thesis and whose guidance has been instrumental throughout my course of study.

When embarking on the PhD as a molecular biologist with little experience in computing, I was fortunate to have been in the company of brilliant programmers – Andy Turner, who very patiently explained the rudiments of MATLAB, Karim Lekadir, for providing the initial FR-IsoMap algorithm and Toby Wood, without whom most of the image processing algorithms and user interfaces for operating the laser system would cease to exist. I am especially grateful to Dr Eileen Gentleman for imparting her cell culture techniques and providing the initial batch of liver cancer cells, a well as for allowing use of equipment in the cell culture lab. In addition, all *in vivo* work in tumour mice would not have been possible without assistance from Dr Nancy Brewig, who deserves a special mention. Ovarian cancer cell lines were kindly provided by Dr Sadaf Ghaem-Maghami with whom I am greatly appreciative.

My sincere gratitude goes to various clinical collaborators who have kindly provided *ex vivo* human cancer tissues for our study. They are Dr Daniel Cohen, Mr Erik Meyer, Dr Pallav Shah, Mr Kenneth Miller and Dr Sadaf Ghaem-Maghami. I would also like to convey my appreciation to Dr Robert Goldin for aiding in the histological analysis of our colorectal tissue samples.

Additionally, I would like say a big thank you to all members of the Biophotonics lab and colleagues from the Institute of Biomedical Engineering for their friendship and with whom I have had the pleasure of sharing countless tea breaks/lunches/dinners/parties with.

Outside of College, I am fortunate to be surrounded by a close-knit group of Singaporean friends who deserve a special mention for ensuring my weekends are always something to look forward to and most importantly for their care and concern during times of need. Finally, I would like to express my gratitude to my family back home for their unfailing love and support throughout the years. Thanks for being there for me!

Abbreviations

2D	Two-dimensional
3D	Three-dimensional
2-NBDG	2-[N-(7-nitrobenz-2-oxa-1,3-diaxol-4-yl)amino]-2-deoxyglucose
5-ALA	5-aminolevulinic acid
ABIR	αVß3 integrin receptor
AH	Acriflavine hydrochloride
ALAD	ALA-dehydratase
ALAS	ALA-synthase
AO	Acridine orange
ATP	Adenosine triphosphate
ATMPn	9-acetoxy-2,7,12,17-tetrakis-(ß-methyoxyethyl)-porphycene
$BaSO_4$	Barium sulphate
BFP	Blue fluorescent protein
BO	Barrett's oesophagus
BPD-MA	Benzoporphyrin-derivative monoacid ring A
C334	Coumarin 334
CCD	Charge-coupled device
CFP	Cyan fluorescent protein
CIS	Carcinoma *in situ*
CO_2	Carbon dioxide
CT	Computed tomography
CV	Cresyl violet perchlorate
DMD	Digital multimirror device
DMEM	Dulbecco's modified Eagle's medium
DNA	Deoxyribonucleic acid
DRS	Diffuse reflectance spectroscopy
ECM	Extracellular matrix
EEM	Excitation-emission matrix
EGFR	Epithelial growth factor receptor
ERCP	Endoscopic retrograde cholangiopancreatography
FAD	Flavin adenine dinucleotide (oxidised)
$FADH_2$	Flavin adenine dinucleotide (reduced)
FBS	Foetal bovine serum
FCE	Fluorescence confocal microendoscopy
FDA	Food and Drug Administration
FDG	2-deoxy-2 [18F] fluoro-D-glucose
FITC	Fluorescein isothiocyante
FL	Fluorescein
FOV	Field of view
FP	Flavoprotein
FR-IsoMap	Fixed reference isomap
FS	Fluorescence spectroscopy
GFP	Green fluorescent protein
GI	Gastrointestinal
H&E	Haematoxylin and eosin
Hb	Haemoglobin
HbO_2	Oxyhaemoglobin
HbR	Deoxyhaemoglobin
HEPES	4-(2-hydroxyethyl)-1 piperazineethanesulfonic acid
HGIL	High-grade intraepithelial lesion
HpD	Hematoporphyrin derivative
HRI	Hyperspectral reflectance imaging
ICG	Indocyanine green

LDL	Low-density lipoprotein
LIFE	Laser-induced fluorescence endoscopy
LSU	Laser scanning unit
LP	Longpass
MANOVA	Multivariate analysis of variance
MD	Mahalanobis distance
MDS	Multidimensional scaling
MEV	Multimodal endoscopic viewfinder
MI	Minimally invasive
MFI	Multispectral fluorescence imaging
MRI	Magnetic resonance imaging
MTHPC	Meso-tetra (hydroxyphenyl)-chlorin
NAD^+	Nicotine adenine dinucleotide (oxidised)
NADH	Nicotine adenine dinucleotide (reduced)
NBI	Narrow-band imaging
NH_3	Ammonia
NHS	National Health Service
NIH	National Institutes of Health
NIR	Near-infrared
OCT	Optical coherence tomography
PBG	Porphobilinogen
PBGD	Porphobilinogen deaminase
PBS	Phosphate buffered saline
Pc	Phthalocyanine
PCA	Principal Component Analysis
PCR	Polymerase chain reaction
PDD	Photodynamic diagnosis
PDT	Photodynamic therapy
PET	Positron emission tomography
PN	Pyridine nucleotide
PpIX	Protoporphyrin IX
QD	Quantum dot
R6G	Rhodamine 6G
RB	Rhodamine B
REC	Research Ethics Committee
RGB	Red-Green-Blue
RGD	Arginine-glycine-aspartic
RPM	Revolutions per minute
RPMI	Roswell Park Memorial Institute
RS	Raman spectroscopy
SBR	Signal to background ratio
SCC	Squamous cell carcinoma
SCID	Severe combined immunodeficiency
SCLC	Small-cell lung cancer
SnET2	Tin etiopurpurin
SPECT	Single photon emission computed tomography
Succinyl-CoA	Succinyl-coenzyme A
TAM	Tumour associated macrophage
TURBT	Transurethral resection of bladder tumour
UHD	Ultra high definition
UV	Ultraviolet
Vis-NIR	Visible and near-infrared
WHO IARC	World Health Organisation International Agency for Research on Cancer
WLB	White-light bronchoscopy
WLE	White-light endoscopy
YFP	Yellow fluorescent protein

Contents

Abstract **5**

Acknowledgements **7**

Abbreviations **9**

Contents **11**

List of Figures **15**

List of Tables **19**

1 Introduction **21**

1.1. The pivotal role of medical imaging in cancer detection and diagnosis 22

1.2. The drive towards multispectral optical imaging techniques 23

1.3. Overview of the thesis 26

1.4. References 29

2 Multispectral Imaging – Principles, Techniques and Motivations **33**

2.1. Introduction 34

2.2. Light-tissue interactions relevant to optical imaging 34

2.3. Fluorescence in biological tissue 35

2.3.1. Definition and basic principles 35

2.3.2. Fluorophores – the origins of fluorescence 37

2.3.2.1. Endogenous fluorophores 37

Amino acids 38

Collagen and elastin 39

Pyridine nucleotides and flavoproteins 41

Porphyrins 41

2.3.2.2. Exogenous fluorophores 42

Molecular dyes 43

Dye-antibody and dye-peptide conjugates 43

Fluorescent and bioluminescent protein probes 44

Photosensitiser probes 45

Quantum dots and nanoparticles 46

2.4. Absorption and scattering events 47

2.5. Optical imaging techniques – the state of the art 49
2.5.1. Overview 49
2.5.2. Fluorescence spectroscopy 50
2.5.3. Diffuse reflectance spectroscopy 56
2.5.4. Fluorescence confocal endomicroscopy 61
2.6. From point-measurements to region-based detection 68
2.7. Summary and conclusions 69
2.8. References 70

3 Multispectral Fluorescence Imaging of Dyes and Endogenous Fluorophores 81
3.1. Introduction 81
3.2. Fluorescence detection of diseased tissue states 83
3.3. Multispectral fluorescence imaging of various fluorescent samples 84
3.3.1. Optical instrumentation 84
3.3.2. Data dimensionality reduction and image analysis technique 86
3.3.3. Initial system validation using fluorescent dye solutions 89
3.3.3.1. Sample preparation and imaging procedure 89
3.3.3.2. Imaging results 91
3.3.4. Further validation using fluorescent collagen gel tissue phantoms 101
3.3.4.1. Tissue phantom preparation and imaging procedure 101
3.3.4.2. Imaging results 104
3.4. Summary 106
3.5. References 108

4 Investigating Human Cancer Tissues with Multispectral Fluorescence and Hyperspectral Reflectance Imaging 111
4.1. Introduction 111
4.2. Imaging fluorescence from various biological tissues 113
4.2.1. Optical instrumentation 113
4.2.2. Data processing technique 115
4.2.3. Dye-stained *ex vivo* lamb kidneys 115
4.2.3.1. Tissue staining and imaging procedure 115
4.2.3.2. Imaging results 116
4.2.4. 5-ALA treated *ex vivo* human small-cell lung cancer tissue 117
4.2.4.1. Tissue preparation and imaging procedure 117
4.2.4.2. Imaging results 118
4.2.5. Untreated *ex vivo* human colorectal tissue 120

4.2.5.1. Tissue preparation, imaging and histopathology procedure 120
4.2.5.2. Imaging and histopathology results 120
4.3. Detecting diffuse reflectance signals from *ex vivo* colorectal cancer tissues 124
4.4. Summary 126
4.5. References 128

5 Evaluating Chemotherapy Response with Fluorescence Confocal Endomicroscopy 131
5.1. Introduction 131
5.2. Classical fluorescence confocal microscopy and the move towards novel *in vivo* systems 132
5.3. Motivations for tissue diagnosis with fluorescence confocal endomicroscopy 135
5.4. Fluorescence confocal endomicroscopy for cellular characterisation 137
5.4.1. Optical instrumentation and image acquisition 137
5.4.2. Optimal contrast agent selection using hepatocellular carcinoma cells 138
5.4.2.1. Sample preparation and imaging procedure 138
5.4.2.2. Imaging results 140
5.4.3. Evaluating chemotherapy response of ovarian adenocarcinoma cells 141
5.4.3.1. Sample preparation and imaging procedure 142
5.4.3.2. Imaging results 145
5.5. Summary 152
5.6. References 153

6 Probing the Morphological and Functional Properties of Tissue with Fluorescence Confocal Endomicroscopy 157
6.1. Introduction 158
6.2. Characterising the morphological appearance of *ex vivo* healthy porcine tissues and human cancer tissues 159
6.2.1. Instrumentation and imaging procedure 159
6.2.2. *In vivo* imaging of healthy porcine tissues 160
6.2.3. *Ex vivo* imaging of human cancer tissues 162
6.2.3.1. Ovarian cancer tissue 162
6.2.3.2. Bladder cancer tissue 164
6.3. Photodynamic diagnostic imaging of photosensitised cancer cells and tumour tissues 166
6.3.1. Photodynamic diagnosis (and therapy) 166
6.3.2. 5-aminolevulinic acid and protoporphyrin IX 168

6.3.3. Instrumentation and imaging procedure 169
6.3.4. *In vitro* imaging of photosensitised human ovarian cancer cells 170
6.3.5. *Ex vivo* imaging of photosensitised human cancer tissues 172
6.3.5.1. Small-cell lung cancer tissue 174
6.3.5.2. Pharyngeal cancer tissue 176
6.3.6. *In vivo* imaging of photosensitised murine tissues 178
6.4. Probing fluorescent signatures from a tumour-specific PET imaging optical analogue 181
6.4.1. Instrumentation and imaging procedure 182
6.4.2. *In vitro* imaging of fluorescent labelled human ovarian cancer cells 182
6.4.3. *In vivo* imaging of tumour-specific fluorescent biomarkers from murine tumour tissue 184
6.5. Multimodal endoscopic viewfinder imaging technique 187
6.5.1. Instrumentation and imaging procedure 190
6.5.2. Viewfinder imaging of photosensitised *ex vivo* bladder cancer tissue 191
6.6. Summary 194
6.7. References 196

7 Conclusions and Future Outlook 201
References 208

Publications and Conferences 211

List of Figures

1.1. NHS budget for England from 2007/8 to 2010/11 24

2.1. Graphical representation of various light-tissue interaction scenarios 35

2.2. Jablonski energy level diagram 36

2.3. Excitation and emission spectra of various endogenous fluorophores 38

2.4. Chemical structures of the amino acids tryptophan, tyrosine and phenylalanine 39

2.5. Molecular structure of the oxidised form of nicotinamide adenine dinucleotide 41

2.6. Three-dimensional structures of the green fluorescent protein and firefly luciferase 45

2.7. Absorption coefficients of the main endogenous absorbers present in biological tissue 48

2.8. Typical example of fluorescence EEMs obtained from the cervical epithelium of a single patient 52

2.9. Fluorescence EEMs of a normal ovary with stromal hyperplasia and corpus albicans compared against an ovary presenting high grade carcinoma 53

2.10. Comparison between a white-light bronchoscopic image and LIFE image of a right lower-lobe bronchus. 54

2.11. White-light/fluorescent images of oral cavity lesions from three patients. 55

2.12. Diffuse reflectance spectral data from normal tissue and an adenomatous polyp together with the modeled spectra 57

2.13. Mean reflectance spectra obtained for all eight tissue diagnostic categories 59

2.14. Conventional white-light and NBI images of familial adenomatosis coli and Barrett's oesophagus 60

2.15. Comparison between FCE and *en face* histology results of different colonic mucosal disease states 63

2.16. FCE images and correponding histological results obtained from *ex vivo* imaging of a bladder cystectomy tissue sample 64

2.17. Images obtained from *in vivo* FCE imaging of a human ovary using topically applied fluorescein sodium dye as contrast agent 65

2.18. Images obtained from *ex vivo* and *in vivo* FCE imaging of human ovaries stained with the contrast agent acridine orange 66

2.19. FCE Images of 5-ALA treated normal and SCC tongue tissue, and a white light microscope image of a histological H&E section of SCC tongue tissue 67

3.1. Diagrammatic representation of the supercontinuum fibre laser system used for MFI experiments in this section of the thesis. 85

3.2. The "Swiss roll" example of a non-linear data set demonstrating the different processing techniques of Isomap and PCA 88

3.3. Diagrammatic representations illustrating the unfolding of the non-linear three-dimensional "Swiss roll" data set onto a two-dimensional space by PCA nd FR-IsoMap 88

3.4. Normalised excitation spectra applied by the supercontinuum imaging system 90

3.5. Raw fluorescence intensity images of single dye solutions and dye mixtures 91

3.6. Example images used to illustrate the image pre-processing step performed prior to data dimensionality reduction with either PCA or FR-IsoMap. 92

3.7. PCA and FR-IsoMap processed images of single dye solutions and two-dye mixtures 93

3.8. Average interclass Mahalanobis distances between dye pairs and within the same dye 97

3.9. Graphical representation of variation in average Mahalanobis distances from sequential MANOVA analyses of two-dye mixtures 98

3.10. Variation in the measured average Mahalanobis distances from PCA and FR-IsoMap processed images of single dyes of increasing concentration 100

3.11. The 13 excitation wavelengths applied for generation of the fluorescence intensity images in the amalgamated dataset 103

3.12. The amalgamated fluorescence image dataset used to create the FR-IsoMap colour map of collagen gel tissue phantoms. 104

3.13. Histogram of the interclass distances between three selected fluorophores. 106

4.1. Diagrammatic representation of the multimodal image acquisition optics 114

4.2. Conventional white light reflectance and Isomap images of the coronal section of an *ex vivo* dye-stained lamb kidney 117

4.3. White light photographs and FR-IsoMap images of human small-cell lung cancer (SCLC) tissues 119

4.4. Normalised average autofluorescence intensity graph of human colorectal tissue samples .122

4.5. Selected representative H&E stained histopathology sections of the imaged human colorectal tissue samples 123

4.6. FR-IsoMap image obtained from the processing of amalgamated intensity image datasets acquired during HRI of human colorectal cancer tissue 125

5.1. Diagrammatic representation of fluorescence confocal microscopy and conventional light microscopy techniques 133

5.2. Morphological changes occurring in the uppermost layers of tissue mucosa with cancer progression. 135

5.3. HepG2 human hepatocellular carcinoma cells stained with different contrast agents during FCE imaging 140

5.4. Bar chart representing the signal to background ratios (SBRs) obtained when HepG2 cells are stained with different contrast agents during FCE imaging 141

5.5. The 3D molecular structure of the cisplatin molecule 143

5.6. Cisplatin molecule binding to DNA to form various adducts 144

5.7. Graphs showing the average attrition rates of ovarian adenocarcinoma cell lines after incubation with various concentrations of cisplatin 148

5.8. FCE images of AO-stained SKOV-5 ovarian adenocarcinoma cells incubated with various concentrations of cisplatin over a 5-day period 149

5.9. FCE images of AO-stained OVCAR-5 ovarian adenocarcinoma cells incubated with various concentrations of cisplatin over a 5-day period 150

5.10. FCE images of AO-stained IGROV-1 ovarian adenocarcinoma cells incubated with various concentrations of cisplatin over a 5-day period 151

6.1. Photograph showing fluorescence confocal endomicroscopy of a porcine ovary in the gloved hand of an operator 160

6.2. FCE images of healthy *in vivo* porcine tissues following topical application of various fluorescent contrast agents 161

6.3. FCE images of *ex vivo* human ovarian cancer tissues demonstrating a heterogeneous morphology.. 163

6.4. FCE images of *ex vivo* human bladder cancer tissues excised via transurethral cold-cut biopsy or diathermy 165

6.5. The haem biosynthetic pathway 168

6.6. Time lapse FCE images of three *in vitro* primary human ovarian cancer cell lines incubated with 5-ALA 171

6.7. Change in signal to background ratios of FCE images with 5-ALA incubation. 172

6.8. Time lapse FCE images from *ex vivo* human small-cell lung cancer tissue incubated with 5-ALA 175

6.9. Graph showing the mean and maximum values of fluorescence intensities at various FCE imaging time points for 5-ALA-incubated human small-cell lung cancer tissues. 176

6.10. Time lapse FCE images from *ex vivo* human pharyngeal cancer tissue incubated with 5-ALA for up to 90 minutes 177

6.11. Graph showing the mean and maximum fluorescence intensity values at various FCE imaging time points for 5-ALA-incubated human pharyngeal cancer tissues 178

6.12. Example FCE images of murine healthy and IGROV-1 tumour tissues *in vivo* acquired at different time points after intravenous injection of 5-ALA 180

6.13. Mean fluorescence intensities obtained from FCE images of various photosensitised murine tissues *in vivo* 181

6.14. FCE images from 3 different human ovarian cancer cell cultures showing either control or fluorescent 2-NBDG-incubated populations 183

6.15. Bar chart representing signal to background ratios from FCE images of three different human ovarian cancer cell populations incubated with 2-NBDG 184

6.16. Example FCE images of healthy and IGROV-1 tumour murine tissues *in vivo* 20 minutes after intravenous injection of 2-NBDG. 185

6.17. Bar chart representing mean fluorescence intensities from FCE images of various *in vivo* murine tissues after intravenous injection of 2-NBDG 186

6.18. Images illustrating the proposed multimodal endoscopic viewfinder (MEV) imaging technique 189

6.19. The excitation wavelengths applied during MFI and HRI for MEV imaging 190

6.20. Graph of normalised fluorescence spectra plotted against excitation wavelength for respective 5-ALA- and non photosensitiser-treated *ex vivo* human bladder tissue samples with various disease conditions. 192

6.21. Example FCE images of 5-ALA treated and untreated *ex vivo* human bladder tissue after 60 minutes of incubation at 37°C temperature and 5% CO_2 193

List of Tables

2.1. Excitation and emission maxima of endogenous fluorophores associated with tissue transformation processes around the onset of carcinogenesis 38

3.1. Combinations of excitation wavelengths and corresponding emission filters used 90

3.2. Average inter- and intraclass Mahalanobis Distances between single dye solutions of 0.3 μm concentration after PCA and FR-IsoMap processing..... 96

3.3. Combinations of excitation wavelengths and corresponding emission filters used. 103

3.4. Matrix of Mahalanobis distances for different wells within Figure 3.9B..... 105

4.1. Imaging modalities and their respective combinations of excitation wavelengths, bandwidths, longpass emission or cross polarising filters and camera integration times. 114

4.2. List of tissue types, 567/510 nm ratiometric scores and disease states of the imaged *ex vivo* human colorectal tissue samples as evaluated by two separate histopathologists. 123

1

Introduction

1.1. The pivotal role of medical imaging in cancer detection and diagnosis 22

1.2. The drive towards multispectral optical imaging techniques 23

1.3. Overview of the thesis 26

1.4. References 29

This thesis is a multidisciplinary body of work involving the assistance and collaborative efforts of biomedical researchers and clinicians from Imperial College London and her affiliated hospitals. Its broad aim is the evaluation of a trio of novel optical endoscopic imaging modalities for minimally invasive cancer detection and diagnosis, with the underlying view of reducing customary reliance on conventional clinical imaging systems in developed nations and the more long-term vision of providing affordable and effective diagnostic technologies in countries of the developing world. Optical techniques under investigation are systematically validated using tissue-simulating phantoms, *in vitro* cell lines, *ex vivo* tissue specimens and *in vivo* tissues. Results are further compared with histopathology where possible to assess overall diagnostic effectiveness with the prevailing gold standard method.

This chapter provides a brief overview of recent cancer statistics, socio-economic factors and clinical motivations relating to the implementation of optical imaging modalities for early cancer detection and diagnosis. As the utility of optical imaging techniques for early cancer detection becomes more apparent, so has clinical and biomedical research interest in the field increased with numerous optical modalities currently under investigation. Three novel optical detection methods are examined in this thesis, namely multispectral fluorescence imaging (MFI), hyperspectral reflectance imaging (HRI) and fluorescence confocal endomicroscopy (FCE) for minimally invasive *in vivo in situ* monitoring of

dysplastic conditions in humans. The outline of contents in proceeding chapters of the thesis is also mentioned.

1.1. The pivotal role of medical imaging in cancer detection and diagnosis

Recent statistics from the World Health Organisation's International Agency for Research on Cancer (WHO IARC) estimated that around 7.6 million people worldwide died from cancer in 2008 (GLOBOCAN 2008). Taking into account future demographic shifts and growth in the world population, this number is projected to rise to approximately 12 million cancer deaths annually by 2030 (Mathers and Loncar, 2006). In an effort to alleviate this global chronic disease burden, besides raising public awareness about cancer prevention and its related symptoms, clinicians and researchers have relied on medical imaging as an important means of early cancer detection and diagnosis. This is especially critical since the stage of diagnosis has been identified as being one of the most fundamental determinants for patient survival for most human cancer types (Pontén *et al.,* 1995; Teppo *et al.,* 1999; Sommerton *et al.,* 2000).

The central aim behind performing an early cancer diagnosis is to allow for recognition of early phenotypic dysplastic/cancerous signatures *in situ*. During which time, it is expected that the tumour remains localised to the organ of origin and has yet to invade surrounding normal tissue regions i.e. undergone metastasis. This is motivated by the fact that the chance for a potential cure is raised many fold if appropriate treatment is administered in a timely way during early disease onset. Cancers found to be amenable to better prognosis and patient survival if found and treated during early onset include the cancers of the breast (Carter *et al.,* 1989; Maguire *et al.,* 1994; Porta *et al.,* 1991; Richards *et al.,* 1999; Sant *et al.,* 2003), stomach (Porta *et al.,* 1991; Barchielli *et al.,* 2001), cervix (Horn *et al.,* 2007), lung (Maguire *et al.,* 1994; Porta *et al.,* 1991), liver (Wang *et al.,* 2008), prostate (Gann, 1997; Vis *et al.,* 2008) and bladder (Maguire *et al.,* 1994; Hellsten *et al.,* 1983). The stage of the tumour during time of initial diagnosis and treatment was also found to be closely related to rates of morbidity and mortality for oral (Sargeran *et al.,* 2008; Subramanian *et al.,* 2009) and colorectal (Maguire *et al.,* 1994; Porta *et al.,* 1991; Cicolallo *et al.,* 2005; Ponz *et al.,* 2000) cancers.

1.2. The drive towards multispectral optical imaging techniques

Clinical imaging systems currently in widespread use include X-rays, magnetic resonance imaging (MRI), computed tomography (CT), single-photon-emission CT (SPECT), positron emission tomography (PET), and ultrasound. These macroscopic, wide-field imaging techniques allow for anatomical and structural information to be obtained at resolutions of between 50 μm and 3 mm from a particular tissue region (Weissleder and Pittet, 2008). Although sufficient for gross interrogation, such techniques usually require biopsies to be taken of the diseased region after imaging. This is followed by histological confirmation before a final comprehensive diagnosis can be made. While it is fair to conclude that macroscopic clinical imaging systems will no doubt continue to enhance patient care and prognosis in the future, the entire imaging process is costly and resource intensive, requiring not only skilled operators but also the support of hospital and histopathology infrastructures. This limits their implementation mainly to larger regional healthcare centres in urban areas with generally middle- to upper-middle income population brackets (Bedard *et al.*, 2010).

With rising treatment costs and increasingly ageing populations, it is not only individual patients who feel the financial strain but also publicly funded healthcare systems in some developed countries as a whole. One such example is the United Kingdom's National Health Service (NHS), whose funding budget for England since its founding has swelled by over ten times that amount to approximately £102 billion in 2009/10 (NHS website). Although the UK government's allocation for the NHS healthcare budget has seen a steady yearly increase (Figure 1.1), a recent report by the NHS has warned that these "modest cash increases could be outstripped by rising costs within the health service" (Jeffreys, 2009). In addition, such financial worries are compounded by mismatches in income tax and budgets on expenditure, a problem facing many European governments of today. To alleviate the financial strains on the UK healthcare system, Andy Burnham, the British government's Health Secretary in 2009, remarked that emphasis had to be made on prevention, quality and innovation so as to maximise overall efficiency of the NHS (Smith, 2009). Novel multispectral optical imaging techniques are expected to play a major role in this process.

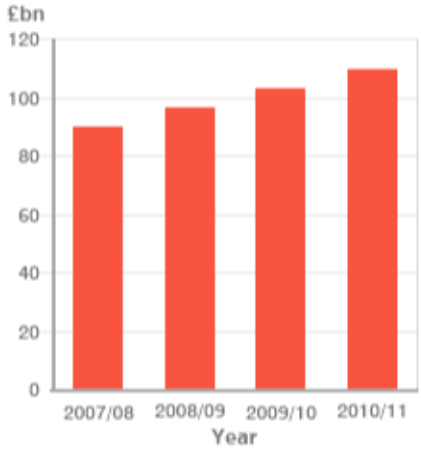


Figure 1.1. NHS budget for England from 2007/8 to 2010/11. (Source: HM Treasury)

Of the 12.7 million new cases of cancer diagnosed worldwide in 2008, more than half that number presented in less developed regions of the globe (GLOBOCAN, 2008) where 80% of patients were found to be at advanced stages of the disease during the time of diagnosis (Tunstall-Pedoe, 2006; Jones *et al.,* 2006). This is attributed most likely to poor healthcare coverage and inadequate cancer diagnostic facilities at the primary care levels in local communities. As the world population continues to grow exponentially, the largest increase is expected to come from Asia and other less developed countries of the world. Consequently, this implies an ever-greater need for affordable yet effective early diagnostic and treatment modalities, which can be easily integrated into local community healthcare systems.

Multispectral optical imaging is an emerging field of medical diagnostics that has the potential to address the current global need for effective early cancer detection in a more affordable, portable and easy-to-use package. In contrast to macroscopic clinical imaging techniques, optical imaging systems can provide not only wide-field macroscopic diagnostic information (with a field of view measuring several square centimetres), but also microscopic cellular-level images of *in vivo* tissue surfaces with resolutions less than 10 μm. As a result, multimodal optical imaging techniques offer a more comprehensive and truly 'early' imaging approach to cancer detection and diagnosis. Furthermore, technological advances in the optics, photonics and microelectronics industries have lead to greater miniaturisation of optical imaging devices; various examples include the PillCam platform (Given Imaging, USA) for capsule-based endoscopic imaging of the gastrointestinal tract and 'chip on a tip' flexible video laryngoscopes (Karl Storz

Endoskope, Germany) for otolaryngological applications. As a solution to third world countries lacking expensive diagnostic facilities and stable electricity, a group led by Richards-Kortum at Rice University in Texas, USA recently reported a US$240 fluorescence microscope system powered only by AA batteries (Miller *et al.*, 2010). The system weighs two and a half pounds and is described to be as effective at diagnosing tuberculosis as professional US$40,000 laboratory systems. Overall, this therefore translates in the long term to greater affordability, enhanced portability and easier implementation of optical diagnostic techniques outside of the hospital setting.

The vast majority of carcinomas, comprising almost 90% of all human cancers, originate from the topmost epithelial tissue layer. This layer comprises of thin sheets of tightly packed cells that line most surfaces of internal structures within the body, the internal cavities (lumens) of hollow organs, as well as the surface of the skin. The epithelial layer lies directly above a fibered meshwork of extracellular proteins known as the basement membrane. This second tissue layer, known also as the basal lamina, effectively separates the epithelia above it from the underlying connective tissue layers it is anchored upon, termed the stroma. The basement membrane serves many functions: 1) a scaffold on which cells of the epithelial layer are adhered to (Weinberg, 2007), 2) a point of attachment for various biological signalling molecules (Tanjore and Kalluri, 2006; Weinberg, 2007), 3) a source of essential proteins required for angiogenesis (Kubota *et al.* 1988), and 4) a mechanical barrier preventing entry of cancer cells originating from the epithelial layer into the stromal tissue beneath (Fenyvesi, 2003; Weinberg, 2007).

Given its high-resolution imaging capabilities, the unique proposition of optical imaging modalities for early cancer detection may therefore be the ability to accurately identify dysplastic/cancerous cells in the surface epithelia before they have broken through the basement membrane and invaded underlying stromal tissue. With this ability to detect the very first signs of cancer with fine detail in real-time, some researchers have coined the phrase 'optical biopsy' to describe various optical imaging approaches such as fluorescence spectroscopic imaging, optical coherence tomography (OCT), diffuse reflectance spectroscopic imaging and fluorescence confocal microendoscopy (FCE), amongst many others.

Further motivations behind the implementation of optical imaging techniques for cancer diagnosis include:

i. Eliminating the need for non-targeted and highly random tissue biopsies for histological analysis; rather, a thorough inspection of suspect tumour tissue regions can be performed *in vivo* using high-resolution optical probes.
ii. Immediate acquisition of diagnostic information that can then be relayed quickly to the clinician and patient.
iii. Reducing healthcare costs as a result of decreasing the need for time-consuming tissue biopsy and histology procedures.
iv. Surgical guidance during the removal of confirmed malignant lesions once they have been accurately identified.
v. Post surgical assessment of tumour resection margins to ensure complete removal of all cancerous tissue and that no remnants are left behind which would otherwise lead to tumour re-growth.

1.3. Overview of the thesis

The work discussed in this thesis concerns the development of a multimodal supercontinuum fibre laser prototype system as applied to multispectral fluorescence imaging (MFI) and hyperspectral reflectance imaging (HRI) procedures, together with the use of a commercially available fluorescence confocal endomicroscopy (FCE) system for novel imaging applications.

Chapter 2 serves as the main introduction to this thesis, setting the overall tone by presenting several key concepts and motivations for the multidisciplinary work being performed. Besides detailing various light-tissue interaction events that are integral to all optical imaging approaches, three mini literature reviews are also included as preambles to the techniques investigated.

Chapter 3 describes MFI experiments on fluorescent dyes and collagen gel tissue phantoms for initial validation of a custom-built multispectral imaging-based spectroscopic system. The aim was to perform laser-induced, excitation-resolved MFI at

the macroscopic level with automated wavelength selection using either a motorised slit or a digital multimirror device (DMD). Also described in depth are two data dimensionality reduction techniques for processing of the acquired greyscale intensity image data, namely Principal Component Analysis (PCA) and fixed reference isometric mapping (FR-IsoMap), resulting in the generation of an RGB colour map for more qualitative analysis of the imaged region.

Chapter 4 extends on work in the previous chapter by investigating the diffuse reflectance properties of lamb and human tissues with HRI in addition to MFI. As a step towards future *in vivo* application, the acquisition optics are now fully incorporated into a laparoscope setup. FR-IsoMap dimensionality reduction is later performed on the acquired fluorescence and diffuse reflectance tissue images for distinguishing between disease states. This demonstrates the potential application of our macroscopic imaging system as a 'red-flag' technique as well as a possible method for performing photodynamic diagnosis (PDD) on photosensitised tissues. Histopathological correlation with the imaging results is also discussed.

Chapter 5 presents preliminary results from FCE performed on various *in vitro* human cancer cell lines with the commercial CellvizioGI FCE system. Our aim was to evaluate the microscopic cellular imaging properties of the system as a method for *ex vivo* cellular analysis and also for understanding the contrast to be expected during future *in vivo in situ* work. Additionally, FCE is applied on chemotherapy drug treated ovarian adenocarcinoma cell lines for monitoring chemotherapy response at the cellular level and as a faster alternative compared to conventional means.

Chapter 6 describes the use of FCE for morphological and functional point imaging of *ex vivo* and *in vivo* tissues from humans and animal tumour models. Characterisation of cancer tissue morphology is performed on healthy and cancerous tissues with the aid of non-specific optical contrast agents. Later, functional tissue properties are investigated using photosensitised and fluorescent-labelled deoxygluocose-treated *in vivo* murine tumours. The chapter concludes with the proposition of a novel multimodal endoscopic viewfinder (MEV) imaging technique for early cancer detection and diagnosis incorporating the three previously described techniques.

Finally, Chapter 7 discusses the possible challenges faced when implementing such optical imaging techniques in a real-time clinical context, lists potential solutions to address these concerns as well as provides an outlook for future work to be performed with these optical diagnostic systems.

1.4. References

About the NHS 2010 [online]. [Accessed 25th September 2010]. Available: http://www.nhs.uk/NHSEngland/thenhs/about/Pages/overview.aspx.

Barchielli A, Amorosi A, Balzi D, Crocetti E, Nesi G. Long-term prognosis of gastric cancer in a European country: a population-based study in Florence (Italy). 10-year survival of cases diagnosed in 1985–1987. *European Journal of Cancer* 2001;**37**:1674–1680.

Bedard N, Pierce M, El-Nagger A, Anandasabapathy S, Gillenwater A, Richards-Kortum R. Emerging roles for multimodal optical imaging in early cancer detection: A global challenge. *Technology in Cancer Research and Treatment* 2010;**9**:211-217.

Carter CL, Allen C. Henson. Relation of tumour size, lymph node status, and survival in 24, 740 breast cancer cases. *Cancer* 1989;**63**:181–187.

Ciccolallo L, Capocaccia R, Coleman MP, Berrino F, Coebergh JW, Damhuis RA, Faivre J, Martinez-Garcia C, Møller H, Ponz de Leon M, Launoy G, Raverdy N, Williams EM, Gatta G. Survival differences between European and US patients with colorectal cancer: role of stage at diagnosis and surgery. *Gut* 2005;**54**:268–273.

Fenyvesi A. The prognostic significance of type IV collagen expression in colorectal carcinomas. *Archive of Oncology* 2003;**11(2)**:65-70.

Gann PH. Interpreting recent trends in prostate cancer incidence and mortality. *Epidemiology* 1997;**8**:117–120.

Hellsten S, Ljungerud G, Glifberg I. Bladder carcinoma. Long-term survival and late recurrence. *Scandinavian Journal of Urology and Nephrology* 1983;**17**:57–61.

Horn LC, Fischer U, Raptis G, Bilek K, Hentschel B. Tumor size is of prognostic value in surgically treated FIGO stage II cervical cancer. *Gynecologic Oncology* 2007;**107**:310–315.

Jeffreys B. 2009. NHS faces huge budget shortfall [online]. [Accessed 25th September 2010]. Available: http://news.bbc.co.uk/1/hi/8091427.stm.

Jones LA, Chilton JA, Hajek RA, Iammarino NK, Laufman L. Between and within: international perspectives on cancer and health disparities. *Journal of Clinical Oncology* 2006;**24**:2204-2208.

Kubota Y, Kleinman HK, Martin GR, Lawley TJ. Role of laminin and basement membrane in the morphological differentiation of human endothelial cells into capillary-like structures. *Journal of Cell Biology* 1988;**107**:41589-41598.

Maguire A, Porta M, Malats N, Gallén M, Piñol JL, Fernandez E. Cancer survival and the duration of symptoms. An analysis of possible forms of the risk function. *European Journal of Cancer* 1994;**30**:785–792.

Mathers CD, Loncar D. New projections of global mortality and burden of disease from 2002 to 2030. *PLoS Medicine* 2006;**3(11)**:e442.

Miller AR, Davis GL, Oden ZM, Razavi MR, Fateh A, Ghazanfari M, Abdolrahimi F, Poorazar S, Sakhaie F, Olsen RJ, Bahrmand AR, Pierce MC, Graviss EA, Richards-Kortum R. Portable, battery-operated, low-cost, bright field and fluorescence microscope. *PLoS One* 2010;**5(8)**:e11890.

Pontén J, Adami HO, Bergström R, Dillner J, Friberg LG, Gustafsson L, Miller AB, Parkin DM, Sparén P, Trichopoulos D. Strategies for global control of cervical cancer. *International Journal of Cancer* 1995;**60**:1–26.

Ponz de Leon M, Benatti P, Di Gregorio C, Fante R, Rossi G, Losi L, Pedroni M, Percesepe A, Roncucci L. Staging and survival of colorectal cancer: are we making progress? The 14-year experience of a specialized cancer registry. *Digestive and Liver Disease* 2000;**32**:312–317.

Porta M, Gallen M, Malats N, Planas J. Influence of "diagnostic delay" upon cancer survival: an analysis of five tumour sites. *Journal of Epidemiology & Community Health* 1991;**45**:225–230.

Richards MA, Westcombe AM, Love SB, Littlejohns P, Ramirez AJ. Influence of delay on survival in patients with breast cancer: a systematic review. *Lancet* 1999;**353**:1119–1126.

Sant M, Allemani C, Capocaccia R, Hakulinen T, Aareleid T, Coebergh JW, Coleman MP, Grosclaude P, Martinez C, Bell J, Youngson J, Berrino F; EUROCARE Working Group. Stage at diagnosis is a key explanation of differences in breast cancer survival across Europe. *International Journal of Cancer* 2003;**106**:416–422.

Sargeran K, Murtomaa H, Safavi SM, Vehkalahti MM, Teronen O. Survival after diagnosis of cancer of the oral cavity. *British Journal of Oral and Maxillofacial Surgery* 2008;**46**:187–191.

Smith R. 2009. NHS will face £15bn budget shortfall due to effects of recession managers warn [online]. [Accessed 25th September 2010]. Available: http://www.telegraph.co.uk/health/healthnews/5485814/NHS-will-face-15bn-budget-shortfall-due-to-effects-of-recession-managers-warn.html.

Subramanian S, Sankaranarayanan R, Bapat B, Somanathan T, Thomas G, Mathew B, Vinoda J, Ramadas K. Cost-effectiveness of oral cancer screening: results from a cluster randomized controlled trial in India. *Bulletin of the World Health Organisation* 2009;**87**:200–206.

Summerton N. General practitioners and cancer: primary care oncology needs more research if it is to develop. *British Medical Journal* 2000;**320**:1090–1091.

Tanjore H, Kalluri R. The role of type IV collagen and basement membranes in cancer progression and metastasis. *American Journal of Pathology* 2006;**168(3)**:715-717.

Teppo L, Dickman PW, Hakulinen T, Luostarinen T, Pukkala E, Sankila R, Söderman B. Cancer patient survival – patterns, comparisons, trends – a population-based Cancer Registry study in Finland. *Acta Oncologica* 1999;**38**:283–294.

The GLOBOCAN Project – GLOBOCAN 2008: Cancer Incidence and Mortality Worldwide in 2008 [online]. [Accessed 3rd June 2010]. Available: http://globocan.iarc.fr/.

Tunstall-Pedoe H. Preventing Chronic Diseases. A Vital Investment: WHO Global Report. *International Journal of Epidemiology* 2006;**35**:1107.

Vis AN, Roemeling S, Reedijk AM, Otto SJ, Schröder FH. Overall survival in the intervention arm of a randomized controlled screening trial for prostate cancer compared with a clinically diagnosed cohort. *European Urology* 2008;**53**:91–98.

Wang JH, Changchien CS, Hu TH, Lee HM, Kee KM, Lin CY, Chen CL, Chen TY, Huang YJ, Lu SN. The efficacy of treatment schedules according to Barcelona Clinic Liver Cancer staging for hepatocellular carcinoma – survival analysis of 3892 patients. *European Journal of Cancer* 2008;**44**:1000–1006.

Weinberg RA. *The Biology of Cancer*. London:Garland Science, Taylor & Francis Group, LLC. 2007.

Weissleder R, Pittet MJ. Imaging in the era of molecular oncology. *Nature* 2008;**452**:580-589.

2

Multispectral Imaging – Principles, Techniques and Motivations

2.1. Introduction **34**

2.2. Light-tissue interactions relevant to optical imaging **34**

2.3. Fluorescence in biological tissue **35**
2.3.1. Definition and basic principles **35**
2.3.2. Fluorophores – the origins of fluorescence **37**
2.3.2.1. Endogenous fluorophores **37**
Amino acids **38**
Collagen and elastin **39**
Pyridine nucleotides and flavoproteins **41**
Porphyrins **41**
2.3.2.2. Exogenous fluorophores **42**
Molecular dyes **43**
Dye-antibody and dye-peptide conjugates **43**
Fluorescent and bioluminescent protein probes **44**
Photosensitiser probes **45**
Quantum dots and nanoparticles **46**

2.4. Absorption and scattering events **47**

2.5. Optical imaging techniques – the state of the art **49**
2.5.1. Overview **49**
2.5.2. Fluorescence spectroscopy **50**
2.5.3. Diffuse reflectance spectroscopy **56**
2.5.4. Fluorescence confocal endomicroscopy **61**

2.6. From point-measurements to region-based detection **68**

2.7. Summary and conclusions **69**

2.8. References **70**

2.1. Introduction

This chapter provides an overview of diagnostic imaging techniques for cancer detection, briefly summarising current clinical imaging techniques and discussing emerging multispectral optical imaging modalities in greater detail. Besides describing the various principles behind optical diagnostic approaches in depth, the chapter also contains short literature reviews that serve as introductions to the three optical imaging modalities explored in this thesis, namely multispectral fluorescence imaging (MFI), hyperspectral reflectance imaging (HRI) and fluorescence confocal endomicroscopy (FCE) together with various combinations of these three methods. The chapter concludes with a short discussion on the merits of optical 'regional' imaging over point-based spectroscopic techniques and the motivations for our work.

2.2. Light-tissue interactions relevant to optical imaging

Biological tissue comprises a myriad of different structural and biochemical components, all of which influence the behaviour of light as it interacts with tissue. When a photon of light arrives at the surface of a tissue boundary e.g. the mucosal epithelium of the colon, one of a series of events may take place as illustrated in Figure 2.1. Scenario A represents reflection events like regular surface reflections whereby the photon is returned directly from the surface of the tissue, yielding very little information about subcellular structures. Scenario B refers to an elastic scattering event where the photon has penetrated deeper into the underlying stroma, undergoes back scattering from various internal tissue structural components, and is then returned to the surface with no change in its overall energy. Scenario C depicts an absorption event whereby the photon's energy is absorbed by chromophores in tissue such as oxyhaemoglobin (HbO_2) and deoxyhaemoglobin (HbR), hence preventing it from being scattered back to the tissue surface. Scenario D illustrates inelastic scattering events such as fluorescence emission or Raman scattering, whereby the energy and wavelength of the proton is altered upon interaction with subcellular biochemical or structural components. Scenarios E and F refer to the majority of light-tissue interaction events whereby the photon penetrates the tissue boundary, becomes diffusely scattered in the underlying stroma and is later either absorbed by a tissue chromophore or diffusely reflected back to the surface respectively.

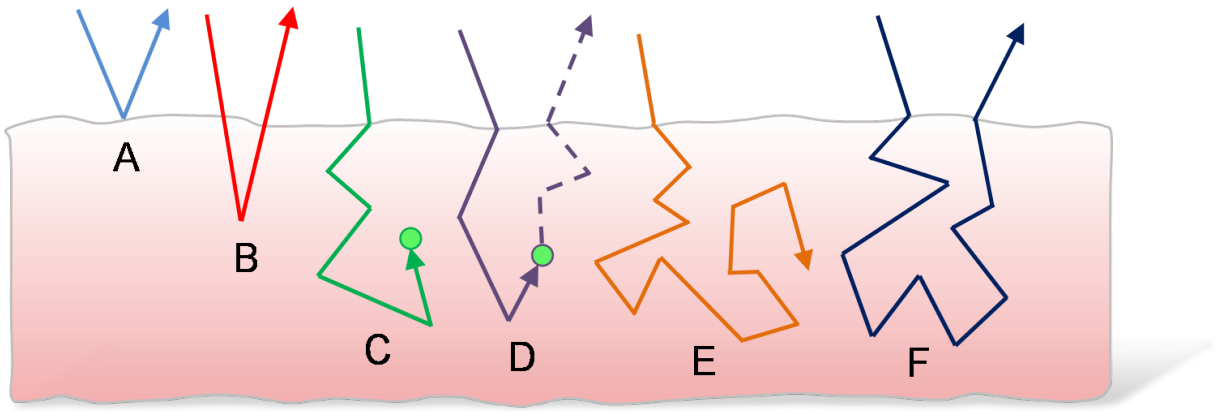


Figure 2.1. Graphical representation of various light-tissue interaction scenarios: reflection (Fresnel or regular) (A); elastic back scattering (B); absorption (C), inelastic events e.g. fluorescence emission or Raman scattering (D); diffuse scattering resulting in photons absorbed into the tissue or scattered back to the atmosphere respectively (E and F). (Adapted from Bigio and Bown, 2004)

For the purposes of this thesis, the discussion shall be focused on fluorescence emission and reflectance events, both of which will be described later in greater detail.

2.3. Fluorescence in biological tissue

2.3.1. Definition and basic principles

Fluorescence is defined as the radiative transition between two electronic states of the same spin multiplicity (Redmond, 2003). It is the emission of light by fluorescent molecules, known as fluorophores, within nanoseconds after absorbing light of a shorter wavelength (Lichtman and Conchello, 2005). This difference between the shorter exciting and longer emitted wavelengths is known as the 'Stokes' shift', which arises due to a loss in energy during rapid decay to the lowest energy states (Lakowicz, 1999).

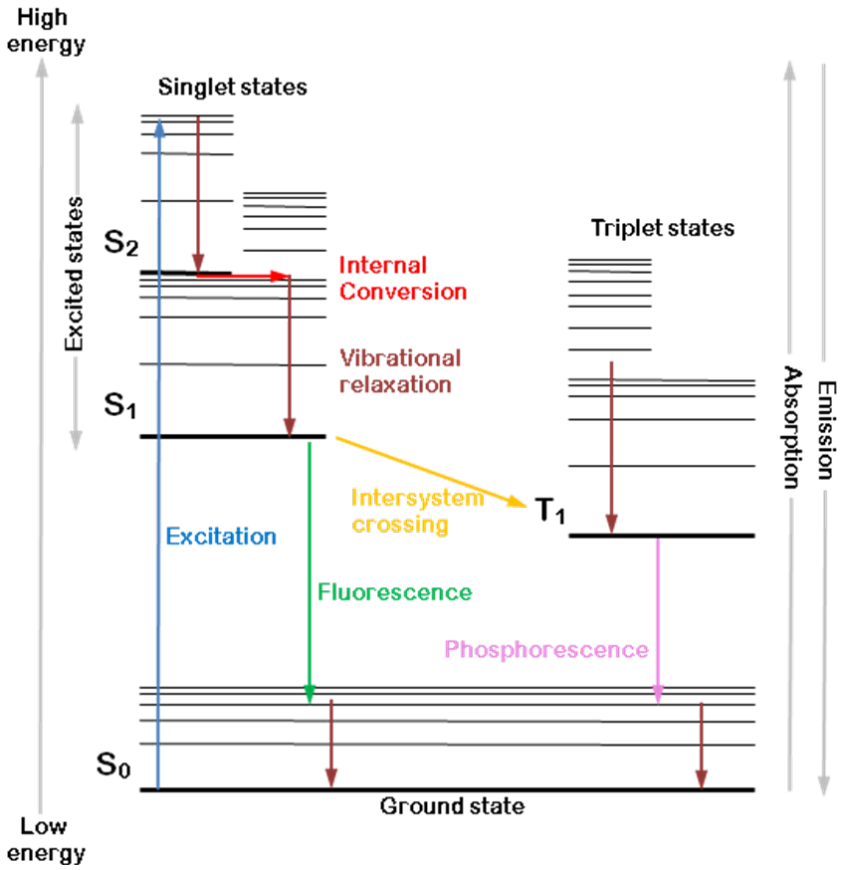


Figure 2.2. Jablonski energy level diagram indicating the ground (S_0) and excited (S_1, S_2) electronic states as well as detailing the various electronic transitions that occur during the processes of absorption and relaxation. The S_2 excited state contains the most energy followed by states S_1 and then S_0.

Figure 2.2 shows a Jablonski energy level diagram indicating the ground (S_0) and excited (S_1, S_2) electronic states, as well as detailing the various electronic transitions that occur during the processes of energy absorption and emission. After absorbing light energy (photons) in the UV/visible region, a fluorophore is rapidly elevated from its ground state (S_0) to its excited state (S_1) with an electron being moved into a different orbital that is further away from the nucleus (Lichtman and Conchello, 2005; Ramanujam, 2000). Occasionally the absorbed photon's energy is large enough to cause the fluorophore to undergo a change in both vibration and rotation. The end result is the movement of an electron into the higher electronic orbitals (elevation to the higher excited state of S_2) (Lakowicz, 1999; Ramanujam, 2000). Once the higher excited states have been reached, the fluorophore then loses its absorbed energy rapidly via processes known as vibrational relaxation and internal conversion until the lowest vibrational level of the S_1 state is attained. From here the fluorophore emits its energy in the form of fluorescence and

returns to its ground state, S_0. Alternatively, energy can also be lost as phosphorescence emission by a process known as intersystem crossing during a transition to the triplet states (Rhys-Williams, 2000). The minimum requirement for fluorescence to occur is for the absorbed photon to have enough energy to bring about the transition of an electron into a higher electronic orbital i.e. the S_0 to S_1 transition (Lichtman and Conchello, 2005).

2.3.2. Fluorophores – the origins of fluorescence

Two broad classes of fluorophores exist – endogenous fluorophores, which occur naturally in biological tissue, and exogenous fluorophores, which are foreign fluorescent agents applied to tissues for enhancing image contrast during various fluorescence imaging procedures.

2.3.2.1. Endogenous fluorophores

Naturally occurring endogenous fluorophores encompass a variety of amino acids, structural proteins, enzymes and their co-enzymes, vitamins, lipopigments and porphyrins, which contribute to the overall detected tissue autofluorescence signal. Through measurement of these autofluorescence signals, it would be possible in theory to elucidate the relative concentrations and redox states of these fluorescent compounds, ultimately revealing the biochemical and disease state of the tissue being studied without the application of exogenous fluorescent agents (Bigio and Bown, 2004; Xu and Povoski, 2007). For most endogenous fluorophores, their excitation maxima range between 250 to 450 nm (UV/visible spectral range), with emission maxima lying between 300 to 700 nm (UV/visible/near-infrared spectral regions) (Figure 2.3). Various endogenous fluorophores have been identified which are believed to be associated with tissue transformation processes around the onset of carcinogenesis (Ramanujam, 2000). These include the amino acids tryptophan (Hubmann *et al.*, 1990) and tyrosine (Ganesan *et al.*, 1998), the structural proteins elastin and collagen (Bottiroli *et al.*, 1995; Romer *et al.*, 1995; Zonios *et al.*, 1996), the metabolic co-enzymes NADH (Andersson-Engels *et al.*, 1990) and FAD (Alfano *et al.*, 1984), and porphyrins (Ghadially *et al.*, 1963). Table 2.1 lists the of excitation and emission maxima of these fluorophores.

Endogenous fluorophores	Excitation maxima (nm)	Emission maxima (nm)
Amino acids:		
Tryptophan	280 - 295	345 - 350
Tyrosine	270 - 275	300 - 320
Structural proteins:		
Collagen	325	400, 405
Elastin	290, 325	340, 400
Metabolic co-enzymes:		
FAD	450	535
NADH	290, 351	440, 460
Porphyrins	400-450	630, 690

Table 2.1. Excitation and emission maxima of endogenous fluorophores identified as being associated with tissue transformation processes around the onset of carcinogenesis. (Adapted from Ramanujam, 2000 and Gillies *et al.*, 2000)

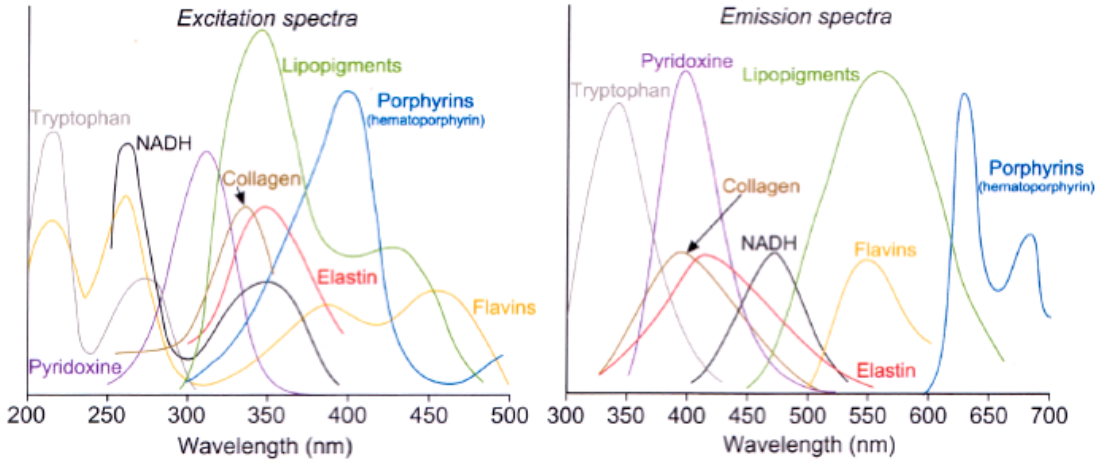


Figure 2.3. Excitation and emission spectra of various endogenous fluorophores present in biological tissue. Spectra are depicted under optimal excitation/emission conditions. (Reproduced from Webb, 2003; Adapted from Wagnieres *et al.*, 1998)

Amino acids

Amino acids make up the fundamental subunits of proteins. Of the 20 different residues in existence, tryptophan, tyrosine and phenylalanine belong to the aromatic class, with each possessing polycyclic aromatic side chains that confer their fluorescent properties (see Figure 2.4, dashed red circles). These three amino acids jointly contribute to the overall protein fluorescence in biological tissue, dominated mostly by emissions from tryptophan which absorbs at the longest wavelength range out of the three residues

(between 280 to 295 nm). In addition, energy absorbed by both tyrosine and phenylalanine is frequently transferred to tryptophan residues of the same protein, further boosting its contribution to the overall observed fluorescence signal (Lakowicz, 1999). Protein fluorescence is often observed at excitation wavelengths around 280 nm and is mainly attributed to tyrosine and tryptophan residues (quantum yields of 0.14 and 0.13 respectively); due to the low quantum yield of phenylalanine (around 0.03), its fluorescence contributions have seldom been observed (Chen *et al.*, 1967).

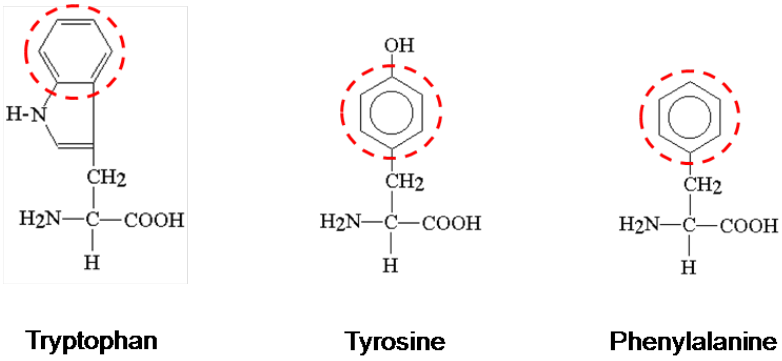


Figure 2.4. Chemical structures of the amino acids tryptophan, tyrosine and phenylalanine. The aromatic rings in each structure (dashed red circles) confer fluorescent properties to these molecules.

Differences in cellular protein content between normal and malignant human oral epithelial cell suspensions were studied by Ganesan and colleagues using a fluorescence spectroscopic approach (Ganesan *et al.*, 1998). The group observed differences in the normalised excitation spectra at 340 nm emission between both cell suspensions and found that this was attributed to differences in the biodistribution of tryptophan and tyrosine between normal and malignant cellular classes. We do not expect elicitation of any fluorescence emissions from these amino acids because the optical systems utilised in this thesis generate laser excitation in the visible to near-infrared spectrum, which lie beyond the absorption maxima of these tissue fluorophores that fluoresce when excited in the ultraviolet range.

Collagen and elastin

Collagen and elastin make up a family of fibrous proteins that serve as mechanical scaffolds for structural support in nearly all organs of the human body.

Collagen proteins are the major proteins of the extracellular matrix (ECM). They form the main component of skin and bone in mammals and constitute approximately 25% of their total protein mass (Alberts *et al.*, 2002). About 20 types of collagen proteins have been discovered to date, with types I, III, II and IV being the most commonly occurring. Type I collagen is the main collagen variety in humans and composes densely packed bundles of thick, coarse fibrils whose primary function is tension resistance. These are localised in areas of the body that experience high mechanical stress e.g. organ capsules, tendons and the adventitial layer of blood vessels (Montes, 1996). Type III collagen is composed of loosely arranged thin individual fibrils (characterised as reticulin fibres) and is found in the dermis of skin, wall linings of blood vessels and the inner muscular walls of the small intestine where they play a structural support role (van der Rest and Garrone, 1991; Montes, 1996). Type II collagen exists as thin fibrils that together make up a fine three-dimensional fibered network. These are found predominantly in hyaline and elastic cartilages of the larynx, trachea and bronchi (Montes, 1996; Mullazehi *et al.*, 2007). Type IV collagen is composed of neither discrete fibres nor fibrils, but rather fine microfibrils of ordered molecules (Montes, 1996). These form a major component of the basement membrane of epithelial tissue, performing a dual function of tissue support and as a filtration barrier against macromolecules (Tanjore and Kalluri, 2006; Fenyvesi, 2003).

Elastin is the main component of elastic fibres present in various vertebrate tissues such as the skin, blood vessels and lungs (Stryer, 1988; Alberts *et al.*, 2000). The presence of a network of elastic fibres in the extracellular matrix of these tissues allows them to be tough yet elastic enough so that they can recoil after transient stretching (Alberts *et al.*, 2000).

Fluorescence has been observed from both collagen (Fujimoto, 1977) and elastin (Deyl *et al.*, 1980). This has been attributed to the occurrence of cross-links within both protein types: hydroxylysyl pyridoline and lysyl pyridinoline in collagen, and desmosine and isodesmosine in elastin (Eyre *et al.*, 1984).

Pyridine nucleotides and flavoproteins

Both pyridine nucleotides (PNs) and flavoproteins (FPs) play an important role in the electron transport chain during the process of adenosine triphosphate (ATP) synthesis (Stryer, 1988; Richards-Kortum and Sevick-Muraca, 1996). Both nicotinamide adenine dinucleotide and flavin adenine dinucleotide function as major electron acceptors during this process when they are in their oxidised forms of NAD^+ and FAD respectively. The fluorescent forms of these electron carriers are the reduced form of PNs, NADH, and oxidised form of FPs, FAD, both of which emit fluorescence when excited with UV and blue light respectively (Ramanujam, 2000; Richards-Kortum and Sevick-Muraca, 1996). Figure 2.5 shows the nicotinamide ring of NAD^+ (dashed red circles) that confers fluorescence to the molecule in this reduced form.

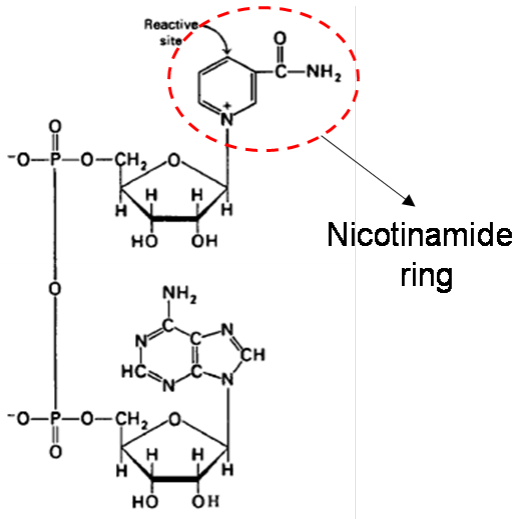


Figure 2.5. Molecular structure of the oxidised form of nicotinamide adenine dinucleotide, NAD^+. The molecule is one of two major electron acceptors during ATP synthesis. The nicotinamide ring (dashed red circles) confers fluorescence to the molecule in its reduced form - NADH. (Adapted from Stryer, 1988; Richards-Kortum and Sevick-Muraca, 1996)

Porphyrins

Porphyrins are precursors in the process of haem biosynthesis and have been found to be the only photosensitiser produced within the human body (Battle, 1993). These endogenous fluorophores give off a red fluorescence with emission maxima at 630 and 700 nm when excited in the blue spectral region between 400 and 450 nm (Ramanujam,

2000) and have also been found to accumulate preferentially in cancerous tissue (Yang *et al.*, 1987; Battle, 1993). Several hypotheses have been proposed to account for this occurrence:

i. Cancer cells have upregulated expression of the low-density lipoprotein (LDL) receptor due to an increased cholesterol requirement. This arises because of increased membrane synthesis during rapid cellular proliferation (Hamblin and Newman, 1994). The increased number of LDL receptors therefore serves as possible points of entry for plasma lipoproteins, which are major carriers of lipophilic porphyrins *in vivo* (Jori *et al.*, 1984).
ii. Tumour regions contain a higher proportion of lipid bodies than the normal surrounding tissue with more hydrophobic cellular membranes. This may result in the preferential accumulation of hydrophobic photosensitisers within the tumour (Freitas, 1990).
iii. Reduced lymphatic drainage to the tumour may result also in a build up of porphyrins, either in the form of aggregates or as protein complexes (Bugelski *et al.*, 1981).
iv. Porphyrin aggregates may be taken up by the tumour in increased amounts due to a higher occurrence of phagocytotic or pinocytotic activity (Jori, 1989).
v. Tumour-associated macrophages (TAMs) contain a high volume of porphyrins. Since TAMs make up about 20-50% of a tumour's cellular content, this may account for the high porphyrin concentration in tumours (Milas *et al.*, 1987).

2.3.2.2. Exogenous fluorophores

Exogenous fluorophores are fluorescent chromophores not naturally present in biological tissue, which may be either organic or synthetic in nature. Whilst various disease conditions have been successfully characterised via intrinsic optical signatures from tissues, image contrast may be further improved following application of these exogenous fluorescent agents for enhancement of certain tissue features or increasing existing levels of tissue autofluorescence during optical detection procedures. A vast selection is available to the biomedical researcher and the reader is directed to (Haugland,

2005) for a detailed list of fluorophores together with information on their spectral properties.

Molecular dyes

Optical imaging has regularly relied upon a variety of non-specific fluorescent dyes to induce observable changes in tissue morphology during disease progression from normal to cancer. Depending on the depth of tissue to be imaged, different dyes may be employed: dyes which absorb and emit fluorescence in the UV/visible wavelength range are often sufficient for imaging shallower, superficial layers of mucosa, while those which absorb and emit in the near-infrared (NIR) wavelength range have been employed for more effective visualisation of deeper mucosal regions. Some examples include fluorescein (and its derivatives), indocyanine green (ICG), cresyl violet, Lugol's solution, acridine orange (AO) and acriflavine hydrochloride (AH), all of which are in current clinical use or trials for cancer detection and diagnosis. Some non-specific dyes have been found to localise to a certain extent in intra- or extracellular spaces due to their size or charge distributions e.g. AH and AO, which bind to DNA and have been previously used for evaluation of confocal microendoscopy imaging procedures (Polglase *et al.*, 2005; Udovich *et al.*, 2007; Pierce *et al.*, 2008), and ICG, which binds to plasma proteins present in blood such as human serum albumin (HSA) (Muckle, 1976; Desmettre *et al.*, 2000).

Dye-antibody and dye-peptide conjugates

With advances in the study of cancer biology, several tumour-associated surface receptors and antigens have been identified which serve as ideal targets for dye-antibody and dye-peptide conjugates.

Work done previously was concentrated on the conjugation of monoclonal antibodies with cyanine dyes for specific binding to tumour cell receptors (Ballou *et al.*, 1995; Ballou *et al.*, 1997; Becker *et al.*, 2001). Further studies by Ballou and colleagues demonstrated the possibility of performing effective tumour visualisation in animal models in vivo using Cy5.5 and Cy7 monoclonal antibody conjugates (Ballou *et al.*, 1998). However various obstacles have impeded its translation to humans such as the possible elicitation

of an adverse immune response, high background fluorescence, long clearance times in the blood, and the fact that these conjugated antibodies require a sufficient amount of accumulation time to produce viable fluorescent signals in target tissues (Folli *et al.*, 1994; Ballou *et al.*, 1995; Xu and Povoski, 2007).

To overcome the limitations posed by dye-antibody conjugates, various groups have investigated the application of dye-peptide conjugates composed of fluorescent dyes covalently bonded to a bioactive peptide molecule. Like dye-antibody conjugates, these are specific to targets over-expressed on tumour cells e.g. the integrin receptors, which play a key role in metastasis and neovascularisation. Studies on the αVß3 integrin receptor subtype (ABIR) have shown that it interacts with a tri-peptide arginine-glycine-aspartic acid (RGD) sequence on adhesion proteins like fibronectin and collagen. Based on this finding, several groups have developed ABIR-targeting RGD peptides conjugated to NIR fluorescent cyanine labels for in vivo optical imaging with encouraging results (Wang *et al.*, 2005; Ye *et al.*, 2006). Similarly, recent studies have also found that lysosomal vesicles play an important part in metastasis, sequestering proteolytic enzymes responsible for breaking down proteins of the ECM (Roshy *et al.*, 2003). This finding was exploited by Li and colleagues who synthesised novel fluorescent probes consisting of glucosamine, an integral lysosomal amino sugar, and a covalently bonded carbocyanine NIR fluorophore, which exhibited efficient cellular uptake and strong intracellular fluorescence in human mammary epithelial cell lines (Li *et al.*, 2006).

Fluorescent and bioluminescent protein probes

Green fluorescent protein (GFP) and luciferases are the two main photoproteins that fall into this class of optical reporters.

GFP is one of the most extensively used fluorescent protein probes for studying sub-cellular processes in tumour cells such as tumour-host interaction, metastasis, gene expression, protein localisation and drug response (Tsien, 1998; Zimmer *et al.*, 2002; Ballou *et al.*, 2005). Its importance in medical science was recognised when the Royal Swedish Academy of Sciences awarded the Nobel Prize in Chemistry 2008 to the original discoverer of GFP and two of its co-developers. To date there exists different variants of GFP such as blue, cyan and yellow fluorescent proteins (BFP, CFP, YFP), which possess

different excitation and emission wavelengths to the original; efforts to develop more variants with altered absorption/emission profiles are ongoing (Choy *et al.*, 2003). For an in-depth review of fluorescent labelling using GFP, please refer to papers by Tsien, 2003 and Lippincott-Schwartz and Patterson, 2003.

Luciferases have been isolated from various sources (fireflies, bacteria, click beetles, sea pansies) and are currently used as bioluminescent reporters for a host of imaging applications, e.g. the development and monitoring of gene therapy treatment strategies (Achilefu, 2004). The main difference between fluorescence and bioluminescence imaging is that the former requires an external excitation light source for activation, whereas the latter technique only requires the presence of an enzyme substrate. As such, one big advantage bioluminescence imaging has over fluorescence imaging is the high sensitivity achieved due to low levels of background noise from autofluorescence (Choy *et al.*, 2003; Achilefu, 2004).

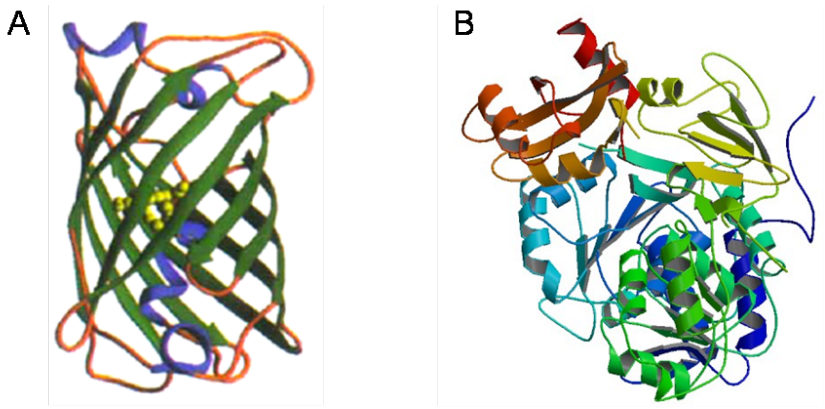


Figure 2.6. Three-dimensional structures of the green fluorescent protein (GFP) (A) and firefly luciferase (B). (Adapted from Yang *et al.*, 1996 (A) and Conti *et al.*, 1996 (B))

Photosensitiser probes

Some exogenous fluorophores currently being evaluated for clinical use were originally developed as photosensitisers for photodynamic therapy (PDT), i.e. utilising light-activated photosensitisers to destroy malignant tumours in the body. Examples of these are hematoporphyrin derivative (HpD), hypericin, phthalocyanine, pheophorbide-a, tin etiopurpurin (SnET2) and meso-tetra-(hydroxyphenyl)-chlorin (MTHPC) (Wagnieres *et al.*, 1998; Ramanujam, 2000).

A notable example of employing a PDT agent for contrast enhancing imaging purposes was demonstrated by Ecker and colleagues, who set out to compare the discrimination obtained using 5-aminolevulinic acid (5-ALA) induced protoporphyrin IX (PpIX) as a tumour marker versus using autofluorescence alone (Ecker *et al.*, 1999). 5-ALA is a precursor in heme biosynthesis. It is not a photosensitiser, but rather is converted intracellularly into the fluorescent photosensitiser PpIX, which accumulates in higher amounts in tumour tissue compared with normal tissue. This has been attributed to a deficiency in ferrochelatase (the enzyme required for PpIX to heme conversion) in tumours as well as other reasons mentioned earlier under the 'Porphyrins' of section 2.3.2.1 of this chapter.

The exploitation of photosensitisers as contrast agents has raised some issues concerning safety and toxicity e.g. skin photosensitivity and non-specific accumulation. To address this, research is being carried out to uncover non-photosensitising agents that bear similar absorption and fluorescent properties to photosensitisers so as to serve as alternative contrast agents. Examples of these are Nile blue and its derivatives as well as the family of carotenoporphyrins (Richards-Kortum and Sevick-Muraca, 1996).

Quantum dots and nanoparticles

Quantum dots (QDs) and nanoparticles (NPs) are small light-emitting particulates composed of polymers, lipids and metals that have emerged as a novel class of fluorescent labels for the early detection and treatment of cancer. These are delivered to tumours *in vivo* via passive or active targeting mechanisms (Gao *et al.*, 2004): under passive conditions, QDs and NPs accumulate preferentially in tumour tissues because of ineffective lymphatic drainage and hyperpermeabilised 'leaky' neovasculatures, resulting in the "enhanced permeability and retention" effect (EPR effect) (Maeda *et al.*, 2000; Jain, 2001); in the active mode, QDs and NPs are 'bioconjugated' to biological ligands such as antibodies, peptides, growth factors and other small molecules for targeting receptors and antigens on the surface of tumour cells with added affinity and specificity (Akerman *et al.*, 2002; Medintz *et al.*, 2005).

Several groups have also demonstrated the use of photosensitiser-conjugated QDs for a more targeted photodynamic therapeutic approach (Samia *et al.*, 2003; Juzenas *et al.*,

2008). Most photosensitisers are known to have poor water solubility and tend to form aggregates in solution, which may affect their photochemical and cell-penetrating properties (Allen *et al.*, 2001). To address this issue as well as alleviate concerns regarding the possible toxicity of QDs (e.g. cadmium-based QDs), NPs are being studied as possible drug delivery vehicles to ensure accurate and efficient transport of photosensitisers to tumour sites. One example is the use of gold nanoparticles stabilised (coated) with a phthalocyanine (Pc) photosensitiser, which demonstrated an enhanced generation of cytotoxic singlet oxygen as compared to free Pc alone (Hone *et al.*, 2002). In the same vein, silica-based nanoparticles containing water-insoluble photosensitisers have been shown to be efficient carriers of the drug in aqueous solution (Roy *et al.*, 2003).

2.4. Absorption and scattering events

Whilst the observation of fluorescence spectra from biological tissues provide information relating to biochemistry and therefore the functional properties of the tissues being studied, further investigation into absorption and scattering events occurring during light-tissue interactions also offers additional diagnostic information complementary to that obtained from fluorescence. This thus allows a more comprehensive elucidation of the tissue's overall state of health.

The main optical absorbers present in biological tissues are haemoglobin (Hb), melanin and water (Wang and Wu, 2007). The two forms of Hb, oxyhaemoglobin (HbO_2) and deoxyhaemoglobin (HbR), each possess different absorption coefficients as seen in Figure 2.7 (Vogel and Venugopalan, 2003). To date, several Hb absorption bands have been identified and these have been found to be at the wavelengths of around 415 nm, 542 nm, 572 nm and 930 nm (Shibuya *et al.*, 2003). Melanin is localised only in the epidermal layers of the skin (top 50 to 100 μm) and in hair follicles (Zonios *et al.*, 2001), and has been found to absorb in the UV-visible wavelength range with low absorption in the near-infrared (NIR) region. Water does not absorb in the UV-visible range and is negligible as an optical absorber when compared to Hb and melanin in this wavelength range. Other common optical absorbers such as proteins and DNA have been found to absorb only in the UV range and not the visible (Campbell and Dwek, 1984). As such, it

can be safe to assume that Hb is the principal optical absorber in the visible range within the human body.

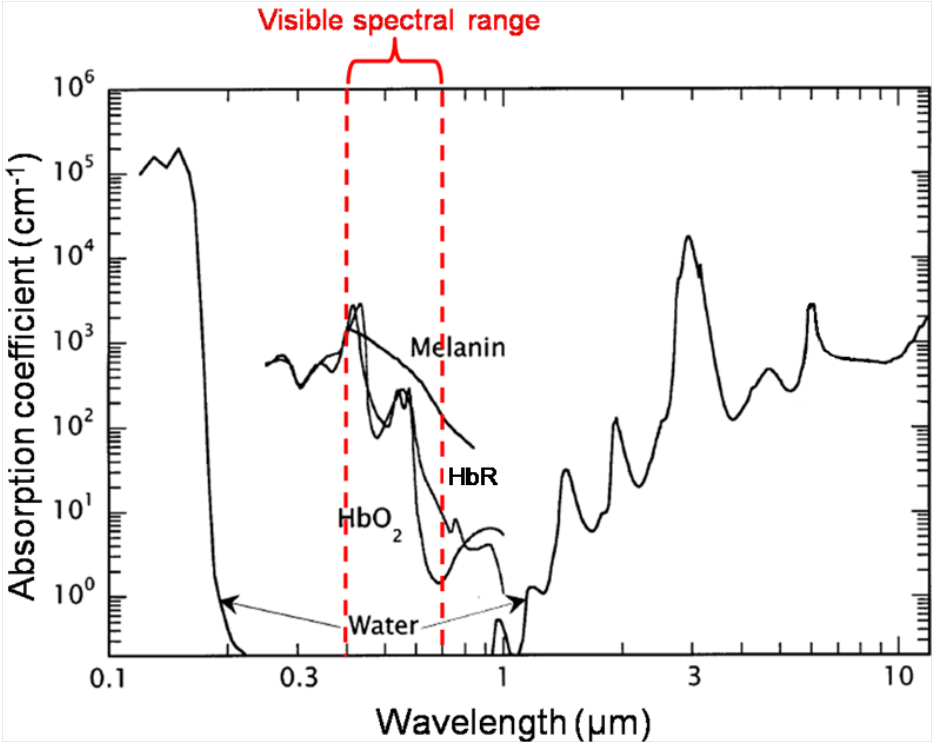


Figure 2.7. Absorption coefficients of the main endogenous absorbers present in biological tissue. (Adapted from Vogel and Venugopalan, 2003)

Optical scattering occurs when light penetrates the tissue boundary and interacts with biological scattering components comprising several tissue microstructures from both the extracellular and intracellular domains. Examples of the former are collagen fibres that are present in the stromal layers of tissue (Saidi *et al.*, 1995), whilst examples of the latter include cellular nuclei (Perelman *et al.*, 1998; Mourant *et al.*, 2000), mitochondria (Beauvoit *et al.*, 1994), and lysosomes and vesicles (Wang and Wu, 2007). Scattering has been shown to occur most strongly when the size of the scatterer matches the optical wavelength of the incoming photon and when the scatterer's refractive index is markedly different to that of its surrounding tissue medium (Wang and Wu, 2007).

The study of optical absorption has allowed various cancer-related changes in tissues to be revealed, e.g. increased Hb concentration due to angiogenesis in malignant and premalignant lesions, as well as conditions of tissue hypermetabolism during tumourigenesis resulting in lowered Hb oxygen saturations (Zonios *et al.*, 1999; Wang *et*

al., 2009; Brown *et al.*, 2009; Li *et al.*, 2010). Studies relating to optical scattering events in tissue have also shed light on the state of collagen fibres in mucosal tissue and size distribution of endogenous optical scatterers such as cellular nuclei (Ferdman and Yannas, 1993; Perelman *et al.*, 1998; Mourant *et al.*, 2000; Brown *et al.*, 2009).

2.5. Optical imaging techniques – the state of the art

2.5.1. Overview

Optical imaging techniques currently in clinical use or under investigation are classified under two broad categories: 1) wide-field imaging techniques and 2) localised point-based methods. The possibility of incorporating these optical imaging techniques into medical endoscope systems allows for minimally invasive *in vivo in situ* monitoring of the human body, hence presenting a novel means of disease detection and diagnosis.

Wide-field imaging encompasses techniques like white-light endoscopy (WLE), chromoendoscopy, fluorescence endoscopy and narrow-band imaging (NBI), all of which have been employed in conjunction with high definition video endoscopes for visualising tissue regions with a field of view measuring a few squared cm. These techniques have been extensively studied especially in the gastrointestinal (GI) tract for investigating disease conditions such as Barrett's oesophagus and ulcerative colitis, and also for discriminating between benign and adenomatous polyps in the colon.

Point-based diagnostic techniques acquire data from single points on tissue surfaces owing to the use of fibre optic probes measuring a few mm in diameter. These can be further separated into two sub-categories: point spectroscopy and point (micro) imaging techniques. The former sub-category, which includes such spectroscopic methods as fluorescence, diffuse reflectance, elastic light scattering and Raman spectroscopy, acquires tissue information in the form of spectral data that is subsequently presented in a graphical format for disease diagnosis; this is based on the idea that different tissue disease states possess different spectral signatures. The latter sub-category covers imaging modalities like fluorescence confocal endomicroscopy and optical coherence tomography

- techniques that allow for the collection of high-resolution cellular-level tissue images over a small field of view.

A myriad of commercial optical imaging systems are also available on the market today. Some examples are the Lucera Spectrum system from Olympus (Japan) for endoscopic narrow-band, autofluorescence and infra-red imaging, the D-Light C system from Karl Storz Endoskope (Germany) for photodynamic diagnostic applications, the VivaScope confocal system from Lucid Inc. (USA) for examination of skin disease conditions and the DySIS spectral imaging system from Forthphotonics (UK) for cervical examination during colposcopic imaging procedures.

The next three sub-sections consist of short reviews that provide background information to the three optical imaging techniques applied in this thesis, namely fluorescence spectroscopy, diffuse reflectance spectroscopy and confocal fluorescence endomicroscopy. The use of each technique in a variety of human organs is covered, with the research papers quoted restricted as much as possible to highly cited examples within the last ten years.

2.5.2. Fluorescence spectroscopy

Fluorescence spectroscopy (FS) involves the optical detection and spectral analysis of light emitted by a fluorophore undergoing a transition from an excited electronic state to a lower electronic state (Vo-Dinh and Cullum, 2003). Different emission spectra are characterised depending on the excitation wavelength of light used, which is also affected by the morphological and biochemical characteristics of the tissue studied. Fluorescence contrast arises when endogenous fluorophores vary in concentration and distribution between different tissue types as well as between different regions and layers of the same tissue (Dacosta *et al.*, 2004). Normal and dysplastic tissues exhibit different fluorescent spectra due to malignant transformations that may alter the type, concentration and micro-distribution of endogenous fluorophores, together with the overall biochemical makeup of the tissue. This thereby results in differences in the measured fluorescence signals (Dekker and Fockens, 2005).

The idea that FS could be used as a quantitative technique to differentiate between normal and malignant tissue was first suggested by Lycette and Leslie in 1965, who

recorded the emission spectra from 330 nm excitation of normal and malignant tissue excised from the oesophagus, stomach, breast and thyroid of human patients (Lycette and Leslie, 1965). Emission spectra obtained from single-point measurements of all excised tissue samples were found to be in the range of 360 and 600 nm, with malignant tissues having lower fluorescence intensities than those of normal tissues from the same patient. Additional work by Alfano *et al.* in the early 1980s provided further evidence that FS could be used for tissue diagnosis: the group measured single-point fluorescence spectra from cancerous and normal kidney and prostate tissues from rats in addition to cancerous bladder tissues from rats and mice *in vitro* using an Argon ion laser emitting at 488 nm (Alfano *et al.*, 1984). Results obtained demonstrated a distinct difference in spectral profiles between normal and cancerous tissues, which the group attributed to distributional differences in flavin and porphyrin between the two tissue disease types.

The ability of FS to detect premalignant and early-cancerous lesions using tissue autofluorescence depends on changes in one or more of the following properties:

i. Concentration and spatial distribution of endogenous fluorophores, absorbers (e.g. haemoglobin (Hb)) and scatterers (e.g. cell membrane, nucleus and other organelles).
ii. Metabolic status of the tissue: NADH is fluorescent only in its reduced form; it has been observed that an increase in NADH fluorescence and decrease in FAD fluorescence in dysplastic cells and tissue is correlated with an increase in cellular metabolic activity.
iii. Biochemical and biophysical microenvironment of the tissue: these may affect the fluorescence quantum yield, position of spectral peaks and line widths, and
iv. Tissue architecture, e.g. the vascular network and thickness of mucosal layers, all of which may affect the fluorescence signal measured at the tissue surface.

Within the last decade, FS has been shown by various groups to have the ability to detect and diagnose different tumour types *in vivo* in various organs of the human body with high degrees of sensitivity and specificity. The following studies have relied solely on

tissue autofluorescence for generation of the emission spectra, without the aid of any exogenous agents for increasing fluorescence contrast.

Chang and colleagues set out to determine the optimal excitation wavelengths for detection of cervical intraepithelial neoplasia through the analysis of fluorescence excitation-emission matrices (EEMs) generated through *in vivo* single-point fluorescence spectroscopic measurements (Chang *et al.*, 2002). A fluorescence EEM often takes the form of a contour map in which fluorescence intensity is plotted as a function of excitation and emission wavelengths for the characterisation of fluorescence properties of a sample (see example in Figure 2.8). In the study using a prototype system, tissue autofluorescence was induced with a Xenon arc lamp at 16 different excitation wavelengths ranging from 330 to 480 nm. Spectral measurements were then taken from 351 separate single-point cervical sites in 146 patients via a fibre optic probe with its 2 mm diameter tip positioned against the cervical epithelium. The acquired data was later analysed with principal component analysis (PCA) and in pairs of diagnostic classes to determine optimal wavelengths that yielded classification algorithms with the greatest sensitivity and specificity. The group concluded that 330-340, 350-380, and 400-450 nm excitation produced the best performance, with sensitivity and specificity for discrimination of squamous normal tissue and high-grade squamous intraepithelial lesions standing at 71% and 77% respectively. This study demonstrates the importance of PCA in the interpretation of FS results.

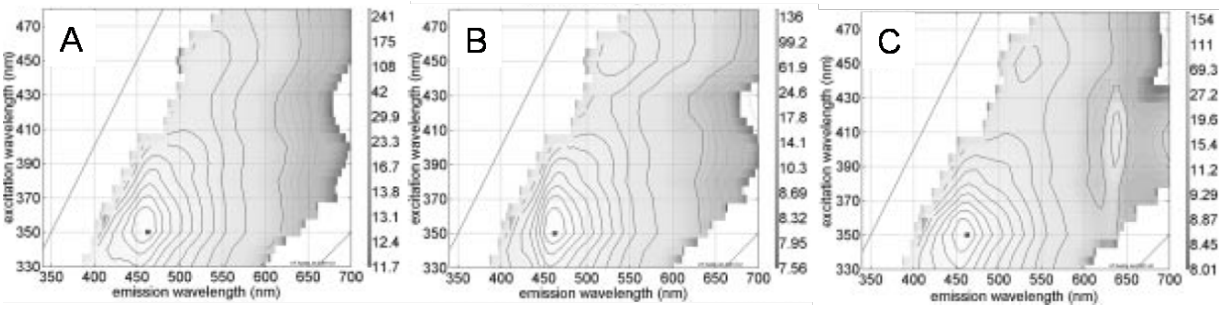


Figure 2.8. Typical example of fluorescence EEMs obtained from the cervical epithelium of a single patient: normal squamous site (A); normal columnar site (B); high-grade squamous intraepithelial lesion (HGIL) (C). Contour lines in the graphs connect points of equal fluorescence intensity. (Adapted from Chang *et al.*, 2002)

The possibility of applying FS as an improved method for the early diagnosis of ovarian neoplasia was investigated by Brewer and colleagues by studying if spectral signatures

differed between normal variations within the ovary, benign neoplasms and ovarian cancer (Brewer *et al.*, 2001). Tissue diagnosis was performed during exploratory laparotomy in patients with a Xenon arc lamp to induce fluorescence at 18 excitation wavelengths from 330 to 500 nm via a fibre optic probe. Fluorescence spectra were collected by the probe at single points on the tissue over a 2 mm circular diameter and used to create fluorescence EEMs for data analysis (Figure 2.9). From their results, the authors found that excitation at 330, 375 and 415 nm appeared the most useful diagnostically and a decrease in fluorescence at 400-430 nm excitation and 460 nm emission was found to be consistent for all the cancerous regions measured. They concluded that FS could serve as an alternative method for detection of subtle differences not apparent with either ultrasound or visual observation of the ovary.

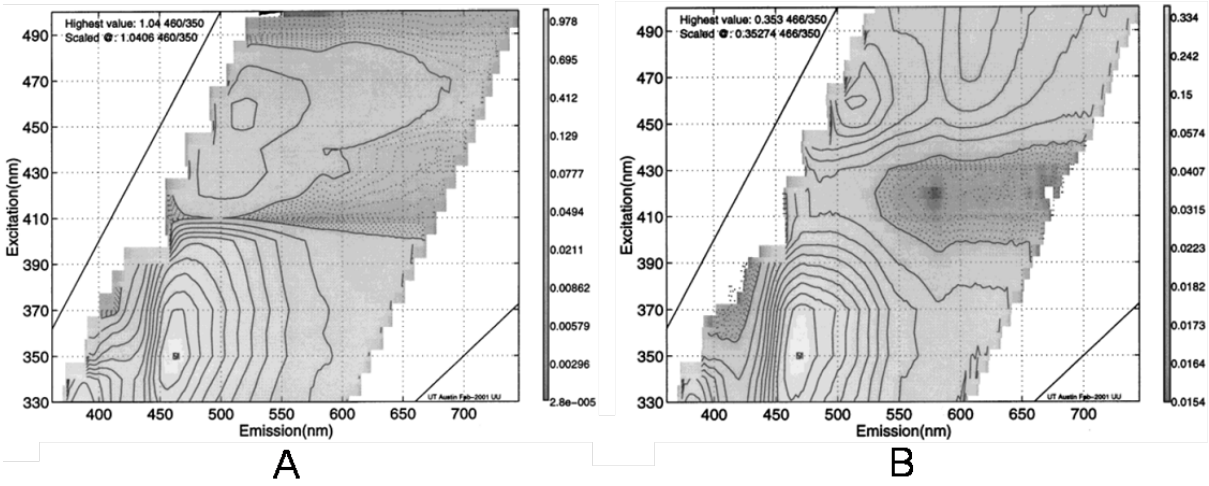


Figure 2.9. Fluorescence EEMs of a normal ovary with stromal hyperplasia and corpus albicans (A) compared against an ovary presenting high grade carcinoma (B). (Adapted from Brewer *et al.*, 2001)

The effectiveness of fluorescence endoscopy for detection of premalignant and early-stage cancerous lesions in the lung, including carcinoma *in situ* (CIS), was demonstrated by Kusunoki and colleagues during a clinical trial of the commercial LIFE (laser-induced fluorescence endoscopy) imaging system (Xillix Technologies; Richmond, BC, Canada; and Olympus Optical; Tokyo, Japan) (Kusunoki *et al.*, 2002). Such lesions are difficult to detect via white-light bronchoscopy (WLB) imaging even for experienced bronchoscopists. During the trial, a fibre optic fibre bundle was used to deliver blue light excitation at 442 nm from a helium-cadmium laser. Imaging results from the LIFE apparatus were later compared with that from conventional WLB and accuracy of diagnosis for each method was found to be 72.7% and 48.6% respectively. The emitted

fluorescence was also collected by a spectrofluorometry system for computer analysis of the emission spectra. Sensitivity of WLB alone for detection of severe dysplasia and cancer was found to be 61.2% with a specificity of 85%. However when coupled with results from LIFE, sensitivity and specificity improved to 89.8% and 78.4% respectively. This indicated that a combination of both techniques could improve the detection of endobronchial lesions, with results obtained via spectrofluorescence analysis giving a more objective basis than evaluation by the naked eye alone during conventional bronchoscopy. In addition, the study also noted that dysplastic and CIS regions exhibited less fluorescence than normal tissue, as seen when comparing white-light images to those obtained from the LIFE system (Figure 2.10).

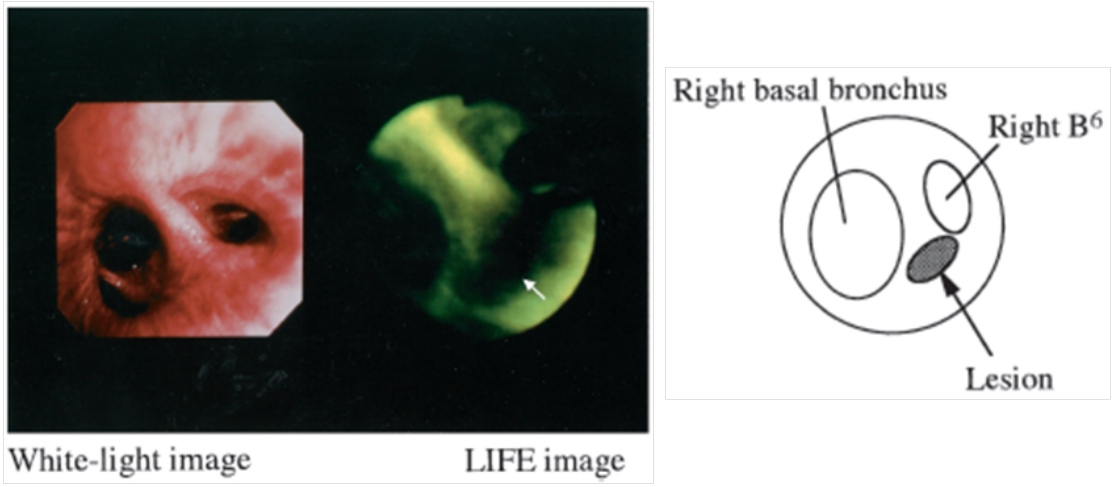


Figure 2.10. Comparison between a white-light bronchoscopic (WLB) image and LIFE image of a right lower-lobe bronchus. Under white light, the carcinoma *in situ* lesion (CIS) appears to occupy the whole area between the right basal bronchus and right bronchiole B^6 (darker red region). This is however not the case in the LIFE image – the CIS lesion was found to be present only in a smaller region. This appears as a darkened patch in the LIFE image (indicated by white arrow). (Adapted from Kusunoki *et al.*, 2002)

Wang and colleagues demonstrated an endoscopic fluorescence imaging method to identify dysplasia associated with adenomatous polyps in the colon (Wang *et al.*, 1999). Their imaging system consisted of an argon ion laser delivering excitation light at the near-UV range of 351 and 364 nm through an optical probe coupled with a standard videocolonoscope adapted for fluorescence identification *in vivo*. During the imaging process, the distance between the distal tip of the endoscope and mucosa was adjusted such that the polyp to be imaged appeared within an approximately 30 by 30 pixel region.

With this technique, dysplasia associated with 12 adenomatous polyps was identified with a sensitivity of 83% from a group of 30 patients, with the fluorescence threshold set to 80% of the average intensity of normal mucosa. All hyperplastic polyps were correctly identified as being non-dysplastic. Adenomatous polyps were also discovered to have decreased fluorescence intensity compared to adjacent regions with normal tissue.

Lane *et al.* described a hand-held imaging device that allowed fluorescence visualisation of precancerous and early cancerous lesions in the oral cavity (Lane *et al.*, 2006). A mercury-based arc lamp was used to produce blue light excitation between the wavelengths of 400 to 460 nm, with green-red fluorescence obtained from endogenous fluorophores present in the oral mucosal tissue (Figure 2.11). By taking histology as the standard benchmark, the device achieved a sensitivity of 98% and specificity of 100% when discriminating normal oral tissue from regions of severe dysplasia, CIS, or invasive carcinoma out of a sample population of 50 sites.

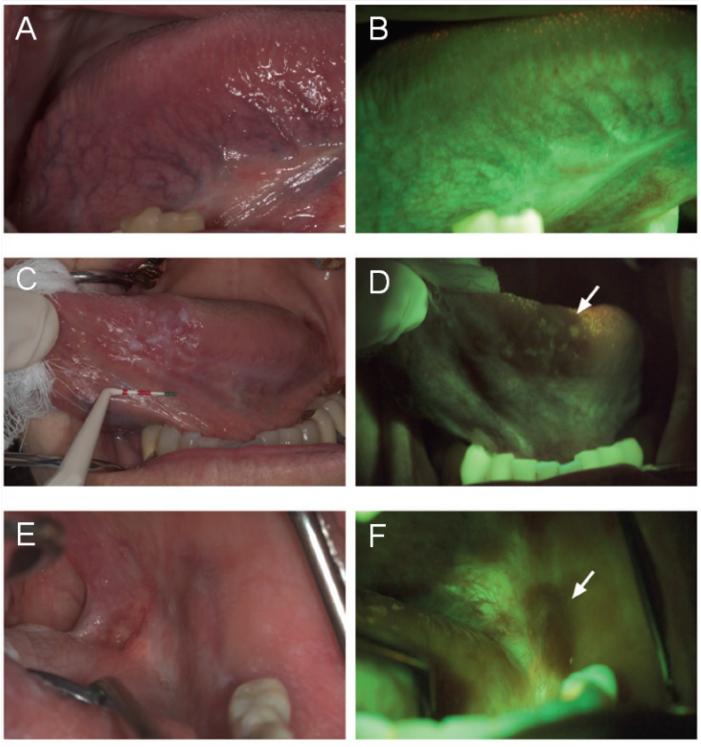


Figure 2.11. Fluorescent images of oral cavity lesions obtained from three patients. White-light and fluorescence images are shown on the left and right respectively: healthy mucosa of the ventral tongue showing a pale-green fluorescence (A and B); ventral tongue of a patient with an oral premalignant lesion, confirmed as severe dysplasia by histology (white arrow indicates biopsied region) (C and D); clinically occult lesion seen as a dark patch (indicated by white arrow) in the fluorescence image (E and F). (Adapted from Lane *et al.*, 2006)

2.5.3. Diffuse reflectance spectroscopy

Besides fluorescence spectroscopic approaches, another promising optical technique most frequently investigated for cancer detection is diffuse reflectance spectroscopy (DRS). DRS typically employs broadband light excitation in the ultraviolet/visible/near-infrared range of the spectrum (from 300 to 800 nm) and has been demonstrated previously to be successful in diagnosing neoplastic changes in the human body, e.g. in tissues of the bladder (Bigio *et al.*, 1995), colon (Zonios *et al.*, 1999), ovary (Utzinger *et al.*, 2001), cervix (Mirabal *et al.*, 2002) and breast (Volynskaya *et al.*, 2008). The hallmark of DRS is its ability to detect light that has been transmitted to the tissue surface after having undergone absorption and scattering events in the deeper underlying layers; this consequently provides information on endogenous absorbers and scatterers present in biological tissue whose biophysical states have been found to become altered during neoplastic development.

Alterations in the spectral reflectance properties of dysplastic/tumour tissues may arise due to:

i. Changes in nuclear size and the resultant nuclear-to-cytoplasmic ratio of cells in the epithelium (Drezek *et al.*, 2003; Mourant *et al.*, 1998),
ii. Neovascularisation, i.e. the formation of new blood capillaries (Dellas *et al.*, 1997; Zonios *et al.*, 1999),
iii. Changes in both HbO and HbR concentrations (Zonios *et al.*, 1999), and
iv. Changes in overall optical properties of the stromal tissue layers (Mirabal *et al.*, 2002; Tromberg, 1998).

Zonios and colleagues obtained DRS data from normal human colonic mucosa and adenomatous colon polyps, colon mucosal surface projections that are precursors of colon cancer, to demonstrate the potential of the technique for obtaining quantitative *in vivo* information of various tissue parameters, i.e. Hb content and relative concentrations of endogenous absorbers and scatterers. Data analysis was performed by means of fitting to an analytical light diffusion model derived earlier by Ferrall *et al.* (Zonios *et al.*, 1999; Ferrall *et al.*, 1992) and the results compared to that from standard histological examination. During the study, DRS spectra were obtained *in vivo* from adenomatous

polyps of 13 patients undergoing routine colonoscopy. A Xenon arc lamp was used as the white light excitation source, an imaging spectrograph dispersed the collected spectra, and a diode array detector was used to detect light between wavelengths of 360 and 685 nm. Light was delivered and collected via a 1.5 mm diameter optical fibre probe that was passed down the accessory channel of a standard colonoscope and put in contact with single points on the tissue. Calibration was performed by means of division by a DRS reference spectrum obtained from a barium sulphate ($BaSO_4$) powder suspension. Spectra were measured from various sites for each studied adenomatous polyp as well as from the normal surrounding colonic mucosa prior to its removal for histological examination (Figure 2.12). From analysis of their data, the group concluded that it was possible to obtain quantitative information from tissue such as Hb concentration, Hb oxygen saturation, effective scatterer size and effective scatterer density using DRS. They also made a number of key observations: 1) Hb is the major and possibly only significant absorber in colon mucosa, 2) adenomatous polyps are characterised by increased Hb concentration over normal mucosa, perhaps as a result of increased microvasculature volume, and 3) average effective scatterer size was larger and average effective scatterer density smaller in polyps compared to normal mucosa due to intracellular scatterer differences.

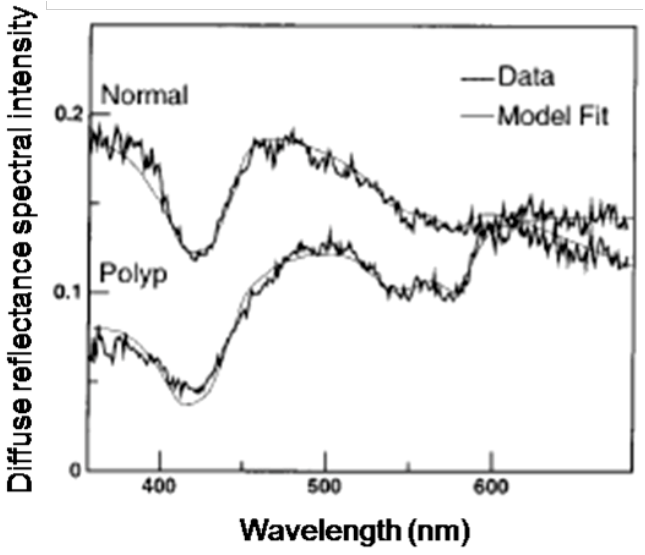


Figure 2.12. Diffuse reflectance spectral data from normal tissue and an adenomatous polyp (thick curves) together with the modeled spectra (thin curves). (Adapted from Zonios *et al.*, 1999)

DRS was explored as a means of differentiating normal, benign neoplasmic and cancerous ovarian tissue by Utzinger *et al.* in order to improve on the currently inadequate conventional methods of ovarian cancer screening tests e.g. CA-125 markers, transvaginal ultrasound and pelvic examination (Utzinger *et al.*, 2001; NIH Consensus 1995). In their study, DRS spectra were collected at 64 sites from normal and neoplastic ovarian tissue at three different source-detector separations in 16 patients undergoing exploratory laparotomy and oophorectomy. Broadband illumination was provided by a Xenon arc lamp equipped with a 295 nm long-pass filter, and a fibre optic probe was used to transmit excitation light as well as collect the diffusely reflected light returning from the underlying tissue layers. The probe tip was put in direct contact with the tissue at single points during data acquisition and DRS spectra between 390 to 590 nm wavelengths were collected. Tissue biopsies were obtained from all interrogated ovarian sites and examined by a gynaecologic pathologist after haematoxylin and eosin (H&E) staining. The biopsied samples were then classified into eight pathological categories ranging from normal to cancer (see mean spectra in Figure 2.13). For data processing, wavelength calibration of the DRS spectra was performed using a mercury light source and the reflectance data were normalised using reference reflectance data recorded from a solution of polystyrene microspheres of 1.072 μm diameter. During data analysis for each diagnostic category (e.g. normal, benign neoplasm, cancer), the following were calculated: average value and standard deviation of spectral intensity at each wavelength, the slope at each wavelength, and integrated intensity between the wavelength ranges of 390 to 590 nm and 440 to 590 nm. From their results, the group observed that both the slope and intensity of DRS spectra may have the ability to discriminate normal from dysplastic conditions of the ovary: slopes between 510 and 530 nm were found to be most promising at all source-detector separations and intensities between 530 and 585 nm measured with a short 1.1 mm source-detector separation were found to provide the most useful discriminatory information. A combination of two parameters of either slope or intensity was found to separate normal ovary from benign neoplasms and cancers with an average sensitivity and specificity of 86 ± 6% and 79 ± 5%, whilst the ability to separate benign neoplasms and normal ovary had an average sensitivity and specificity of 86 ± 4% and 80 ± 8% respectively. In conclusion, DRS was found to be a promising tool for the identification of normal and cancerous ovarian tissue via a minimally-invasive procedure in near real time.

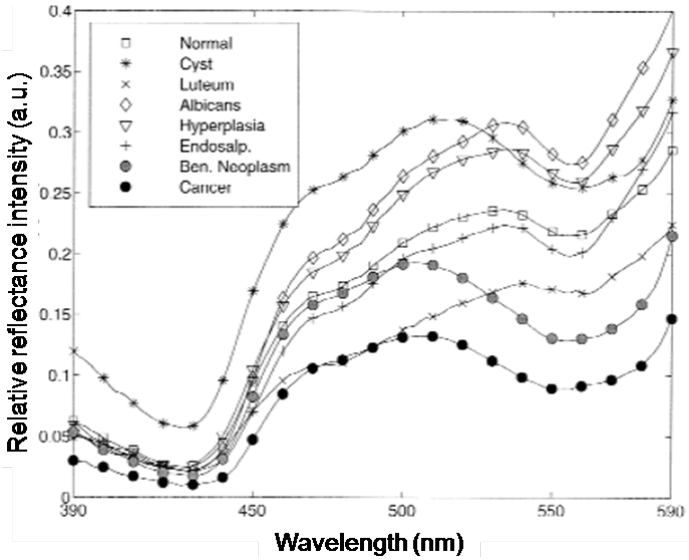


Figure 2.13. Mean reflectance spectra obtained for all eight tissue diagnostic categories with the optical fibre at position 1. (Adapted from Utzinger *et al.*, 2001)

In recent years, a reflectance imaging technique known as narrow-band imaging (NBI) has been generating a substantial amount of clinical results and uptake. The technique differs from conventional endoscopic white-light illumination methods in that it uses narrow illumination bandwidths with the aid of special optical filters for imaging of tissue mucosa. Due to these narrowed illumination wavelengths of light, tissue regions are imaged in shorter depth sections, therefore allowing more discrete and enhanced highlighting of tissue features at various depths as well as for effective visualisation of blood vessels and mucosal microvascular patterning. The technique is often compared with and has been shown to be superior to chromoendoscopy, which involves topical staining of the mucosa with biocompatible dyes such as indigo carmine or methylene blue prior to optical interrogation.

One of the first groups to demonstrate the clinical benefits of NBI was Gono and colleagues who conducted a series of NBI experiments, each formulated to evaluate differences in image contrast and colour between narrow- and broadband illuminations (Gono *et al.*, 2004). Comparisons were also made between NBI and standard screening methods applied during colonoscopy and oesophagoscopy such as magnified chromoendoscopy and magnifying video endoscopy. The medical video endoscope system used was a commercial CLV-U40 unit from Olympus Optical, Japan, consisting

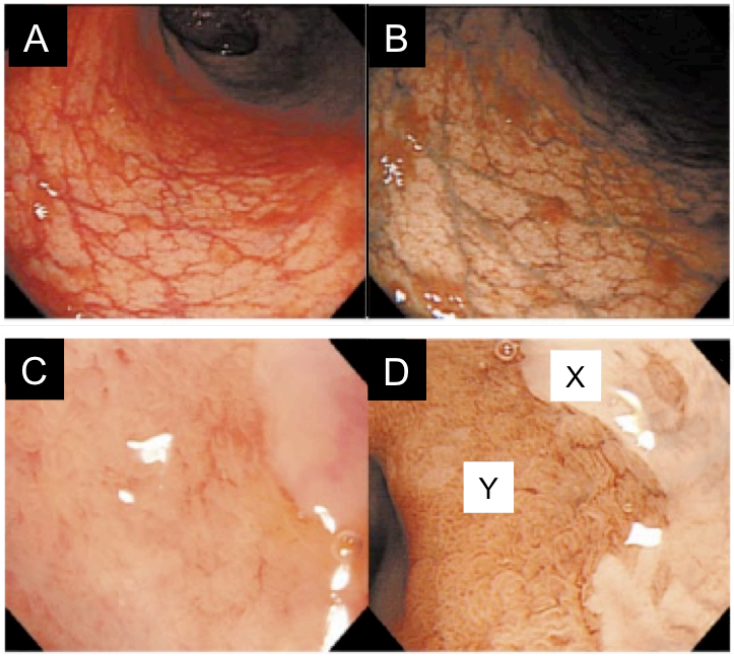


Figure 2.14. Conventional white-light and NBI images of familial adenomatosis coli (A and B) and Barrett's oesophagus (C and D). The area labelled X refers to an area of normal oesophagus tissue, whilst area Y corresponds to a mucosal region of Barrett's oesophagus with a textured vascular pattern clearly visible. (Adapted from Gono *et al.*, 2004)

of a Xenon lamp and a filter disk where three optical interference filters could be mounted at one time for sequential illumination as the disk rotates. Experiments involved NBI imaging of the underside of the human tongue as well as the colon and oesophagus during colonoscopy and Barrett's oesophagus (BO) endoscopy respectively using five narrow-band and three broadband illuminations. Imaging results obtained demonstrated that the appearance of vascular patters were dependent on the class of blood vessels present, central wavelength applied and illumination bandwidth. Contrast of the capillary pattern in the superficial tissue layer of the tongue was markedly improved when using narrow-band illumination at 415 ± 30 nm, an observation not seen with conventional white-light imaging. Later, different combinations of narrow- and broadband filter sets were studied for optimal pit pattern appearance during colour imaging of the tongue, and this was found to be the narrow-band filter set (415 ± 30 nm, 445 ± 30 nm and 500 ± 30 nm). This narrow-band filter set was subsequently used for clinical tests during colonoscopy and oesophagoscopy. NBI images from colonoscopy showed a clearer representation of small polyps of familial adenomatous coli than white-light images (see Figures 2.14A and B). These polyps appeared as brown patches in the

NBI image with blood vessels seen as a blue patterning (Figure 2.14B). NBI images from BO were also found to give clearer visualisation of BO pit patterns than conventional white-light images (Figure 2.14C and D). In conclusion, the group found that NBI displayed clear clinical benefits, preventing small adenomas and cancers in the colon from being missed, hence enabling more accurate biopsies for patients at high risk of developing cancer.

Since its first applications in the GI tract, NBI has now been successfully applied for endoscopic cancer diagnosis in a host of other organs of the human body. Various recent examples include the use NBI for the detection of upper urinary tract urothelial tumours (Traxer *et al.*, 2009); during videobronchoscopy for the assessment of tumour extension in centrally located lung cancers (Bojan *et al.*, 2009); in combination with magnifying endoscopy for the detection of early squamous cell carcinoma in the oropharynx and hypopharynx (Saito *et al.*, 2009); and for the improved detection of pancreaticobiliary diseases during cholangiopancreatoscopy (Shah and Chen, 2009).

2.5.4. Fluorescence confocal endomicroscopy

Fluorescence confocal endomicroscopy (FCE) is a novel endoscopic imaging modality based on the optical principles of bench-top confocal microscopes. The technique allows for real-time *in vivo in situ* imaging of intact tissues at subcellular μm resolution, allowing for *en face*, almost histological-grade assessment of the tissue region under investigation without the need for biopsy. Much interest has been generated since first publication of the FCE technique in 2004 with initial clinical studies concentrating on its diagnostic applications in the oesophagus and GI tract (Kiesslich *et al.*, 2004; Goetz and Kiesslich, 2010). Since then, FCE imaging has been applied for visualisation of diseases in the lung (Thiberville *et al.*, 2006), oral cavity (Thong *et al.*, 2007a), liver (Goetz *et al.*, 2008), cervix (Tan *et al.*, 2009), bladder (Sonn *et al.*, 2009) and ovaries (Tanbakuchi *et al.*, 2010). The method has also been extended to the detection of tumour-specific fluorescence signals e.g. from 5-aminolevulinic acid (5-ALA) induced protoporphyrin IX (PpIX) in photosensitised tissues (Thong *et al.*, 2007b) and FITC-labelled anti-EGFR antibodies on the surface of tumour tissue (Goetz *et al.*, 2009).

Two main FCE systems are being used for research today: both are commercial systems with one developed jointly between Pentax (Tokyo, Japan) and Optiscan (Victoria, Australia) and the other by Mauna Kea Technologies (Paris, France). Though the two systems differ markedly in optical setup, both perform a similar function and have been found to produce images of similar quality. More technical details of these two commercial FCE systems will be covered later in chapter 5 of this thesis. Other prototype FCE systems are also under investigation: one was first presented in its entirety by Rouse and colleagues in 2002, which has since been improved upon and packaged as a 'confocal microlaparoscope' as recently described in a publication by Tanbakuchi and colleagues (Rouse *et al.*, 2002; Tanbakuchi *et al.*, 2010). Another prototype system was recently used by Zhong and colleagues to detect tumour nodules in a mouse model of ovarian cancer by imaging fluorescence from the photodynamic therapy agent benzoporphyrin-derivative monoacid ring A (BPD-MA) (Zhong *et al.*, 2009).

Wang *et al.* showed the effective use of the Cellvizio-GI FCE system from Mauna Kea Technologies for assessment of colonic mucosa *in vivo* (Wang *et al.*, 2007). Using topically applied fluorescein contrast agent (5 mg/mL), their aim was to demonstrate functional differences in both uptake and distribution of the dye by colonic crypts in order to distinguish between normal, hyperplasia and adenoma conditions. A total of 54 subjects were included in their study (mean age 65 ± 10 years). FCE imaging was performed *in vivo* at 488 nm laser excitation with the instrument's flexible confocal miniprobe passed down the instrument channel of a colonoscope and put in direct contact with the tissue. Image acquisition took two to three minutes per site and a pinch biopsy was obtained from each imaged site for histological comparison. From their imaging results, the group observed differences in fluorescein localisation and dynamics from the crypt lumen to lamina propria for different disease conditions. FCE diagnostic results were also well correlated with those obtained from histology with normal, hyperplastic and tubular and villous adenomatous mucosa showing distinct morphological characteristics (Figure 2.15). The group also compared lamina propria / crypt fluorescence contrast ratios and found that a greater value was attained for normal than lesional mucosa across all subjects. On average, fluorescence contrast ratios were shown to decrease with severity of disease. Based on their findings, the group concluded that FCE represented a new

method of histopathological evaluation for real time *in vivo* assessment of the functional properties of disease tissues.

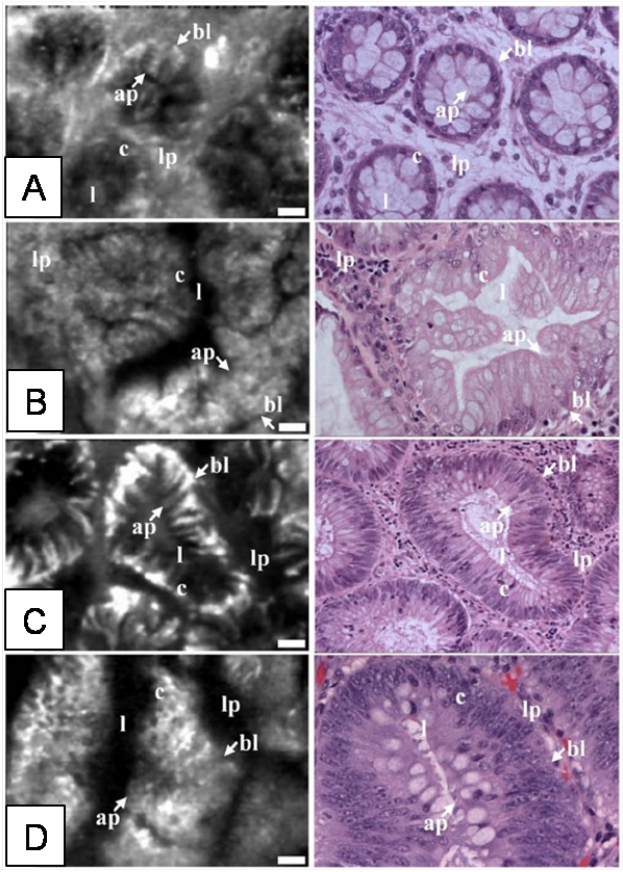


Figure 2.15. Comparison between FCE and en face histology results of different colonic mucosal disease states: normal mucosa (A), hyperplasia (B), tubular adenoma (C), villous adenoma (D). Various structural tissue features can be distinguished from both image sets: crypt lumens (l), epithelial cells (c) and their apical (ap) and basolateral (bl) borders, and the lamina propria (lp). (Adapted from Wang *et al.*, 2007)

Sonn and colleagues recently reported on the use of FCE for visualising and distinguishing between benign lesions and malignant tumours in the human bladder (Sonn *et al.*, 2009). The group hypothesised that FCE would serve as an adjunct to conventional white-light cystoscopy and improve on the accuracy of the technique by providing high resolution images of the bladder urothelium for pathological diagnosis. Fresh bladder tissue specimens obtained from four patients were imaged *ex vivo* by the fibred confocal miniprobe Cellvizio FCE system after topical application of fluorescein sodium (0.05%) for optical contrast. Following pathologic evaluation, specimens were found to have conditions ranging from high-grade invasive transitional cell carcinoma,

high-grade invasive primary bladder adenocarcinoma and multifocal CIS. Figure 2.16 shows both FCE images and histological results obtained from the patient with multifocal CIS, which compares a grossly normal tissue region exhibiting uniform cellular structures (Figure 2.16A) with a region of CIS displaying denuded mucosa, lymphocytic infiltrate and local haemorrhage (Figure 2.16B). As observed, a good correspondence between both FCE images and histology was achieved. In conclusion, the group noted that whilst depth penetration of the confocal miniprobe would prove insufficient for providing information concerning the degree of tumour invasion, FCE would nonetheless complement other novel image techniques and ultimately improve on current white-light cystoscopic approaches.

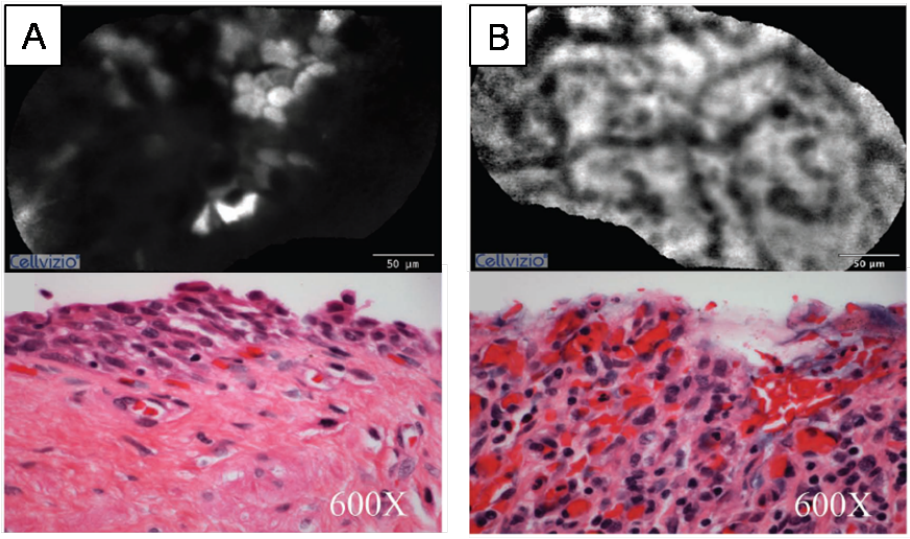


Figure 2.16. FCE images and correponding histological results obtained from *ex vivo* imaging of a bladder cystectomy tissue sample containing regions of normal mucosa (A) and multifocal carcinoma *in situ* (B). (Adapted from Sonn *et al.*, 2009)

An FCE approach for imaging the ovary epithelium *in vivo* was recently described by Tanbakuchi *et al.* as applied using a prototype confocal microlaparoscope system (Tanbakuchi *et al.*, 2010). The pilot study consisted of 21 patients presenting with normal and cancerous ovarian tissue disease states. FCE imaging was performed using the 3 mm diameter objective lens at the positioned at the tip of the microlaparoscope, which provided a 450 µm field of view and lateral resolution of 3 µm. Image acquisition was carried out with the microlaparoscope tip in contact with the ovarian epithelium and 488 nm laser excitation was used to excite the topically applied contrast agents, namely fluorescein sodium (FL; 1.0 %) and acridine orange (AO; 330 µM/L). The fluorescence

signal is subsequently collected by the objective lens and relayed back to the optical scanning unit via a coherent fibre-optic bundle. Further technical details about the system are discussed in separate papers by the same group (Rouse *et al.*, 2004; Tanbakuchi *et al.*, 2009). With regards to contrast agents, the group noted that FL binds non-specifically to tissue proteins, thus resulting in low contrast FCE images with limited diagnostic value for ovarian cancer detection as seen in Figure 2.17. The nuclear stain AO was therefore used as an alternative, which was previously demonstrated successfully for the detection of ovarian cancer (Srivastava *et al.*, 2008). Ovarian tissue was first imaged *in vivo* within an endobag to prevent spreading of the dyes to nearby organs, followed by *ex vivo* imaging immediately after resectioning. Acquired images from both *ex vivo* and *in vivo* FCE imaging with AO are shown in Figure 2.18, showing good image contrast with sufficient resolution to differentiate between different cellular structures in both imaging settings. Based on the study's results, the group commented that their FCE approach with a confocal microlaparoscope could be effectively used in a surgical setting for imaging of the ovary *in vivo*.

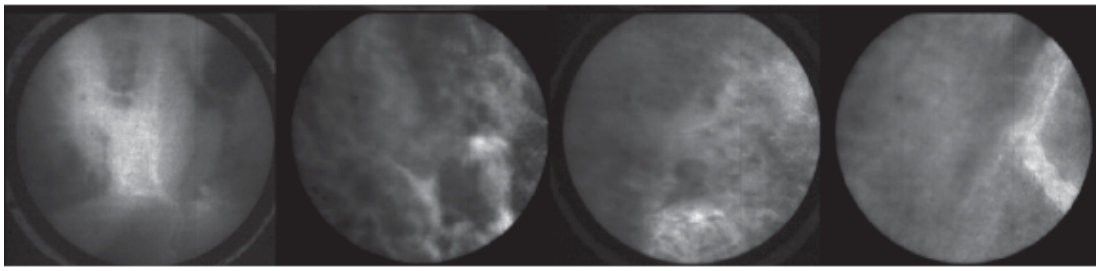


Figure 2.17. Images obtained from *in vivo* FCE imaging of a human ovary using topically applied fluorescein sodium dye as contrast agent. Due to non-specific binding, the image suffers from low resolution and contrast with instances of uneven pooling of the dye observed. (Adapted from Tanbakuchi *et al.*, 2010)

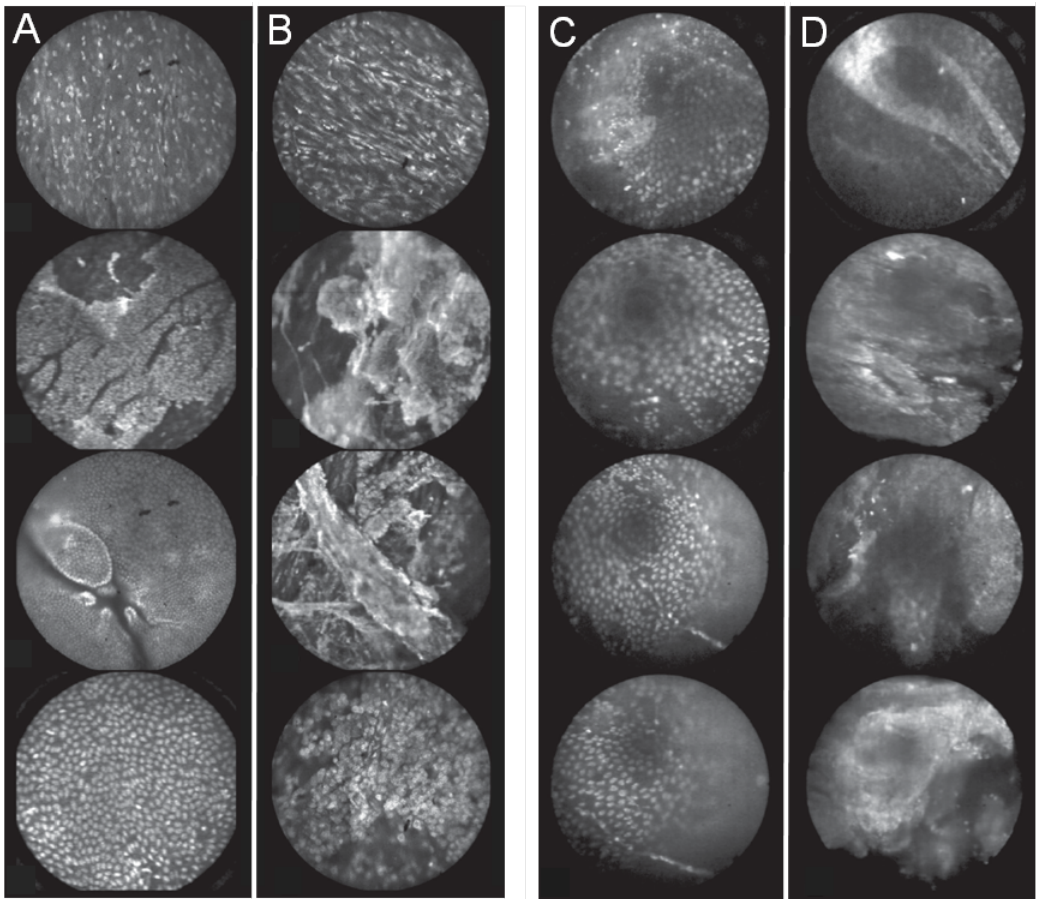


Figure 2.18. Images obtained from *ex vivo* (A and B) and *in vivo* (C and D) FCE imaging of human ovaries stained with the contrast agent acridine orange: normal ovarian epithelium (A and C); abnormal/adenomatous ovarian epithelium (B and D). Image contrast obtained was sufficient to identify various tissue structures associated with different ovarian disease states. (Adapted from Tanbakuchi *et al.*, 2010)

A novel application of FCE was demonstrated by Thong and colleagues who performed FCE imaging for detection of 5-ALA induced PpIX fluorescence in the oral cavity (Thong *et al.*, 2007b). A prototype based on the Pentax/Optiscan FCE system with a rigid probe was used in their study to image three healthy volunteers and three patients with squamous cell carcinoma (SCC) of the tongue. 5-ALA (0.4 % in PBS) was applied topically in the oral cavities of all human subjects with an incubation period of at least 30 minutes. FCE imaging at 488 nm laser excitation was then performed between 30 and 120 minutes from the start of 5-ALA administration at. After imaging, tongue tissue from SCC patients was excised for histological processing. Figures 2.19A to C show FCE images of 5-ALA treated normal tongue tissue acquired at 45, 90 and 120 minutes after 5-ALA application. Clear images were obtained as early as the 45-min imaging time

point. Figures 2.19D and E show an FCE image and white light microscope image of a histological section of an SCC tongue respectively. The authors noted that their system was able to distinguish between normal and SCC tongue tissue by highlighting that FCE images of the normal tongue in Figures 2.19A - C appear different to that of the SCC tongue in Figure 2.19D based on 5-ALA induced PpIX fluorescence. The FCE image in Figure 2.19D was also observed to be comparable to that of histology in Figure 2.19E. The study's conclusion was that FCE had the potential of diagnosing oral cavity malignancies such as SCC of the tongue based on PpIX fluorescence emissions from tissue.

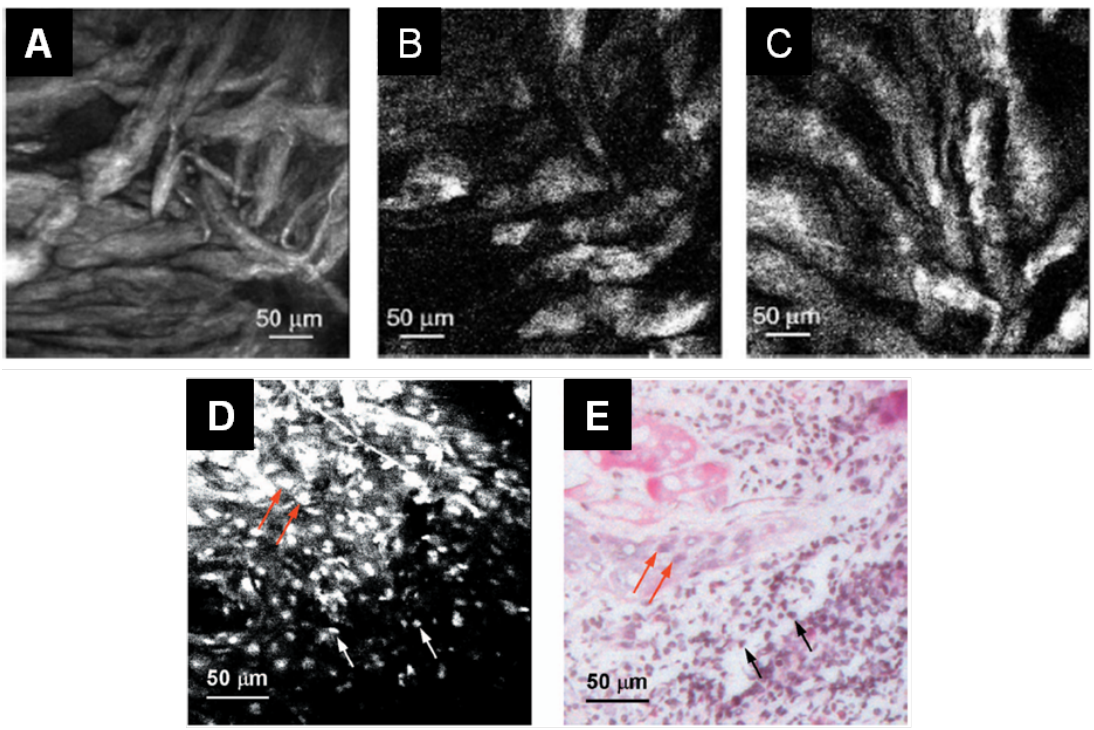


Figure 2.19. FCE Images of 5-ALA treated normal (A to C) and SCC (D) tongue tissue, and a white light microscope image of a histological H&E section of SCC tongue tissue (E) from human subjects. FCE images of normal tongue tissue captured at 45, 90 and 120 minutes respectively after 5-ALA administration (A, B and C); FCE image of SCC human tongue tissue after 5-ALA application (no incubation time specified), with red arrows indicating SCC epithelium and white arrows representing inflammatory cells (D); white light histological section of SCC human tongue tissue, with SCC region indicated by red arrows and surrounding inflammatory cells indicated by black arrows (E). (Adapted from Thong *et al.*, 2007)

2.6. From point-measurements to region-based detection

Conventional optical spectroscopic modalities such as FS, DRS and Raman spectroscopy (RS) typically employ fibre optic probes for the simultaneous delivery and collection of excitation light and emitted signals from single points on tissue samples. In line with improvements in optical systems design and the long-term view of performing minimally invasive *in vivo in situ* procedures, these fibre optic probes have also been greatly miniaturised and currently measure only a few millimetres in diameter. Some limitations exist however with these improvements in probe design, such as a small and limited field of view (FOV) or sensing area and acquisition of inconsistent tissue spectral data.

Owing to the spatially restricted sensing area of the small fibre optic probe lens and point sampling process, the spectral information acquired from a single point is usually insufficient to reach a full and proper diagnosis. Consequently, spectral data has to be sampled from other points around the same organ to attain a more complete diagnostic picture. Such tissue sampling is performed randomly most of the time, akin to random tissue biopsies, due to the large tissue area and multiple points to be sampled. Like random biopsies, this may also result in high miss rates and false-negative results. One possible solution is to combine optical imaging methods with more established clinical diagnostic approaches like MRI, PET or ultrasound for image co-registration. This would however detract from our original purpose of creating a solely optical approach to tissue diagnosis.

Inconsistent spectral data collected during inter- and intra-session data acquisitions arises as a result of different probe-tissue contact pressures. This occurs because of direct contact of the probe with tissue and the lack of any force feedback mechanisms, leading to tissue deformation and interruption of vasculature perfusion. With conventional probe-based optical techniques, such a problem is usually unavoidable; direct probe-tissue contact is needed to prevent induction of any spectral artifacts caused either by refractive index mismatches between the tissues and surrounding medium or as a result of possible inconsistencies in spectral illumination-collection geometry. A study of probe contact on rat liver and heart tissues found that increasing contact pressure lead to considerable increases in diffuse reflectance spectra intensities between 450 and 600 nm, with a marked increase also in the overall fluorescence spectra intensity (Ti and Lin,

2008). The explanation was that high probe contact pressures lead to decreases in local blood volume (ischemia), essentially reducing the amount of light-absorbing haemoglobin at the sampled points and causing a corresponding increase in detected amounts of diffuse reflected light. As a result of this local ischemic state, metabolic activity was slowed down in turn, hence causing an accumulation of NAD^+ and FAD and a concomitant increase in flavin fluorescence emissions (Vishwasrao *et al.*, 2005).

Imaging work in this thesis is geared towards developing novel optical imaging modalities with the aim of overcoming limitations posed by standard spectroscopic approaches. All techniques investigated are imaging-based extensions of conventional optical methods, each incorporating the latest advancements in optical hardware and design for achieving enhanced detection over their predecessors. These techniques shall be described in greater detail in the subsequent chapters with all imaging experiments performed within the context of early cancer detection and diagnosis *in vivo in situ*.

2.7. Summary and conclusions

This chapter provided a brief overview of the rationales behind the use of emerging optical imaging techniques for early cancer diagnosis. Various principles behind such optical diagnostic approaches were mentioned together with a series of short reviews covering the multimodal and multispectral optical imaging techniques used throughout this thesis for disease detection, staging and surgical planning. The section concluded with motivations for our current work involving the move towards more 'regional' cancer detection in a minimally invasive *in vivo in situ* setting.

2.8. References

Achilefu S. Lighting up tumors with receptor-specific optical molecular probes. *Technology in Cancer Research & Treatment* 2004;**3(4)**:393-409.

Akerman ME, Chan WCW, Laakkonen P, Bhatia SN, Ruoslahti E. Nanocrystal targeting in vivo. *Proceedings of the National Academy of Sciences USA* 2002;**99**:12617-12621.

Alberts B, Johnson A, Lewis J, Raff M, Roberts K, Walter P. *Molecular Biology of the Cell*, 4th edn. New York: Garland Science. 2002.

Alfano R, Tata D, Cordero J, Tomashefsky P, Longo F, Alfano M. Laser induced fluorescence spectroscopy from native cancerous and normal tissue. *IEEE Journal of Quantum Electronics* 1984;**20(1)**:1507-1511.

Allen CM, Sharman WM, Van Lier JEJ. Current status of phthalocyanines in the photodynamic therapy of cancer. *Porphyrins Phthalocyanines* 2001;**5**:161-169.

Andersson-Engels S, Johansson J, Stenram U, Svanberg K, Svanberg S. Malignant tumor and atherosclerotic plague diagnosis using laser-induced fluorescence. *IEEE Journal of Quantum* Electronics 1990;**26(12)**:2207-2217.

Ballou B, Ernst LA, Waggoner AS. Fluorescence imaging of tumors in vivo. *Current Medicinal Chemistry* 2005;**12**:795-805.

Ballou B, Fisher GW, Deng JS, Hakala TR, Srivastava M, Farkas DL. Cyanine fluorochrome-labeled antibodies in vivo: assessment of tumor imaging using Cy3, Cy5, Cy5.5, and Cy7. *Cancer Detection and Prevention* 1998;**22(3)**:251-257.

Ballou B, Fisher GW, Hakala TR, Farkas DL. Tumor detection and visualization using cyanine fluorochrome-labeled antibodies. *Biotechnology Progress* 1997;**13**:649-658.

Ballou B, Fisher GW, Waggoner AS, Farkas DL, Reiland JM, Jaffe R, Mujumdar RB, Mujumdar SR, Hakala TR. Tumor labelling in vivo using cyanine-conjugated monoclonal antibodies. *Cancer Immunology Immunotherapy* 1995;**41**:257-263.

Battle AMDC. Porphyrins, porphyrias, cancer and photodynamic therapy: a model of carcinogenesis. *Journal of Photochemistry and Photobiology* 1993;**B20**:5-22.

Beauvoit B, Kitai T, Chance B. Contribution of the mitochondrial compartments of the optical properties of the rat liver: a theoretical and practical approach. *Biophysical Journal.* 1994;**67**:2501-2510.

Becker A, HEssenius C, Licha K, Ebert B, Sukowski U, Semmier W, Wiedenmann B, Grotzinger C. Receptor-targeted optical imaging of tumors with near-infrared fluorescent ligands. *Nature Biotechnology* 2001;**19**:327-331.

Bigio IJ, Bown SG. Spectroscopic sensing of cancer and cancer therapy. *Cancer Biology and Therapy* 2004;**3(3)**:259-267.

Bojan Z, Branislav P, Aleksandra J, Goran S, Miroslav ID, Illja A, Zivka E, Milana P, Nevena S, Milan A. Influence of narrow band imaging (NBI) videobronchoscopy on the assessment of central lung cancer extension and therapeutic decision. *Cancer Investigation* 2009;**27**:918-923.

Bottiroli G, Croce AC, Locatelli D, Marchesini R, Pignoli E, Tomatis S, Cuzzoni C, Di Palma S, Dalfante M, Spinelli P. Natural fluorescence of normal and neoplastic human colon – a comprehensive *ex vivo* study. *Lasers in Surgery and Medicine* 1995;**16(1)**:48-60.

Brewer M, Utzinger U, Silva E, Gershenson D, Bast RC Jr, Follen M, Richards-Kortum R. Fluorescence spectroscopy for in vivo characterization of ovarian tissue. *Lasers in Surgery and Medicine* 2001;**29(2)**:128-135.

Brown JQ, Vishwanath K, Palmer GM, Ramanujam N. Advances in quantitative UV-visible spectroscopy for clinical and pre-clinical application in cancer. *Current Opinion in Biotechnology* 2009;**20(1)**:119-131.

Bugelski PJ, Porter CW, Dougherty TJ. Autoradiographic distribution of hematoporphyrin derivative in normal and tumor tissue of the mouse. *Cancer Research* 1981;**41**:4606-4612.

Campbell ID, Dwek RA. *Biological Spectroscopy*. New York: Benjamin-Cummings Publishing Co. 1984.

Chang SK, Follen M, Malpica A, Utzinger U, Staerkel G, Cox D, Atkinson EN, MacAulay C, Richards-Kortum R. Optimal excitation wavelengths for discrimination of cervical neoplasia. *IEEE Transactions in Biomedical Engineering* 2002;**49(10)**:1102-1111.

Chen RF. Fluorescence quantum yields of tryptophan and tyrosine. *Analytical Letters* 1967;**1(1)**:35-42.

Choy G, Choyke P, Libutti SK. Current advances in molecular imaging: Noninvasive in vivo bioluminescent and fluorescent optical imaging in cancer research. *Molecular Imaging* 2003;**2(4)**:303-312.

Conti E, Franks NP, Brick P. Crystal structure of firefly luciferase throws light on a superfamily of adenylate-forming enzymes. *Structure* 1996;**4(3)**:287-298.

Dacosta R, Wilson BC, Marcon NE. Optical techniques for the endoscopic detection of dysplastic colonic lesions. *Current Opinion in Gastroenterology* 2004;**21**:70-79.

Dekker E, Fockens P. Advances in colonic imaging: new endoscopic imaging methods. *European Journal of Gastroenterology and Hepatology* 2005;**17(8)**:803-808.

Dellas A, Moch H, Schulthesis E, Feichter G, Almendral AC, Gudat F, Torhorst J. Angiogenesis in cervical neoplasia: Microvessel quantification in precancerous lesions and invasive carcinomas with clinicopathological correlations. *Gynecologic Oncology* 1997;**67**:27-33.

Desmettre T, Devoisselle JM, Mordon S. Fluorescence properties and metabolic features of indocyanine green (ICG) as related to angiography. *Survey of Ophthalmology* 2000;**45(1)**:15-27.

Deyl Z, Macek K, Adam M, Vancíková O. Studies on the chemical nature of elastin fluorescence. *Biochimica et Biophysica Acta* 1980;**625(2)**:248-254.

Drezek R, Guillaud M, Collier T, Boiko I, Malpica A, Maaulay C, Follen M, Richards-Kortum R. Light scattering from cervical cells throughout neoplastic progression: influence of nuclear morphology, DNA content, and chromatin texture. *Journal of Biomedical Optics* 2003;**8(1)**:7-16.

Eker C, Montán S, Jaramillo E, Koizumi K, Rubio C, Andersson-Engels S, Svanberg K, Svanberg S, Slezak P. Clinical spectral characterisation of colonic mucosal lesions using autofluorescence and delta aminolevulinic acid sensitisation. *Gut* 1999;**44(4)**:511-8.

Eyre DR, Paz MA, Gallop PM. Cross-linking in collagen and elastin. *Annual Review of Biochemistry* 1984;**53**:717-748.

Farrell TJ, Patterson MS, Wilson BC. A diffusion theory model of spatially resolved, steady-state diffuse reflectance for the non0incasive determination of tissue optical properties. *Medical Physics* 1992;**19**:879-888.

Ferdman AG, Yannas IV. Scattering of light from histologic sections: a new method for the analysis of connective tissue. *Journal of Investigative Dermatol*ogy 1993;**100**:710-716.

Folli S, Westermann P, Braichotte D, Pelegrin A, Wagnieres G, can den Bergh J, Mach JP. Antibody-indocyanine conjugates for immunophotodetection of human squamous cell carcinoma in nude mice. *Cancer Res*earch 1994;**54**:2643-2649.

Freitas I. Lipid accumulation, the common feature to photosensitizer-retaining normal and malignant tissues. *Journal of Photochemistry and Photobiology B-Biology* 1990;**7**:359-361.

Fujimoto D. The structure of pyridinoline, a collagen crosslink. *Biochemical and Biophysical Research Communications* 1997;**76(4)**:1124-1129.

Ganesan S, Sacks PG, Yang Y, Katz A, Al-Rawi M, Savage HE, Schantz SP, Alfano RR. Native fluorescence spectroscopy of normal and malignant epithelial cells. *Cancer Biochemistry Biophysics* 1998;**16**:365-373.

Gao X, Cui Y, Levenson RM, Chung LWK, Nie S. In vivo cancer targeting and imaging with semiconductor quantum dots. *Nature Biotechnology* 2004;**22(8)**:969-976.

Ghadially FN, Neish WJP, Dawkins HC. Mechanisms involved in the production of red fluorescence of human and experimental tumors. *Journal of Pathology and Bacteriology* 1963;**85**:77-92.

Gillies R, Zonios G, Anderson RR, Kollias N. Fluorescence excitation spectroscopy provides information about human skin *in vivo*. *Journal of Investigative Dermatology* 2000;**115**:704–707.

Goetz M, Kiesslich R. Advances of endomicroscopy for gastrointestinal physiology and diseases. *American Journal of Physiology – Gastrointestinal and Liver Physiology* 2010;**298(6)**:G797-806.

Goetz M, Kiesslich R, Dienes HP, Drebber U, Murr E, Hoffman A, Kanzler S, Galle PR, Delaney P, Neurath MF. In vivo confocal laser endomicroscopy of the human liver: a novel method for assessing liver microarchitecture in real time. *Endoscopy* 2008;**40(7)**:554-562.

Goetz M, Ziebart A, Foersch S, Vieth M, Waldner MJ, Delaney P, Galle PR, Neurath MF, Kiesslich R. In vivo molecular imaging of colorectal cancer with confocal endomicroscopy by targeting epidermal growth factor receptor. *Gastroenterology* 2010;**138(2)**:435-446.

Goldman ER, Balighian ED, Mattoussi H, Kuno MK, Mauro JM, Tran PT, Anderson GP. Avidin: A natural bridge for quantum dot-antibody conjugates. *Journal of the American Chemical Society* 2002;**124**:6378-6382.

Gono K, Obi T, Yamaguchi M, Ohyama N, Machida H, Sano Y, Yoshida S, Hamamoto Y, Endo T. Appearance of enhanced tissue features in narrow-band endoscopic imaging. *Journal of Biomedical Optics* 2004;**9(3)**:568-577.

Hamblin MR, Newman EL. On the mechanism of the tumor-localizing effect in photodynamic therapy. *Journal of Photochemistry and Photobiology B-Biology* 1994;**23(1)**:3-8.

Haugland RP. *Molecular Probes: The Handbook - A Guide to Fluorescent Probes and Labeling Technologies,* 10th ed. Invitrogen. 2005.

Hone DC, Walker PI, Evans-Gowing R, FitzGerald S, Beeby A, Chambrier I, Cook MJ, Russell DA. Generation of cytotoxic singlet oxygen via phthalocyanine-stabilized gold nanoparticles: a potential delivery vehicle for photodynamic therapy. *Langmuir* 2002;**18**:2985-2987.

Hubmann MR, Leiner MJP, Schaur RJ. Ultraviolet fluorescence of human sera: I. Sources of characteristic differences in the ultraviolet fluorescence spectra of sera from normal and cancer-bearing humans. *Clinical Chemistry* 1990;**36(11)**:1880-1883.

Jain RK. Delivery of molecular medicine to solid tumors: lessons from *in vivo* imaging of gene expression and function. *Journal of Controlled Release* 2001;**74**:7-25.

Jori G. In vivo transport and pharmacokinetic behaviour of tumour photosensitizers. In: *Photosensitizing Compounds: Their Chemistry, Biology and Clinical Use* (Ciba Foundation Symposia, Harnett S, eds). Chichester: Wiley & Sons Ltd. 1989;78-86.

Jori G, Beltramini M, Reddi E, Salvato B, Pagnan A, Ziron L, Tomio L, Tsanov T. Evidence for a major role of plasma-lipoproteins as hematoporphyrin carriers *in vivo*. *Cancer Letters* 1984;24:291-297.

Juzenas P, Chen W, Sun YP, Coelho MAN, Generalov R, Generalova N, Christensen IL. Quantum dots and nanoparticles for photodynamic and radiation therapies of cancer. *Advanced Drug Delivery Reviews* 2008;**60**:1600-1614.

Kiesslich R, Burg J, Vieth M, Gnaendiger J, Enders M, Delaney P, Polglase A, McLaren W, Janell D, Thomas S, Nafe B, Galle PR, Neurath MF. Confocal laser endoscopy for diagnosing intraepithelial neoplasias and colorectal cancer in vivo. *Gastroenterology* 2004;**127(3)**:706-713.

Kusunoki Y, Imamura F, Uda H, Mano M, Horai T. Early detection of lung cancer with laser-induced fluorescence endoscopy and spectrofluorometry. *Chest* 2000;**118(6)**:1776-1182.

Lakowicz JR. *Principles of Fluorescence Spectroscopy*, 2nd edn. New York: Kluwer Academic/Plenum Publishers. 1999.

Lane PM, Gilhuly T, Whitehead P, Zeng H, Poh CF, Ng S, Williams PM, Zhang L, Rosin MP, MacAulay CE. Simple device for the direct visualization of oral-cavity tissue fluorescence. *Journal of Biomedical Optics* 2006;**11(2)**:024006.

Li C, Greenwood TR, Bhujwalla ZM, Glunde K. Synthesis and characterization of glucosamine-bound near-infrared probes for optical imaging. *Organic Letters* 2006;**8(17)**:3623-3626.

Li LQ, Wei HJ, Guo ZY, Yang HQ, Wu GY, Xie SS, Zhong HQ, Li XY, Zhao QL, Guo X. Oxygenated hemoglobin diffuse reflectance ratio for in vitro detection of human gastric pre-cancer. *Laser Physics* 2010;Online first.

Lichtman JW, Conchello JA. Fluorescence microscopy. *Nature Methods* 2005;**2(12)**:910-919.

Lippincott-Schwartz, J, Patterson G. Development and use of fluorescent protein markers in living cells. *Science* 2003;**300**:87-91.

Lycette RM and Leslie RB. Fluorescence of malignant tissue. *Lancet* 1965;**2**:436.

Maeda H, Wu J, Sawa T, Matsumura Y, Hori K. Tumor vascular permeability and the EPR effect in macomolecular therapeutics: a review. *Journal of Controlled Release* 2000;**65**:271-284.

Medintz IL, Uyeda HT, Goldman ER, Mattoussi H. Quantum dot bioconjugates for imaging, labelling and sensing. *Nature Materials* 2005;**4**:435-446.

Milas L, Wike J, Hunter N, Volpe J, Basic I. Macrophage content of murine sarcomas and carcinomas – associations with tumor-growth parameters and tumor radiocurability. *Cancer Research* 1987;**47**:1069-1075.

Mirabal YN, Chang SK, Atkinson EN, Malpica A, Follen M, Richards-Kortum R. Reflectance spectroscopy for in vivo detection of cervical precancer. *Journal of Biomedical Optics* 2002;**7(4)**:587-594.

Montes GS. Structural biology of the fibres of the collagenous and elastic systems. *Cell Biology International* 1996;20(1):15-27.

Mourant JR, Bigio IJ, Boyer J, Conn RL, Johnson T, Shimada T. Spectroscopic diagnosis of bladder cancer with elastic light scattering. *Lasers in Surgery and Medicine* 1995;**17**:350-357.

Mourant JR, Canpolat M, Brocker C, Esponda-Ramos O, Johnson TM, Matanock A, Stetter K, Freyer JP. Light scattering from cells: the contribution of the nucleus and the effects of proliferative status. *Journal of Biomedical Optics* 2000;**5(2)**:131-137.

Mourant JR, Hielscher AH, Eick AA, Johnson TM, Freyer JP. Evidence of intrinsic differences in the light scattering properties of tumorigenic and nontumorigenic cells. *Cancer* 1998;**84(6)**:366-374.

Muckle TJ. Plasma proteins binding of indocyanine green. *Biochemical Medicine* 1976;**15**:17-21.

Mueller M, Georgakoudi I, Zhang Q, Wu J, Feld MS. Intrinsic fluorescence spectroscopy in turbid media: disentangling effects of scattering and absorption. *Applied Optics* 2001;**40(25)**:4633-4646.

Mullazehi M, Mathsson L, Lampa J, Rönnelid J. High anti-collagen type-II antibody levels and induction of proinflammatory cytokines by anti-collagen antibody-containing immune complexes *in vitro* characterise a distinct rheumatoid arthritis phenotype associated with acute inflammation at the time of disease onset. *Annals of the Rheumatic Diseases* 2007;**66**:537–541.

NIH Consensus Development Panel on Ovarian Cancer: Ovarian cancer screening, treatment and follow-up. *JAMA* 1995;**273**:491-497.

Perelman LT, Backman V, Wallace M, Zonios G, Manoharan R, Nusrat A, Shields S, Seiler M, Lima C, Hamano T, Itzkan I, Van Dam J, Crawford JM, Feld MS. Observation of periodic fine structure in reflectance from biological tissue: a new technique for measuring nuclear size distribution. *Physical Review Letters* 1998;**80**:627-630.

Pierce MC, Javier DJ, Richards-Kortum R. Optical contrast agents and imaging systems for detection and diagnosis of cancer. *International Journal of Cancer* 2008;**123**:1979-1990.

Polglase AL, McLaren WJ, Skinner SA, Kiesslich R, Neurath MF, Delaney PM. A fluorescence confocal endomicroscope for in vivo microscopy of the upper- and the lower-GI tract. *Gastrointestional Endosc*opy 2005;**62(5)**:686-695.

Ramanujam N. Fluorescence Spectroscopy In Vivo. In: *Encyclopedia of Analytical Chemistry* (Meyers RA, ed). Chichester: John Wiley & Sons Ltd. 2000;20-56.

Redmond RW. Introduction to Fluorescence and Photophysics. In: *Handbook of Biomedical Fluorescence* (Mycek MA, Pogue BW, eds). New York: Marcel Dekker, Inc. 2003.

van der Rest M, Garrone R. Collagen family of proteins. *FASEB Journal* 1991;**5**:2814-2823.

Rhys-Williams AT. *An introduction to fluorescence spectroscopy*. Beaconsfield: PerkinElmer Ltd. 2000.

Richards-Kortum R, Sevick-Muraca E. Quantitative optical spectroscopy for tissue diagnosis. *Annual Review of Physical Chemistry* 1996;**47**:555-606.

Römer TJ, Fitzmaurice M, Cothren RM, Richards-Kortum R, Petras R, Sivak MV Jr, Kramer JR Jr. Laser-induced fluorescence microscopy of normal colon and dysplasia in colonic adenomas: implications for spectroscopic diagnosis. *American Journal of Gastroenterology* 1995;**90(1)**:81-87.

Roshy S, Sloane BF, Moin K. Pericellular cathepsin B and malignant progression. *Cancer Metastasis Reviews* 2003;**22(2-3)**:271-86.

Rouse AR, Kano A, Gmitro AF. Development of a fiber-optic confocal microendoscope for clinical endoscopy. *Proceedings of SPIE* 2002;**4613**;244-253.

Rouse AR. Kano A, Udovich JA, Kroto SM, Gmitro AF. Design and demonstration of a miniature catheter for a confocal microendoscope. *Applied Optics* 2004;**43**:5763-5771.

Roy I, Ohulchanskyy TY, Pudavar HE, Bergey EJ, Oseroff AR, Morgan J, Dougherty TJ, Prasad PN. Ceramic-based nanoparticles entrapping water-insoluble photosensitizing anticancer drugs: a novel drug−carrier system for photodynamic therapy. *Journal of the American Chemical Society* 2003;**125**:7860.

Saidi IS, Jacques SL, Tittel FK. Mie and Rayleigh modelling of visible-light scattering in neonatal skin. *Applied Optics* 1995;**34**:7410-7418.

Saito M, Yamashita K, Murakami K, Onodera K, Shimixu H, Kaneto H, Shinomura Y. Detection rate of pharyngeal cancer in high-risk groups by endoscopic examination with narrow band imaging (NBI): single-center experience in 103 patients. *Gastrointestinal Endoscopy* 2009;**69(5)**:AB209.

Samia ACS, Chen X, Burda C. Semiconductor quantum dots for photodynamic therapy. *Journal of the American Chemical Society* 2003;**125**:15736-15737.

Shah RJ, Chen YK. Video cholangiopancreatoscopy (CP) with narrow band imaging (NBI): Spectrum of mucosal and vascular patterns in patients with pancreaticobiliary (PB) pathology. *Gastrointestinal Endoscopy* 2009;**69(5)**:AB117.

Shibuya K, Hoshino H, Chiyo M, Iyoda A, Yoshida S, Sekine Y, Iizasa T, Saitoh Y, Baba M, Hiroshima K, Ohwada H, Fujisawa T. High magnification bronchovideoscopy combined with narrow band imaging could detect capillary loops of angiogenic squamous dysplasia in heavy smokers at high risk for lung cancer. *Thorax* 2003;**58(11)**:989-995.

Smith AM, Duan H, Mohs AM, Nie SM. Bioconjugated quantum dots for in vivo molecular and cellular imaging. *Advanced Drug Delivery Reviews* 2008;**60**:1226-1240.

Sonn GA, Mach KE, Jensen K, Hsiung PL, Jones SN, Contag CH, Wang TD, Liao JC. Fibered confocal microscopy of bladder tumors: an ex vivo study. *Journal of Endourology* 2009;**23(2)**:197-201.

Srivastava S, Rodriguez J, Rouse A, Brewer M, Gmitro A. Computer-aided identification of ovarian cancer in confocal microendoscope images. *Journal of Biomedical Optics* 2008;**13**:024021.

Stryer L. *Biochemistry*. New York: WH Freeman and Company. 1988.

Tan J, Guinn MA, Delaney PM, McLaren WJ. Detection of cervical intraepithelial neoplasia in vivo using confocal endomicroscopy. *Gynaecological Oncology* 2009;**116**:1663-1670.

Tanbakuchi AA, Rouse AR, Udovich JA, Hatch KD, Gmitro AF. A clinical confocal microlaparoscope for real-time in vivo optical biopsies. *Journal of Biomedical Optics* 2009;**14**:044030.

Tanbakuchi AA, Udovich JA, Rouse AR, Hatch KD, Gmitro AF. In vivo imaging of ovarian tissue using a novel confocal microlaparoscope. *American Journal of Obstetrics and Gynecology* 2010;**202(1)**:90.e1-9.

Thiberville L, Moreno-Swirc S, Vercauteren T, Peltier E, Cavé C, Bourg Heckly G. In vivo imaging of the bronchial wall microstructure using fibered confocal fluorescence microscopy. *American Journal of Respiratory and Critical Care Medicine* 2007;**175(1)**:22-31.

Thong PS, Kho KW, Zheng W, Harris M, Soo KC, Olivo M. Development of a laser confocal endomicroscope for in vivo fluorescence imaging. *Journal of Mechanics in Medicine and Biology* 2007a;**7(1)**:11-18.

Thong PS, Olivo M, Kho KW, Zheng W, Mancer K, Harris M, Soo KC. Laser confocal endomicroscopy as a novel technique for fluorescence diagnostic imaging of the oral cavity. *Journal of Biomedical Optics* 2007b;**12(1)**:014007.

Ti Y, Lin WC. Effects of probe contact pressure on in vivo optical spectroscopy. *Optics Express* 2008;**16(6)**:4250-4262.

Traxer O, Alqahtani S, Geavlete B. Narrow band imaging (NBI) vs white light endoscopic imaging (WL) for detection of the upper urinary tract urothelial tumors (UUT-UT). *Journal of Endourology* 2009;**23(s1)**:A23.

Tromberg B. Optical and physiological properties of tumors. In: *OSA Annual Meeting*, 1998.

Tsien RY. Imagining imaging's future. *Nature Reviews Molecular Cell Biology* 2003;**4**:SS16-SS21.

Tsien RY. The green fluorescent protein. *Annual Review of Biochem*istry 1998;**67**:509-544.

Udovich JA, Rouse AR, Tanbakuchi A, Brewer MA, Sampliner R, Gmitro AF. Confocal microendoscope for use in a clinical setting. *Proceedings of SPIE* 2007;**6432**.

Utzinger U, Brewer M, Silva E, Gershenson D, Blast RCB, Follen M, Richards-Kortum R. Reflectance spectroscopy for in vivo characterization of ovarian tissue. *Lasers in Surgery and Medicine* 2001;**28**:56-66.

Vishwasrao HD, Heikal AA, Kasischke KA, Webb WW. Conformational dependence of intracellular NADH on metabolic state revealed by associated fluorescence anisotropy. *Journal of Biological Chemistry* 2005;**280**:25119-25126.

Vo-Dinh T, Cullum BM. Fluorescence Spectroscopy for Biomedical Diagnosis. In: *Biomedical Photonics Handbook* (Vo-Dinh T, ed). Florida: CRC Press Boca Raton. 2003.

Vogel A, Venugopalan V. Mechanisms of pulsed laser ablation of biological tissues. *Chemical Reviews* 2003;**103**:577-644.

Volynskaya Z, Haka AS, Bechtel KL, Fitzmaurice M, Shenk R, Wang N, Nazemi J, Dasari RR, Feld MS. Diagnosing breast cancer using diffuse reflectance spectroscopy and intrinsic fluorescence spectroscopy. *Journal of Biomedical Optics* 2008;**13(2)**:024012.

Wagnières GQ, Star WM. Wilson BC. *In vivo* fluorescence spectroscopy and imaging for oncological applications. *Photochemistry and Photobiology* 1998;**68(5)**:603-632.

Wang HW, Jiang JK, Lin CH, Lin JK, Huang GJ, Yu JS. Diffuse reflectance spectroscopy detects increased haemoglobin concentration and decreased oxygenation during colon carcinogenesis from normal to malignant tumors. *Optics Express* 2009;**17(4)**:2805-2817.

Wang LV, Wu HI. *Biomedical Optics: Principles and Imaging.* New Jersey: John Wiley & Sons, Inc. 2007.

Wang TD, Crawford JM, Feld MS, Wang Y, Itzkan I, Van Dam J. In vivo identification of colonic dysplasia using fluorescence endoscopic imaging. *Gastrointestinal Endoscopy* 1999;**49(4)**:447-455.

Wang TD, Friedland S, Sahbaie P, Soetikno R, Hsiung PL, Liu JT, Crawford JM, Contag CH. Functional imaging of colonic mucosa with a fibered confocal microscope for real-time in vivo pathology. *Clinical Gastroenterology and Hepatology* 2007;5(11):1300-1305.

Wang W, Ke S, Wu Q, Charnsangavej C, Gelovani JG, Abbruzzese JL, Li C, Gurfinkel M, Sevick-Muraca EM. Near-infrared optical imaging of integrin alpha v beta 3 in human tumor xenografts. *Molecular Imaging* 2004;**3**:343-351.

Webb SED. *Development and Application of Widefield Fluorescence Lifetime Imaging.* PhD Thesis, University of London. 2003.

Xu RX, Povoski SP. Diffuse optical imaging and spectroscopy for cancer. *Expert Review of Medical Devices* 2007;**4(1)**:83-95.

Yang F, Moss LG, Phillips GN Jr. The molecular structure of green fluorescent protein. *Nature Biotechnology* 1996;**14(10)**:1246-1251.

Yang YL, Ye YM, Li FM, Li YF, Ma PZ. Characteristic autofluorescence for cancer diagnosis and its origin. *Lasers in Surgery and Medicine* 1987;**7(6)**:528-532.

Ye Y, Bloch S, Xu B, Achilefu S. Design, synthesis and evaluation of near infrared fluorescent multimeric RGD peptides for targeting tumors. *Journal of Medicinal Chemistrry* 2006;**49**:2268-2275.

Zhong W, Celli JP, Rizvi I, Mai Z, Spring BQ, Yun SH, Hasan T. In vivo high-resolution fluorescence microendoscopy for ovarian cancer detection and treatment monitoring. *British Journal of Cancer* 2009;**101**:2015-2022.

Zijlstra WG, Buursama A, Meeuwsen-van der Roest WP. Absorption spectra of human fetal and adult oxyhemoglobin, de-oxyhemoglobin, carboxyhemoglobin, and methemoglobin. *Clinical Chemistry* 1991;**37(9)**:1633-1638.

Zimmer M. Green fluorescent protein (GFP): Applications, structure, and related photophysical behaviour. *Chemical Rev*iews 2002;**102**:759-781.

Zonios G, Bykowski J, Kollias N. Skin melanin, hemoglobin, and light scattering properties can be quantitatively assessed in vivo using diffuse reflectance spectroscopy. *Journal of Investigative Dermatology* 2001;**117**:1452-1457.

Zonios G, Cothren RM, Arendt JT, Wu J, Van Dam J, Crawford JM, Manoharan R, Feld MS. Morphological model of human colon tissue fluorescence. *IEEE Transactions in Biomedical Engineering* 1996;**43(2)**:113-122.

Zonios G, Perelman LT, Backman V, Monoharan R, Fitzmaurice M, Van Dam, J, Feld, MS. Diffuse reflectance spectroscopy of human adenomatous polyps in vivo. *Applied Optics* 1999;**38(31)**:6628-6637.

3

Multispectral Fluorescence Imaging of Dyes and Endogenous Fluorophores

3.1. Introduction 81
3.2. Fluorescence detection of diseased tissue states 83
3.3. Multispectral fluorescence imaging of various fluorescent samples 84
3.3.1. Optical instrumentation 84
3.3.2. Data dimensionality reduction and image analysis technique 86
3.3.3. Initial system validation using fluorescent dye solutions 89
3.3.3.1. Sample preparation and imaging procedure 89
3.3.3.2. Imaging results 91
3.3.4. Further validation using fluorescent collagen gel tissue phantoms 101
3.3.4.1. Tissue phantom preparation and imaging procedure 101
3.3.4.2. Imaging results 104
3.4. Summary 106
3.5. References 108

3.1. Introduction

This chapter discusses the development of a new multispectral imaging-based spectroscopic system for performing laser-induced fluorescence imaging on tissues at the macroscopic level (and reflectance imaging in subsequent chapters). It is our aim to incorporate the system onto a laparoscope or flexible endoscope, allowing for the possibility of minimally-invasive *in vivo in situ* multispectral fluorescence imaging (MFI).

Conventional point-based fluorescence spectroscopy (FS) studies performed by other groups have successfully demonstrated the technique's ability to quantitatively detect malignant changes in a host of different human tissues as well as detect signals from

specific molecular contrast agents *in vivo*. Our imaging approach differs from these single point spectroscopy systems in that instead of acquiring only point-based quantitative tissue information, the technique results in the generation of larger region-based tissue colour maps of the interrogated area. This takes into account quantitative tissue spectral data, whilst allowing the diagnostic results to be presented in an easily accessible colour image format for qualitative assessment. Compared to other spectroscopy techniques, we believe that our excitation-resolved MFI approach has some advantages over emission-resolved methods, while still being useful for disease detection and classification. One major advantage of this unique approach is that light from our supercontinuum fibre laser source is rapidly tuned without requiring many emission filters, therefore allowing easier adaptation of laparoscopes and endoscopes and integration with multispectral reflectance and polarization resolved imaging techniques in the future.

MFI experiments performed in this chapter are focused on macroscopic imaging and serve as initial system validation for our tuneable supercontinuum laser system. Two different optical system setups were used in this chapter for imaging two distinct sets of fluorescent samples. The first setup utilised a mechanical wavelength selection method with a limited number of excitation wavelengths for imaging fluorescent dye solutions possessing excitation wavelengths similar to that of naturally-occurring endogenous fluorophores. The second setup expanded on this wavelength range towards a hyperspectral imaging system by utilising a digital multimirror device (DMD) during imaging of collagen gel tissue phantoms containing the same fluorescent dyes with the addition of the endogenous fluorophores flavin adenine dinucleotide (FAD) and protoporphyrin IX (PpIX).

The ability of two different dimensionality reduction algorithms to discriminate between different fluorescent species is also assessed and compared using the generated spectral image data, namely principal component analysis (PCA) and fixed-reference isomap (FR-IsoMap). A one-way multivariate analysis of variance (MANOVA) is applied on the resulting PCA and FR-IsoMap colour images as a means of comparing the specificity and sensitivity achieved by the two different dimensionality reduction techniques.

3.2. Fluorescence detection of diseased tissue states

Conventional procedures for the detection of dysplasia and carcinoma in biological tissues involve a series of random biopsies followed by histological examination of the resectioned tissue specimens. Although considered the current gold standard, this process is highly intrusive and results in a considerable amount of bleeding during resectioning, making it more difficult to clearly identify dysplastic/cancerous regions during the procedure. The untargeted nature of the tissue biopsy also results in sampling errors, which increases cost and further delays the time taken for correct diagnosis. The use of FS as an alternative 'optical biopsy' technique is therefore potentially useful as it causes considerably less trauma to the patient, has no or very few side effects, is a simple and quick procedure to carry out with results known within a matter of minutes, and can detect small cancerous lesions better than currently available diagnostic methods (Ramanujam, 2000a).

FS has been demonstrated by various groups to have the ability to detect and diagnose different tumour types in vivo in a range of biological tissues including the oral cavity (Müller *et al.*, 2003; Lane *et al.*, 2006), oesophagus (Georgakoudi *et al.*, 2001, Wallace *et al.*, 2005), colon (Mycek *et al.*, 1998; Wang *et al.*, 1999), cervix (Georgakoudi *et al.*, 2002; Chang *et al.*, 2002), and ovary (Brewer *et al.*, 2001) with a high degree of sensitivity and specificity. All of the above studies solely exploited tissue autofluorescence, i.e. no exogenous fluorescent agents were employed for increasing fluorescence contrast.

In contrast to the various FS studies that utilise tissue autofluorescence for disease detection such as those mentioned above and outlined in section 2.5.2 of chapter 2, several others have also relied upon the application of exogenous contrast agents for discriminating between tumourous and healthy tissues. These applied fluorescent agents may either be untargeted, e.g. fluorescein (FL) or indocyanine green (ICG), or tumour-targeting, e.g. tumour cell receptor-targeting dye-peptide or dye-antibody conjugates. Although the current specificity of FS is not as high as histopathological analysis, the high sensitivity of the technique means that it may serve as a useful 'red flag' technique for tissue biopsy guidance.

3.3. Multispectral fluorescence imaging of various fluorescent samples

As an extension to current point-based fluorescence detection methods, we propose a new excitation-resolved imaging based technique whereby spectral information is acquired on a larger regional basis (approximately 10 squared cm area) as opposed to a single point (a few mm squared area) by convention. The rationale is that since tissues are sampled over a wider area with our MFI approach, this would result in reduced procedure times, lower sampling errors and ultimately improved imaging efficiency and detection specificity. Additionally, it has often been noted that there are large amounts of inter- and intra-subject variability in the fluorescence spectral signature. As such, imaging over such a large area is likely to provide a useful background reference signal from the normal tissue signal for a particular patient. Imaging tissues via an excitation-resolved approach with application of a larger wavelength range will also elicit more comprehensive fluorescence contributions from the myriad of different endogenous fluorophores present in biological tissues. This therefore maximises the spectral information acquired and gives a better overall indication of the tissues' state of health.

As a prelude to MFI experiments in the next chapter involving actual biological tissue samples and for the purposes of initial system validation, we performed preliminary imaging experiments on fluorescent samples, namely fluorescent dye solutions and a collagen gel-based tissue phantom containing fluorescent dyes and endogenous fluorophores. For presentation of the final diagnostic imaging data, 'regional' images captured at different excitation wavelengths are subjected to post-processing by a dimensionality reduction technique: this selects only the most meaningful quantitative data parameters and generates colour maps of the interrogated tissue regions, thereby resulting in a final imaging format containing tissue diagnostic information that is intuitive and less complicated to interpret.

3.3.1. Optical instrumentation

All MFI work performed in this chapter utilised a newly developed supercontinuum fibre laser system emitting broadband pulsed light generated in highly non-linear holey fibre between the wavelength ranges of 460 – 1800 nm (see diagram of setup in Figure 3.1).

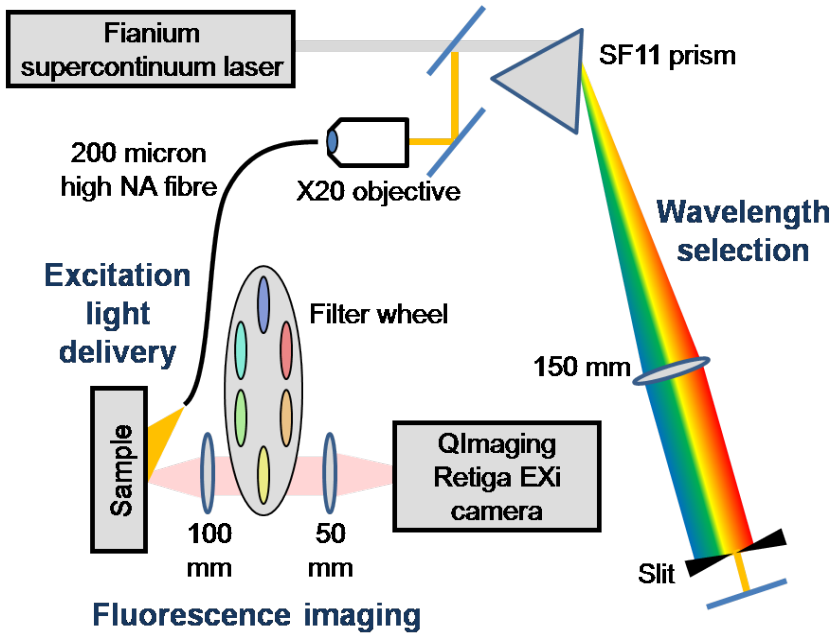


Figure 3.1. Diagrammatic representation of the supercontinuum fibre laser system used for MFI experiments in this section of the thesis. The sample shown is a multi-well PCR plate containing fluorescent dyes and fluorophore solutions of known excitation wavelength.

The experiment on different fluorescent dye solutions described in section 3.3.3 used a mechanical wavelength selection method and a limited number of excitation wavelengths. The system in section 3.3.4 expanded on this wavelength range by utilising a digital multimirror device (DMD) for rapid and automated wavelength selection. Output from the supercontinuum fibre laser source (Fianium SC450-2, replaced in subsequent chapters by Fianium SC400-4, producing light down to 400 nm) was transmitted through a home-built computer controlled spectral filter that consisted of a dispersive prism (SF2 or SF11) and motor controlled slit (based on a scheme by Dunsby *et al.*, 2004). The spectrally filtered light was then coupled into two metres of high NA (numerical aperture) polymer-clad 200 μm core diameter optical fibre (Thorlabs BFL37-200) using a x20 achromatic microscope objective. This fibre was selected to efficiently deliver light to the sample, whilst simultaneously illuminating a large field of view. The tip of the optical fibre was positioned approximately 120 mm away from the horizontal samples, pointing upwards at the underside of the samples during imaging. Emitted fluorescence from the samples was imaged onto a CCD (QImaging Retiga EXi) by two achromatic lenses with focal lengths of 50 and 100 mm respectively separated by a mirror at 45 degrees to allow the camera to be mounted horizontally. Although the excitation source is tuned in excitation spectroscopy, the emission filter also needs to be changed in

coarse steps to ensure that the excitation wavelength is always below the long-pass cut-on wavelength. For the selection of these emission filters, an electronically controllable filter wheel containing three longpass interferometric filters (cut-on wavelengths of 500, 550 and 600 nm) was positioned between the two lenses. Depending on the excitation wavelengths applied, a corresponding filter with suitable cut-on wavelengths was employed for obtaining sufficient signal for the fluorescence emission data. Additionally, light above 800 nm was filtered in a special filter block such that no infrared light passed into the spectral filter.

3.3.2. Data dimensionality reduction and image analysis technique

The key advantage of the supercontinuum fibre laser imaging system described earlier in section 3.3.1 is its unique ability to utilise combinations of several acquisition parameters (e.g. excitation and emission wavelengths), thus increasing its discrimination capability. As a consequence, analysis of the acquired image data is not as straightforward due to the large number of data dimensions generated. One solution to overcome this is to reduce the number of dimensions to a few underlying axes, whilst preserving the degree of variability that was present in the original data set as much as possible. This is performed with the aim of producing a new intuitive format for characterisation of biological tissue. One such approach is to reduce the data dimensionality to three components and to subsequently construct a representative colour map of the imaged region using the new 3-dimensional coordinates as the respective red, green and blue channels of the final RGB colour map image.

To achieve this, we first applied principal component analysis (PCA; Jolliffe, 2002; Jackson, 2003) to our data using the MatLab software package (Mathworks Inc., Natick, MA). PCA is a widely used technique for dimensionality reduction. It is a linear orthogonal transformation that aims to find directions that exhibit the maximum amount of variation in the cloud of original pixel data points. The technique involves the use of eigenvalue decomposition or singular value decomposition to extract a set of orthogonal axes from the covariance matrix of the original data. The end result is the generation of a linear model incorporating the axis with the main variation that can then be used to describe the tissue data.

However, PCA is not the most optimal dimensionality reduction technique to employ if the data cloud to be analysed lies on a more complex manifold with non-linear characteristics. To address this, a non-linear method of dimensionality reduction should be used instead, a number of which have been developed in recent years. One such technique is isometric mapping (Isomap) (Tenenbaum *et al.*, 2000), which preserves the inter-point dissimilarity relationships in the manifold in a manner similar to multidimensional scaling (MDS), whilst using geodesic distances to describe the shape of the manifold and thus the non-linear characteristics of the data.

The difference in approach between PCA and Isomap may be intuitively described by referring to the "Swiss roll" diagram depicting a non-linear data set (Figure 3.2; Tenenbaum *et al.*, 2000). This cloud of data points represents some real physical signal expressed in three dimensions. The points can all be said to lie on a curved plane in three dimensions and a non-linear method of finding the distances between the different points is desirable before applying MDS. PCA effectively only considers the Euclidian distance, or shortest distance between the points (blue line), which clearly underestimates the distance between the points when the underlying curved plane is taken into account. Conversely, Isomap takes into account the shortest geodesic distance (red line), between the two circled arbitrary points and hence accounts for the non-linearity of the data. In this case the points appear to be deceptively close in the data cloud when in actual fact they are not when considering the manifold. The results of applying PCA and Isomap/MDS to this data set and projecting onto a two dimensional (2D) space is illustrated in Figure 3.3. PCA fails to detect the true dimensionality of the data cloud, hence resulting in non-optimal processing of the non-linear information as illustrated by the mixing of coloured points in the 2D data plane (Figure 3.3B). On the other hand, Isomap faithfully preserves the local geometry of nearby data points in the 2D plane as seen by retention of the coloured pattern from the original 3D manifold (Figure 3.3C) (Law and Jain, 2006).

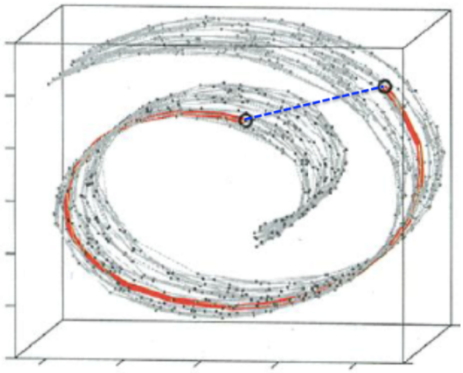


Figure 3.2. The "Swiss roll" example of a non-linear data set demonstrating the manner in which Isomap exploits geodesic distances (red line) on a non-linear manifold for accurate dimensionality reduction. This is in contrast to PCA, which utilises the Euclidean distances (blue dashed line) of the manifold, hence resulting in non-optimal processing of non-linear data sets. (Adapted from Tenenbaum *et al.*, 2000)

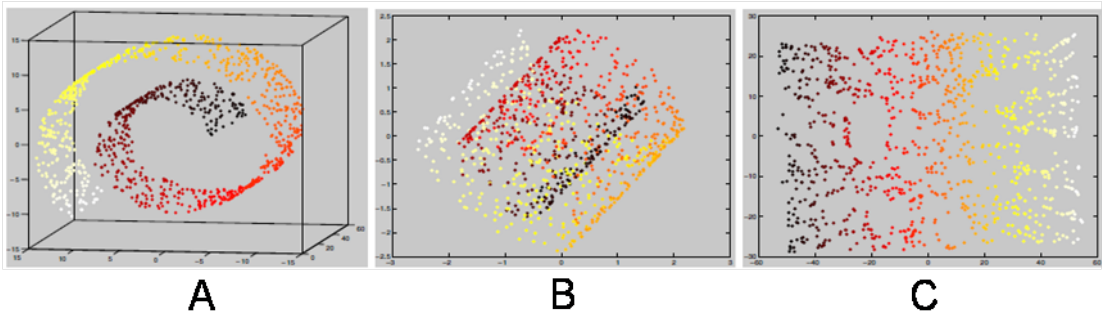


Figure 3.3. Diagrammatic representations illustrating the unfolding (dimensionality reduction) of the non-linear three-dimensional "Swiss roll" data set (A) onto a two-dimensional space by PCA (B) and Isomap (C) respectively. (Adapted from Law and Jain, 2006)

When the Isomap technique is applied to different datasets from the same tissue type however, results produced have been found to be non-comparable. This has been attributed to the fact that Isomap produces an optimal embedding only up to a geometrical transformation of the axes. To address this issue, IsoMap was adapted to generate consistent embedding between samples. This new method is called fixed-reference isomap (FR-IsoMap), which is based on the construction of a coordinate system that is fixed by applying Isomap to a training set that was selected as best representing the variation and tissue characteristics of the specific experiment. Therefore for the treatment of new test data, instead of reapplying Isomap, a mapping is computed

for each pixel onto the training set such that the inter-point distances to the nearest neighbours in the training set are well preserved. This therefore allows the generation of consistent mappings across samples and more meaningful and comparable colour maps for accurate tissue characterisation. More technical details about the method can be found in the papers on this topic (Lekadir *et al.*, 2006; Koh *et al.*, 2007).

The end result of our image processing procedure is the generation of an RGB colour map of the interrogated tissue region, with R, G and B dimensions of each pixel comprising the intensities from each of three dimensions representing the most meaningful data from the original manifold. In our case these three dimensions are obtained via dimensionality reduction of the original data set using either the PCA or FR-IsoMap techniques.

3.3.3. Initial system validation using fluorescent dye solutions

3.3.3.1. Sample preparation and imaging procedure

Various fluorescent dyes were chosen for imaging that possessed excitation wavelengths similar to that of flavin adenine dinucleotide (FAD) and porphyrins – endogenous constituents of biological tissue that are believed to be involved in the transformation processes around the onset of carcinogenesis (Ramanujam, 2000b). These were chosen to demonstrate the system's ability to distinguish dyes with similar fluorescence spectra and in various different concentrations.

The fluorescent dyes imaged (and absorption maxima) consisted of coumarin 334 (C334; 450 nm), fluorescein (FL; 512 nm), rhodamine 6G (R6G; 530 nm), rhodamine B (RB; 552 nm) and cresyl violet perchlorate (CV; 601 nm). Each dye solution was made up to various concentrations in 99% ethanol, which has been found to only absorb in the ultraviolet range between 200 to 250 nm (Liu *et al.*, 2003; Liu *et al.*, 2005). This is below our intended excitation range in the visible and near-infrared (Vis-NIR) spectrum, implying that ethanol may therefore be used as a suitable solvent for our fluorescent dyes. In fact, no fluorescence was observed in a control solution of 99% ethanol alone.

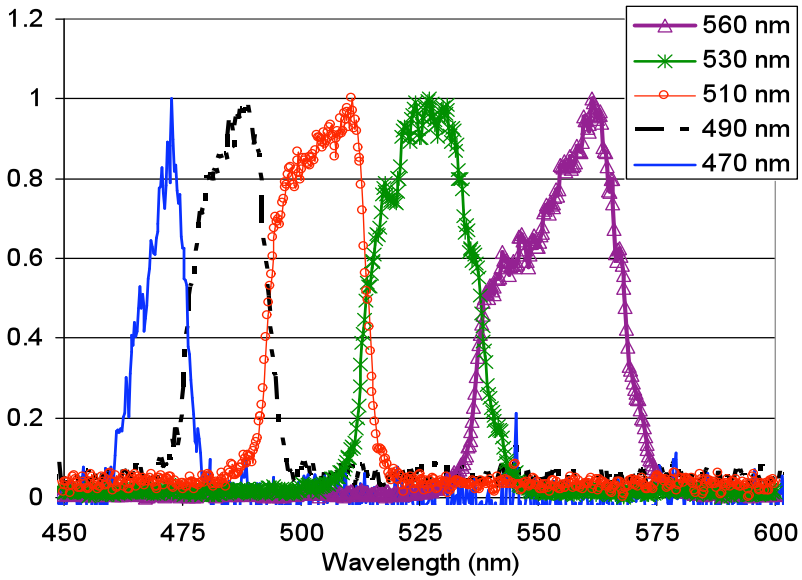


Figure 3.4. Normalised excitation spectra applied by the supercontinuum imaging system.

Dye solutions were pipetted into 100 µl multi-well clear glass bottomed PCR (polymerase chain reaction) plates for imaging. Two validation tests were performed: the first test set consisted of single dye solutions of varying concentrations (0.3 µM, 1.0 µM, 3.0 µM and 10.0 µM) and the second test set of two-dye mixtures made up in various proportions to a final combined concentration of 3.0 µM. Imaging experiments were performed using the supercontinuum fibre laser imaging system described in section 3.3.1. The system was set up to generate five different excitation wavelengths as shown in Figure 3.4, and these were paired up with longpass interferometric filters with cut-on wavelengths of 500, 550 and 600 nm as listed in Table 3.1.

Excitation wavelength (nm)	Excitation bandwidth (nm)	Emission filter
470	10	Longpass 500 nm
490	20	Longpass 500 nm
490	20	Longpass 550 nm
510	20	Longpass 550 nm
530	25	Longpass 600 nm
560	35	Longpass 600 nm

Table 3.1. Combinations of excitation wavelengths and corresponding emission filters used.

3.3.3.2. Imaging results

Two sets of raw intensity images (Figure 3.5) were captured during excitation-resolved fluorescence spectroscopic imaging of single dye solutions and dye mixtures using the supercontinuum laser imaging system described previously in section 3.3.1. The samples were excited with six different combinations of excitation spectra and emission filters (500, 550 or 600 nm longpass) as listed in Table 3.1.

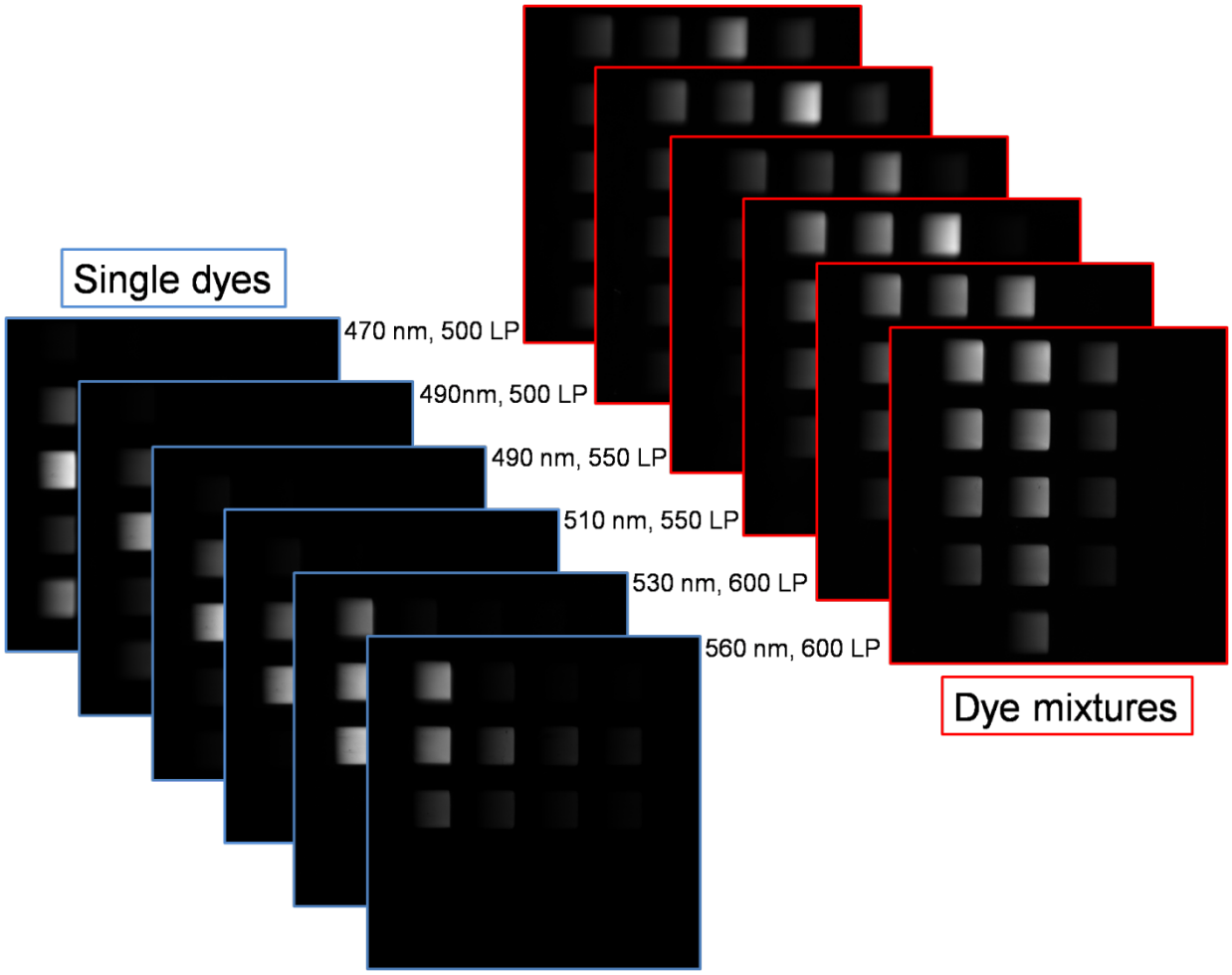


Figure 3.5. Raw fluorescence intensity images of single dye solutions (blue outlines) and dye mixtures (red outlines) acquired at six different combinations of excitation wavelengths and long pass (LP) emission filters (listed in Table 3.1).

Prior to processing with either the PCA or FR-IsoMap dimensionality reduction techniques, both sets of raw intensity images were subject to some pre-processing using the MatLab software package (Mathworks Inc., Natick, MA). First, pixel values from the

recorded background images i.e. images recorded without any sample, were subtracted from the respective raw intensity images of single dyes or dye mixtures for each excitation spectrum/emission filter combination (see examples in Figure 3.6). Bright-field images recorded using a reflectance standard as the sample (Figure 3.6B) also had their respective background images subtracted. In the final normalisation step, background-subtracted intensity images were divided by background-subtracted bright-field images for each respective wavelength/filter combination. The presence of noise meant that the signal error would propagate through and it was therefore important to achieve good signal to noise ratios to avoid this. Resultant image pixel values obtained from this last pre-processing step were subsequently processed by PCA or FR-IsoMap for generation of the final RGB colour images of the interrogated regions.

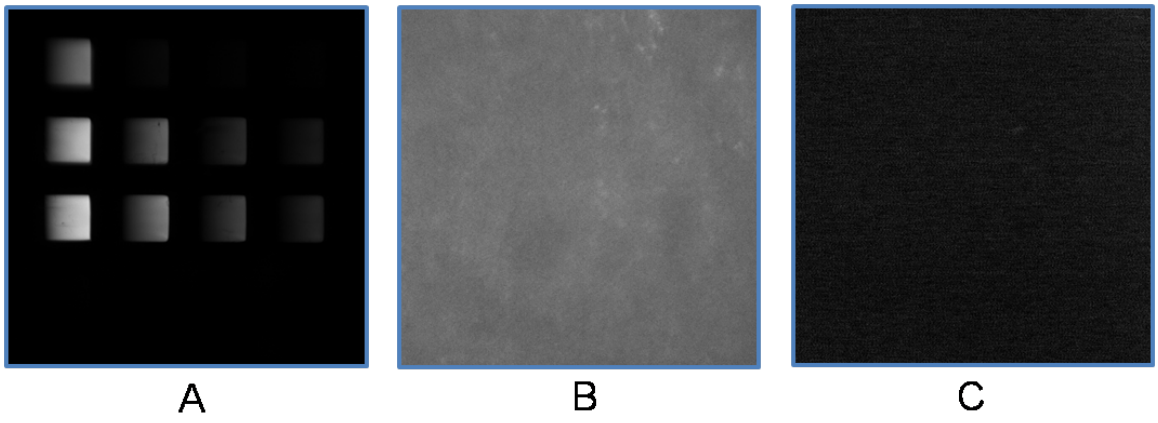


Figure 3.6. Example images used to illustrate the image pre-processing step performed prior to data dimensionality reduction with either PCA or FR-IsoMap: intensity image (A); bright-field image (B); background image (C).

Figure 3.7 represents the MFI images of fluorescent dye solutions obtained after processing of pixel data with PCA (Figures 3.7A and C) and FR-IsoMap (Figures 3.7B and D). For FR-IsoMap, pixel data from the acquired images were treated as the training data set. Figures 3.7A and 3.7B are processed images of single dye solutions at concentrations of 0.3 μM, 1.0 μM, 3.0 μM and 10.0 μM, whereas Figures 3.7C and 3.7D are the processed images of two-dye mixtures mixed in different proportions to a total concentration of 3.0 μM.

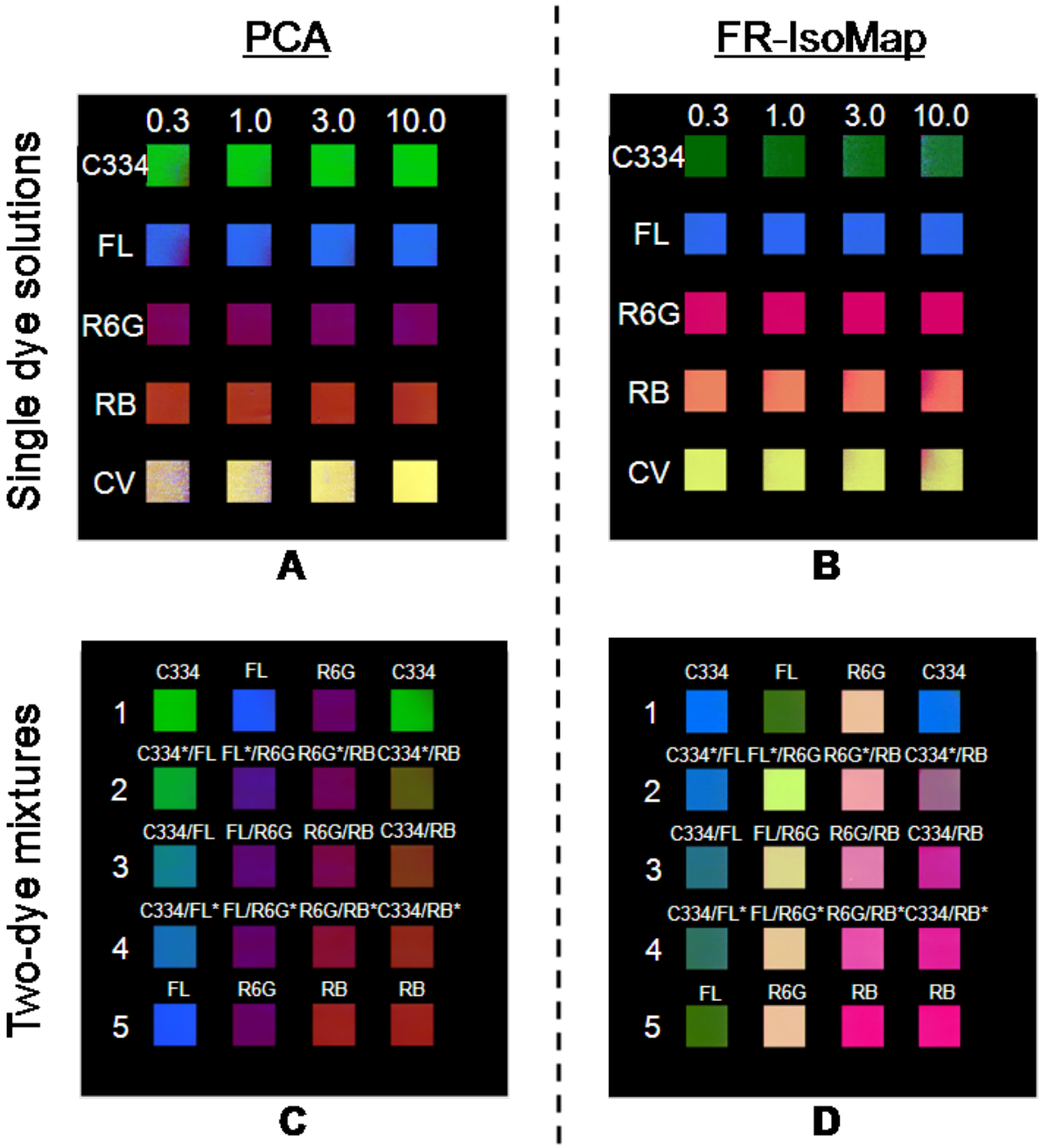


Figure 3.7. PCA and FR-IsoMap processed images of single dye solutions made up to different concentrations in 99% ethanol (marked in μM) (A and B) and two-dye mixtures of 3.0 μM total concentration (C and D). For rows 2 and 4 of the dye mixtures (C and D), the asterisks (*) denote the dyes that are present in higher proportions (75%) in the two-dye mixture. Dyes in row 3 are present in equal amounts. Note that the fourth columns of C and D are presented the opposite way round from the others.

PCA and FR-IsoMap processed images of single dye solutions (Figures 3.7A and B) clearly indicate that both techniques can accurately distinguish between different dye solutions with different excitation maxima based on their final mapped RGB values. It also demonstrates that different dye concentrations i.e. different overall fluorescent intensities, still result in the same colour being generated for each dye in the RGB colour space regardless of whether PCA or FR-IsoMap is applied to the data. When comparing Figures 3.7A and B qualitatively by eye, the colours and contrast between each dye displayed in the PCA image (Figure 3.7A) and FR-IsoMap image (Figure 3.7B) appear similar. Therefore to investigate and quantify the actual degree of separation of pixels in the 3D RGB colour space of each technique, more in-depth analysis will have to be performed later.

The PCA and FR-IsoMap-processed images of the two-dye mixtures (Figures 3.7C and D) displayed a smooth gradation of colour when transitioning from one dye type to the next. This demonstrated the possibility of applying both dimensionality reduction techniques to discriminate between mixtures of fluorescent dyes of different absorption maxima. An interesting observation is in row three of the two-dye colour images where both dyes are present in equal amounts: regardless of the difference in absorption maxima between the two dyes, e.g. a large 102 nm gap between C334 and RB or a small 18 nm difference between FL and R6G, both PCA and FR-IsoMap can effectively map the dye combinations to their own distinct three-dimensional RGB colour space. This implies a high degree of specificity of both techniques for discrete classification of samples of different fluorophores and combinations of fluorophores and may therefore be useful for tissue imaging where the relative abundance of different fluorophores conveys diagnostic capability.

Whilst the above explanation of these results provides an intuitive interpretation of the experiment, it is desirable to compare the two techniques quantitatively. For this we have carried out a Multivariate Analysis of Variance (MANOVA) to both PCA and FR-IsoMap processed images. This technique assesses the null hypothesis that the colour pixel means of dye solutions in each well are of the same *n*-dimensional multivariate vector, and that any observable difference within each well is as a result of random chance. To perform this analysis, a test region of roughly 1900 - 2000 pixels was

manually chosen from each well in the image (approximately $4/5^{th}$ of the total pixels in each well). Information obtained after applying MANOVA with MatLab included:

i. *d*, the number of dimensions of the means in the analysed dataset,
ii. the *p* values i.e. the calculated probability for each dimension, which is the estimated probability of rejecting the null hypothesis; *p* values less than 0.05 imply that the result obtained is significant and the null hypothesis may be rejected, and
iii. a vector of Mahalanobis Distances (MDs) measured from each pixel to the mean of its chosen region, and a matrix of average MDs between the selected regions. The MD is a quantifiable distance measure of likeness between two or more classes (where the classes in this case are the pixels of wells containing different fluorescent samples) or the likeness within a class (i.e. the pixels within each fluorescent well sample) where different data patterns can be distinguished and analysed. The greater the MD between two classes, the higher the degree of separation between them in the Euclidian space and hence the more dissimilar they are, and vice-versa.

The MD is calculated using the following equation:

$$MD_i = \sqrt{(x_i - \bar{x})C_{\mathrm{x}}^{-1}(x_i - \bar{x})^{\mathrm{T}}} \qquad \text{for } i = 1 \text{ to } n$$

where x_i is the input intensity of a given pixel in the sampled region within each well, $\bar{x}$ is the mean intensity of the pixels in that selected region, C_x^{-1} is the inverse of the covariance matrix of all pixel intensities within that selected well region and $(x_i - \bar{x})^{\mathrm{T}}$ is the transpose of the vector $(x_i - \bar{x})$.

Following MANOVA analysis of Figures 3.7A and B of the single dye solutions, the algorithm returned values of $d = 3$ and $p < 0.005$, which signified highly accurate identification of the classes when represented as three RGB colour channels for both PCA and FR-IsoMap dimensionality reduction techniques. Table 3.2 shows the average MDs obtained between combinations of single dye-pairs of 0.3 μM concentration and the average MD within each well for each dye. For accurate classification, it is desirable

for measured intra-dye MDs to be small, meaning that the cloud of data points mapped onto the three-dimensional colour space is well localised and therefore similar in colour. For the converse reason, it is also desirable for the inter-dye MDs obtained to be large. The low 0.3 μM dye concentration was selected to compare the sensitivity of both PCA and FR-IsoMap techniques – a test to see which method could accurately distinguish the various dyes in this 'worst-case scenario' of least fluorescence and therefore highest relative background and noise levels.

	C334	FL	R6G	RB	CV
C334	7.56 **0.17**	155.58 **534.78**	342.34 **1534.00**	445.75 **1476.04**	610.43 **1317.62**
FL	155.58 **534.78**	7.38 **0.19**	104.15 **1337.89**	228.42 **1311.31**	382.92 **1128.52**
R6G	342.34 **1534.00**	104.15 **1337.89**	0.23 **0.24**	63.19 **161.59**	308.05 **498.41**
RB	445.75 **1476.04**	228.42 **1311.31**	63.19 **161.59**	0.48 **0.28**	131.14 **109.31**
CV	610.43 **1317.62**	382.92 **1128.52**	308.05 **498.41**	131.14 **109.31**	19.99 **0.08**

Table 3.2. Average interclass Mahalanobis Distances between single dye solutions of 0.3 μM concentration after PCA (normal text) and FR-IsoMap (bold text) processing (unshaded). The average intraclass MD is also shown (shaded).

From Table 3.2, it can be observed that a larger average inter-well MD was obtained between almost all single dye solutions of 0.3 μM concentration when results were processed by FR-IsoMap. This indicates that single dyes were better separated from each other with this dimensionality reduction technique compared to PCA. Intraclass MDs within the same dye solution obtained after FR-IsoMap processing were also much smaller compared to PCA for almost all dye solutions. This again signified more discrete and accurate classification of each single dye type to within its own distinctive RGB colour space. Note that the ratio of inter- to intra-MDs is far greater for FR-IsoMap than PCA, providing further evidence that this technique distinguishes the different dyes better.

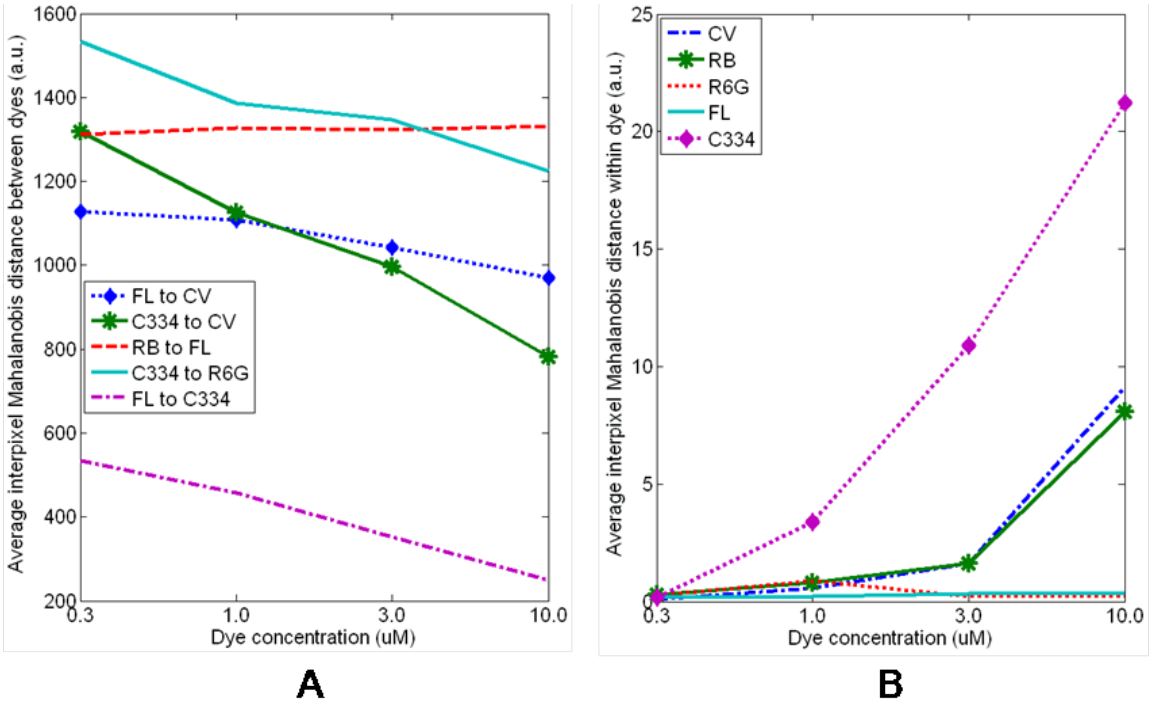


Figure 3.8. Average interclass Mahalanobis distances between dye pairs (A) and within the same dye (B). FR-IsoMap performance declined as dye concentrations increased from 1.0 μM to 10.0 μM, with corresponding decreases in the average interclass distance between almost all dyes (A) and increases in the average interclass distance within each dye (B).

MANOVA was later applied to the PCA and FR-IsoMap-processed images of 1.0 μM, 3.0 μM and 10.0 μM single dye concentrations (Figures 3.7A and B). The results demonstrated a decline in FR-IsoMap performance as dye concentration increased from 1.0 μM to 10.0 μM, with decreases in average interclass MDs between almost all dyes and increases in interclass MDs, as shown respectively in Figures 3.8A and B. The decline in FR-IsoMap performance was most significant compared to PCA at 10.0 μM dye concentrations, implying that the FR-IsoMap technique performs most optimally at lower dye concentrations, i.e. low fluorescence emission levels, up to a threshold of about 3.0 μM concentration in this instance.

MANOVA was then applied for the analysis of PCA and FR-IsoMap processed images from the second test set of two-dye mixtures of 3.0 μM concentration (Figures 3.7C and D). The analysis returned values of $d = 3$ and $p < 0.005$ across all images indicating a significant result in the three dimensional representation, with MDs having much larger values overall compared to those from the first test set of single dye solutions (results not shown).

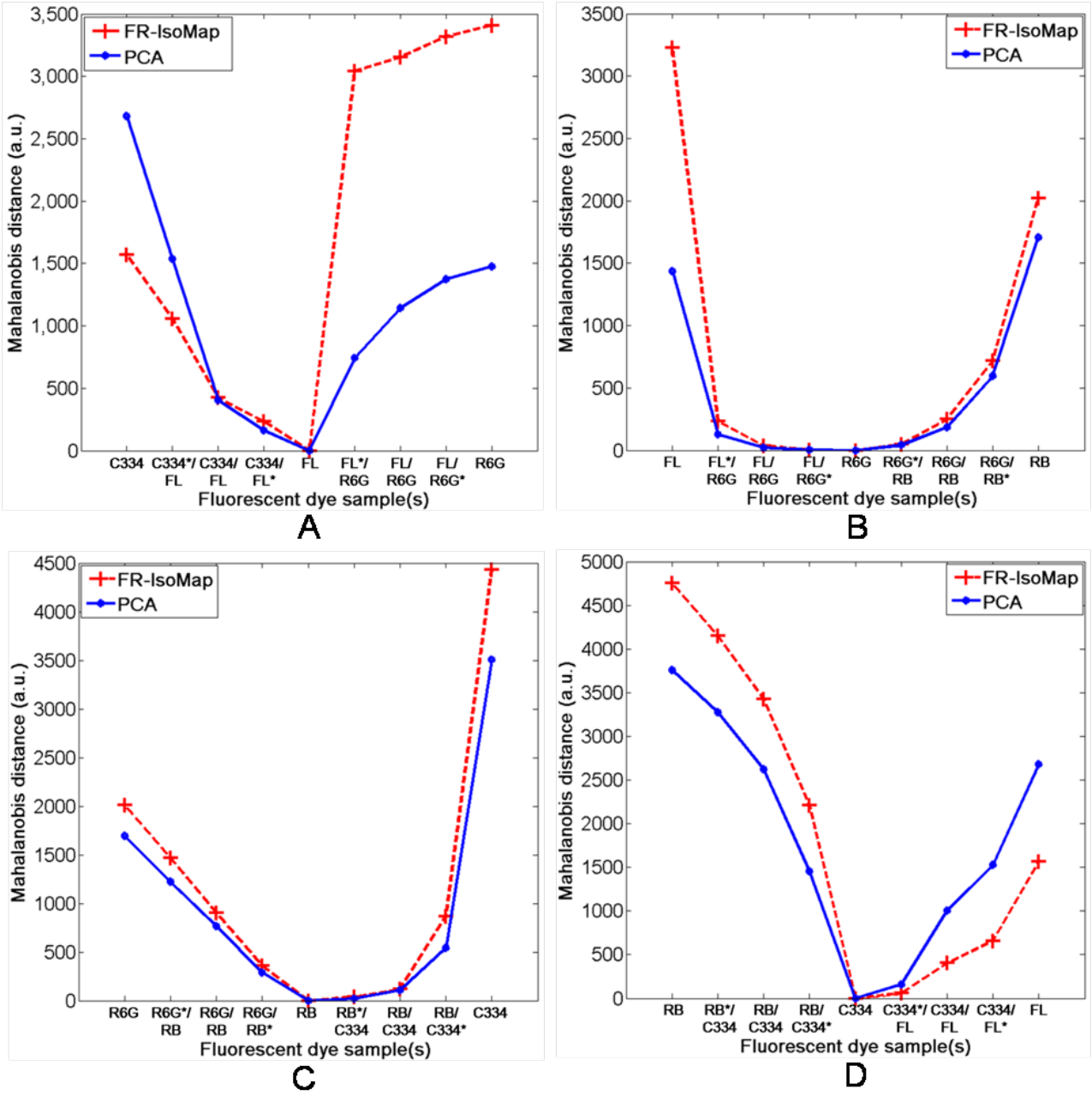


Figure 3.9. Graphical representation of variation in average Mahalanobis distances from sequential MANOVA analyses of two-dye mixtures of 3.0 μM total concentration. In each case, the pure dye of interest is positioned in the centre of the x-axis. On the left and right of this central dye is an increasing concentration of one of the other dyes. Red dashed curves represent the FR-IsoMap technique and blue curves represent PCA. Sequential analyses are shown for various dye groups: C334–FL–R6G (A); FL–R6G–RB (B); R6G–RB–C334 (C); RB–C334–FL (D). The asterisks (*) denote the dyes that are present in higher proportions in the two-dye mixture.

To determine the data dimensionality reduction technique that best discriminated two-dye mixtures, MDs obtained from the sequential MANOVA analysis of selected PCA and FR-IsoMap-processed images of two-dye mixtures were plotted and compared as shown in Figure 3.9. This served to 'unwrap' the pixel data from the RGB colour space, allowing a clearer display of the spread in MD values obtained from MANOVA of both techniques in two dimensions. It is evident from the figure that FR-IsoMap (red dashed curve in graphs) gave a wider spread of MDs than PCA (blue curves) - more than two times in some instances - indicating better discrimination. This type of test has implications for the distinction of a specific spectral signature of varying intensity upon a background signal of varying intensity, for instance when attempting to detect a specific fluorophore on top of a fluorescent background. Although FR-IsoMap does not produce better discrimination across all samples, it should be noted that the smaller inter-sample MDs for FR-IsoMap is not represented in Figure 3.8 and FR-IsoMap is a better technique for overall discrimination.

The effects of dye concentration were next investigated on PCA and FR-IsoMap processing results. To test this, MANOVA analysis was performed on PCA and FR-IsoMap processed single-dye images of 0.3 μM, 1.0 μM, 3.0 μM and 10.0 μM concentrations (Figures 3.7A and B) to investigate the average intraclass MDs within each dye. As seen in Figure 3.10, results indicated that both techniques demonstrated a minor change in MDs following the increase in concentration from 0.3 μM to 3.0 μM for most dyes. Greater increases in MDs occurred during the 3.0 μM to 10.0 μM transition for both PCA and FR-IsoMap techniques, with the latter demonstrating a larger change overall. However, the scales of these graphs have been exaggerated compared with the graphs comparing the MDs between dye groups and overall these changes are all very small. This finding demonstrates that both dimensionality reduction techniques can function relatively independent of concentration changes and therefore across a wide range of intensity values.

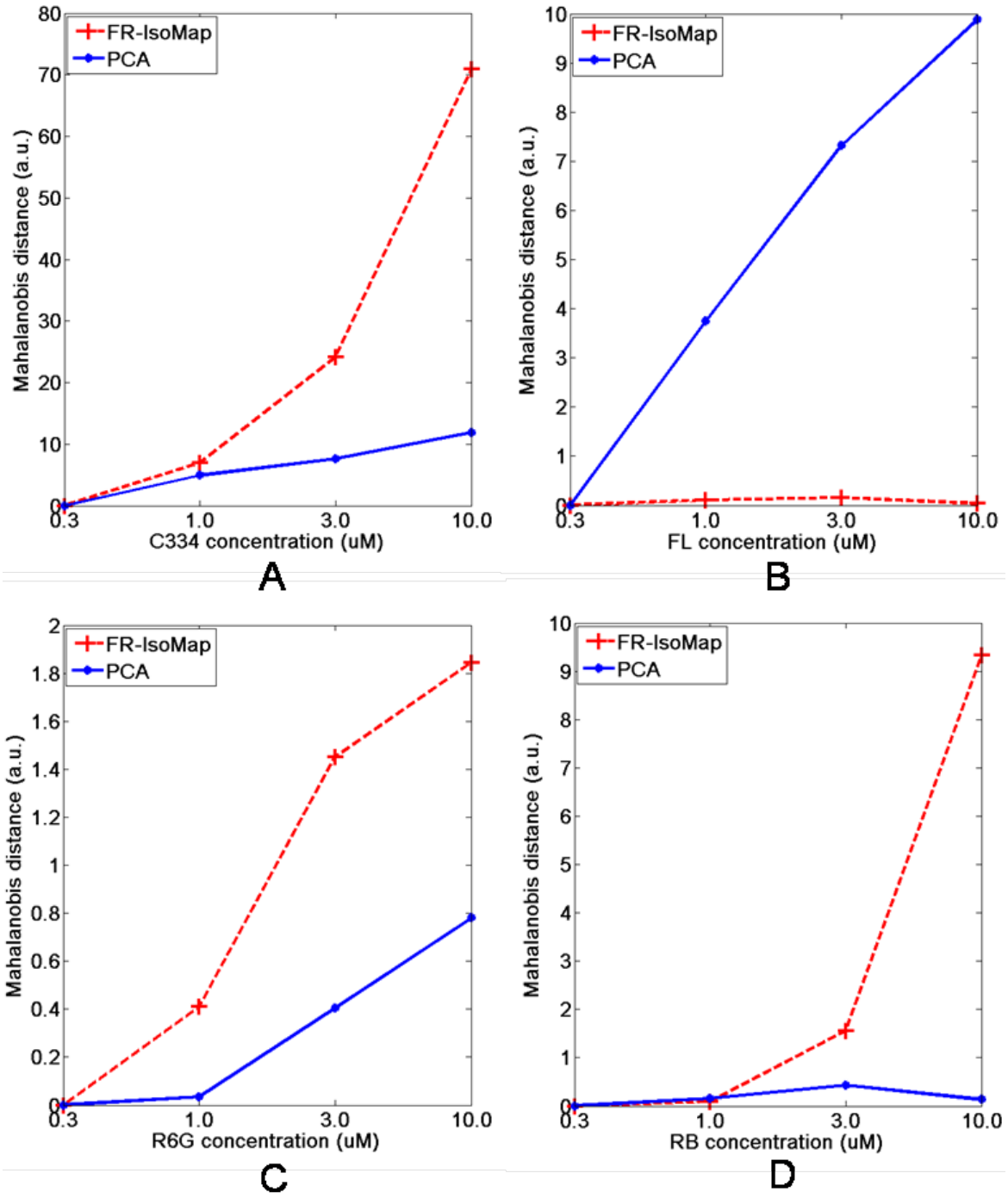


Figure 3.10. Variation in the measured average intraclass Mahalanobis distances from PCA (blue curve) and FR-IsoMap (red curve) processed images of single dyes of increasing concentration (0.3 to 10.0 µM.): C334 (A), FL (B), R6G (C) and RB (D). Greater changes occurred during the 3.0 µM to 10.0 µM concentration increase for both PCA and FR-IsoMap.

3.3.4. Further validation using fluorescent collagen gel tissue phantoms

Optical tissue phantoms have been used since the early 1980s to simulate properties of biological tissues in the fields of biology and medicine. Besides allowing better understanding of the optical characteristics of tissues, they also serve as useful tools for the development of clinical imaging modalities like magnetic resonance imaging and computer tomography systems as well as those found in the field of biomedical optics (Das *et al.*, 1997; Wagnieres *et al.*, 1998). Several types of liquid and solid phantoms have been created to date which attempt to mimic the inhomogeneous properties of human tissue (Moffitt *et al.*, 2006).

As the next step towards tissue-based experiments and also to investigate if fluorescence originating from tissue-simulating media could be detected by our MFI system, a biologically relevant collagen gel tissue phantom was fabricated based on a protocol described by Sokolov and colleagues into which fluorescent dye and endogenous fluorophores were included (Sokolov *et al.*, 2002).

3.3.4.1. Tissue phantom preparation and imaging procedure

Type I collagen used for fabricating the gel phantom was harvested manually using a surgical scalpel from tail tendons of adult (200 – 400 g) Sprague-Dawley rats provided by Central Biomedical Services, Imperial College London, UK. Once extracted from tail tendons, the collagen fibres were placed out to dry on a paper towel, weighed, and then transferred into 0.1% v/v acetic acid solution at 4 °C for a period of five days until complete solubilisation was achieved. Collagen fibres were added to the acid solution at a ratio of 1 g dried collagen to 300 ml acetic acid. After being completely solubilised, the resulting collagen solution was cleared by centrifugation (20 minutes at 10,000 rpm) and the supernatant (i.e. the solubilised collagen solution) subsequently removed and stored separately at 4 °C. To bring about gel formation, eight parts of the collagen solution were mixed with one part sterile 10x PBS buffer and one part sterile 0.2 M HEPES (pH 7.3). The mixture was then placed in an incubator set at 37 °C for gelation to occur, with the entire process complete in about 45 minutes.

For the purpose of imaging, collagen gel phantoms were made up in 24-well cell culture plates (15.0 mm well diameter) to a final gel thickness of 3 mm. Mixed into the collagen gel solution prior to gelation were fluorescent dyes and endogenous fluorophores made up to a final concentration of 3.0 μM. Dyes used were similar to those described in section 3.3.3.1, together with inclusion of the endogenous fluorophores flavin adenine dinucleotide (FAD; 450 nm absorption) and protoporphyrin IX (PpIX; absorption between 400 to 450 nm). Optical absorbers and scatterers were also added to the collagen gel solutions in each well before gelation to create a more realistic tissue phantom. Human haemoglobin (Sigma-Aldrich, UK) was added as the absorbing agent at 5.0 mg per well. The scattering agent consisted of 0.97 μm diameter silicon microspheres (Polysciences Europe GmbH) added at an amount of 3.0 mg per well. This was to simulate scattering from tissue microstructures such as cell nuclei, mitochondria, and lysosomes due to a difference in refractive index between the microspheres and collagen gel medium. We expect the type of scattering to be Mie scattering as a result of the 0.97 μm diameter size of the homogenous microspheres.

The supercontinuum fibre laser system used for this set of experiments was similar to the system described previously in section 3.3.1 but with a few modifications. The main difference was the addition of a digital micromirror device (DMD; Texas Instruments, USA), which allowed for faster and more automated selection of a wider excitation wavelength range from the filtered output of the fibre laser source (450 – 800 nm) compared to the original motor-controlled slit. In the optical setup, the retroreflecting mirror was replaced with the DMD and angled 45° to the incident beam to reflect light at an approximately 90° angle of deflection. The DMD is made up of hundreds of thousands of movable and highly reflective micromirrors measuring approximately 10.8 by 10.8 microns in size (Texas Instruments product brochure). Movements of each of these micromirror elements may be electronically controlled. When an incident ray of light arrives at the surface of the mirror elements, applying a voltage to one or more of these movable elements may modulate its reflected path. The applied voltage switches the mirror postition by an angle of +/- 12°. Since each element may be individually controlled, it is thus possible to select a predetermined set or combinations of elements on the DMD and switch them on or off. When a spectrum of light is incident on the DMD, switching on a predefined combination of micromirror elements would therefore allow only selected wavelengths to be reflected towards a target whilst rejecting the

remaining wavelengths. As such, even different combinations of wavelengths may be selected simultaneously for sample excitation. Due to significant diffraction occurring from the DMD, only one of the output orders was used during our imaging procedures.

During imaging, a total of 13 different excitation wavelengths were used (shown in Figure 3.11), which were paired up with three longpass interferometric filters of 500, 550 and 600 nm cut-on wavelengths respectively used (refer to Table 3.3). This spread of excitation wavelengths was selected in order to target the absorption maxima of every fluorescent dye and fluorophore used in the study. Exposure timing of the camera was set at 0.01 seconds with four averages recorded for each field.

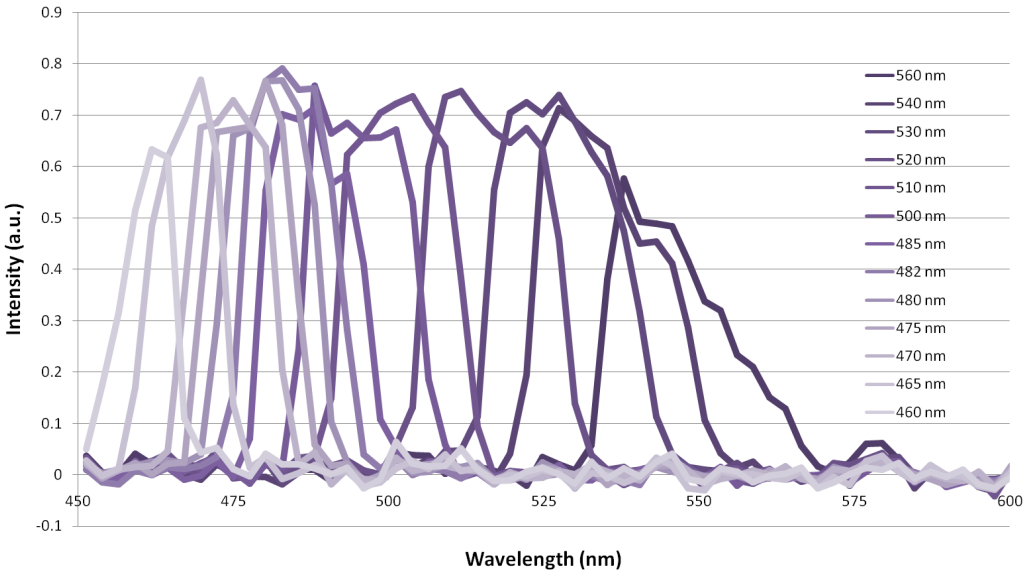


Figure 3.11. The 13 excitation wavelengths applied for generation of the fluorescence intensity images in the amalgamated dataset (refer to Figure 3.12A).

Excitation wavelength (nm)	Emission filter
460	Longpass 500 nm
465	Longpass 500 nm
470	Longpass 500 nm
475	Longpass 500 nm
480	Longpass 500 nm
482	Longpass 550 nm
485	Longpass 550 nm
500	Longpass 550 nm
510	Longpass 550 nm
520	Longpass 550 nm
530	Longpass 600 nm
540	Longpass 600 nm
560	Longpass 600 nm

Table 3.3. Combinations of excitation wavelengths and corresponding emission filters used.

3.3.4.2. Imaging results

Results from MFI of collagen gel tissue phantoms in this section were processed using only the FR-IsoMap dimensionality reduction technique. Data extracted from multiple imaging runs of fluorescent collagen gel phantoms produced an amalgamated image dataset that was subsequently used to generate the fixed reference colour map. These imaging runs consisted of data recorded from multiple laboratory sessions and repeated collagen sample preparations both with and without scattering spheres included to simulate tissue scattering. A 'pre-processing' step was performed to subtract the background image, followed by normalisation using the integrated fluorescence (bright-field images) from all 13 images on a pixel-by-pixel basis as in section 3.3.3.2.

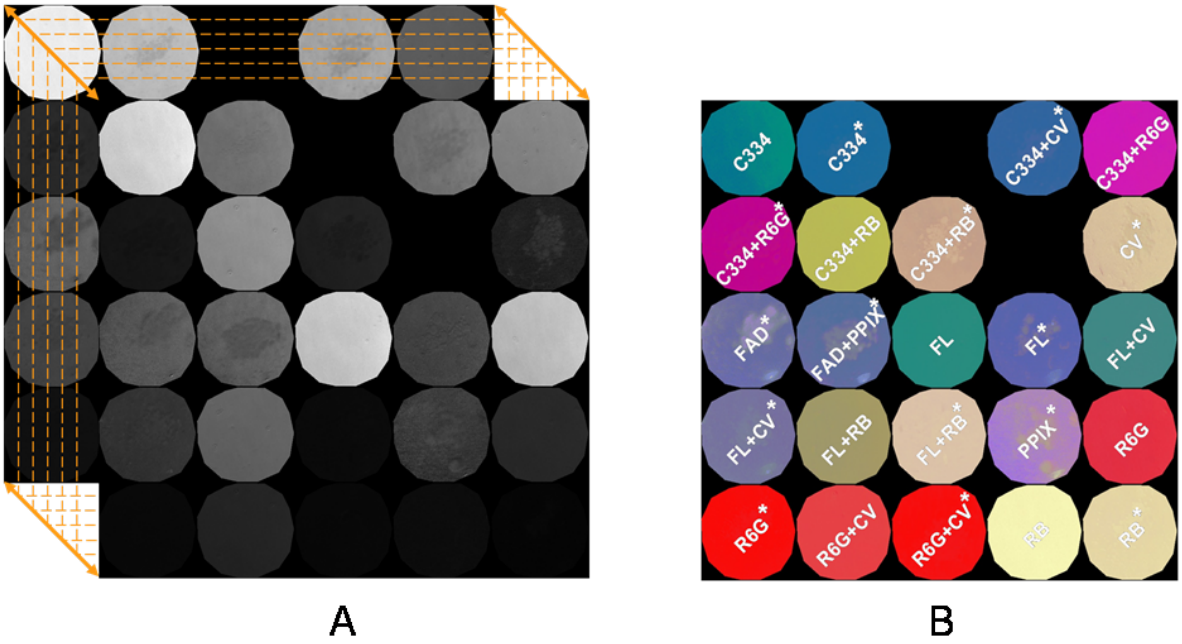


Figure 3.12. The amalgamated fluorescence image dataset (A) used to create the FR-IsoMap colour map (B) of collagen gel tissue phantoms embedded with fluorescent dyes and fluorophores. Dye/fluorophore abbreviations are as described in the text, and wells labelled with an asterisk contain both scattering microspheres and haemoglobin. The black wells are tissue phantoms that have been masked out due to insufficient fluorescence emissions so as to not interfere with the final FR-IsoMap embedding.

Figure 3.12A is an example input image dataset comprising stitched greyscale fluorescence intensity images of fluorescent collagen gel phantoms imaged at various excitation wavelengths. Consistent colouring is seen for identical fluorophores in the

processed images in Figure 3.12B both with and without scattering microspheres and haemoglobin present. Good contrast was also achieved between different dye/fluorophore samples, even for those with similar excitation spectra. Scattering microspheres are especially evident in some wells in Figure 3.12B where they have agglomerated in the middle of those wells. This occurrence has significantly altered the optical properties of the wells at these locations and has resulted in a change in colour in those parts of the wells, hence the dyes/fluorophores in those wells are not accurately and clearly delineated in the fixed reference map. The presence of non-agglomerated scatterers in other locations does not appear to have significantly altered the colour. The presence of haemoglobin and scattering microspheres resulted in an alteration of the FR-IsoMap classification for some wells containing identical fluorophores, an effect attributed to absorption of green fluorescence by haemoglobin.

	C334	CV	FAD	FL	PpIX	R6G	RB
C334	5.04	1714.54	656.87	43.43	1368.15	3826.77	2337.65
CV	1714.54	2.95	436.56	1230.06	150.88	1786.08	170.22
FAD	656.87	436.56	14.73	401.14	152.06	1620.43	1020.17
FL	43.43	1230.06	401.14	0.32	967.85	3211.41	1804.51
PpIX	1368.15	150.88	152.06	967.85	18.06	1372.90	567.97
R6G	3826.77	1786.08	1620.43	3211.41	1372.90	0.70	2908.86
RB	2337.65	170.22	1020.17	1804.51	567.97	2908.86	1.08

Table 3.4. Matrix of Mahalanobis distances (MDs) for different wells selected from within Figure 3.9B. Shaded boxes indicate intraclass MDs within individual dyes, while unshaded boxes represent the interclass MDs between different dye types in different wells.

To evaluate the effect of the presence of noise within the fixed reference map, MANOVA analysis was applied to calculate the MDs from each pixel to the mean of its region within each well together with a matrix containing the average MDs between pairs of pixel region means in different wells (see section 3.3.3.2 for a more detailed explanation). Typical results from MANOVA analysis of representative wells from Figure 3.12B are shown in Table 3.4, where significant interclass MDs between different dye/fluorophore samples and small intraclass MD variation within individual samples (diagonal elements) are evident. A graphical representation of this information is also

shown in Figure 3.13 of the C334, FAD and PpIX, showing clear discrimination between these fluorophores that possess similar excitation maxima.

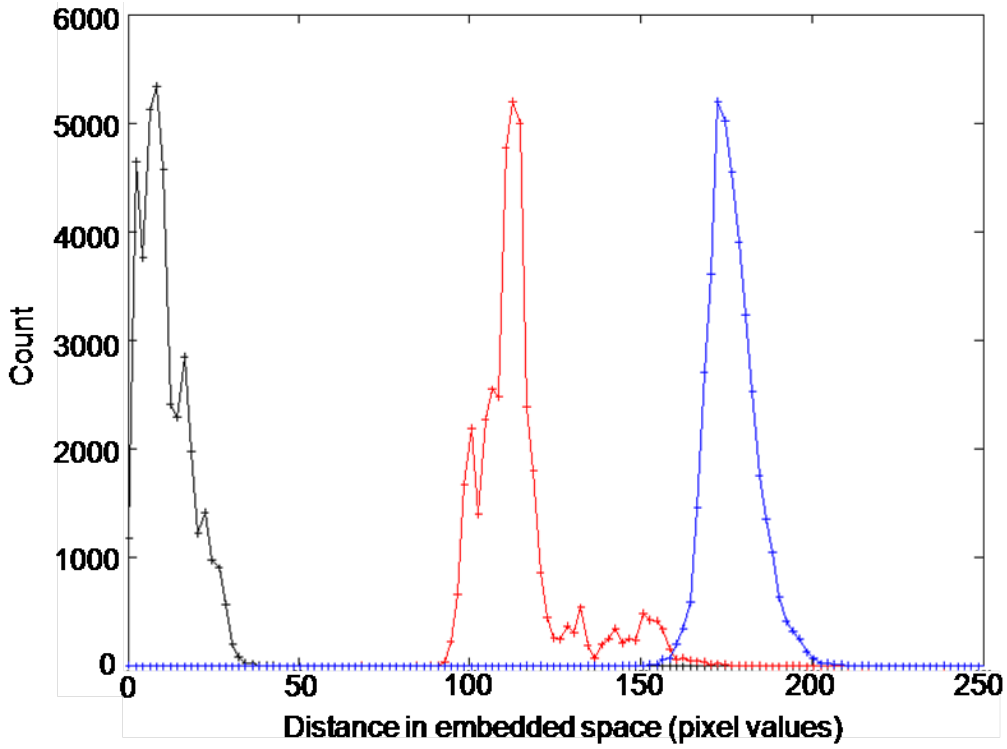


Figure 3.13. Histogram of the interclass distances between three selected fluorophores: C334 (black curve), FAD (red curve) and PpIX (blue curve), showing excellent discrimination.

3.4. Summary

Experiments in this chapter have demonstrated our excitation resolved fluorescence imaging system's ability to effectively illuminate and detect fluorescence spectra over a wider field of view as compared to conventional point-based fluorescence spectroscopy systems. The end goal of our regional sampling approach would be the recording of intensity images of biological tissues undergoing illumination at multiple excitation wavelengths via a rigid or flexible endoscope. By subsequent processing of these intensity images with FR-IsoMap, a representative RGB colour map of the interrogated tissue regions would be generated that would highlight areas with the most variability. This therefore takes into account quantitative spectral data, whilst allowing the imaging results to be presented in an easily accessible colour map format for more straightforward qualitative assessment.

By comparing image processing results of PCA and FR-IsoMap from fluorescent dye solutions, we have shown that both dimensionality reduction techniques can provide accurate separation of dyes by their respective fluorescence emissions. At lower dye concentration levels i.e. lower fluorescence intensities, FR-IsoMap processing produced larger separation values (MDs) between dyes and smaller interclass MDs within dyes when compared to PCA. This indicates that dye types were better distinguished by FR-IsoMap under these conditions, and also implies that the technique would be able to better discriminate the various endogenous fluorophores present in biological tissue at low fluorescence intensity levels. Besides being able to distinguish between different dyes in mixtures, FR-IsoMap was also shown to be relatively independent of concentration at lower dye concentrations, hence exhibiting the operational robustness of this technique under normal physiological conditions.

Having shown the improved discrimination ability of the FR-IsoMap technique over PCA, the former was subsequently employed for the processing of image data obtained from MF imaging of fluorescent collagen gel tissue phantoms. The resulting fixed reference colour maps displayed excellent contrast across different dye/fluorophore gel phantoms and consistent colouring between identical samples, as analysed via MANOVA.

We believe that our imaging-based approach could be a more intuitive, and consequently more effective, method for the classification of spectrally distinct samples based on their fluorescence emission profiles than spectroscopy alone. One of the next steps is the validation of the technique using actual tissues from both animal models and humans, as well as further modification of the supercontinuum laser system to acquire an additional mode of imaging: hyperspectral reflectance imaging (HRI) as discussed in the next chapter.

3.5. References

Brewer M, Utzinger U, Silva E, Gershenson D, Bast RC Jr, Follen M, Richards-Kortum R. Fluorescence spectroscopy for in vivo characterization of ovarian tissue. *Lasers in Surgery and Medicine* 2001;**29(2)**:128-135.

Chang SK, Follen M, Malpica A, Utzinger U, Staerkel G, Cox D, Atkinson EN, MacAulay C, Richards-Kortum R. Optimal excitation wavelengths for discrimination of cervical neoplasia. *IEEE Transactions in Biomedical Engineering* 2002;**49(10)**:1102-1111.

Das BB, Liu F, Alfano RR. Time-resolved fluorescence and photon migration studies in biomedical and model random media. *Reports on Progress in Physics* 1997;**60(2)**:227-292.

Dunsby C, Lanigan PMP, McGinty J, Elson DS, Requejo-Isidro J, Munro I, Galletly N, McCann F, Treanor B, Onfelt B, Davis M, Neil MAA, French PMW. An electronically tuneable ultrafast laser source applied to fluorescence imaging and fluorescence lifetime imaging microscopy. *Journal of Physics D - Applied Physics* 2004;**37(23)**:3296-3303.

Georgakoudi I, Jacobson BC, Van Dam J, Backman V, Wallace MB, Müller MG, Zhang Q, Badizadegan K, Sun D, Thomas GA, Perelman LT, Feld MS. Fluorescence, reflectance, and light-scattering spectroscopy for evaluating dysplasia in patients with Barrett's esophagus. *Gastroenterology* 2001;**120(7)**:1620-1629.

Georgakoudi I, Sheets EE, Müller MG, Backman V, Crum CP, Badizadegan K, Dasari RR, Feld MS. Trimodal spectroscopy for the detection and characterization of cervical precancers in vivo. *American Journal of Obstetetrics and Gynecology* 2002;**186(3)**:374-382.

Jackson JE. *A User's Guide to Principal Components*. New Jersey: John Wiley & Sons, Inc. 2003.

Jolliffe IT. *Principal Component Analysis*, 2nd edn. New York: Springer. 2002.

Koh KR, Lekadir K, Elson DS, Yang GZ. Excitation/emission resolved fluorescence imaging with FR-IsoMap. *Proceedings of Medical Image Understanding and Analysis – MIUA* 2007, University of Wales, Aberystwyth.

Lane PM, Gilhuly T, Whitehead P, Zeng H, Poh CF, Ng S, Williams PM, Zhang L, Rosin MP, MacAulay CE. Simple device for the direct visualization of oral-cavity tissue fluorescence. *Journal of Biomedical Optics* 2006;**11(2)**:024006.

Law MHC, Jain AK. Incremental nonlinear dimensionality reduction by manifold learning. *IEEE Transactions on Pattern Analysis and Machine Intelligence* 2006;**28(3)**:377-391.

Lekadir K, Elson DS, Requejo-Isidro J, Dunsby C, McGinty J, Galletly N, Stamp G, French PMW, Yang GZ. Tissue characterization using dimensionality reduction and fluorescence imaging. *Medical Image Computing and Computer-Assisted Intervention – MICCAI* 2006;**2**:586-593.

Liu Y, Lan X, Gao S, Shen Z, Lu J, Ni XW. The comparison of fluorescent spectra on acetic acid and ethanol solutions. *Proceedings of SPIE* 2003;**5254**:526-530.

Liu Y, Lan XF, Shen ZH, Lu J, Ni XW. Influence of excitation light wavelength on the fluorescence spectra of ethanol solutions. *Guang Pu Xue Yu Guang Pu Fen Xi* 2005;**25(2)**:242-245.

Moffitt T, Chen YC, Prahl SA. Preparation and characterization of polyurethane optical phantoms. *Journal of Biomedical Optics* 2006;**11(4)**:041103.

Müller MG, Valdez TA, Georgakoudi I, Backman V, Fuentes C, Kabani S, Laver N, Wang Z, Boone CW, Dasari RR, Shapshay SM, Feld MS. Spectroscopic detection and evaluation of morphologic and biochemical changes in early human oral carcinoma. *Cancer* 2003;**97(7)**:1681-1692.

Mycek MA, Schomacker KT, Nishioka NS. Colonic polyp differentiation using time-resolved autofluorescence spectroscopy. *Gastrointestinal Endoscopy* 1998;**48(4)**:390-394.

Ramanujam N. Fluorescence spectroscopy of neoplastic and non-neoplastic tissues. *Neoplasia* 2000a;**2(1-2)**:89-117.

Ramanujam N. Fluorescence spectroscopy in vivo. In: *Encyclopedia of Analytical Chemistry* (Meyers RA, ed.). Chichester: John Wiley & Sons Ltd. 2000b;20-56.

Richards-Kortum R, Sevick-Muraca E. Quantitative optical spectroscopy for tissue diagnosis. *Annual Review of Physical Chemistry* 1996;**47**:555-606.

Sokolov K, Galvan J, Myakov A, Lacy A, Lotan R, Richards-Kortum R. Realistic three-dimensional epithelial tissue phantoms for biomedical optics. *Journal of Biomedical Optics.* 2002;**7(1):**148-156.

Tenenbaum JB, de Silva V, Langford JC. A global geometric framework for nonlinear dimensionality reduction. *Science* 2002;290(5500):2319-2323.

Wagnieres GA, Star WM, Wilson BC. In vivo fluorescence spectroscopy and imaging for oncological applications. *Photochemistry and Photobiology* 1998;**68(5)**:603-632.

Wallace MB, Tunnell J, Wildi SM, Jost C, Nazemi J, McGee S, Mirkovic J, Galindo L, Dasari R, Feld M. Real time optical detection of dysplasia in Barrett's esophagus using tri-modal (diffuse reflectance, fluorescence, light-scattering) spectroscopy. *Gastroenterology* 2005;**128(4)**:A51(Suppl. 2).

Wang TD, Crawford JM, Feld MS, Wang Y, Itzkan I, Van Dam J. In vivo identification of colonic dysplasia using fluorescence endoscopic imaging. *Gastrointestinal Endoscopy* 1999;**49(41)**:447-455.

Yang YL, Ye YM, Li FM, Li YF, Ma PZ. Characteristic autofluorescence for cancer diagnosis and its origin. *Lasers in Surgery and Medicine* 1987;**7(6)**:528-532.

4

Investigating Human Cancer Tissues with Multispectral Fluorescence and Hyperspectral Reflectance Imaging

4.1. Introduction 111
4.2. Imaging fluorescence from various biological tissues 113
4.2.1. Optical instrumentation 113
4.2.2. Data processing technique 115
4.2.3. Dye-stained *ex vivo* lamb kidneys 115
4.2.3.1. Tissue staining and imaging procedure 115
4.2.3.2. Imaging results 116
4.2.4. 5-ALA treated *ex vivo* human small-cell lung cancer tissue 117
4.2.4.1. Tissue preparation and imaging procedure 117
4.2.4.2. Imaging results 118
4.2.5. Untreated *ex vivo* human colorectal tissue 120
4.2.5.1. Tissue preparation, imaging and histopathology procedure 120
4.2.5.2. Imaging and histopathology results 120
4.3. Detecting diffuse reflectance signals from *ex vivo* colorectal cancer tissues 124
4.4. Summary 126
4.5. References 128

4.1. Introduction

This chapter discusses the development of an *in vivo*, *in situ* multimodal optical imaging system for performing laser-induced excitation-resolved multispectral fluorescence imaging (MFI) and hyperspectral reflectance imaging (HRI) designed for cancer detection. Following initial system calibration and characterisation of fluorescence from solutions and collagen gel phantoms in the previous chapter, imaging experiments in this section were aimed at further developing the system as a minimally-invasive optical

biopsy tool for discrimination between neoplastic and non-neoplastic tissues within the human body. Additionally, all acquired fluorescence and diffuse reflectance images were processed by the FR-IsoMap dimensionality reduction technique, resulting in the generation of a red-green-blue (RGB) colour map for more intuitive interpretation of the final imaging results.

Initial multimodal imaging experiments employed MFI in the visible and near-infrared (visible/NIR) wavelength range on fluorescent dye-stained *ex vivo* lamb kidneys for demonstration of the system's ability to discriminate between different exogenous fluorophores as well as the discriminatory effectiveness of FR-IsoMap processing. This was also to assess future potential applications of the system such as aiding *in vivo* delivery of exogenous markers e.g. dye-antibody/peptide conjugates and fluorescent protein probes, and as a 'red-flag' technique for tracking cancerous growths via fluorescence from tumour-specific photosensitisers e.g. protoporphyrin IX (PpIX).

The MFI system was then later applied to imaging of freshly resectioned human small cell lung cancer (SCLC) tissue treated with the photosensitiser pro-drug 5-aminolevulinic acid (5-ALA). This was to evaluate the ability of the system to differentiate between photosensitiser-treated and untreated tissues based on fluorescence emissions from 5-ALA induced PpIX, and to display that difference with FR-IsoMap processing of the acquired fluorescence intensity images.

In a second set of experiments, the potential of a combined MFI-HRI approach was investigated to determine if this dual combination could be used as a means of discrimination between healthy and cancerous untreated human colorectal tissues using only autofluorescence and reflectance signals. As a gold standard comparison test, fluorescence intensity graphs and FR-IsoMap images from respective MFI and HRI of the colorectal tissues were assessed against results from histopathology to determine overall accuracy and effectiveness of the dual MFI/HRI endoscopic imaging technique for cancer detection.

4.2. Imaging fluorescence from various biological tissues

Three different types of biological tissues were used in our imaging experiments: *ex vivo* dye-stained lamb kidneys, 5-ALA photosensitised small-cell lung cancer (SCLC) tissue and untreated human colorectal cancer tissue. This was obtained from various sources and prepared in different ways for subsequent MFI procedures with our supercontinuum laser imaging setup. Imaging results in the form of greyscale intensity images for each tissue type are then subject to data processing by the FR-IsoMap dimensionality reduction technique for presentation of the final results as RGB colour images.

4.2.1. Optical instrumentation

The supercontinuum fibre laser based imaging system used for excitation-resolved MFI and HRI work in this chapter was almost identical to the setup previously employed in section 3.3.4 of chapter 3 with a few slight modifications. A liquid light guide was used to deliver excitation light to the horizontal sample and a rigid laparoscope (Olympus, Japan) positioned about 70 mm above the sample was used to collect the spectrally filtered fluorescence emissions. The emitted fluorescence spectra were passed through 600, 650 or 700 nm longpass filters for MFI or a crossed polariser to minimize specular reflections for HRI. The filtered spectra were eventually focused by the exit aperture onto a CCD camera (QImaging Retiga EXi) for recording of the resultant intensity images. A diagram of this multimodal imaging system is shown in Figure 4.1.

For respective MFI and HRI experiments, two different sets of excitation wavelengths were applied, each with a different combination of central wavelengths, excitation bandwidths, inclusion of different filters (longpass emission or cross polarising) and camera integration times (see Table 4.1).

For MFI, 30 different excitation wavelengths from 465 to 645 nm were applied to the tissue samples, each with excitation bandwidths of between 3 and 15 nm. Owing to the use of narrower excitation bandwidths, less light was transmitted through the system and the camera integration time was thus set at 3.0 seconds to allow for brighter recorded images. Longpass filters with cut-on wavelengths of 600, 650 and 700 nm were also

included in the setup for this first imaging modality to allow for transmission and recording of fluorescence signals above that emission wavelength.

For HRI, a total of 31 excitation wavelengths from 466 to 641 nm were applied, each with a broader excitation bandwidth of between 30 and 40 nm. Due to the higher amounts of light being transmitted, camera integration time was set to a shorter 0.5 seconds compared to the MFI setup. Only a cross polarising filter was used for this second modality.

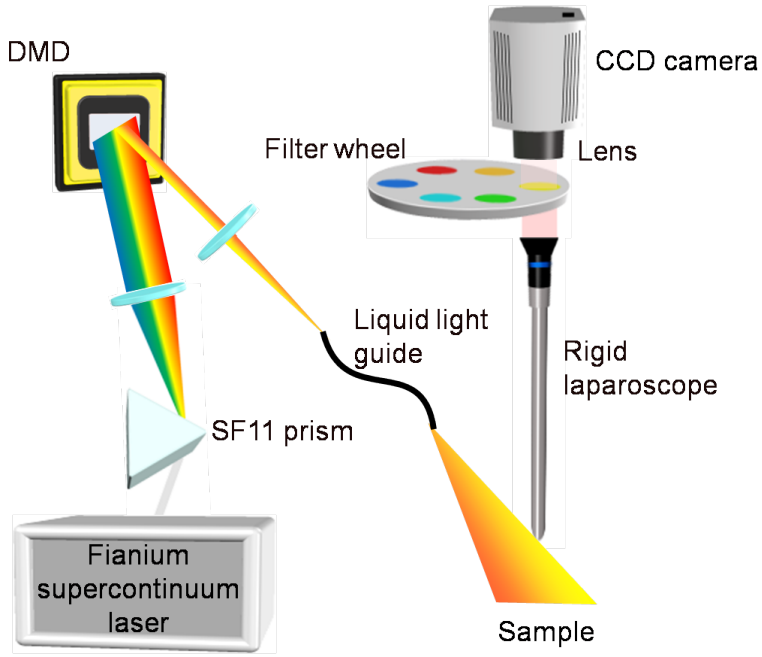


Figure 4.1. Diagrammatic representation of the multimodal image acquisition optics. DMD: digital multimirror device.

Imaging modality	Excitation wavelengths	Excitation bandwidth	Emission filter	Integration time (sec.)
Multispectral fluorescence imaging (MFI)	30 wavelengths: 465 to 645 nm	3 to 15 nm	Longpass 600, 650 and 700 nm	3.0
Hyperspectral reflectance imaging (HRI)	31 wavelengths: 466 to 641 nm	30 to 40 nm	Crossed polariser	0.5

Table 4.1. Imaging modalities and their respective combinations of excitation wavelengths, bandwidths, longpass emission or cross polarising filters and camera integration times.

4.2.2. Data processing technique

As with chapter 3, use of this multimodal imaging system resulted in the acquisition of a large quantity of closely spaced spectral images. The challenge was to find a method to best present the resultant stack of monochromatic images in a meaningful and easily comprehensible manner. We therefore employed the FR-IsoMap algorithm that was employed previously in section 3.3.2 for processing of intensity images of fluorescent dyes and a collagen gel tissue phantom. Once again, dimensionality reduction by FR-IsoMap resulted in the multi-point spectrum of each pixel being mapped to three data dimensions containing the most meaningful data parameters of the original manifold. Each of the three dimensions was later assigned to the red, green and blue channels of an RGB colour image and were presented as such for more intuitive interpretation of the diseased tissues. As before, some pre-processing was performed on the raw intensity images prior to FR-IsoMap analysis involving background subtractions and normalisation with bright-field images. This was to eliminate spatial variation in illumination and also account for the variation in laser output intensities across all wavelengths.

4.2.3. Dye-stained *ex vivo* lamb kidneys

Ex vivo lamb kidneys stained with exogenous fluorescent dyes were used as tissue phantoms for MFI in the visible and near-infrared (visible/NIR) spectral range. These initial experiments were to demonstrate the system's ability to discriminate between different exogenous fluorophores as well as the discriminatory effectiveness of FR-IsoMap processing. Another objective of the MFI experiment was to assess future potential applications of the system such as aiding in *in vivo* delivery of exogenous markers e.g. dye-peptide conjugates and fluorescent protein probes, and for tracking of cancerous growths via fluorescence from tumour-specific photosensitisers e.g. protoporphyrin IX (PpIX).

4.2.3.1. Tissue staining and imaging procedure

Fresh lamb kidneys that had not been previously frozen were obtained from a local butcher and prepared within two hours of their purchase. Each kidney was coronally

sectioned with a surgical scalpel, dividing the kidney into two equal halves. The freshly sectioned inner sides of each bisected kidney were then gently washed with distilled water to remove any stray tissue pieces and dabbed dry with disposable paper towels. Following this, the fluorescent dyes rhodamine 6G (R6G; 530 nm absorption maxima) and rhodamine B (RB; 552 nm absorption maxima) were carefully applied in two separate bands to the bisected inner side of one kidney half-section. The relative positions of the applied dyes on the inner kidney surface were noted prior to MFI. Our experimental aim was to demonstrate both the laser excitation and image acquisition abilities of our multimodal imaging system as well as the discriminatory effectiveness of the FR-IsoMap technique for differentiating the two dyes.

4.2.3.2. Imaging results

As observed from the lamb kidney images in Figure 4.2, good discrimination was achieved from emitted fluorescence of the two different dyes applied following FR-IsoMap processing. These are visible as two distinct coloured bands that run across the kidney's surface in the FR-IsoMap colour image (Figure 4.2B) – the pink and yellow coloured bands belonging to R6G and RB respectively. Upon closer inspection, it is also evident that the applied fluorescent dyes highlighted various anatomical features of the internal kidney by non-specific binding/accumulation, e.g. the major and minor calyces and renal pyramids. Such results thus indicate the potential of the MFI system for visualising specific tissue structures in clear detail together with the added advantage of detecting fluorescence emissions associated with that particular tissue e.g. from quantum dots, dendrimers or tissue-specific dye-antibody tags. Based on this observation, a possible area of application of our MFI approach is in minimally invasive fluorescence detection of sentinel lymph nodes; previous studies have successfully demonstrated the use of fluorescence from the near-infrared indocyanine green (ICG) fluorophore for successful identification of sentinel lymph nodes during incidences of breast or gastric cancers (Miyashiro *et al.*, 2008; Murawa *et al.*, 2009).

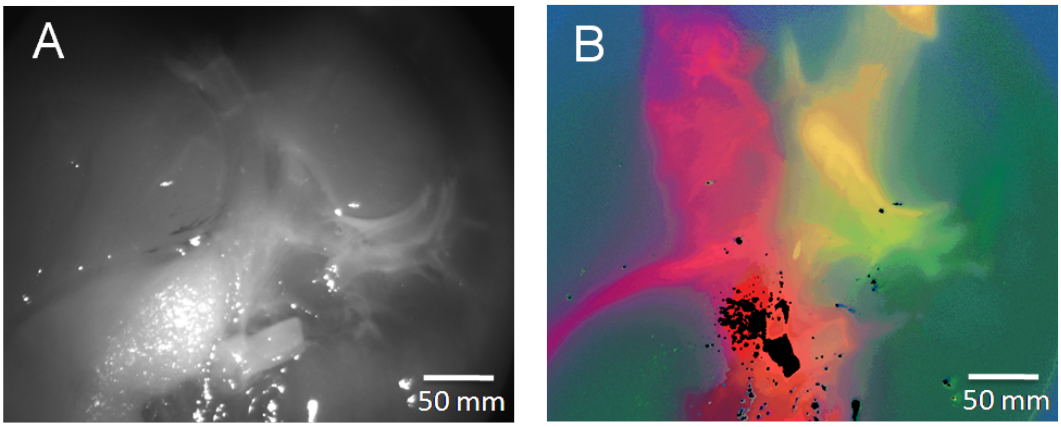


Figure 4.2. Conventional white light reflectance (A) and FR-IsoMap (B) images of the coronal section of an *ex vivo* lamb kidney. Two fluorescent dyes of different excitation wavelengths were painted across the coronally sectioned kidney's inner surface prior to MFI. This is observed in the FR-IsoMap image as two differently coloured bands – pink (rhodamine 6G) and yellow (rhodamine B). The black patches in (B) are regions of saturated fluorescence, which were masked out from the original intensity images prior to FR-IsoMap processing.

4.2.4. 5-ALA treated *ex vivo* human small-cell lung cancer tissue

5-aminolevulinic acid (5-ALA) is a photosensitising pro-drug that induces an increased endogenous accumulation of the autofluorescent fluorophore protoporphyrin IX (PpIX) in cancerous tissues. The phenomenon occurs due to a breakdown in the haeme biosynthetic pathway in cancer cells, which is otherwise intact in normal cells. The aim of this experiment was to evaluate the ability of our imaging system to detect differences in PpIX contents between 5-ALA treated and untreated human small-cell lung cancer (SCLC) tissue using MFI, and to subsequently display that difference using FR-IsoMap processing of the acquired intensity images akin to a photodynamic diagnostic approach.

4.2.4.1. Tissue preparation and imaging procedure

Human SCLC tissue samples were obtained from routine surgical resectioning of lung cancer patients undergoing clinical evaluation at the Royal Brompton Hospital (Royal Brompton & Harefield NHS Trust, London, UK) by Dr Pallav Shah, Consultant Physician and Honorary Senior Lecturer, National Heart and Lung Institute, Imperial College London. Informed consent was obtained from all patients before the

commencement of surgery. All imaging experiments involving *ex vivo* human tissues in this sub-section and the next were performed under ethical approval from the Outer West London Research Ethics Committee, National Research Ethics Service, UK (REC reference number 08/H0719/37).

Human SCLC tissue were first placed in a clean Petri dish containing sterile Dulbecco's modified Eagle's medium (DMEM) immediately after resectioning and processed within the aseptic environment of a flow hood. These were then transferred into a separate dish filled with 25.0 ml sterile phosphate buffered saline (PBS) and gently washed by dripping PBS over them using a sterile Pasteur pipette. The samples were next placed in another clean Petri dish containing 25.0 ml DMEM and 10% Pen-Strep solution (penicillin and streptomycin antibiotics solution); these were again gently washed in the same drip fashion using DMEM/Pen-Strep solution from the same dish. Tissue samples were left to immerse for a further 2 minutes before washing was repeated to kill any remaining foreign agents before being cut into small roughly 5 mm by 5 mm sizes and placed in a cell culture flask containing 25.0 ml of DMEM containing 10% foetal bovine serum (FBS), 1.0% Pen-Strep solution and 2.0 mM glutamine. At this point, 5-ALA was added into the mixture to a final concentration of 1.0 mM before the flask was placed in an incubator set at 37.0 ºC and 5.0% CO_2 and left to incubate for a period of 24 hours before MFI was performed.

4.2.4.2. Imaging results

Following a 24-hour incubation period with 5-ALA, human SCLC tissue samples were removed from their culture flask and washed with sterile PBS before MFI was performed. The resultant intensity images obtained were subject to FR-IsoMap processing and these are presented in Figures 4.3B and 4.3D. Under normal white light conditions, both SCLC tissue samples appeared virtually identical (refer to Figures 4.3A and 4.3C). However with multispectral excitation, the SCLC tissue sample treated with 5-ALA produced a strong fluorescent signal (Figure 4.3B), as opposed to only a very faint signal visible in the untreated control sample (Figure 4.3D). This observation was expected, i.e. the observation of strong fluorescent signals from 5-ALA treated SCLC tissue is due to accumulation of larger amounts of 5-ALA induced PpIX as compared to lower quantities of endogenously present PpIX in the untreated control cancer tissue.

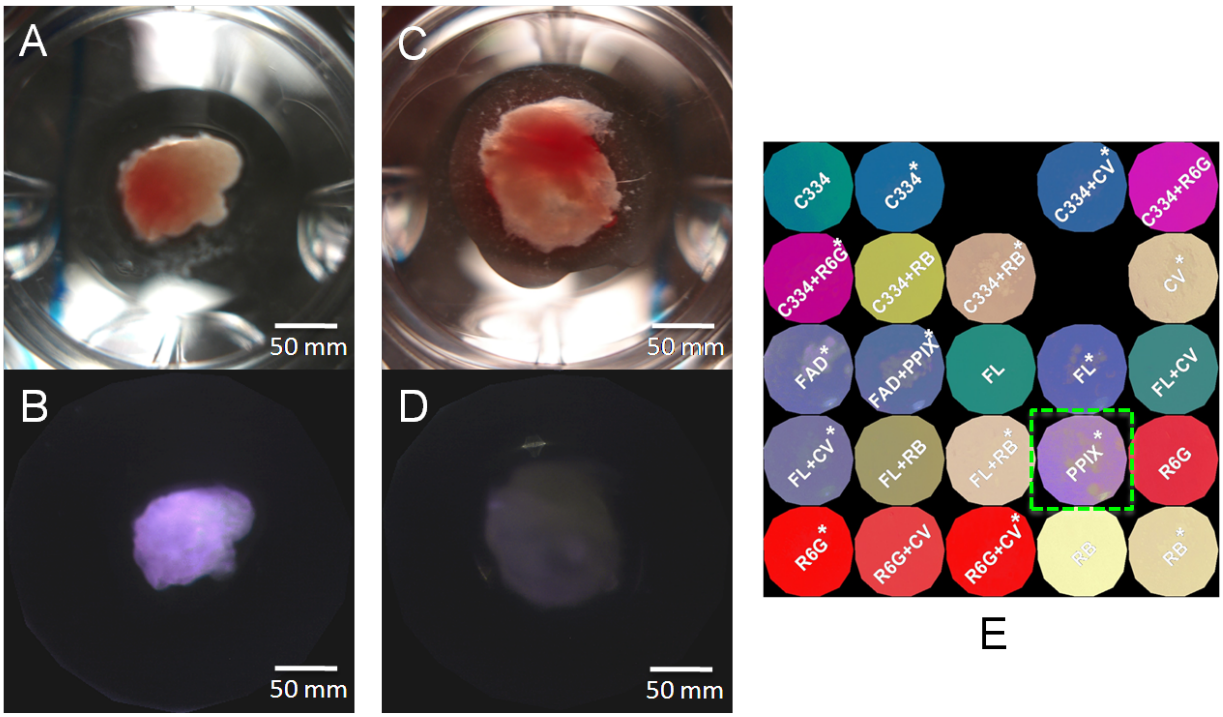


Figure 4.3. White light photographs and FR-IsoMap images of human small-cell lung cancer (SCLC) tissues. The tissue sample in (A/B) was imaged following a 24-hour incubation period with the photosensitiser 5-ALA, whereas the untreated control sample in (C/D) was left to incubate without any drug for 24 hours in DMEM alone. The FR-IsoMap image of fluorescent collagen tissue phantoms from the previous chapter (Figure 3.12) is included (E).

Owing to the use of a similar colour visualisation scheme and fixed reference dataset for embedding, the 5-ALA treated SCLC tissue (Figure 4.3B) appeared similar in colour to that of endogenous PpIX embedded in a collagen gel tissue phantom from the previous chapter (Figure 4.3E, within dashed-green box). Good correlation between the two different PpIX samples in different media effectively shows that FR-IsoMap can accurately and consistently map (classify) fluorescence from PpIX to the same discrete location within the defined 3D RGB colour space in different environments. Imaging results from this round of MFI experiments are clinically significant as they imply the possibility of detecting the presence of fluorescent exogenous markers amidst a highly scattering/absorbing environment of biological tissues. Besides demonstrating the possibility of using our supercontinuum imaging system as a photodynamic diagnostic tool, this paves the way for further MFI experiments for the detection of tumour-specific fluorescence signals.

4.2.5. Untreated *ex vivo* human colorectal tissue

Frozen *ex vivo* human colorectal tissue samples were obtained from a tissue bank for the ensuing MFI experiments. Currently, the application of exogenous fluorophores still poses clinical issues with regards to target specificity and overall toxicity. The aim of performing MFI in this section was therefore to excite detectable levels of autofluorescence from endogenous fluorophores such as porphyrins and flavin adenine dinucleotide (FAD) from both cancer and healthy colorectal tissues as a means of distinguishing between the two classes.

4.2.5.1. Tissue preparation, imaging and histopathology procedure

Human colorectal tissue samples were sourced from Mr Kenneth Miller, Manager, the Cancer Research UK Primary Colorectal Tissue Bank situated at St Mark's Hospital, Northwick Park (North West London Hospitals NHS Trust, London, UK). 7 frozen colorectal tissue samples were obtained in total, comprising 3 pieces of normal mucosa and 4 pieces of adenocarcinoma at various stages of differentiation. The tissues measured approximately 0.5 to 1.5 cm in each dimension. Prior to MFI and subsequent HRI procedures, colorectal tissue samples were stored in a -80.0°C freezer and thoroughly thawed before commencement of imaging.

After completion of all MFI and HRI experiments, colorectal tissue samples were sent for histopathological analysis. This was for comparison of this current gold standard screening technique against FR-IsoMap processed HRI colour images as shown later in Figure 4.6. The tissue samples were processed via standard histopathology techniques and a consultant histopathologist blinded to the clinical details of the colorectal tissues, Dr Robert Goldin from the Department of Histopathology at Imperial College London, later confirmed the pathological diagnosis for all tissue samples.

4.2.5.2. Imaging and histopathology results

FR-IsoMap colour maps produced from MFI intensity images of *ex vivo* colorectal tissues did not manage to provide any conclusive differences between the various samples. This was possibly due to the low amounts of endogenous fluorophores present in the thawed tissue, leading to low levels of autofluorescence. Another factor was light absorption by

haemoglobin, which would cause an attenuation of the overall detected fluorescence signal. Since fresh (never frozen) *ex vivo* colorectal tissue sections have been shown to emit autofluorescence in previous studies at 442, 450 and 488 nm excitation (Bottiroli *et al.*, 1995; Zavadil *et al.*, 2005; Horak *et al.*, 2006), it is presumed the freezing process led to a change in tissue fluorophore content and consequently the overall autofluorescence contribution.

As such, the acquired greyscale intensity images were used to construct a fluorescence intensity graph for extraction of indicative scores across all individual samples as shown in Figure 4.4. The graph was created by calculating the average fluorescence intensity for each greyscale image at the respective excitation wavelengths, followed by normalisation using the 'area under the curve' technique to obtain an indication of the relative fluorescence emissions at each excitation wavelength. This graphical format of presenting the tissue fluorescence results is akin to that from conventional fluorescence spectroscopic studies.

Two distinct peaks are seen around the 510 and 567 nm excitation points on the graph for all colorectal cancer tissues. At the 510 nm peak, dysplastic/cancerous tissues seemed to emit a lower amount of autofluorescence than normal tissues. One probable explanation for this occurrence are a reduction in FAD content (450 and 520 nm excitation maxima) and corresponding increase in NADH – an indication of higher metabolic activity in dysplastic/cancerous tissues as compared to normal tissues (Chance, 1989; Banerjee *et al.*, 1998; Drezek *et al.*, 2001; Sokolov *et al.*, 2002; Wu *et al.*, 2006). At the 567 nm peak, dysplastic/cancerous tissues were found to emit higher autofluorescence than normal tissues. At first, it was suspected that these peaks may have arisen due to troughs in the graphs caused by haemoglobin (Hb) absorption. However this was not found to be the case since Hb absorption bands only occur at around 415 nm, 542 nm, 572 nm and 930 nm. This may therefore be attributed to the occurrence of a higher concentration of lipid bodies in tumours, which have been found to serve as sites for synthesis of prostaglandin-E_2. This forms part of a group of hormone-like substances known to be involved in colorectal carcinoma cell growth and motility (Sheng *et al.*, 2001; Accioly *et al.*, 2008).

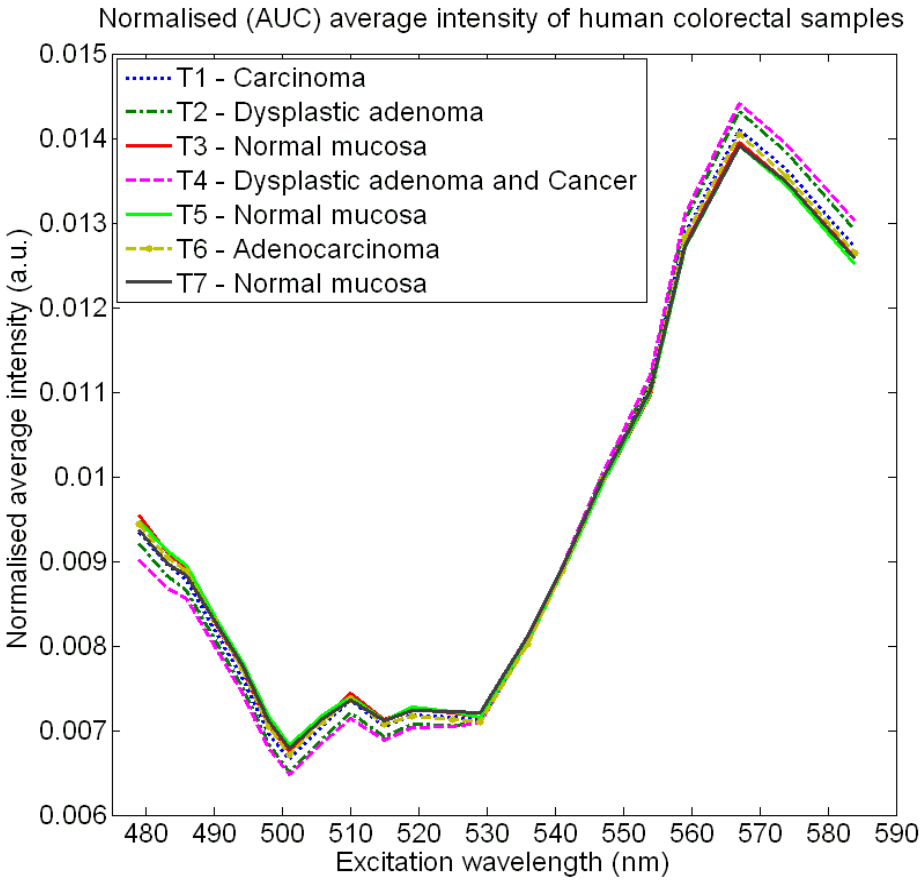


Figure 4.4. Normalised average autofluorescence intensity graph of human colorectal tissue samples. Two distinct peaks are seen around 510 and 567 nm excitation in all tissue samples, which are attributed to FAD and lipid bodies respectively. (Tissues disease states as reported by Dr Robert Goldin)

Ratiometric scores were generated as a means of discrimination between normal and dysplastic/cancerous colorectal tissue samples. This was performed by dividing the normalised average fluorescence intensity values at the second 567 nm peak by that of the first 510 nm peak for all samples, results of which are shown in Table 4.2 together with histopathology reports from both histopathologists. From this 567/510 nm ratio, there is clear evidence that dysplastic/cancer tissue samples possess higher scores than normal samples, although the difference is relatively small. Representative H&E stained histopathology sections from selected colorectal tissues are also presented (see Figure 4.5). These were selected to display examples of surface epithelia, crypt patterns and lamina propria mucosae from the various colorectal tissue disease states: normal (tissue T3), dysplastic adenoma (tissue T2) and moderately differentiated adenocarcinoma (tissue T6) (refer to Table 4.2).

Sample	Tissue Type	Histopathology results		567/510 nm ratio
		As reported by St Mark's Hospital histopathologist of tissues resectioned from a neighbouring area to the actual biopsied site	As reported by Dr Robert Goldin of actual biopsied tissues	
T1	Rectum	Moderately differentiated adenocarcinoma, Dukes C1	Carcinoma	2.0003
T2	Sigmoid colon	Moderately differentiated adenocarcinoma, Dukes C1	Dysplastic adenoma	2.0655
T3	Colon	Normal mucosa	Normal mucosa	1.9563
T4	Sigmoid colon	Moderately differentiated adenocarcinoma, Dukes B	Dysplastic adenoma and possible carcinoma	2.0927
T5	Right colon	Poorly differentiated adenocarcinoma, Dukes B	Normal mucosa	1.9563
T6	Descending colon	Moderately differentiated adenocarcinoma, Dukes D	Moderately differentiated adenocarcinoma	1.9864
T7	Colon	Normal mucosa	Normal mucosa	1.9562

Table 4.2. List of tissue types, 567/510 nm ratiometric scores and disease states of the imaged *ex vivo* human colorectal tissue samples as evaluated by two separate histopathologists.

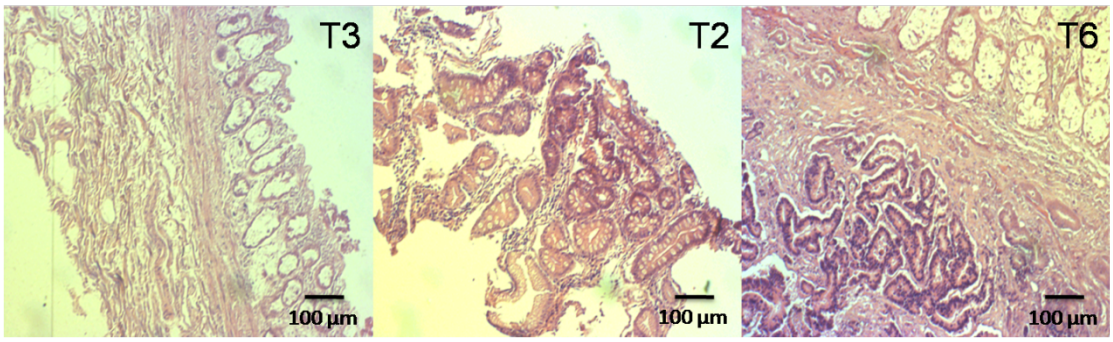


Figure 4.5. Selected representative H&E stained histopathology sections of the imaged human colorectal tissue samples. Each is an example of a different disease state: normal mucosa (T3); dysplastic adenoma (T2); moderately differentiated adenocarcinoma (T6) (based on the histopathology report from Dr Robert Goldin).

MFI experiments performed in section 4.2 utilised excitation spectra generated by a supercontinuum fibre laser between the wavelengths of 465 and 645 nm. This spectral range is recognised to be towards the longer end of biological autofluorescence interest. More autofluorescence could have been elicited from endogenous fluorophores present in colorectal tissue such as the structural proteins collagen and elastin, and the amino acids tryptophan and tyrosine if spectral coverage of the laser was tuned to below 400 nm. This hypothesis warrants further experiments employing a different optical setup, although this may raise several biological safety issues mostly concerning exposure to ultraviolet (10 to 400 nm) radiation. In addition, different illumination fibres would have to be used in our endoscope since those currently in use would cause significant attenuation of any excitation light below 400 nm.

4.3. Detecting diffuse reflectance signals from *ex vivo* colorectal cancer tissues

Hyperspectral reflectance imaging (HRI) was performed on all healthy and cancerous *ex vivo* human colorectal tissue samples. For ease of data manipulation and analysis, individual images obtained from each tissue sample per excitation wavelength were stitched together to form a single combined intensity image. FR-IsoMap was then used to process the whole stack of combined greyscale intensity images to generate a final RGB colour map image as shown in Figure 4.6, where obvious differences in colour and contrast are discernable between the various tissue samples. This is most likely due to structural variation between different tissue disease states, e.g. mucosal thickening and increased microvasculature in tumour tissues, ultimately resulting in changes in optical absorption and scattering properties. This led to different diffuse reflectance signals being recorded from healthy and cancer tissues.

An obvious trend is noticeable in the HRI FR-IsoMap image (Figure 4.6): cancerous and dysplastic tissues (i.e. samples T1, T2, T4 and T6) appear a dull pink or purplish colour as compared to the more contrasting and brightly coloured blue and greenish normal tissue samples (samples T3 and T7). With the exception of colorectal tissue sample T5, FR-IsoMap processed HRI images therefore displayed good correlation with histopathology results on the whole (refer to Table 4.2). This demonstrated the ability of our imaging

system to elicit spectral differences in both healthy and cancerous human colorectal tissues, as well as demonstrates the discriminatory effectiveness of the FR-IsoMap processing technique.

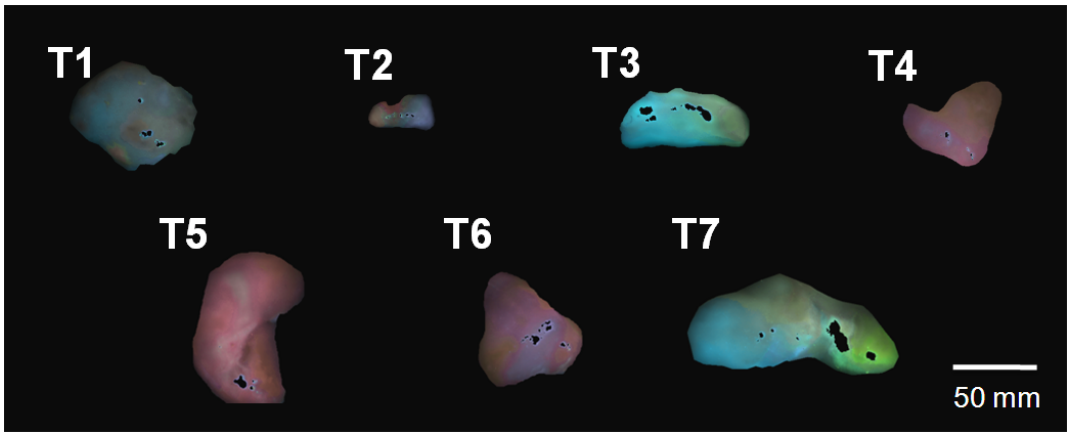


Figure 4.6. FR-IsoMap image obtained from the processing of amalgamated intensity image datasets acquired during HRI of human colorectal cancer tissue. Note: The HSV representation value plane of the final image was modified to account for the integrated fluorescence intensity at each pixel.

There was however an inconsistency with tissue sample T5, which had differing disease classifications: the sample given the grading of "moderately differentiated adenocarcinoma, Dukes B" by the histopathologist from St Mark's Hospital, whilst our histopathologist collaborator, Dr Robert Goldin, diagnosed it as "normal mucosa" (refer to Table 4.2). This could have been due to natural tissue variation and the sampling of tissue from neighbouring biopsy sites by the St Mark's histopathologist as opposed to the actual piece of biopsied tissue that was tested by Dr Goldin. Based on the FR-IsoMap image, our technique has classified sample T5 as being similar to the other dysplastic adenomatous tissue samples, namely samples T4 and T6, with similar colour and contrast visible between all three (Figure 4.6). Such histopathological discrepancies in interpreting disease states highlight the ongoing challenge in validating the effectiveness of various biophotonic techniques - an issue affecting the field as a whole of which no satisfactory solution has been found at present. Barring intra- and inter-observer variability, it is only through a standardised grading scheme that a conclusive outcome may be reached.

An integral part of colorectal cancer diagnosis is staging of the disease according to how far the cancer has spread in the body. Staging is performed following various clinical tests

such as a barium enema, sigmoidoscopy or colonoscopy, or imaging procedures e.g. MRI, CT or ultrasound. Two common colorectal cancer grading systems are in use: 1) the Dukes grading system, consisting of four stages from A to D in increasing order of disease severity, and 2) the TNM (Tumour Node Metastasis) classification system, which is gradually taking over from the Dukes system - T (1 to 4) describes the size of the tumour and its degree of invasiveness through the mucosal wall, N (1 or 2) describes the presence of cancer cells in the lymph nodes and M (0 or 1) gives an indication as to whether the cancer has spread to other organs throughout the body (i.e. undergone metastasis).

Since different colours in the FR-IsoMap RGB images correspond to different tissue disease states, increased utility of the technique could be achieved by matching different colours to those of various tissue stages from either the Dukes (only stages A and B) or TNM classification systems. Such colour coding according to established cancer staging systems will speed up diagnosis rates and allow for more straightforward correlation between imaging results and histopathology should the need arise. To attain such accurate degrees of correlation, further MFI and HRI experiments should be performed on different *in vivo* and *ex vivo* tissues of varying disease states for more complete spectral characterisation with our imaging system. This would also lead to the generation of a more comprehensive FR-IsoMap training set for added precision in colour mapping of different disease classes.

4.4. Summary

MFI and HRI experiments performed in this chapter were geared towards further development of our proposed *in vivo*, *in situ* multimodal optical imaging system using *ex vivo* biological tissue samples. As a follow-up from earlier experiments involving fluorescent dyes and collagen tissue phantoms, *ex vivo* imaging was carried out on dye-stained healthy lamb kidney tissue, 5-aminolevulinic (5-ALA) photosensitiser-treated human small-cell lung cancer (SCLC) tissue and untreated healthy and cancerous human colorectal tissues for characterising and understanding the spectral signals that would be obtained during future *in vivo* procedures. As before, all acquired greyscale intensity images of the *ex vivo* tissues were subject to further processing using the FR-IsoMap

dimensionality reduction algorithm, resulting in the generation of an RGB colour map of the imaged region for qualitative disease assessment.

MFI performed on *ex vivo* dye-stained kidneys showed that the 'regional' tissue sampling approach of our macroscopic imaging technique could be used as an effective 'red-flag' to target tumour tissue-specific fluorescent agents for further optical or physical biopsies. Examples of these exogenous fluorophores include quantum dots, dendrimers and dye-antibody tags.

The ability of the multimodal imaging system to function as a photodynamic diagnostic (PDD) tool was also effectively demonstrated via successful detection of 5-ALA induced tumour-specific protoporphyrin IX (PpIX) fluorescence from *ex vivo* SCLC tissue samples. 5-ALA treated and untreated SCLC tissues were clearly differentiated based on differences in photosensitiser fluorescence during MFI.

MFI experiments were carried out on untreated *ex vivo* healthy and cancer human colorectal tissues to ascertain if discrimination between different disease states could be achieved using only autofluorescence and diffuse reflectance signals. MFI did not detect sufficient autofluorescence from the tissue samples for a conclusive FR-IsoMap analysis. Therefore, fluorescence intensity graphs were constructed, which managed to allow discrimination between the different tissue disease states based on autofluorescence peaks from FAD and possibly lipid bodies (510 and 567 nm respectively). A ratiometric analysis was also performed on fluorescence intensities obtained at these peaks, resulting in different ratiometric scores obtained between the different colorectal tissue samples. In addition to MFI, HRI was also performed on the untreated *ex vivo* colorectal tissue. Good discrimination was obtained from the resulting FR-IsoMap RGB image with dysplastic/cancerous and normal tissue samples appearing differently coloured.

HRI FR-IsoMap images and MFI intensity graphs achieved good correlation with histopathology overall. In the long term, greater utility is expected from the technique by coupling of FR-IsoMap classification with established disease staging systems such as Dukes or TNM. Further *ex vivo* and *in vivo* MFI and HRI experiments are expected so as to properly characterise the system and build up a comprehensive FR-IsoMap training set for more efficient and accurate colour mapping of disease conditions.

4.5. References

Accioly MT, Pacheco P, Maya-Monteiro CM, Carrossini N, Robbs BK, Oliveira SS, Kaufmann C, Morgado-Diaz JA, Bozza PT, Viola JBP. Lipid bodies are reservoirs of cyclooxygenase-2 and sites of prostaglandin-E_2 synthesis in colon cancer cells. *Cancer Research* 2008;**68**:1732-1740.

Banerjee B, Miedema B, Chandrasekhar HR. Emission spectra of colonic tissue and endogenous fluorophores. *American Journal of Medical Sciences* 1998;**316(3)**:220-226.

Bottiroli G, Croce AC, Locatelli D, Marchesini R, Pignoli E, Tomatis S, Cuzzoni C, Di Palma S, Dalfante M, Spinelli P. Natural fluorescence of normal and neoplastic human colon: a comprehensive "ex vivo" study. *Lasers in Surgery and Medicine* 1995;**16(1)**:48-60.

Chance B. Metabolic heterofeneities in rapidly metabolisnig tissues. *Journal of Applied Cardiology* 1989;**4(4)**:207-221.

Drezek R, Sokolov K, Utzinger U, Boiko I, Malpica A, Follen M, Richards-Kortum R. Understanding the contributions of NADH and collagen to cervical tissue fluorescence spectra: modeling, measurements, and implications. *Journal of Biomedical Optics* 2001;**6(4)**:385-396.

Horak L, Zavadil J, Duchac V, Javorsky S, Kostka F, Svec A, Lezal D. Auto-fluorescence spectroscopy of colorectal carcinoma: ex vivo study. *Journal of Optoelectronics and Advanced Materials* 2006;**8(1)**:396-399.

Miyashiro I, Miyoshi N, Hiratsuka M, Kishi K, Yamada T, Ohue M, Ohigashi H, Yano M, Ishikawa O, Imaoka S. Detection of sentinel node in gastric cancer surgery by indocyanine green fluorescence imaging: comparison with infrared imaging. *Annals of Surgical Oncology* 2008;**15(6)**:1640-1643.

Murawa D, Hirche C, Dresel S, Hünerbein M. Sentinel lymph node biopsy in breast cancer guided by indocyanine green fluorescence. *British Journal of Surgery* 2009;**96(11)**:1289-1294.

Sheng H, Shao J, Washington MK, DuBois RN, Prostaglandin E_2 increases growth and motility of colorectal carcinoma cells. *Journal of Biological Chemistry* 2001;**276(21)**:18075-18081.

de Silva V, Tenenbaum JB. Global versus local methods in nonlinear dimensionality reduction. *Advances in Neural Information Processing Systems* 2003;**15**:721-728.

Sokolov K, Galvan J, Myakov A, Lacy A, Lotan R, Richards-Kortum R. Realistic three-dimensional epithelial tissue phantoms for biomedical optics. *Journal of Biomedical Optics* 2002;**7(1)**:148-156.

Wu YC, Qu JN. Autofluorescence spectroscopy of epithelial tissues. *Journal of Biomedical Optics* 2006;**11(5)**:0540231-11.

Zavadil J, Lezal D, Horak L, Duchac V, Prochazka M. Autofluorescence spectroscopy of malignant tissue. *Journal of Optoelectronics and Advanced Materials* 2005;**7(2)**:1023-1028.

5

Evaluating Chemotherapy Response with Fluorescence Confocal Endomicroscopy

5.1. Introduction 131

5.2. Classical fluorescence confocal microscopy and the move towards novel *in vivo* systems 132

5.3. Motivations for tissue diagnosis with fluorescence confocal endomicroscopy 135

5.4. Fluorescence confocal endomicroscopy for cellular characterisation 137

5.4.1. Optical instrumentation and image acquisition 137

5.4.2. Optimal contrast agent selection using hepatocellular carcinoma cells ... 138

5.4.2.1. Sample preparation and imaging procedure 138

5.4.2.2. Imaging results 140

5.4.3. Evaluating chemotherapy response of ovarian adenocarcinoma cells 141

5.4.3.1. Sample preparation and imaging procedure 142

5.4.3.2. Imaging results 145

5.5. Summary 152

5.6. References 153

5.1. Introduction

This chapter presents preliminary results from imaging work performed on various *in vitro* human hepatocellular and ovarian cancer cell lines with the CellvizioGI fluorescence confocal endomicroscope system. Our aim was to evaluate the microscopic cellular imaging properties of the system as a method for *ex vivo* cellular analysis and also to better understand the contrast found during future *in vivo in situ* work. A short introduction is included, which covers the principles behind conventional fluorescence confocal microscopy and the development of novel *in vivo* confocal imaging systems. Various motivations supporting fluorescence confocal endomicroscopy (FCE) as a technique for early cancer detection and diagnosis are also discussed.

The first series of FCE experiments set out to evaluate the overall image quality and contrast obtained when applying a selection of different exogenous fluorescent contrast agents during imaging. The fluorescent agents used, namely fluorescein (FL), acriflavine hydrochloride (AH) and acridine orange (AO), were assessed during FCE imaging of an *in vitro* human hepatocellular carcinoma cell line, HepG2, with the aim of selecting the optimal contrast agent for all future FCE experiments.

Imaging results are also presented from FCE imaging of three *in vitro* human ovarian adenocarcinoma cell lines – SKOV-5, OVCAR-5 and IGROV-1 – that had earlier been exposed to the platinum-based chemotherapy drug cisplatin. The aim of this study was to explore the use of FCE as a possible method for monitoring cisplatin chemotherapy response of ovarian adenocarcinoma cells at the cellular level *in vivo*. Response to chemotherapy was determined over a five-day drug exposure period by assessment of both cell numbers and cellular morphology using FCE.

5.2. Classical fluorescence confocal microscopy and the move towards novel *in vivo* systems

Classical fluorescence confocal microscopy was born out of the need for a more effective and higher-resolution method for viewing biological specimens, especially thicker diffusing samples of tissue (Webb, 1996; Wilson, 2003). The method offers a marked improvement over conventional light microscopy in that it allows a greater reduction in out-of-focus light – extraneous signals produced from structures present on top of and below the desired focal plane – providing a clear, fine-detailed and focused image from a thin section within the tissue sample (White *et al.*, 1987). This is achieved due to the specimen being illuminated by a point source of light, usually a laser beam, which is focused to a single spot in the sample, with the emitted fluorescence signals detected via a spatially restricted pinhole detector (Wilson, 2003) (Figure 5.1). Since interior sections of thicker tissue pieces (up to ~500 μm) can be effectively imaged, this eliminates the need for physical sectioning and mounting of the specimen on a microscope slide, hence allowing samples to be viewed in their natural state. The possibility of scanning deeper through samples point-by-point in various optical sections also allows a three-

dimensional image of the tissue specimen to be reconstructed for more complete visualisation.

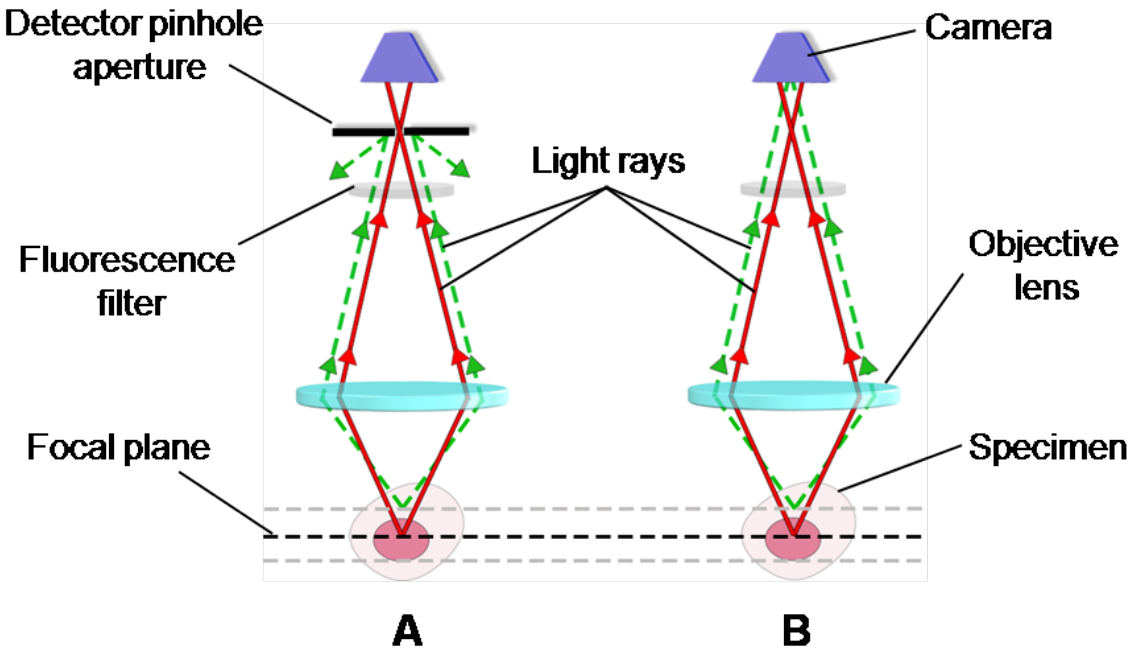


Figure 5.1. Diagrammatic representation of fluorescence confocal microscopy (A) and conventional light microscopy (B) techniques. The presence of the pinhole aperture in the confocal microscope system enables rejection of out-of-focus light rays, resulting in the production of a clearer, finer detailed and more focused image from a thin section within the specimen than conventional light microscopy. Absence of a pinhole aperture in the latter system allows collection of both in-focus and out-of-focus light from a thicker plane of the specimen, resulting in obscuration of finer details in the ensuing image.

Recent advances in the field have enabled miniaturisation of the bench-top fluorescence confocal microscope into a more portable probe-based imaging system for use in an endoscopic setting (Evans and Nishioka, 2005; Kiesslich *et al.*, 2007; Kiesslich and Tajiri, 2010). Such systems, known as fluorescence confocal endomicroscopes or fluorescence endoconfocal microscopes, enable minimally invasive imaging of the human body *in vivo* and *in situ*, generating real-time cellular-level *en face* images with a similar resolution to histology – a procedure termed the 'optical biopsy'. There are two such fluorescence confocal endomicroscope systems currently in commercial production, one produced jointly between Pentax (Tokyo, Japan) and Optiscan (Victoria, Australia), and the other by Mauna Kea Technologies (Paris, France) and known as the CellvizioGI. Though similar in function, the systems differ in optical instrumentation setup: the

Pentax/Optiscan system comprises a complete endoscope with a miniaturised scanning confocal microscope incorporated at its tip, while the CellvizioGI is a probe-based system whose confocal miniprobe can be inserted down the accessory channel of any standard endoscope (Dunbar and Canto, 2008). In the interest of compatibility with current research in our group, we have chosen to work with the CellvizioGI system for all our FCE experiments.

The CellvizioGI system is compatible with most existing endoscope systems and consists of three core components: 1) a laser scanning unit (LSU), 2) a desktop computer unit containing the system controls and image processing software, and 3) a flexible fibered confocal miniprobe that is placed in contact with tissue surfaces during image acquisition (Laemmel *et al.*, 2004, Wang *et al.*, 2007). Different confocal miniprobes are available depending on the diagnostic application: the GastroFlex for oeso-gastro-duodenoscopy, the CholangioFlex for endoscopic retrograde cholangiopancreatography (ERCP), the ColoFlex for colonoscopy and the AlveoFlex for bronchoscopic procedures; these have lateral resolutions of 3.5 μm. In addition, ultra high definition (UHD) variants of the GastroFlex and ColoFlex miniprobes are available, which have lateral resolutions of 1.4 μm.

Two classes of the Cellvizio LSU exist, one emitting laser excitation at 488 nm and the other at 660 nm, with the latter system used more widely used in small animal imaging procedures in a setup known as the CellvizioLAB. The CellvizioGI LSU used in our group emits at a wavelength of 488 nm (collection bandwidth between 500 to 650 nm), allowing for the elicitation of autofluorescence from tissue structures containing endogenous fluorophores such as elastin (420 and 500 nm absorption) flavin adenine dinucleotide (FAD; 450 nm absorption) and porphyrins (400 to 450 nm absorption). One limitation however is that tissue structures not naturally autofluorescent around the 488 nm excitation wavelength have to be first stained with exogenous fluorescent agents such as fluorescein or acridine orange for creating imaging contrast, leading to possible toxicity concerns and ethical approval issues.

5.3. Motivations for tissue diagnosis with fluorescence confocal endomicroscopy

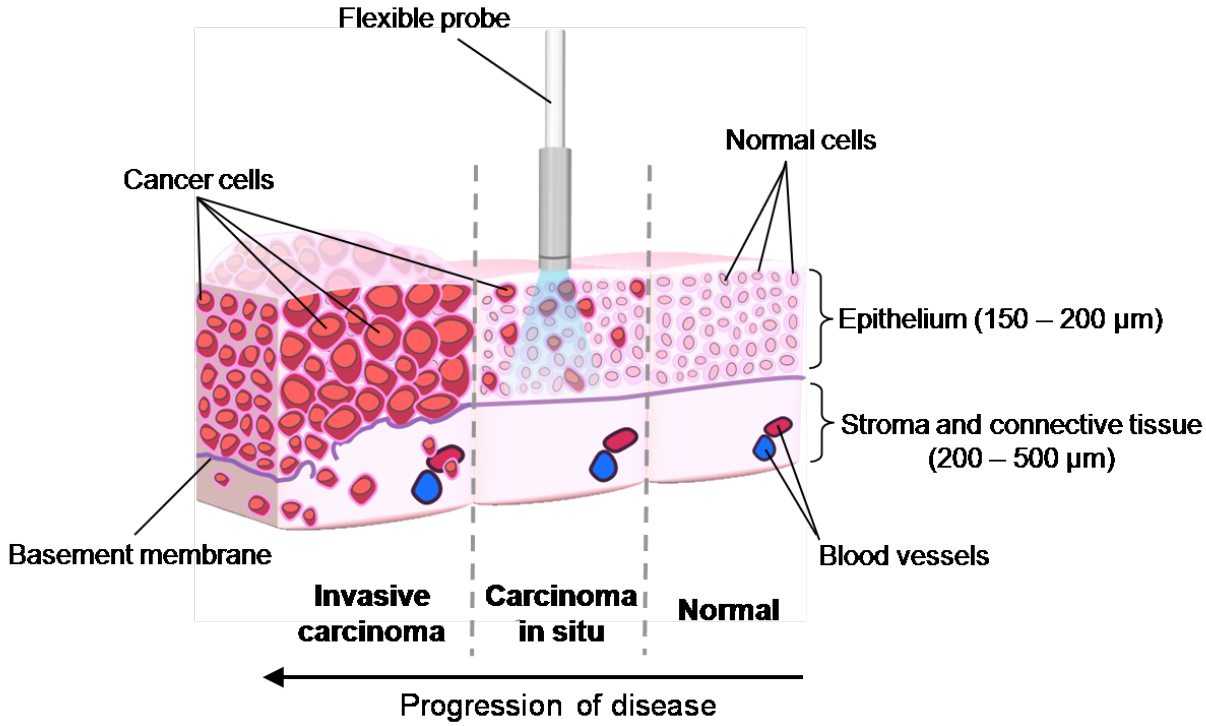


Figure 5.2. Morphological changes occurring in the uppermost layers of tissue mucosa with cancer progression.

For most human cancers, the earliest morphological changes occur at the uppermost layers of tissue. These are usually confined to the epithelium of the diseased organ, located within the first 150 to 200 µm of the mucosal surface (Figure 5.2). Carcinoma *in situ* (CIS) is the intermediate premalignant stage between normal and invasive/metastatic carcinoma, where any malignant cells remain contained within the epithelium and have yet to penetrate the underlying basement membrane – a process known as metastasis (Zhuang *et al.*, 1995; Arpino *et al.*, 2005). Disease progression from normal to invasive carcinoma has been estimated to take roughly 5 to 20 years, with the long developmental period between normal to CIS presenting as a possible window for early detection, diagnosis and treatment (Pierobon *et al.*, 2007).

Current methods for cancer diagnosis in hollow organs such as the lung, bladder and gastrointestinal tract involve a multi-step process: Firstly, imaging of the diseased organ is carried out via conventional approaches such as X-ray, CT or ultrasound to localise the

tumour or suspected cancerous regions. Since it is not possible to extract microscopic, cellular-level information from the diseased tissue via these modalities, further analysis has to be carried out on the tissue histologically. Therefore, pinch biopsies of the suspect regions are next performed minimally-invasively using a pair of endoscopic forceps. This stage of the sampling process may be random in nature, for instance due to the white-light imaging approach of the video endoscope, which makes it difficult to differentiate normal from diseased tissue even for the most experienced of operators, especially during early cancer onset. Consequently, biopsied tissue samples are then sent to a pathologist where they are fixed, sectioned and mounted on a microscope slide for histological examination. It is essential to note however that such processing eliminates the opportunity to obtain morphological and functional features of tissues that would have otherwise been present in its fresh and unprocessed form, resulting in a possible loss of important diagnostic information. Although it can be performed intrasurgically, this process from initial imaging of suspect tissue regions to confirmation of the disease by a pathologist typically requires several weeks to complete, leading to a delay in the implementation of treatment.

To date, FCE has been employed by various groups for the successful visualisation of malignant tissue changes in the upper- and lower-gastrointestinal tract (Hoffman *et al.*, 2006), lungs (Thiberville *et al.*, 2007), ovaries (Tanbakuchi *et al.*, 2008) and bladder (Sonn *et al.*, 2009). Compared to conventional screening methods, FCE has the potential to detect cancers earlier during the course of the disease and in a shorter amount of time. Via this optical biopsy approach, *in vivo* information on tissue morphology can be accurately obtained in real time and at high resolution, dramatically reducing patient waiting times and eliminating the requirement for random tissue biopsies. Another distinct advantage of the FCE system is its ease of operation and portability, allowing for use even by non-expert operators. In the long run therefore, patients will benefit from having reduced waiting times as well as lowered healthcare costs.

5.4. Fluorescence confocal endomicroscopy for cellular characterisation

5.4.1. Optical instrumentation and image acquisition

The CellvizioGI fluorescence confocal endomicroscope system is based on the principles of classical fluorescence confocal microscopy and was designed to complement currently available imaging techniques such as MRI, CT, PET, ultrasound, SPECT, *etc.*, effectively serving as the link between macroscopic imaging modalities more commonplace in the clinic with conventional bench-top microscope systems popular in the field of biology. All our experiments utilised the GastroFlex Type Z confocal miniprobe.

During data acquisition, the excitation beam produced by the 488 nm semiconductor laser of the laser scanning unit (LSU) is scanned by two mirrors located at the proximal end of the miniprobe: a 4 kHz oscillating mirror that scans horizontally (line scanning) and a 12 kHz galvanometric mirror that scans vertically (frame scanning). The laser beam is thereby raster scanned across the proximal face of the GastroFlex Type Z confocal miniprobe (2.6 mm outer diamter) containing about 30,000 individual optical fibres at a resultant frame rate of 12 kHz. The laser beam that is directed sequentially into each optical fibre is then focused onto the target specimen by a distally-located gradient index micro-objective lens that has a 0 μm working distance, 600 μm field of view, and lateral and depth resolution of 3.5 μm and 15 μm respectively. Images are acquired *en face* at a rate of 12 frames per second at a depth of between 80 to 120 μm and in 70 μm optical sections. The resulting fluorescence from the excited specimen is subsequently collected by the micro-objective lens and is refocused back into the same illumination fibre that was used for excitation. The confocality of the CellvizioGI system is conferred by the small diameter of each optical fibre core (1.9 μm), which effectively functions as a pinhole, restricting out-of-focus light during both initial excitation and image acquisition. The final raw image is then reconstructed from the fluorescence intensity measurements detected by an avalanche photodiode, with a longpass filter in place to reject any reflected excitation light.

5.4.2. Optimal contrast agent selection using hepatocellular carcinoma cells

Initial FCE experiments were performed on HepG2 hepatocellular carcinoma cells originating from the liver of a 15-year-old Caucasian male (Knowles *et al.*, 1980). The cells were stained with different fluorescent contrast agents to establish the dye that provided optimal image contrast during FCE imaging. Three popular contrast agents were investigated: acridine orange (AO), fluorescein (FL) and acriflavine hydrochloride (AH). AO is a commonly used fluorescent agent for confocal microscopy and endomicroscopy that preferentially stains nuclear DNA and cytoplasmic RNA (Rouse and Gmitro, 2000; Gareau *et al.*, 2008). FL has many applications in biomedicine, e.g. fluorescein angiography for examination of the retina of the eye and also for cell labelling during flow cytometry procedures (Flowers, 1973; Darzynkiewicz *et al.*, 2000). FL has been found to stain the cell cytoplasm as well as the extracellular matrix (Paramsothy and Leong, 2010). AH is the next most widely used contrast agent after FL, which binds predominantly to nuclear DNA with high affinity (Roth *et al.*, 1967; Paramsothy and Leong, 2010).

With regards to health and safety concerns of the contrast agents used, FL and AH exhibit very low risk of cytotoxicity, with both dyes approved by the United States Food and Drug Adminstration (FDA) – the former for *in vivo* applications and the latter for use in a number of selected *in vivo* procedures. AO has also recently been awarded FDA approval (investigational new drug 102603) for *in vivo* imaging of the ovaries within an endobag (Tanbakuchi *et al.*, 2010). In this manner, the contrast agent is contained within the endobag during imaging and is thus prevented from spreading to other neighbouring organs. Nonetheless, AO has been recognised to be moderately cytotoxic in nature, which limits its *in vivo* application in humans.

5.4.2.1. Sample preparation and imaging procedure

HepG2 carcinoma cells were obtained from Dr Eileen Gentleman, Research Associate, Department of Materials, Imperial College London and cultured in 35 mm diameter plastic cell-culture dishes containing sterile Dulbecco's Modified Eagle's Medium (DMEM) solution, 10% foetal bovine serum (FBS) and incubated at 37°C and 5% CO_2.

The cells were allowed to grow until a confluent layer was formed, a process taking about 2 to 3 days, before FCE imaging was carried out.

All three contrast agents chosen for comparison were made up in different concentrations – FL: 0.05 mM, AH: 0.05% w/v and AO: 3.0 μg/ml. These concentrations were chosen after a survey of the literature to identify commonly used concentrations for each respective dye. Contrast agents were topically applied into each cell-culture dish containing 2 ml of HepG2 cells and culture media until the desired final concentration was attained approximately two minutes before FCE imaging was performed. It was thought originally that DMEM might possibly interfere with the recorded signal, requiring it to be removed from the cell-culture dishes and replaced with 1x phosphate buffered saline (PBS) and contrast agents prior to imaging. Upon several attempts however, it was observed that a large proportion of cells were being dislodged from the surface of the dish during removal of the liquid. DMEM was therefore left in the dish with the cells, whilst contrast agents were gently introduced directly with a pipette since DMEM was not found to be fluorescent at 488 nm and as such did not interfere with the final results.

The CellvizioGI system was switched on 15 minutes prior to imaging to allow for warming up of the confocal miniprobe and semiconductor laser. Automatic control of the laser's output power by the system was also disabled under the image acquisition software's preferences panel so that the final images obtained would not be automatically adjusted for minor intensity variations that might arise as a result of the sample itself. Prior to system calibration, the miniprobe lens head was first washed with 70% ethanol followed by distilled water before being wiped dry with a soft paper towel. Calibration was performed with the miniprobe's head pointing away from any object and held in air. This process took roughly 45 seconds and was performed each time a different sample was being imaged or once every 20 minutes if it was the same sample that was being studied. During image acquisition, the miniprobe was held in place using a miniature V-clamp (VH-1; Thorlabs, Ltd., Cambridgeshire, UK) and was lowered steadily until the miniprobe's lens was in contact with the sample, i.e. until the sample came into view on the computer screen. For imaging of cells, the plastic cell-culture dishes in which they were grown were placed on top of a small translation stage (NanoMax MAX302/M;

Thorlabs, Ltd., Cambridgeshire, UK), allowing for minute translational adjustments in the X, Y and Z axes during image acquisition with the confocal miniprobe.

5.4.2.2. Imaging results

Performing FCE imaging with the three aforementioned contrast agents produced results of markedly differing image quality and contrast (Figure 5.3). Visual inspection of the results showed that FL produced images with the lowest contrast, which resulted in the background noise appearing more significant (Figure 5.3A). Imaging with AH produced images with slightly improved contrast (Figure 5.3B). Optimal image contrast i.e. clear visual distinction between the brightly fluorescent HepG2 cells and dark background was achieved when imaging with AO, resulting in images with the appearance of no or very low background noise (Figure 5.3C).

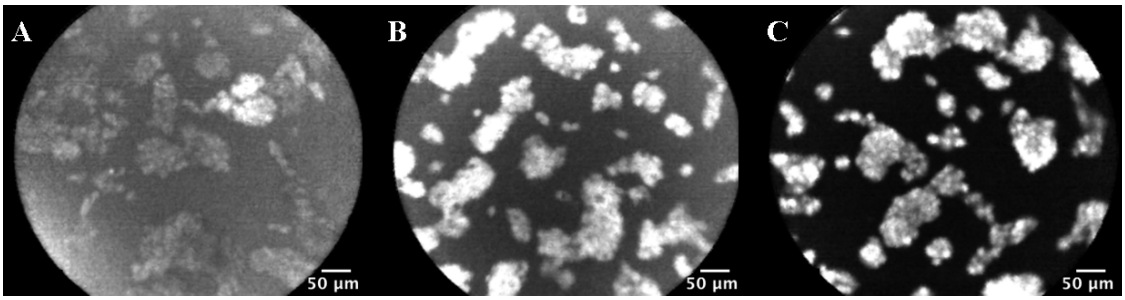


Figure 5.3. HepG2 human hepatocellular carcinoma cells stained with different contrast agents during FCE imaging: fluorescein (FL; 0.05 mM) (A), acriflavine hydrochloride (AH; 0.05% w/v) (B) and acridine orange (AO; 3.0 µg/ml) (C). Optimum image contrast is achieved when imaging with AO.

Since no quantitative information on pixel intensity was available at this point, FCE images were further analysed using MatLab (The Mathworks, Inc., MA, USA) to determine the signal intensity to background ratios (SBRs) for all three image sets. This provides an indication of how distinct the fluorescence signal was from the background: the greater the ratio, the better the image contrast achieved. This was performed by calculating the mean intensity of an approximately 15 by 15 pixel region of cells in the image, and dividing this by the standard deviation of the pixel intensities from a neighbouring background region of the same area size. Results from this analysis are presented as a bar chart in Figure 5.4: FCE imaging with FL and AH produced images

with an average SBR of about 35 and 62 respectively. On the other hand, imaging with AO resulted in images with an average SBR of about 150 – more than twice that achieved with AH. Conclusively, AO was found to provide optimal image contrast out of all three contrast agents during FCE.

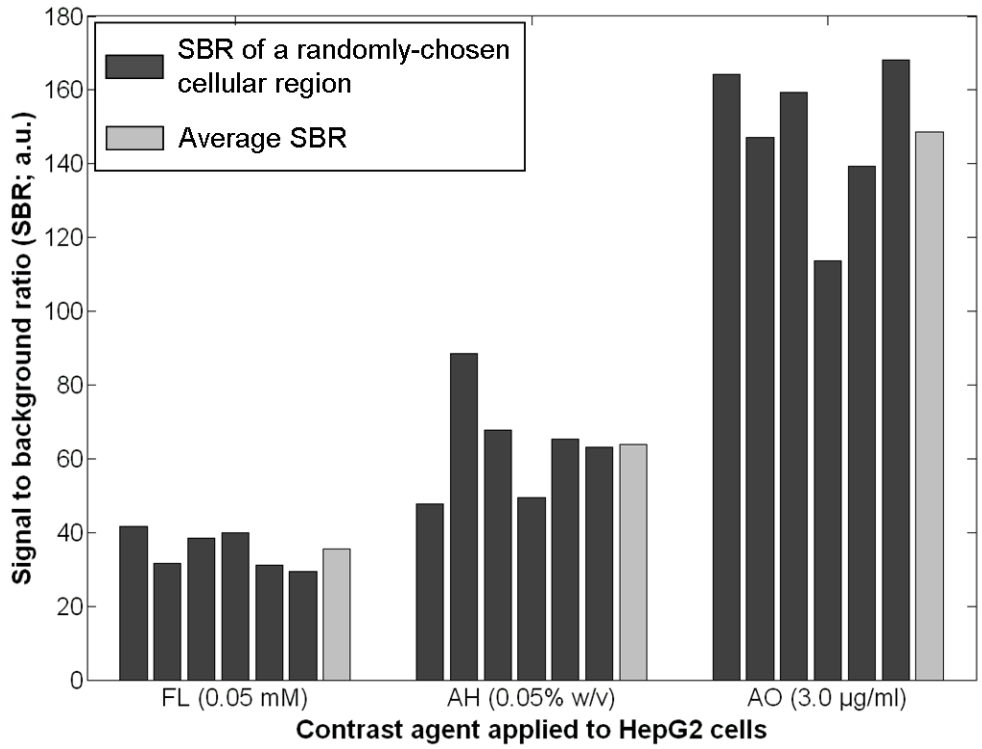


Figure 5.4. Bar chart representing the signal to background ratios (SBRs) obtained when HepG2 cells are stained with different contrast agents during FCE imaging. FCE images of HepG2 cells stained with acridine orange (AO) (Figure 5.3C) have the largest SBRs, as compared to fluorescein (FL) and acriflavine hydrochloride (AH) (Figures 5.3A and 5.3B respectively), indicating comparatively better image contrast.

5.4.3. Evaluating chemotherapy response of ovarian adenocarcinoma cells

Ovarian cancer is currently the fifth most common cancer amongst women in the UK with epithelial ovarian cancer – or cancer of the outer ovarian tissue layer - making up 90% of all reported cases (CancerHelp UK website). Like most cancers, treatment involves either surgery, radiotherapy, chemotherapy or a combination of these methods, depending on the stage of the disease.

Assessing the variable response of ovarian cancer to chemotherapy typically takes several months using currently available detection methods. These include radiological scans such as CT and ultrasound, as well as blood tests for the CA 125 tumour marker. Recently, the minimally invasive second-look laparascopy technique has also generated significant interest for detecting ovarian cancer recurrence (Davila and Estape, 2001). However this white light-based imaging approach has also been shown to have high false-negative detection rates of about 55%, with limited sensitivity and optical resolution for detecting small residual tumour nodules (Zhong *et al.*, 2009).

Since it is possible to perform imaging at the cellular level with FCE, earlier assessment of chemotherapy response could be achieved by monitoring the morphological changes occurring within the tumour during chemotherapy via such a minimally invasive (MI) endoscopic imaging modality. Our hypothesis was that there would be quantifiable evidence of cellular attrition across all ovarian adenocarcinoma cell lines following incubation with cisplatin, together with a noticeable change in cellular morphology. Therefore as a prelude to future imaging experiments involving chemotherapy-treated ovarian cancer tissue, we first ascertained if response to chemotherapy could be detected from cisplatin-exposed *in vitro* human ovarian adenocarcinoma cell lines using FCE imaging. Possible parameters evaluated *in vitro* included cellular morphology and fluorescence signal changes with different cisplatin doses as well as what signals that could be expected when imaging cells undergoing apoptosis (programmed cell death) as a result of cisplatin exposure.

5.4.3.1. Sample preparation and imaging procedure

Cisplatin (cis-diamminedichloroplatinum(II)) is a platinum (II) complex consisting of a central platinum ion surrounded by two ammonia groups (-NH_3) in the *cis* position and two chloride (-Cl) ligands that dissociate when the molecule becomes bound to duplex DNA (Figure 5.5) (Go and Adjei, 1999). Cisplatin, together with carboplatin and oxaliplatin, make up a class of platinum-based chemotherapy drugs currently in widespread clinical use for the treatment of human malignancies (Alderden *et al.,* 2006).

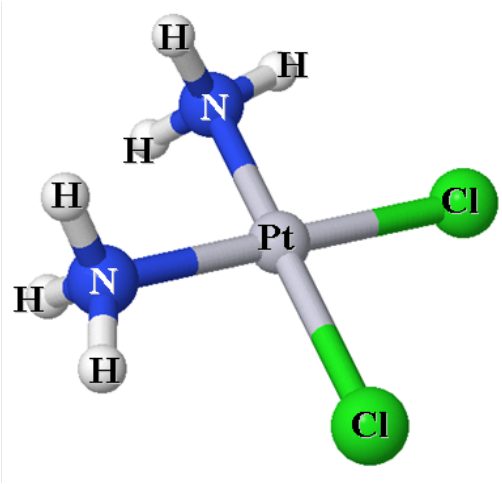


Figure 5.5. The 3D molecular structure of the cisplatin (cis-diamminedichloroplatinum(II)) molecule consisting of a central platinum ion surrounded by two ammonia groups in the *cis* position and two chloride ligands (the 'leaving' groups).

Since the serendipitous discovery of its anticancer activity by Rosenberg and colleagues at the University of Michigan in the 1960s, cisplatin has been demonstrated to be highly effective against several cancers, particularly those of the testes and ovaries, with overall cure rates for testicular cancer exceeding 90% and reaching nearly 100% if the disease is treated in its early stages and following additional surgery (Wang and Lippard 2005, Alderden *et al.,* 2006). In addition, cisplatin has shown significant efficacy during chemotherapeutic treatments for cancers of the head and neck, cervix, bladder, oesophagus, as well as both small- and non-small cell lung cancers (Go and Adjei 1999, Wang and Lippard 2005).

Various studies have indicated that cisplatin mediates its anticancer activity by forming a variety of covalent DNA adducts, whereby the central platinum ion becomes bound to the N^7 positions of adjacent purine bases, guanine and/or adenine, which make up the DNA backbone (Hambley 1997, Go and Adjei 1999, Zamble and Lippard 1995, Alderden *et al.,* 2006). This predominantly results in the formation of two major intrastrand bifunctional adducts: one with GpG sequences (60% or more) and the other with ApG sequences (about 25%); other crosslinks that may form occasionally include monofunctional intrastrand, interstrand and protein-DNA adducts (Figure 5.6) (Zamble and Lippard 1995, Lippert, 1999).

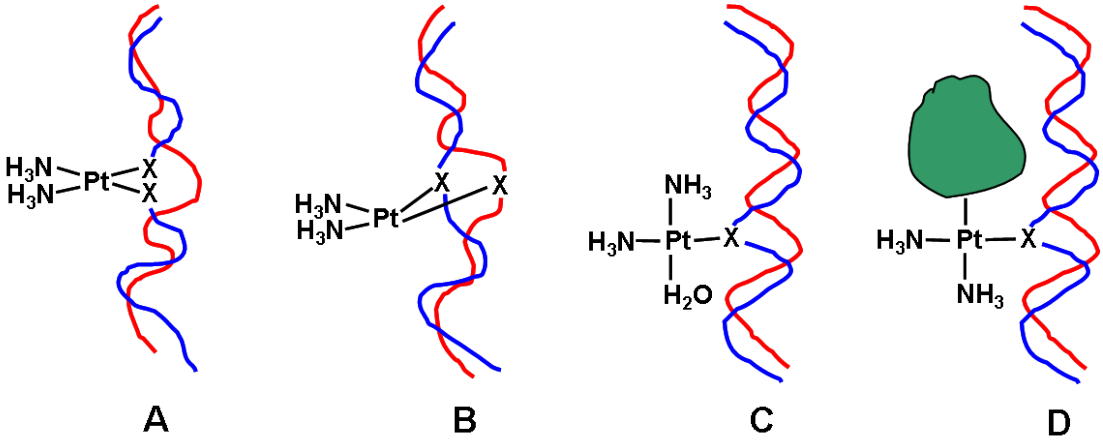


Figure 5.6. Cisplatin molecule binding to DNA to form various adducts: intrastrand bifunctional adduct (A); interstrand bifunctional adduct (B); monofunctional adduct (C); protein-DNA adduct (D). X denotes the purine base i.e. guanine or adenine, which becomes bound to the central platinum ion of the cisplatin molecule. (Figure adapted from Zamble and Lippard, 1995)

The consequence of this is tumour cell-cycle arrest at the G1, S or G2 phases of cell division and ultimately apoptosis due to a breakdown in DNA repair mechanisms (Lippert, 1999, Go and Adjei 1999, Alderden *et al.,* 2006). Other cellular events influenced by the action of cisplatin may include the inhibition of sodium-potassium dependent adenosine triphosphate (ATP) hydrolysis activity, altered mitochondrial and calcium channel functioning, and altered amino acid transport (Go and Adjei, 1999; Shionoya *et al.*, 1986; Guarino *et al.*, 1979; Vassilev *et al.*, 1987; Gordon and Gattone, 1986).

In order to assess the signals expected both *ex vivo* and *in vivo in situ*, we set out to characterise the response of human ovarian adenocarcinoma cells to the chemotherapy drug cisplatin. Three cell lines were studied: SKOV-5, OVCAR-5 and IGROV-1, all of which were sourced from our clinical collaborator at Hammersmith Hospital (Imperial College Healthcare NHS Trust), Dr Sadaf Ghaem-Maghami, Clinical Senior Lecturer, Division of Surgery, Oncology, Reproductive Biology and Anaesthetics, Imperial College London. SKOV-5 adenocarcinoma cells are clones of the SKOV-3 cell line derived from the ovarian carcinoma ascitic fluid of a 64-year-old Caucasian female (Fogh *et al.*, 1977); OVCAR-5 adenocarcinoma cells were established from an ovarian cancer patient who had not received prior chemotherapeutic intervention (Hamilton *et al.*, 1989); IGROV-1 adenocarcinoma cells were obtained from the tumour of a 47-year-old Caucasian woman

suffering from stage III ovarian cancer (Bénard *et al.*, 1985). All three cells lines have been documented to be sensitive to the cisplatin chemotherapy drug in the literature.

Cells were cultured in 35-mm plastic cell-culture dishes containing sterile RPMI 1640 medium, 10% foetal bovine serum (FBS) and penicillin-streptomycin antibiotics. Each cell line was incubated at 37°C and 5% CO_2 for a period of five days together with varying concentrations of the platinum-based chemotherapy agent cisplatin (Teva UK Limited): 0 μM, 2.5 μM, 5.0 μM, 25.0 μM and 75.0 μM. For OVCAR-5 adenocarcinoma cells, the lowest 2.5 μM cisplatin dose was replaced with a 150.0 μM concentration to see if there was any discernible difference at this high drug dose. Imaging was performed in the same manner as described in section 5.4.3.1, with cell samples placed on top of a translation stage during image acquisition with the confocal miniprobe.

5.4.3.2. Imaging results

To test our hypothesis that there would be quantifiable cellular attrition and changes in cell morphology with cisplatin chemotherapy, FCE imaging was performed on each cisplatin-exposed cell line after topical staining with acridine orange contrast agent (AO; 3.0 μg/mL), which was previously shown to in section 5.4.2.2 to provide optimal image contrast during imaging of HepG2 hepatocellular carcinoma cells. FCE imaging was carried out approximately every 24 hours from initial addition of cisplatin up till a total period of five days for all ovarian adenocarcinoma cell lines incubated with different concentrations of the chemotherapy drug. Qualitative assessment of cellular morphology was done by eye and cell numbers were recorded. Given the possibility that cells would reach a large number over the five days of incubation and potentially make quantification difficult especially for control populations, the area for recording of cell numbers was limited to approximately 0.3 mm^2 – or ¼ the field of view of the CellvizioGI confocal miniprobe. Bias during the quantification process was avoided by shifting the miniprobe to 16 different, regularly spaced pre-determined spots in the cell culture dish for all cell lines by placing a white card with inked markings below the culture dish as a positioning guide.

As seen in Figure 5.7, apart from control populations, all ovarian adenocarcinoma cell lines incubated with cisplatin displayed greater attrition rates as a result of increased cellular apoptosis following the rise in chemotherapy drug concentrations.

SKOV-5 cells displayed excellent response to cisplatin treatment. Although cells incubated with 75.0 μM cisplatin reached a higher number on day four than those incubated with 25.0 μM cisplatin, the trend in cell number variation and final cell counts obtained at the end of the experiment on day four were generally proportional to the concentration of cisplatin applied (Figure 5.7A). One might expect the final cell numbers obtained on day four with 75.0 μM and 25.0 μM cisplatin to be reversed; however this can be explained by the high concentration of cisplatin used (75.0 μM) which may have had a physiological effect on the cells, thus leading to an alteration in the trend of results, or perhaps also due to unequal pipetting of cells into the culture dishes at the beginning of the experiment.

OVCAR-5 cellular attrition exhibited a similar trend to the SKOV-5 cells (see Figure 5.7B). A higher 150.0 μM concentration of cisplatin was included in the experiment although the overall trend of cellular attrition remained unchanged.

Like SKOV-5 and OVCAR-5, IGROV-1 also responded in a similar fashion to the anticancer effects of cisplatin. From Figure 5.7C, it is noticeable that the rate of cellular attrition is proportional to the concentration of cisplatin applied: untreated control populations displayed a slight general increase in cell numbers across days zero to four, whilst cisplatin-treated populations showed a decreasing trend with the rate of attrition related more or less to the level of cisplatin concentration. The IGROV-1 cell line grows and divides at a faster rate than SKOV-5 and OVCAR-5 cells, thus explaining the larger average number of 10.4 cells per 0.3 mm^2 imaged area at the beginning of the experiment on day zero.

For understanding the *in vivo* imaging of ovarian cancer cells it is also useful to observe the shapes and morphology of the cells. Cisplatin-treated ovarian adenocarcinoma cell lines exhibited elongated and enlarged pseudopodial protrusions - a trait that was particularly evident when cells were incubated with lower 2.5 μM and 5.0 μM cisplatin concentrations, especially in SKOV-5 and OVCAR-5 cell populations (see Figures 5.8 –

10). Pseudopodial protrusions play an active role in tumour cell motility and migration (Jia *et al.*, 2005) and their enlargement/elongation at lower cisplatin concentrations may not be directly linked to the effects of cisplatin alone, since such lower drug concentrations do not totally inhibit tumour cell growth and division as evidenced from Figure 5.7. It is possible that this pseudopodial enlargement/elongation occurred in response to normal cell growth but due to the formation of adducts by cisplatin DNA binding, cell division did not take place successfully. Hence the end result is larger individual cells containing cisplatin-bound DNA and more cytoplasmic content in the form of enlarged pseudopodial protrusions. Further evidence for this is that cells exposed to the lower cisplatin concentrations (2.5 μM and 5.0 μM) displayed distinctly larger cell nuclei compared to the untreated controls, providing further evidence that the drug mediates its anticancer effects via various binding interactions with cellular DNA as mentioned earlier in section 5.4.3.1.

Overall, it appeared that cell size and morphology was significantly affected at the higher cisplatin concentrations of 25.0 μM, 75.0 μM and 150 μM: with the exception of IGROV-1 cells, all ovarian adenocarcinoma cells were visibly reduced in size at these high concentrations compared to control populations, with much smaller nuclei and no or very little observable pseudopodial protrusions. Owing to the small size of IGROV-1 cells (~10 to 30 μm) and the high uptake of AO contrast agent in their nuclei, it was difficult to distinguish any visible difference in morphology between the controls and treated cells across all five days of the experiment (see Figure 5.10). As this could also be due to the spatial resolution of our current confocal miniprobe (3.5 μm), it would be useful in future work to perform this experiment again using an ultra high definition miniprobe with a smaller spatial resolution of 1.0 μm for improved cellular visualisation.

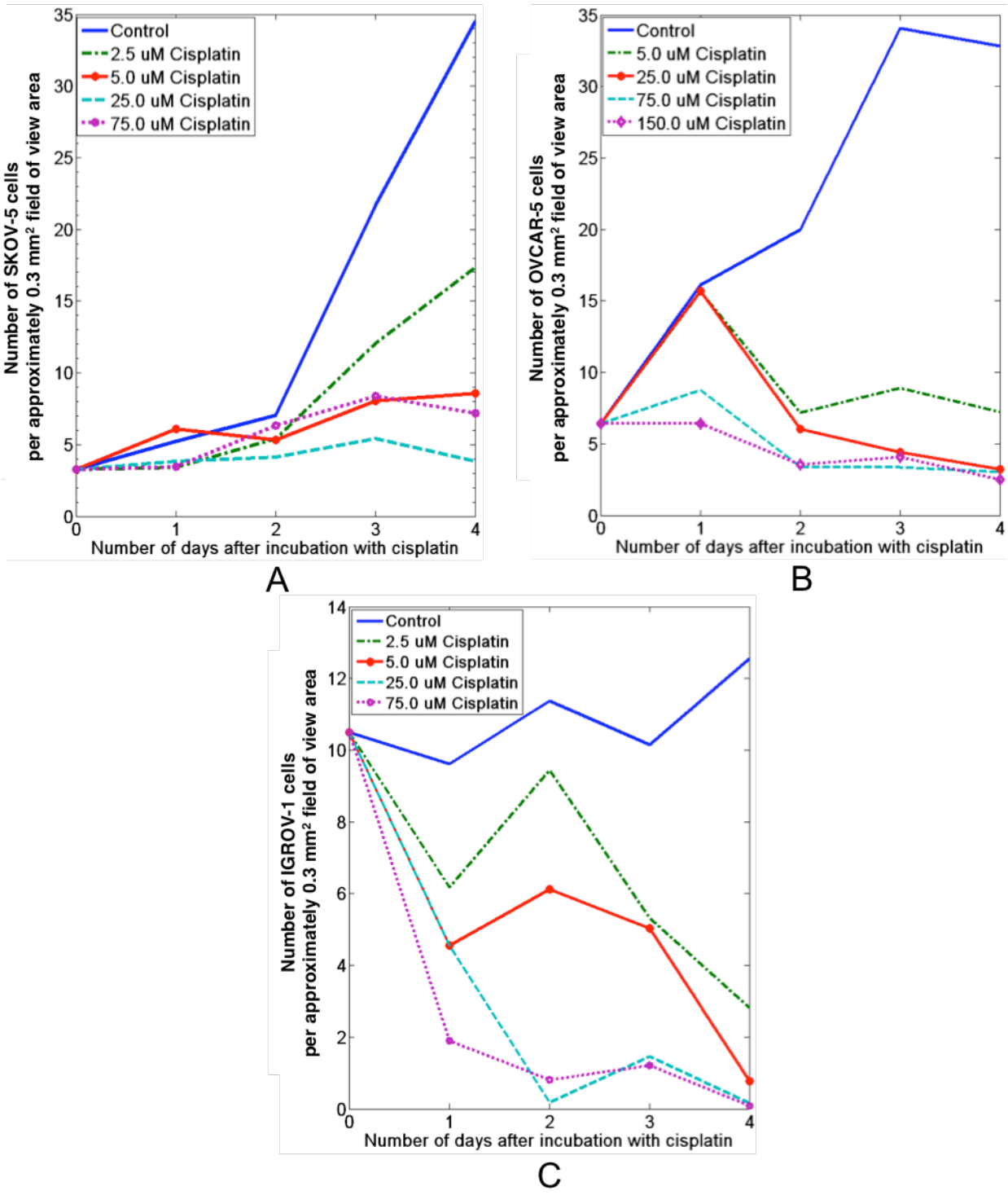


Figure 5.7. Graphs showing the average attrition rates of ovarian adenocarcinoma cell lines after incubation with various concentrations of cisplatin. Cells numbers were recorded approximately every 24 hours over a five-day period and within pre-determined areas on the cell culture dish: SKOV-5 cells (A), OVCAR-5 cells (B), IGROV-1 cells (C). All curves are coloured in the same manner according to its relative concentration within that graph.

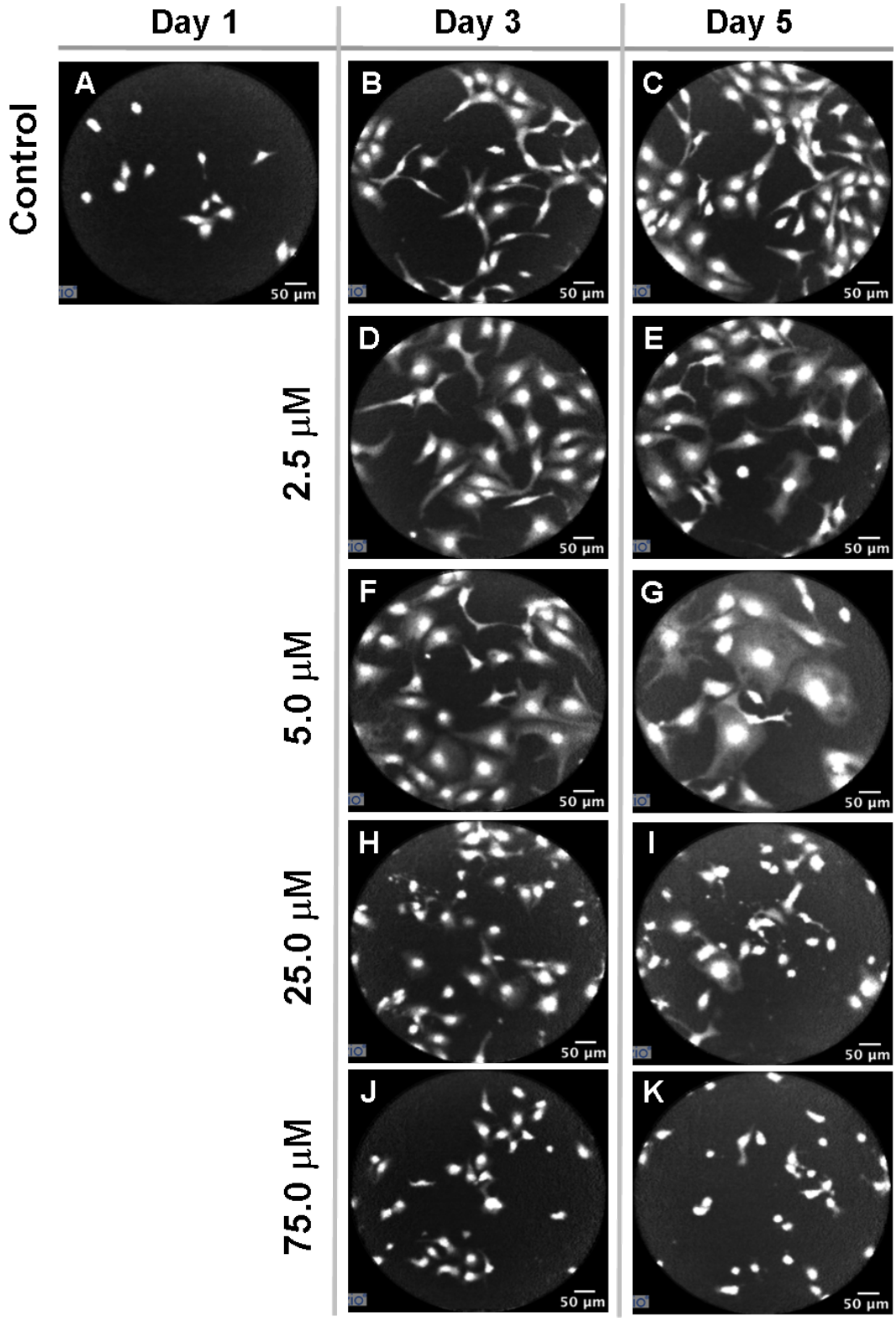


Figure 5.8. FCE images of AO-stained SKOV-5 ovarian adenocarcinoma cells incubated with various concentrations of cisplatin over a five-day period. Cells exhibited elongated/enlarged pseudopodial protrusions and larger cell nuclei at 2.5 µM and 5.0 µM cisplatin concentrations. Cell growth was arrested above this concentration level with most cells appearing smaller in size than the control populations at days 3 and 5.

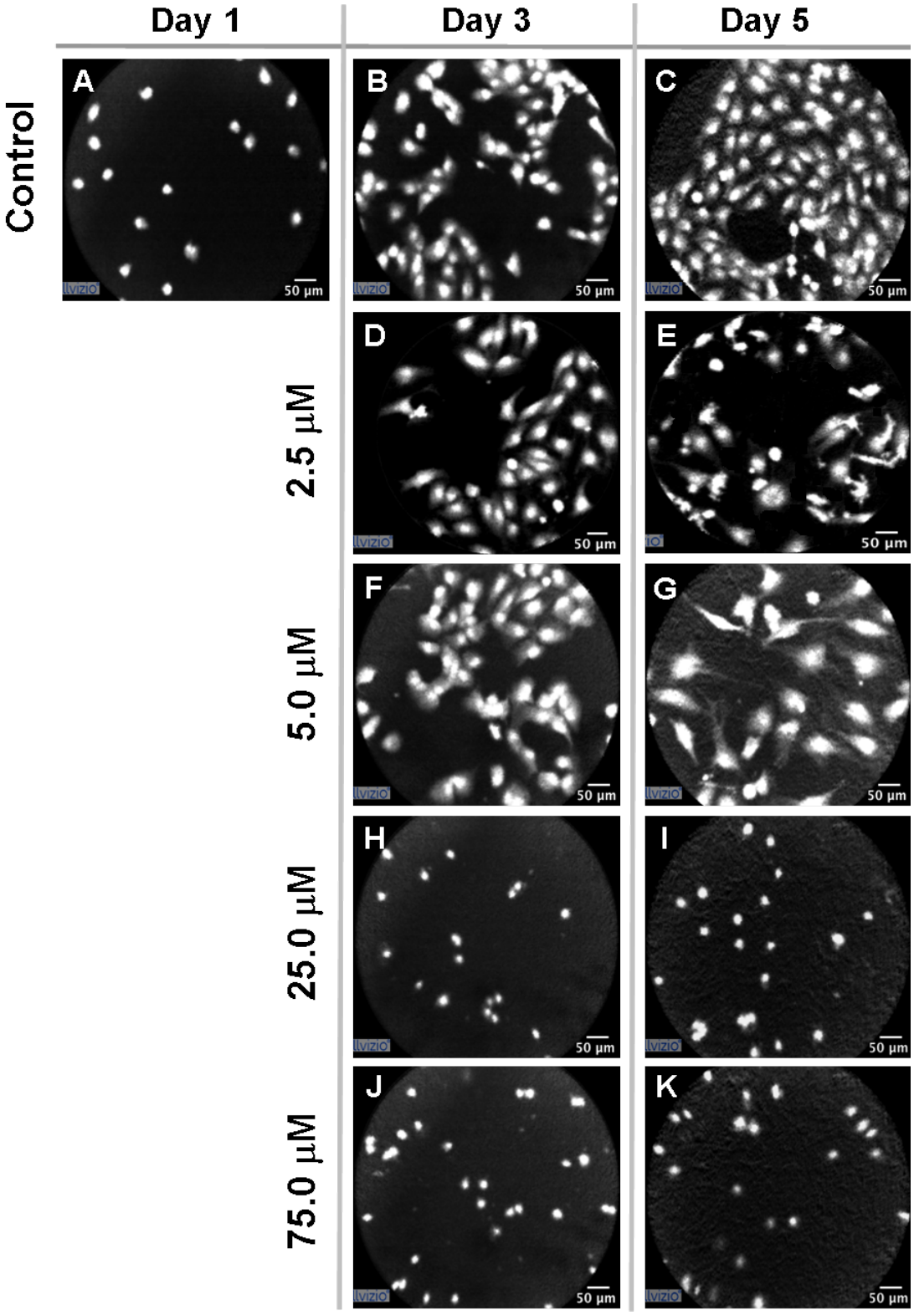


Figure 5.9. FCE images of AO-stained OVCAR-5 ovarian adenocarcinoma cells incubated with various concentrations of cisplatin over a five-day period. Cellular nuclei and pseudopodia exhibited size increases in line with cisplatin concentration increases between 0 and 5.0 µM. Growth was inhibited at 25.0 µM and 75.0 µM cisplatin concentration, with treated cells appearing morphologically smaller than control populations at days 3 and 5.

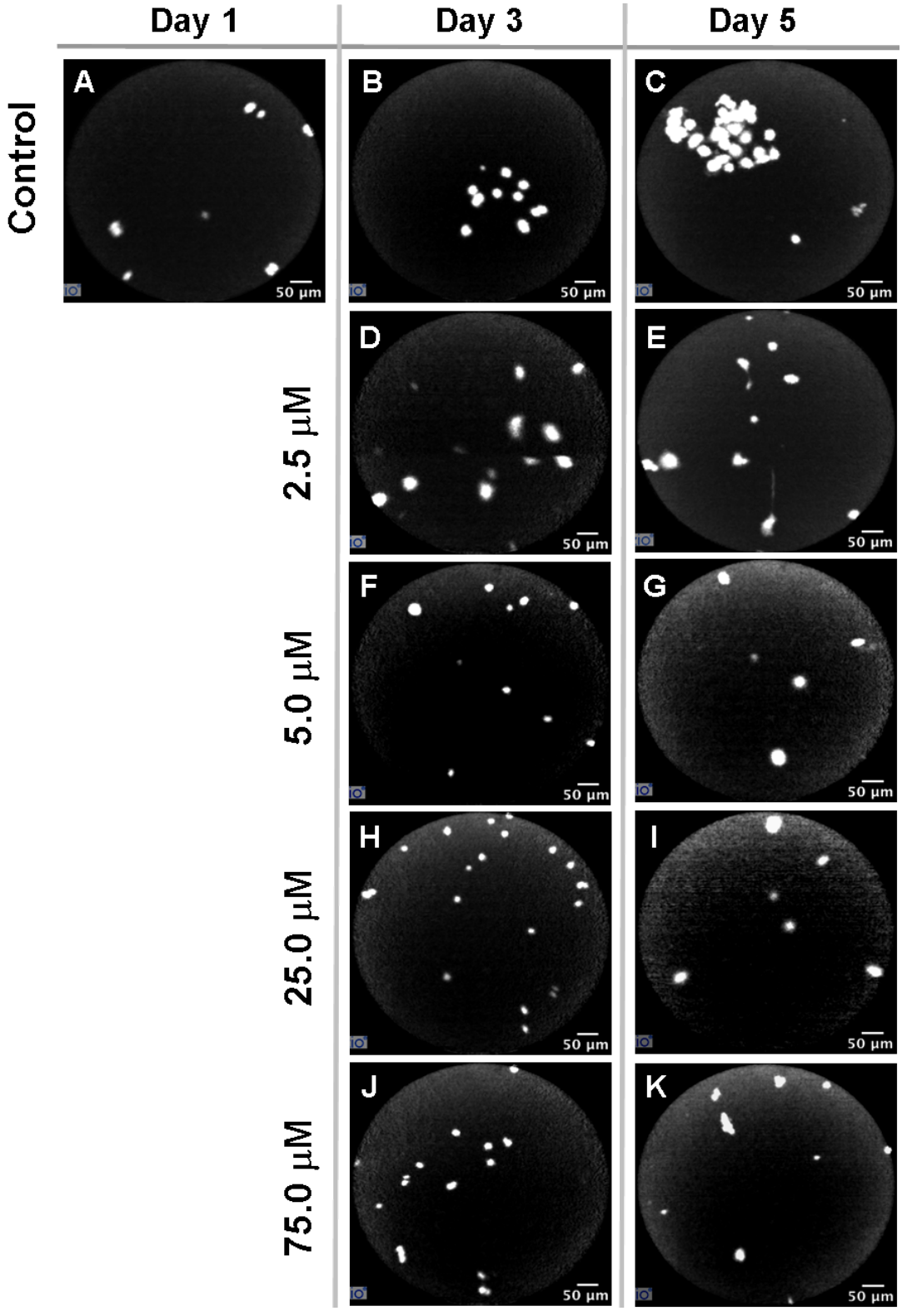


Figure 5.10. FCE images of AO-stained IGROV-1 ovarian adenocarcinoma cells incubated with various concentrations of cisplatin over a five-day period. High uptake of AO contrast agent in addition to the small size of individual cells made it difficult to evaluate the effects of cisplatin based on cell morphology alone. Most cells appeared similar in size and shape across all five days of incubation with different cisplatin concentrations.

5.5. Summary

Preliminary FCE experiments in this chapter have effectively demonstrated the system's ability to visualise various cancer cells in high resolution and at μm scales. Imaging experiments involving the use of various commonly applied fluorescent contrast agents have also established AO as the optimal contrast agent for cellular imaging, with AO images having larger signal to background ratios (SBRs) achieved compared to the other dyes. Good uptake of AO was readily observed across all cell lines within two minutes of dye application with excellent staining of cell nuclei clearly visible; the strongly fluorescent nuclei allowed easy identification of individual cells.

In addition, we have successfully shown the potential application of FCE for effective assessment of chemotherapy treatment outcomes. This was demonstrated on three cisplatin-exposed human ovarian adenocarcinoma cell lines over a five-day period, with chemotherapy response evaluated via changes in cellular morphology and by quantification of cell numbers using FCE imaging. There was an issue however with the morphological visualisation of IGROV-1 cells due to their small sizes and strongly fluorescent nuclei obscuring any fine cellular details. As a solution, we intend to use a higher definition confocal miniprobe with a smaller spatial resolution of 1.0 μm for imaging of these cells at a later date.

FCE results obtained in this chapter have demonstrated the possibility of assessing adenocarcinoma cellular response to cisplatin chemotherapy by quantification of cell numbers and visualisation of cellular morphology. These will serve as useful background work for future studies on cancer tissues, allowing a better understanding of the signals and contrast that will be obtained during imaging experiments on *ex vivo* tissue samples and *in vivo in situ* in animal models of human cancer.

5.6. References

Alderden RA, Hall MD, Hambley TW. The discovery and development of cisplatin. *Journal of Chemical Education* 2006;**83**:728.

Arpino G, Laucirica R, Elledge RM. Premalignant and in situ breast disease: biology and clinical implications. *Annals of Internal Medicine* 2005;**143(6)**:446-457.

Bénard J, Da Silva J, De Blois MC, Boyer P, Duvillard P, Chiric E, Riou G. Characterization of a human ovarian adenocarcinoma line, IGROV1, in tissue culture and in nude mice. *Cancer Research* 1985;**45(10)**:4970-4979.

Buczek-Thomas JA, Chen N, Hasan T. Integrin-mediated adhesion and signalling in ovarian cancer cells. *Cell Signaling* 1998;**10(1)**:55-63.

Cancer Research UK. Ovarian cancer risks and causes [online]. *CancerHelp UK* 2010. Available: http://www.cancerhelp.org.uk/index.htm. Assessed 8th September 2010.

Darzynkiewicz Z, Bedner E. Analysis of apoptotic cells by flow and laser scanning cytometry. *Apoptosis* 2000;**322**:18-39.

Davila GW, Estape R. Gynecologic laparoscopy. *Surgical Oncology Clinics of North America* 2001;**10(3)**:557-569.

Dunbar K, Canto M. Confocal endomicroscopy. *Current Opinion in Gastroenterology* 2008;**24(5)**:631-637.

Evans JA, Nishioka NS. Endoscopic confocal microscopy. *Current Opinion in Gastroenterology* 2005;**21**:578-584.

Flower RW. Injection technique for indocyanine green and sodium fluorescein dye angiography of eye. *Investigative Ophthalmology* 1973;**12(12)**:881-895.

Fogh J, Wright WC, Loveless JD. Absence of HeLa cell contamination in 169 cell lines derived from human tumors. *Journal of the National Cancer Institute* 1977;**58(2)**:209-214.

Gareau DS, Li Y, Huang B, Eastman Z, Nehal K, Rajadhyaksha M. Confocal mosaicing microscopy in Mohs skin excisions: feasibility of rapid surgical pathology. *Journal of Biomed Optics* 2008;**13(5)**:054001.

Go RS, Adjei AA. Review of the comparative pharmacology and clinical activity of cisplatin and carboplatin. *Journal of Clinical Oncology* 1999;**17(1)**:409-422.

Gordon JA, Gattone VH. Mitochondrial alterations in cisplatin-induced acute renal failure. *American Journal of Physiology* 1986;**250**:F991-F998.

Guarino AM, Miller DS, Arnold ST, Pritchard JB, Davis RD, Urbanek MA, Miller TJ, Litterst CL. Platinate toxicity: Past, present and prospects. *Cancer Treatment Reports* 1979;**63**:1475-1483.

Hambley TW. The influence of structure on the activity and toxicity of Pt anti-cancer drugs. *Coordination Chemistry Reviews* 1997;**166**:181-223.

Hamilton TC, Lai GM, Rothenberg ML, Fojo A, Young RC, Ozols RF. Drug resistance. In: *Cancer Treatment and Research* (Ozols RF, ed). Boston: Kumar. 1989:151-169.

Hoffman A, Goetz M, Vieth M, Galle PR, Neurath MF, Kiesslich R. Confocal laser endomicroscopy: technical status and current indications. *Endoscopy* 2006;**38(12)**:1275-1283.

Jia ZJ, Barbier L, Stuart H, Amraei M, Pelech S, Dennis JW, Metalnikov P, O'Donnell P, Nabi IR. Tumor cell pseudopodial protrusions. *Journal of Biological Chemistry* 2005; 280(34):30564-30573.

Kiesslich R, Goetz M, Nieth M, Galle PR, Neurath MF. Technology insight: confocal laser endoscopy for in vivo diagnosis of colorectal cancer. *Nature Clinical Practice Oncology* 2007;**4**:480-490.

Kiesslich R, Tajiri H. Advanced Imaging in Endoscopy. In: *Gastrointestinal Endoscopy* (Classen M, Tytgat GNJ, Lightdale CJ, eds). Stuttgart: Georg Thieme Verlag. 2010:**3**.

Knowles BB, Howe CC, Aden DP. Human hepatocellular carcinoma cell lines secrete the major plasma proteins and hepatitis B surface antigen. *Science* 1980;**209(4455)**:497-499.

Laemmel E, Genet M, Le Goualher G, Perchant A, Le Gargasson JF, Vicaut E. Fibered Confocal Fluorescence microscopy (Cell-viZio) facilitates extended imaging in the field of microcirculation. *Journal of Vascular Research* 2004;**41(5)**:400–411.

Lippert B. *Cisplatin: chemistry and biochemistry of a leading anticancer drug* (Lippert B, ed). Zurich: Verlag Helvetica Chimica Acta; Weinheim: Wiley-VCH. 1999.

Paramsothy S, Leong RWL. Fluorescein contrast in confocal laser endomicroscopy. *Nature Reviews Gastroenterology and Hepatology* 2010;**7**:366-368.

Pierobon M, Geho D, Belluco C, Liotta LA. Invasion and Metastasis. In: *The Cancer Handbook, 2nd Ed.* (Alison MR, ed). New Jersey: John Wiley & Sons, Inc. 2007;**16**.

Roth D, London M, Manjon M. Binding specificity and affinity of acriflavine for nucleic acids. *Stain Technology* 1967;**42(3)**:125-132.

Rouse AR, Gmitro AF. Multispectral imaging with a confocal microendoscope. *Optics Letters* 2000;**25(23)**:1708-1710.

Shionoya S, Lu Y, Scanlon KJ. Properties of amino acid transport systems in K562 cells sensitive and resistant to *cis*-diamminedichloro-platinum(II). *Cancer Research* 1986;**46**:3445-3448.

Sonn GA, Mach KE, Jensen K, Hsiung PL, Jones SN, Contag CH, Wang TD, Liao JC. Fibered confocal microscopy of bladder tumors: an ex vivo study. *Journal of Endourology* 2009;**23(2)**:197-201.

Tanbakuchi AA, Rouse AR, Udovich JA, Hatch KD, Gmitro AF. A clinical confocal microlaparoscope for real-time in vivo optical biopsies. *Journal of Biomedical Optics* 2009 **14(4)**:044030.

Tanbakuchi AA, Udovich JA, Rouse AR, Hatch KD, Gmitro AF. In vivo imaging of ovarian tissue using a novel confocal microlaparoscope. *American Journal of Obstetrics and Gynecology* 2010;**202(1)**:90.e1-9.

Thiberville L, Moreno-Swirc S, Vercauteren T, Peltier E, Cave C, Heckly GB. *In vivo* imaging of the bronchial wall microstructure using fibered confocal fluorescence microscopy. *American Journal of Respiratory and Critical Care Medicine* 2007;**175**:22–31.

Vassilev PM, Kanazirska MP, Charamella LJ, Dimitrov NV, Tien HT. Changes in calcium channel activity in membranes from cis-diammine-dichloroplatinum(II)-resistant and -sensitive L1210 cells. *Cancer Research* 1987;**47(2)**:519-522.

Wang TD, Friedland S, Sahbaie P, Soetikno R, Hsiung PL, Liu JTC, Crawford JM, Contag CH. Functional imaging of colonic mucosa with a fibered confocal microscope for real time in vivo pathology. *Clinical Gastroenterology and Hepatology* 2007;**5(11)**:1300–1305.

Wang D, Lippard SJ. Cellular processing of platinum anticancer drugs. *Nature Reviews Drug Discovery* 2005;**4(4)**:307-320.

Webb RH. Confocal optical microscopy. *Reports on Progress in Physics* 1996;**59**:427-471.

White JG, Amos WB. Confocal microscopy comes of age. *Nature* 1987;**328**:183-184.

Wilson T. Confocal Microscopy. In: *Biomedical Photonics Handbook* (Vo-Dinh T, ed). Boca Raton: CRC Press. 2003;**10**.

Zamble DB, Lippard SJ. Cisplatin and DNA repair in cancer chemotherapy. *Trends in Biochemical Sciences* 1995;**20(10)**:435-439.

Zhong W, Celli JP, Rizvi I, Mai Z, Spring BQ, Yun SH, Hasan T. In vivo high-resolution fluorescence microendoscopy for ovarian cancer detection and treatment monitoring. *British Journal of Cancer* 2009;**101**:2015-2022.

Zhuang Z, Merino MJ, Chuaqui R, Liotta LA, Emmert-Buck MR. Identical allelic loss on chromosome 11q13 in microdissected *in situ* and invasive human breast cancer. *Cancer Research* 1995;**55:**467-471.

6

Probing the Morphological and Functional Properties of Tissue with Fluorescence Confocal Endomicroscopy

6.1. Introduction 158

6.2. Characterising the morphological appearance of *ex vivo* healthy porcine tissues and human cancer tissues 159

6.2.1. Instrumentation and imaging procedure 159

6.2.2. *In vivo* imaging of healthy porcine tissues 160

6.2.3. *Ex vivo* imaging of human cancer tissues 162

6.2.3.1. Ovarian cancer tissue 162

6.2.3.2. Bladder cancer tissue 164

6.3. Photodynamic diagnostic imaging of photosensitised cancer cells and tumour tissues 166

6.3.1. Photodynamic diagnosis (and therapy) 166

6.3.2. 5-aminolevulinic acid and protoporphyrin IX 168

6.3.3. Instrumentation and imaging procedure 169

6.3.4. *In vitro* imaging of photosensitised human ovarian cancer cells 170

6.3.5. *Ex vivo* imaging of photosensitised human cancer tissues 172

6.3.5.1. Small-cell lung cancer tissue 174

6.3.5.2. Pharyngeal cancer tissue 176

6.3.6. *In vivo* imaging of photosensitised murine tissues 178

6.4. Probing fluorescent signatures from a tumour-specific PET imaging optical analogue 181

6.4.1. Instrumentation and imaging procedure 182

6.4.2. *In vitro* imaging of fluorescent labelled human ovarian cancer cells 182

6.4.3. *In vivo* imaging of tumour-specific fluorescent biomarkers from murine tumour tissue 184

6.5. Multimodal endoscopic viewfinder imaging technique 187

6.5.1. Instrumentation and imaging procedure 190

6.5.2. Viewfinder imaging of photosensitised bladder cancer tissue 191

6.6. Summary 194

6.7. References 196

6.1. Introduction

This chapter describes the application of fluorescence confocal endomicroscopy (FCE) for the characterisation of cancer and healthy states in both *ex vivo* and *in vivo* tissues from humans and animal models of disease. Coupled with this are preliminary FCE imaging studies involving *in vitro* primary cancer cell lines; these serve as foundation work for understanding signals that will be acquired during the ensuing tissue-based procedures. All imaging experiments were designed to interrogate the morphological or functional properties of cells or tissues under investigation.

The chapter begins with imaging experiments on *ex vivo* healthy porcine tissues to study various biological tissue staining protocols during FCE using different fluorescent contrast agents, namely fluorescein (FL), acriflavine hydrochloride (AH) and acridine orange (AO). With the optimal contrast agent established, further FCE imaging was performed on *ex vivo* human ovarian and bladder cancer tissues following topical dye application. This was to characterise morphological features of tumour tissues for enhanced discrimination. Imaging experiments in this section were carried out to investigate a protocol for *ex vivo* tissue staining that can be eventually used *in vivo*, and also for evaluating the use of FCE as a method of performing real-time intrasurgical histopathology.

The FCE technique was then explored as a potential photodynamic diagnostic (PDD) modality during imaging of 5-aminolaevulinic acid (5-ALA) photosensitiser treated *in vitro* human ovarian cancer primary cell lines, *ex vivo* human pharyngeal and small-cell lung cancer tissues, and *in vivo* murine tumour tissue. Our aim was to ascertain if 5-ALA induced protoporphyrin IX (PpIX) fluorescence originating from cancer cells and tumour tissues could be detected using the FCE confocal miniprobe.

The possibility of imaging across different resolution scales in conjunction with positron emission tomography (PET) imaging was also explored by applying FCE imaging for detection of the tumour-specific fluorescent optical biomarker 2-[*N*-(7-nitrobenz-2-oxa-1,3-diaxol-4-yl)amino]-2-deoxyglucose (2-NBDG). 2-NBDG is a fluorescently labelled 2-deoxyglucose molecule analogous to 2-deoxy-2 [^{18}F] fluoro-D-glucose (FDG) used in PET imaging that is readily taken up by actively metabolising cancer cells. Although well

established in the field of oncology, FDG PET imaging suffers from poor spatial resolution, which poses a considerable limitation especially for the purposes of early cancer detection. FCE imaging with 2-NBDG was thus investigated to determine if cellular level resolution could be achieved using the technique both *in vitro* and *in vivo* in human ovarian cancer cells and a murine model of ovarian cancer respectively.

In addition, a novel multimodal endoscopic viewfinder (MEV) imaging approach based on the combination of multispectral fluorescence imaging (MFI), hyperspectral reflectance imaging (HRI) and FCE imaging modalities is proposed as a potential method for more accurate and targeted tissue diagnosis. We demonstrate this technique on 5-ALA photosensitiser-treated *ex vivo* human bladder cancer tissues.

6.2. Characterising the morphological appearance of *ex vivo* healthy porcine tissues and human cancer tissues

6.2.1. Instrumentation and imaging procedure

FCE imaging was performed on *in vivo* healthy porcine and *ex vivo* human cancer tissues with the CellvizioGI fluorescence confocal endomicroscope system (Mauna Kea Technologies, France). The system's laser emitted at 488 nm excitation and imaging was performed with the GastroFlex Type Z confocal miniprobe as described in section 5.4.1 of the previous chapter.

During *in vivo* FCE imaging of various healthy porcine internal organs, the target organ was held steadily by hand while the miniprobe was gently placed on the organ and translated slowly across its surface. Figure 6.1 shows the procedure being performed on a porcine ovary. *Ex vivo* FCE imaging of human cancer tissues were performed with the tissues placed in 60 mm diameter cell culture dishes. The entire imaging procedure was carried out by hand with the confocal miniprobe placed gently on the surface of the tissues and slowly moved around. It should be noted that this stage of the procedure is very delicate and difficult to perform due to the highly pressure-sensitive nature of the acquisition optics; too strong a pressure applied with the miniprobe on the tissues and the final FCE images obtained would be out of focus.

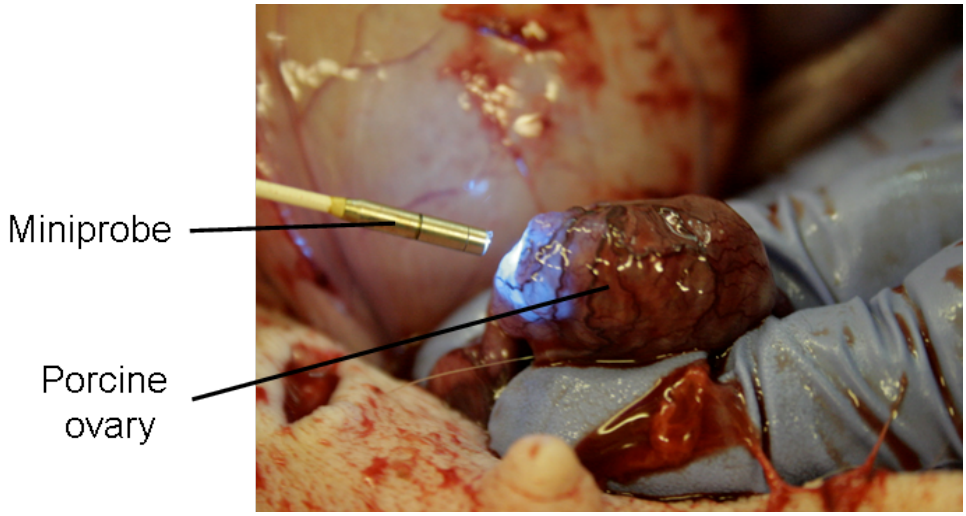


Figure 6.1. Photograph showing fluorescence confocal endomicroscopy (FCE) of a porcine ovary in the gloved hand of an operator. Note that the FCE confocal miniprobe is in contact with the surface of the ovary during image acquisition.

6.2.2. *In vivo* imaging of healthy porcine tissues

In vivo FCE imaging was performed on a terminally anaesthetised sow at the Northwick Park Centre for Medical Research, North West London Hospitals NHS Trust, where a midline laparotomy was performed on the animal to allow access to its internal organs. The procedure was carried out under an Animal License from the Home Office Animals for Scientific Procedure Act 1986 (License No. PPL 80/2297 – "The Validation of a Flexible Endoscopic Robot for Use in Human NOTES Applications"). Healthy *in vivo* porcine tissues imaged by FCE included those of the ovaries, bladder, peritoneum and spleen. Three contrast agents were topically applied to the surfaces of the animal's target organs five minutes prior to imaging using a plastic Pasteur pipette: 1) acridine orange (AO; 10.0 μg/mL in 1x PBS), 2) acriflavine hydrochloride (AH; 0.05% w/v in 1x PBS) and 3) fluorescein (FL; 0.05 mM in 1x PBS). This was to find the dye that provided optimal image contrast during FCE imaging of biological tissues. The reader is directed to section 5.4.2 and its listed references for a more detailed description of each contrast agent and its cellular binding targets.

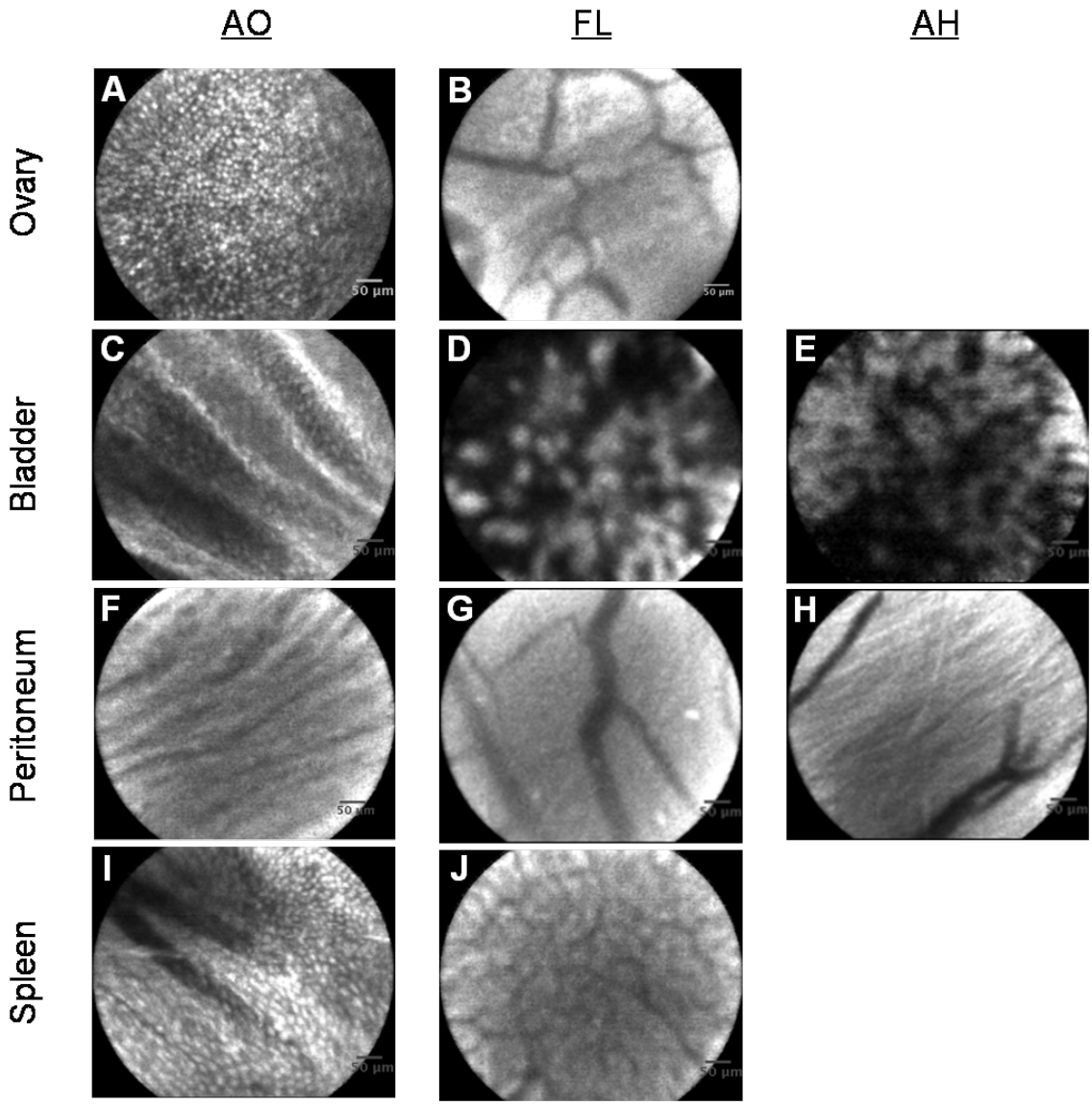


Figure 6.2. FCE images of healthy *in vivo* porcine tissues following topical application of various fluorescent contrast agents, namely acridine orange (AO; 10.0 µg/ml), fluorescein (FL; 0.05 mM) and acriflavine hydrochloride (AH; 0.05 % w/v).

Imaging results in Figure 6.2 exhibit the varied extents by which each contrast agent stains the different *in vivo* porcine tissues. Upon visual inspection, it is evident that AO provides the best image contrast out of the three dyes: FCE images of AO-stained tissues are clear and in focus with bright fluorescent dots highlighting cell nuclei, especially in ovarian and splenic tissues (Figures 6.2A and I). Images of FL and AH-stained tissues on the other hand appear 'hazy' and out of focus, with limited discernable cellular features. Unfortunately, FCE images of AH-stained ovary and spleen were not saved due to an electrical error. During the FCE procedure however, AH tissue images were found to be

of a (poor) quality similar to that of bladder and peritoneal tissue (Figures 6.2E and H). As such, the final experimental outcome remained unaffected. Based on these results, AO was chosen as the optimal contrast agent for all subsequent FCE imaging experiments in this chapter.

6.2.3. *Ex vivo* imaging of human cancer tissues

Surplus and anonymised fresh human cancer tissue samples were sourced via routine resectioning procedures through our clinical collaborators at the Imperial College Healthcare NHS Trust hospitals. Informed consent was obtained from all patients prior to tissue resectioning and all experiments were carried out with ethical approval from the Outer West London Research Ethics Committee, National Research Ethics Service, United Kingdom (REC Reference No. 08/H0719/37 – "Multimodal Optical and Spectroscopic Imaging of Human Cancer Tissues *Ex Vivo*").

The *ex vivo* human cancer tissues imaged for this part of our study were obtained from various hospitals:

i. Ovarian cancer tissue – sourced from Hammersmith Hospital, Imperial College Healthcare NHS Trust from Dr Sadaf Ghaem-Maghami, Clinical Senior Lecturer, Division of Surgery, Oncology, Reproductive Biology and Anaesthetics, Imperial College London, and
ii. Bladder cancer tissue – sourced from St Mary's Hospital and Charing Cross Hospital, Imperial College Healthcare NHS Trust from Mr Erik Mayer, Clinical Research Fellow, Division of Surgery, Oncology, Reproductive Biology and Anaesthetics, Imperial College London, and Mr Daniel Cohen, Clinical Research Fellow, Department of Surgery and Cancer, Imperial College London.

6.2.3.1. Ovarian cancer tissue

Surplus *ex vivo* human ovarian cancer tissue harvested during ovarian cancer debulking surgery were subjected to FCE imaging. The tissues were topically stained with AO (10.0 μg/mL in 1x PBS) using a plastic Pasteur pipette five minutes prior to the start of

imaging; this was performed within one hour after tissues were excised from patients. The ovarian cancer tissues imaged measured approximately 1.0 to 3.0 cm in diameter and ranged from either softer stromal to firmer cyst-like specimens. Uptake of contrast agent was found to be excellent with various microscopic tissue structures clearly visible after about three minutes of AO application.

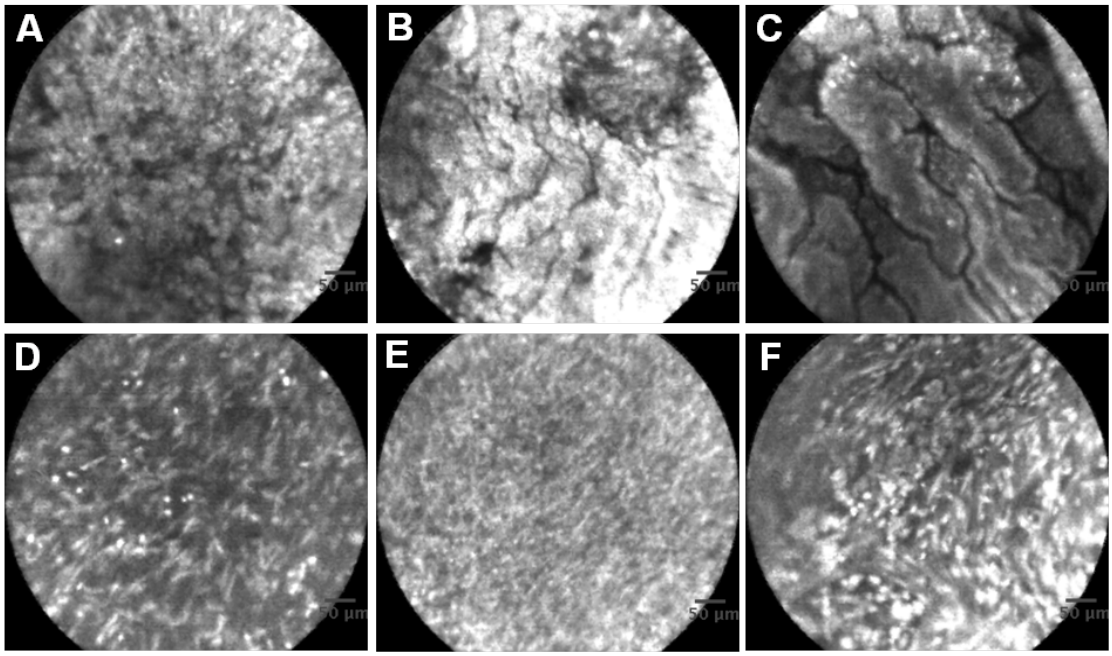


Figure 6.3. FCE images of *ex vivo* human ovarian cancer tissues demonstrating a heterogeneous morphology. Imaging was performed following topical application of AO contrast agent (10.0 µg/mL): Softer stromal tissue regions displaying irregular cellular clusters and spongy, frond-like structural contours (A to C); Firmer cyst-like tissue regions exhibiting a diffuse, fibrous appearance with clear evidence of cellular pleomorphism and nuclear hyperchromatism (D to F).

FCE images obtained of *ex vivo* ovarian cancer tissues clearly demonstrated the heterogeneous morphological nature of the tissues (Figure 6.3). Images recorded of the softer ovarian stromal tissue showed clusters of irregularly shaped cells (Figure 6.3A) and spongy, frond-like tissue contours (Figures 6.3B and C). The firmer cyst-like ovarian cancer tissue presented a more diffuse and fibrous appearance (Figures 6.3D and E) with evidence of cellular pleomorphism - the occurrence of many different cellular forms, and nuclear hyperchromatism, referring to the degeneration of cell nuclei (Figure 6.3F). As with healthy *ex vivo* porcine tissues imaged earlier in section 6.2.2, extra care had to be

taken during imaging to achieve the right amount of contact pressure at the tip of the confocal miniprobe for obtaining optimal focus and image quality.

These *ex vivo* FCE results give a good indication as to what fluorescent signals and image contrast we would acquire during future *in vivo* tissue imaging procedures. Since ovarian tissue samples were imaged fresh and within one hour of surgical removal, we expect to visualise similar tissue microstructures *in vivo*. Using FCE we have managed to successfully characterise the morphology of cancerous ovarian tissue, demonstrating the possibility of applying the technique for *in vivo* diagnosis of diseased tissue states. Based on encouraging results from chapter 5 involving chemotherapy-treated ovarian adenocarcinoma cells, a further *in vivo* application of FCE could be the assessment of cancer tissue response to chemotherapy. This would allow the drug response of cancer tissues to be known in a much shorter amount of time than conventional assessment methods such as MRI, PET and CT imaging.

6.2.3.2. Bladder cancer tissue

Excess human bladder cancer tissue was obtained with informed consent from patients undergoing routine TURBT (transurethral resection of bladder tumour) procedures for removal of superficial cancerous growths on the bladder wall. The procedure involves insertion of a rigid tube called a cystoscope up the urethra and into the bladder, followed by the introduction of either a wire loop or biopsy forceps through the cystoscope for tissue removal. With the former, an electric current is passed through the wire loop and is used to ablate any tumour tissue whilst cauterising and sealing off the wound simultaneously – a process known as diathermy. The use of the latter is termed a cold-cut biopsy because tumour tissue is cut away without any burning occurring. All TURBT procedures were performed with patients under general or regional anaesthesia.

Bladder cancer tissues were imaged with the FCE miniprobe within one hour after removal from the patient and topically stained with acridine orange (AO) dye (10.0 μg/mL in 1x PBS) prior to imaging. Both cold-cut and diathermy-excised bladder cancer tissues were imaged and the results are presented in Figure 6.4. As with ovarian cancer tissues imaged previously, there was fast uptake of AO within about three minutes of application with cellular structures clearly visible in cold-cut samples (Figures 6.4B and

C). The characteristic irregular and polymorphic appearance of cancer tissues could also be made out (Figure 6.4C). Unstained cold-cut samples displayed only weak specks of autofluorescence (Figure 6.4A). This was however the opposite case for diathermy samples, which exhibited strong autofluorescence from the diathermied surfaces of unstained tissue (Figure 6.4D). The level of autofluorescence was high enough such that application of AO did not appear to have any effect on the acquired FCE images (Figures 6E and F). This was an unexpected result, and after further investigation it was found that the reason for autofluorescence originating from diathermied tissues may be attributed to heat denatured collagen and elastic fibres in the tissue dermal layers (Vo *et al.*, 2001; Lin *et al.*, 2006). This has important implications for the possible application of FCE for intrasurgical imaging, since thermally induced fluorescence from diathermy tissue dissections may obscure fluorescence emissions from the applied contrast agent.

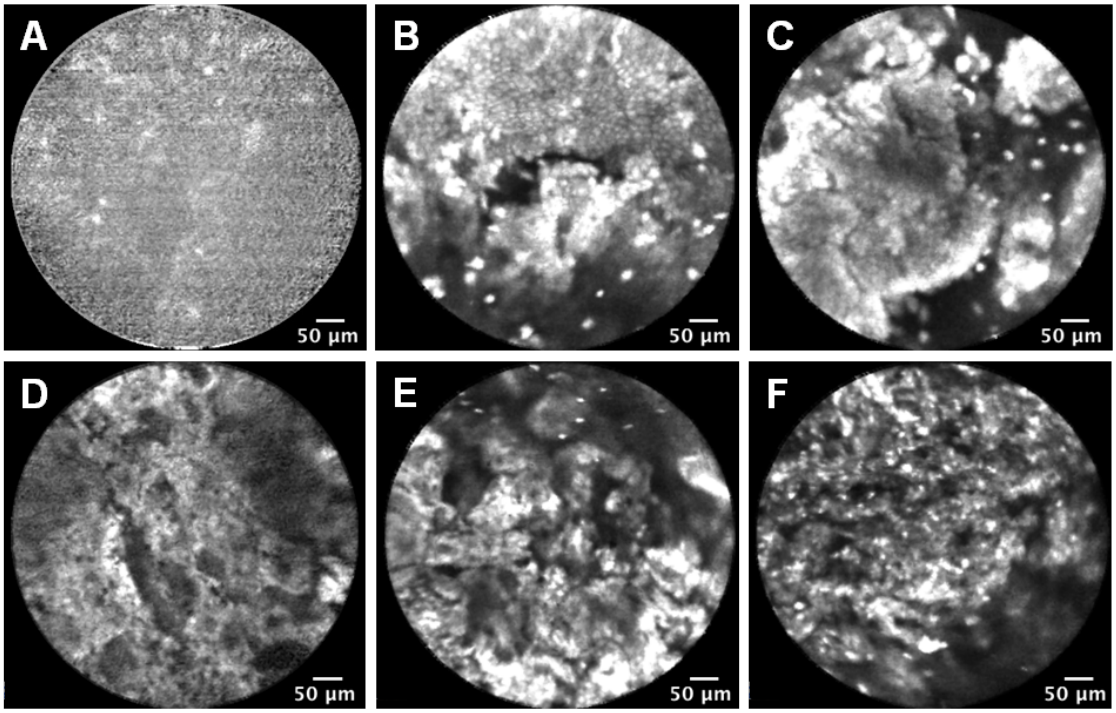


Figure 6.4. FCE images of *ex vivo* human bladder cancer tissues excised via transurethral cold-cut biopsy (A to C) or diathermy (D to F). Tissues were imaged both unstained and after topical application of acridine orange dye (AO; 10.0 µg/mL): unstained (A and D); AO-stained (B, C, E and F).

6.3. Photodynamic diagnostic imaging of photosensitised cancer cells and tumour tissues

The aim of this series of experiments involving the photosensitiser pro-drug 5-aminolevulinic acid (5-ALA) was to assess the potential of applying FCE as a photodynamic diagnostic (PDD) modality. Using 5-ALA-treated *in vitro* human ovarian cancer cell lines, *ex vivo* human cancer tissues and *in vivo* murine tumour tissues, our aim was to ascertain if 1) the FCE system could effectively detect 5-ALA induced protoporphyrin IX (PpIX) fluorescence emissions from cancer cells and tissues, and 2) to track the variation in PpIX fluorescence signals in these cells and tissues over time. The purpose of the latter was to establish the most favourable imaging time window where highest fluorescence intensities could be obtained for achieving optimal image contrast. An additional objective was to exploit the high spatial resolution of the confocal miniprobe for resolving PpIX localisation in specific organelles within photosensitised cells *in vitro* and within tissues; this could serve as a possible method for distinguishing between different cell types and their respective functions.

At the time of experiment, no suitable protocol for PDD imaging with FCE using a fibered confocal miniprobe had been established in the literature. As such we began initial FCE-PDD imaging experiments by first imaging photosensitised cell lines to ascertain detection of PpIX fluorescence before moving on to whole *ex vivo* and *in vivo* tissues. FCE imaging experiments were conducted as far as possible within an environment maintained at physiological conditions: cell lines were imaged *in vitro* within an incubator set at 37°C temperature and 5% CO_2; *ex vivo* tissues were left to incubate with 5-ALA at 37°C temperature and 5% CO_2 in an incubator most of the time and taken out of the solution only at 15 minute intervals for FCE imaging procedures lasting no longer than 30 seconds; photosensitised murine tissues were imaged *in vivo* immediately after culling of the animals.

6.3.1. Photodynamic diagnosis (and therapy)

The photochemotherapy of superficial tumours, a treatment modality popularly known as photodynamic therapy (PDT), involves administration of a class of tumour-localising, light-activated drugs called photosensitisers or a photosensitising pro-drug to induce oxidative cellular damage mediated by the reactive oxygen species for a curative or

palliative outcome (Dougherty *et al.*, 1998; Henderson and Gollnick, 2003; Vrouenraets *et al.*, 2003).

PDT has many distinct advantages over conventional therapeutic approaches for the treatment of solid tumours. Since it can be implemented as a convenient outpatient procedure, this will correspondingly translate to shortened treatment times and lowered hospitalisation costs. PDT also does not adversely affect other standard cancer therapies such as radiotherapy and chemotherapy and can hence be applied either before, after or even adjuvantly. Another advantage is that PDT is cosmetically superior to surgery, leaving no scarring during tissue removal. Additionally, the method possesses double selectivity, requiring both the application of drug and the delivery of light to the affected area (endoscopically, if the target tissue is within the body); either component on its own will not induce any damaging cytotoxic effects on tissues. Most importantly, PDT can be repeated without the build up of toxicity or inducement of any tumour resistance and tissue hypersensitivity. One characteristic disadvantage of the technique however is the development of skin photosensitivity, requiring the patient to stay indoors and to avoid exposure to bright light for a few days. This side effect has since been greatly improved upon with each new generation of photosensitisers developed.

Widely used photosensitisers such as hematoporphyrin derivative (HpD) and Photofrin II exhibit preferential accumulation in tumour tissue. Like all chemotherapeutic interventions, tissue selectivity of the applied drug is of utmost importance to ensure as minimal damage as possible to healthy regions of tissue surrounding the tumour. Various hypotheses have been put forth linking this accumulation selectivity to differences between normal and tumour tissue properties, although the exact mechanisms for this phenomenon are still unclear (Dougherty *et al.*, 1998; Wilson, 2002). Owing to the high degree of tissue specificity of photosensitisers, fluorescence detection of these molecules has been exploited as a means of distinguishing tumour from normal tissues for the purpose of surgical guidance and monitoring of PDT treatment outcomes (Wilson, 2002; Kelty *et al.*, 2002).

A large number of PDT/PDD studies have been reported by various groups, mostly for the photodynamic detection and treatment of cancers in the human body. Such examples include PDD imaging of tumour tissues in the gastrointestinal tract (Mayinger *et al.*, 1999;

Endlicher and Messmann, 2004), oesophagus (Mayinger *et al.*, 2001; Claydon and Ackroyd, 2004), bladder (Denzinger and Burger, 2008; D'Hallewin *et al.*, 2002; Bordier *et al.*, 2010), breast (Ladner *et al.*, 2001; Frei *et al.*, 2004), oral cavity (Zheng *et al.*, 2004; Hamad *et al.*, 2009), pharyngo-larynx (Csanady *et al.*, 2003) and ovary (Löning *et al.*, 2004; Zeisser-Labouèbe *et al.*, 2006; Zhong *et al.*, 2009).

6.3.2. 5-aminolevulinic acid and protoporphyrin IX

Of the various photosensitisers currently in clinical application for PDT, much research has been focused around the use of the photosensitiser pro-drug 5-ALA. Unlike other PDT agents, 5-ALA itself does not bring about a photosensitising effect, but rather gets processed intracellularly to produce the endogenous photosensitiser molecule PpIX.

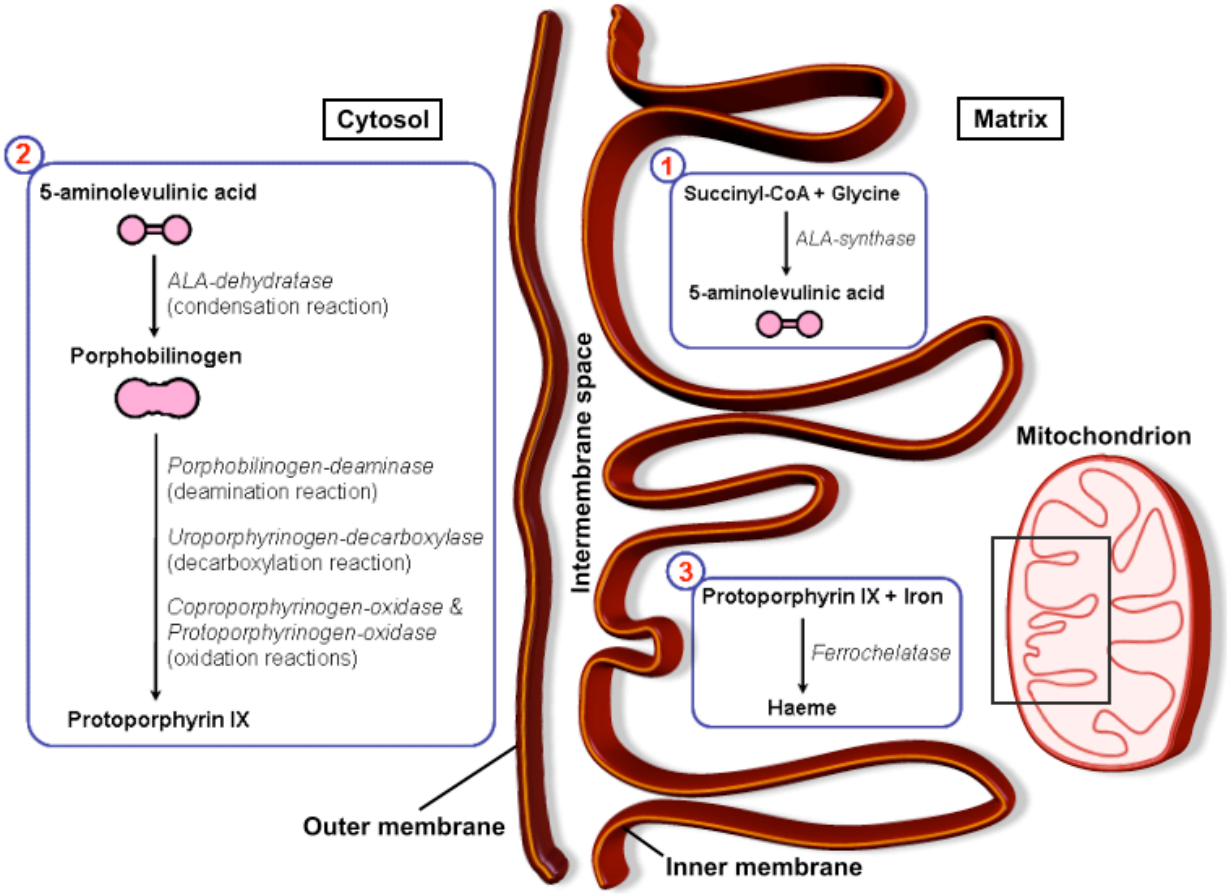


Figure 6.5. The haem biosynthetic pathway showing the various enzymatic reactions and metabolic precursors involved leading to the production of haem in normal cells.

Both 5-ALA and PpIX are naturally occurring metabolic precursors present along the pathway for haem biosynthesis (Kennedy *et al.*, 1992; Peng *et al.*, 1997; Bartošová and Hrkal, 2000) (refer to Figure 6.5). Synthesis of 5-ALA is the initial step in this three-stage process, which occurs in the mitochondrial matrix between succinyl-coenzyme A (succinyl-CoA) and the amino acid glycine, and is catalysed by the enzyme ALA-synthase (ALAS). In the next stage, 5-ALA migrates from the mitochondrial matrix into the intercellular cytosol where its two molecules undergo a condensation reaction in the presence of the cytosolic enzyme ALA-dehydratase (ALAD) to form porphobilinogen (PBG). PBG goes through a further series of sequential reactions involving catalysis by a host of different enzymes – deamination (by PBG-deaminase), decarboxylation (by uroporphyrinogen-decarboxylase) and then oxidation (by coproporphyrinogen-oxidase and protoporphyrinogen-oxidase) – to produce PpIX. The final stage of the pathway involves the incorporation of iron (Fe^{2+}) to PpIX to produce haem, a reaction localised in the mitochondrial matrix and catalysed by the inner-membrane enzyme ferrochelatase.

The haem biosynthetic pathway has been found to be disrupted during malignant tissue transformations, resulting in altered enzymatic activity. For instance, the activity of porphobilinogen-deaminase (PBGD), which converts PBG to uroporphyrinogen, was found to be elevated in certain tumours (Schoenfeld *et al.*, 1988; Kondo *et al.*, 1993), whereas that of the ferrochelatase enzyme, which catalyses haem production from iron and PpIX, was found to be lowered (Rubino *et al.*, 1966; Kondo *et al.*, 1993; El-Sharabasy *et al.*, 1992; van Hillegersberg *et al.*, 1992). As a consequence, increased PpIX accumulation was observed in tumour cells, indicating that these are significantly more photosensitised than normal cells and are as such natural targets for PDT. This implies that the introduction of more 5-ALA into the pathway would cause a corresponding increase in the amount of PpIX being produced in these malignant tumour cells, hence allowing for more targeted detection of cancer tissue via photodynamic detection of PpIX fluorescence.

6.3.3. Instrumentation and imaging procedure

As with section 6.2.1, FCE imaging was performed with the CellvizioGI system from Mauna Kea Technologies (France) using the GastroFlex Type Z confocal miniprobe. 5-ALA photosensitised *in vitro* human cancer cell lines and *ex vivo* human cancer tissues

were examined using a time-lapse imaging approach with images acquired every five minutes per cell/tissue sample. The setup of the imaging procedure was identical to section 5.4.2.1, with cancer cells imaged on a fixed translation stage for fine μm lateral adjustment of the culture dishes and the utilisation of a V-clamp to hold the confocal miniprobe firmly in place. *Ex vivo* cancer tissue samples and *in vivo* murine tissues were imaged by hand, with the former procedure performed in 60 mm diameter plastic dishes (as in section 6.2.1). Automatic control of the CellvizioGI system's laser was set to the 'off' mode to prevent automated adjustment of laser power for boosting signal strength during episodes of low fluorescence. This was to allow for a fair comparison of intensity values across all images and samples.

6.3.4. *In vitro* imaging of photosensitised human ovarian cancer cells

Three human primary ovarian cancer cell lines studied previously i.e. SKOV-5, OVCAR-5 and IGROV-1 (see chapter 5.4.3) were chosen as targets for photodynamic diagnosis with FCE-PDD imaging. These were cultured under standard physiological conditions in 35 mm plastic cell-culture dishes containing sterile RPMI 1640 media, 10% foetal calf serum (FCS), penicillin-streptomycin antibiotics and the photosensitiser pro-drug 5-ALA (1.0 mM). Cell lines were incubated over a period of 240 minutes and imaged *in vitro* at five-minute intervals with the FCE miniprobe. This time-lapse imaging approach was to allow for observation of 5-ALA-induced PpIX fluorescent signal levels to establish an optimal imaging time window for future imaging experiments where PpIX fluorescence was at its highest.

Visual examination of the imaging results in Figure 6.6 demonstrates an improvement in image quality and contrast with increasing 5-ALA incubation time across all adenocarcinoma cell lines. Although not comparable to images of acridine orange (AO)-stained cells in terms of clarity and contrast (first row of Figure 6.6), 5-ALA-treated cell images still exhibited sufficient contrast for clear distinction between individual cells. This improvement in image quality over time can be quantified as an increase in the signal to background ratios (SBRs) of the acquired FCE images, which reached a peak at t = 60 minutes across all cell lines with optimal image contrast achieved between t = 25 and 75 minutes (Figure 6.7). This was calculated in the same manner using MatLab (The Mathworks, Inc., MA, USA) as described in section 5.4.2.2 of the previous chapter. We

expect to observe a similar trend in detected PpIX fluorescence when imaging photosensitised tissues over time, but with even stronger fluorescence intensities during FCE imaging *in vivo*. This is due to the lack of FCS in biological tissues, whose presence has been shown to cause the efflux of PpIX from *in vitro* 5-ALA-treated cell cultures (Weir *et al.*, 1995; Bartošová and Hrkal, 2000).

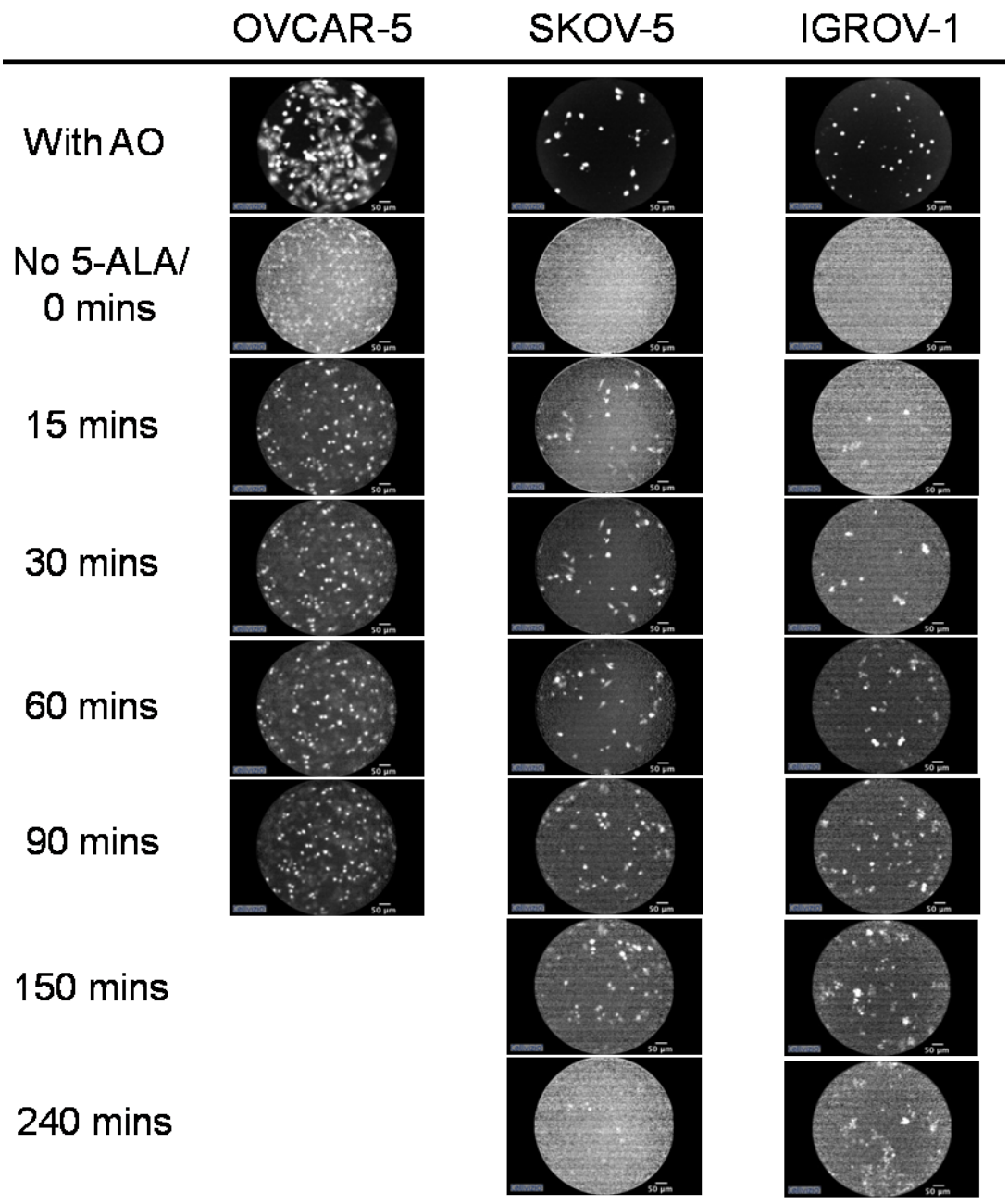


Figure 6.6. Time-lapse FCE images of three *in vitro* primary human ovarian cancer cell lines incubated with 5-ALA (1.0 mM) for up to a period of 240 minutes. Cells were also stained with acridine orange (AO) contrast agent (3.0 µg/mL) to provide a 'gold-standard' comparison with signals obtained from 5-ALA induced PpIX fluorescence.

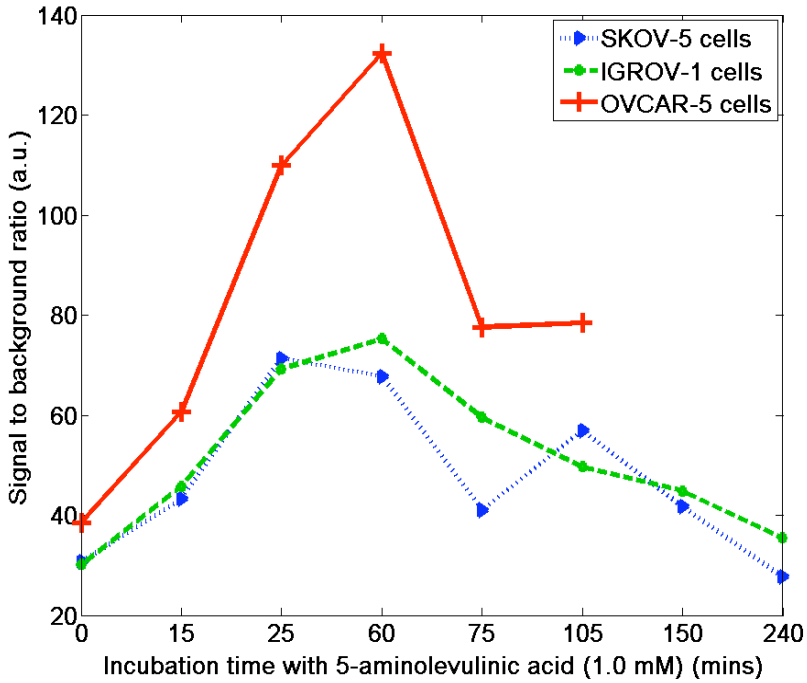


Figure 6.7. Change in signal to background ratios of FCE images with 5-ALA incubation. Peak contrast is reached at t = 60 mins with optimal contrast achieved from t = 25 - 75 mins.

6.3.5. *Ex vivo* imaging of photosensitised human cancer tissues

With the optimal time window for observing PpIX fluorescence established in the previous section from FCE-PDD imaging of photosensitised *in vitro* primary cancer cells, the next experimental phase was to perform the same imaging approach on photosensitised *ex vivo* human cancer tissues to observe a similar 5-ALA-induced PpIX fluorescence effect.

Since 5-ALA has to be converted to PpIX intracellularly, we had to ensure that the excised *ex vivo* cancer tissues were maintained alive for a few hours during the course of our imaging experiments to achieve viable results. To verify if this was possible, we first performed a quick survey of the literature and found that similar *ex vivo* imaging experiments had previously been performed:

Karrer *et al.* incubated *ex vivo* samples of perilesional skin and basal cell carcinomas excised from human patients with 9-acetoxy-2,7,12,17-tetrakis-(ß-methyoxyethyl)-porphycene (ATMPn), a photosensitiser pro-drug (Karrer *et al.*, 1997). The depth of ATMPn penetration was later measured at 2, 6, 16 and 20 hours after application by

observation of red PpIX fluorescence emitting from the epidermal tissue layer. In a separate study, Maisch and colleagues demonstrated the successful conversion of 5-ALA to PpIX in an *ex vivo* normal porcine skin by comparing PpIX fluorescence intensity and depth of penetration following incubation with a 5-ALA cream and an emulsion containing an ester of 5-ALA (aminolevulinate methyl ester hydrochloride) (Maisch *et al.*, 2009). PpIX fluorescence was detected from three hours after initial cream/emulsion application with increases in fluorescence intensity measured up to the end of observation at 12 hours.

Various fresh, surplus *ex vivo* human cancer tissues were imaged with the FCE-PDD technique: small-cell lung cancer (SCLC), pharyngeal cancer and bladder cancer tissues. These were sourced through various routine resectioning procedures from patients who had given their informed consent. As before, all imaging work was performed under ethical approval from the relevant Research Ethics Committee (REC Reference No. 08/H0719/37). The sources of human cancer tissues imaged in this section were as follows:

i. SCLC and pharyngeal cancer tissues – sourced from the National Heart and Lung Institute, Royal Brompton Hospital, Royal Brompton & Harefield NHS Foundation Trust from Dr Pallav Shah, Consultant Physician and Honorary Senior Lecturer, National Heart and Lung Institute, Imperial College London; and
ii. Bladder cancer tissue – sourced from St Mary's Hospital and Charing Cross Hospital, Imperial College Healthcare NHS Trust as mentioned previously in section 6.2.3.

Resectioned tissues were immediately placed in chilled Hartmann's solution after surgical removal. Thirty minutes or less thereafter, tissues were transferred into a 50 ml incubator flask containing warm Hartmann's and 5-ALA photosensitiser pro-drug (1.0 mM) and placed in an incubator set at 37°C and 5% CO_2. Tissues were removed from the incubator flask at various time intervals for FCE imaging up till a maximum of 120 minutes. Image acquisition lasted about 30 to 45 seconds per sample, and these were immediately returned to warm Hartmann's/5-ALA solution for continued

photosensitiser exposure. All cancer tissue samples showed good correlation with histopathological results (not shown).

6.3.5.1. Small-cell lung cancer tissue

Human small-cell lung cancer tissues were incubated in Hartmann's/5-ALA solution up to a maximum of 120 minutes. The tissues measured 0.3 to 0.5 cm in diameter and were imaged by FCE at various time points throughout incubation: t = 0, 15, 30, 45, 60 and 120 minutes.

Lung cancer tissues exhibited some degree of autofluorescence from the outset of FCE imaging prior to 5-ALA incubation. This was attributed to the presence of pulmonary elastin fibres, which constitute a large percentage of the total protein content present in the lung interstitium (Starcher, 1986). Tissue fluorescence was seen to increase progressively from basal levels with incubation time, most likely due to the rise in amounts of 5-ALA-induced PpIX in tumour cells (refer to Figure 6.8). FCE image quality improved correspondingly, with optimal contrast achieved at around t = 45 minutes. At this time point, cellular-level details were visible in the tissue images with individual cells clearly discernable. Beyond 45 minutes of 5-ALA incubation, image contrast started to deteriorate gradually in line with the drop in fluorescence signal levels – this is observed in the FCE images from time point t = 60 minutes onwards.

Overall, detected PpIX fluorescence in lung tissue reached peak intensity between t = 30 and 60 minutes, as evident from the increase in both mean and maximum fluorescence signal levels measured during this time window (see graph in Figure 6.9). PpIX fluorescence also peaked at identical time points (t = 45 minutes) for both the mean and maximum fluorescence. This was calculated using the Cellvizio Viewer statistical histogram software, which allows for quantification of statistical data from the acquired FCE images.

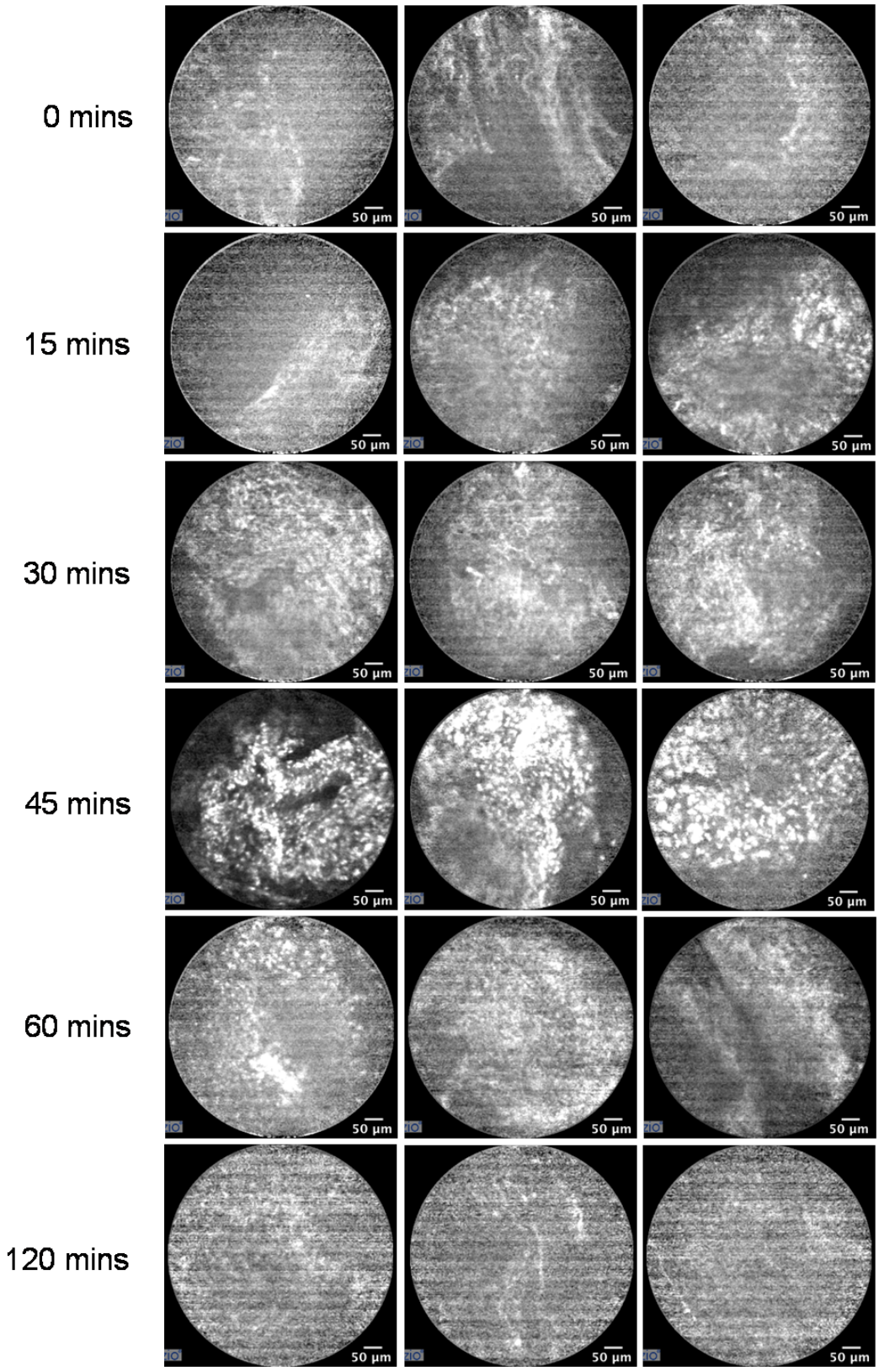


Figure 6.8. Time-lapse FCE images from *ex vivo* human small-cell lung cancer tissue incubated with 5-ALA (1.0 mM) for up to a period of 120 minutes. Detected PpIX fluorescence reached peak intensity between t = 30 and 60 minutes, as evident from the improved image contrast and higher mean/maximum fluorescence during this time window.

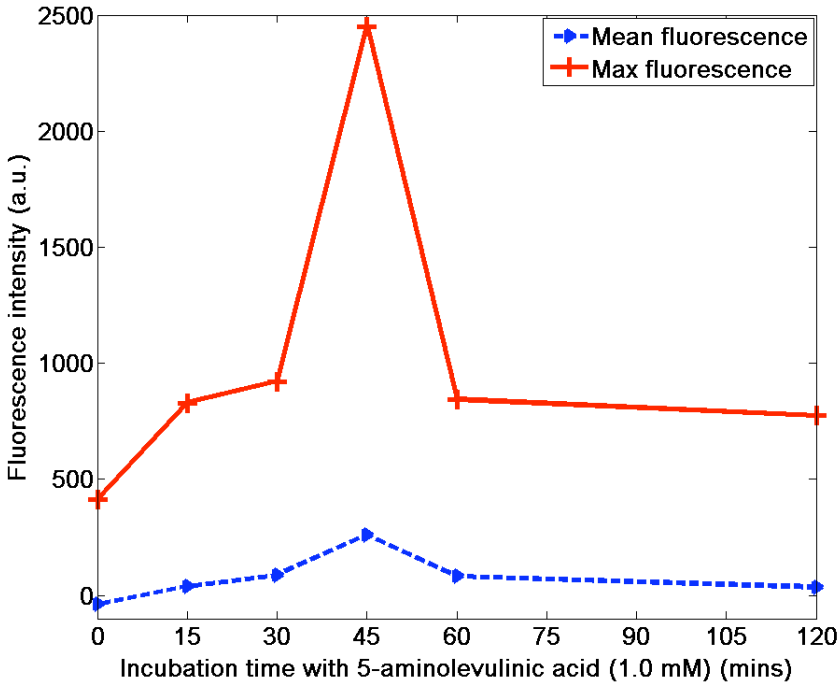


Figure 6.9. Graph showing the mean and maximum values of fluorescence intensities at various FCE imaging time points for 5-ALA-incubated human small-cell lung cancer tissues.

6.3.5.2. Pharyngeal cancer tissue

As with lung cancer tissues, human pharyngeal cancer tissues were incubated similarly in warm Hartmann's solution containing the 5-ALA photosensitiser pro-drug (1.0 mM). Incubation was carried out at 37°C and 5% CO_2 for a total duration of 90 minutes, with the tissues taken out of the incubator flask at 15 or 30 minute intervals for FCE imaging. Pharyngeal cancer tissues obtained were much larger in size compared with lung cancer tissues, measuring 1.0 to 1.5 cm in diameter.

FCE imaging results in Figure 6.10 exhibit a gradual rise in the detected tissue fluorescence from the outset till the end of image acquisition at t = 90 minutes. This led to a consequent improvement in image contrast over time with some tissue structural detail discernible in the FCE images from t = 30 minutes onwards. These are seen as fine tissue striations and are most likely due to the presence of elastic fibres in pharyngeal tissue, which allow for movement and structural support during swallowing and respiration (Kim *et al.*, 1998). The rise in tissue fluorescence was quantified as before using the Cellvizio Viewer statistical histogram software, where mean and maximum values were calculated as shown in the graph in Figure 6.11. Both mean and maximum

fluorescence values displayed similar trends with peak levels attained after about 60 minutes of 5-ALA incubation. This was attributed to the increase in 5-ALA-induced PpIX produced by cells in the imaged cancer tissue over time.

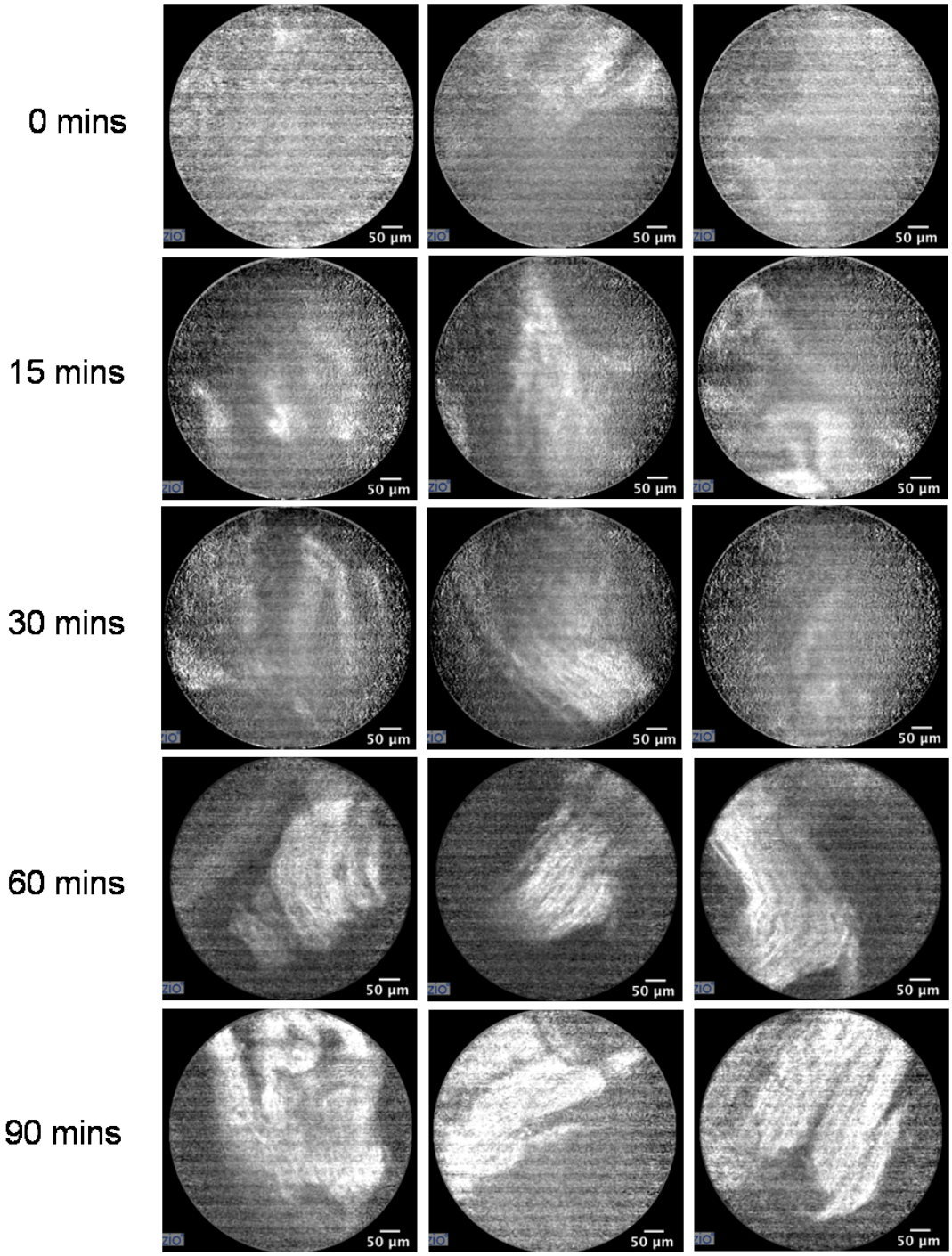


Figure 6.10. Time-lapse FCE images from *ex vivo* human pharyngeal cancer tissue incubated with 5-ALA (1.0 mM) for up to 90 minutes. PpIX fluorescence intensity increased gradually from the start of incubation, with an observable improvement in image contrast and signal to noise ratios over time up until t = 90 minutes.

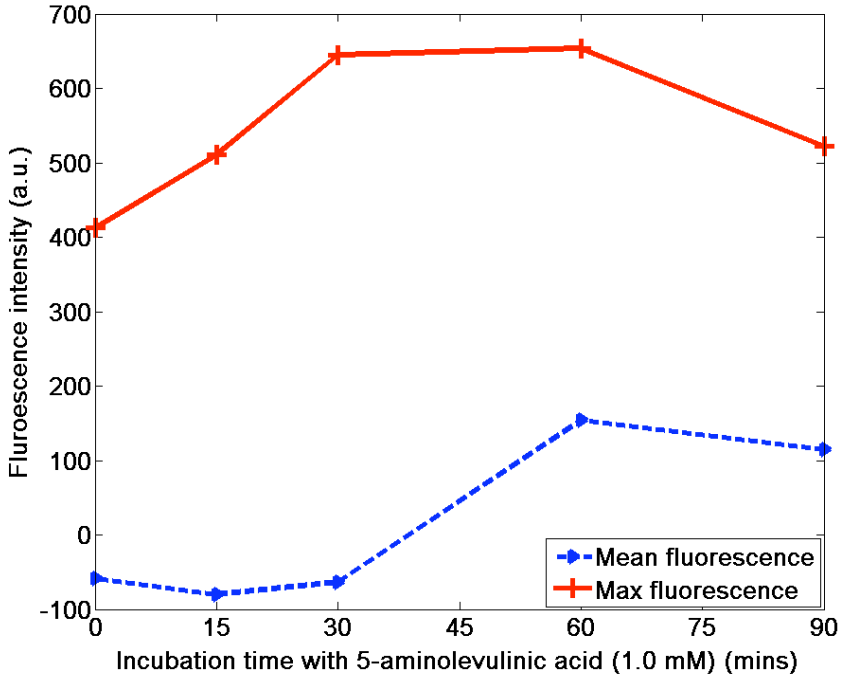


Figure 6.11. Graph showing the mean and maximum values of fluorescence intensities at various FCE imaging time points for 5-ALA-incubated human pharyngeal cancer tissues.

6.3.6. *In vivo* imaging of photosensitised murine tissues

Following on from earlier FCE-PDD imaging experiments involving 5-ALA treated *in vitro* ovarian adenocarcinoma cells and *ex vivo* human cancer tissues, the next stage was *in vivo* validation of the technique on photosensitised tumours in a murine ovarian cancer model. Ethical approval for this section of the study was granted by the UK Home Office under the Animals (Scientific Procedures) Act 1986 (Project License Number PIL 70/22548 – "Immunotherapy and Imaging in Ovarian Cancer").

Six-eight week old SCID-beige mice (n = 2) were chosen as the tumour model, each injected subcutaneously in the upper right thigh with IGROV-1 human ovarian cancer cells ($1x10^7$) cultivated following standard methods. Imaging was performed about ten days after injection of cancer cells, where tumours reached a size of approximately 5.0 mm in diameter. Mice were injected with 5-ALA (250 mg/kg body weight; titrated with sodium hydroxide to pH 6.5 in 1x PBS) intravenously via the tail vein while being anaesthetised by inhalation. All tumour-bearing animals were killed by cervical dislocation before FCE imaging was performed *in vivo* on tumour tissues and normal organs at 90 and 180 minutes after 5-ALA injection. As a positive control (PC), FCE

imaging was performed on the normal organs of a non tumour-bearing naive mouse 120 minutes after 5-ALA injection. A negative control (NC) mouse was also imaged, which did not receive any 5-ALA injection.

Example *in vivo* FCE-PDD imaging results from murine tissue are shown in Figure 6.12, with fluorescence signals quantified using the Cellvizio Viewer statistical histogram software as before (section 6.3.5.1) and presented in graphical form (Figure 6.13). Very low levels of detectable 5-ALA induced PpIX fluorescence signals were seen from subcutaneous IGROV-1 tumours at both the 90-minute (Figure 6.12A) and 180-minute (Figure 6.12H) imaging time points, with mean intensity levels remaining around that measured from the negative control tumour (Figure 6.13, teal dotted line). This was unexpected as the CellvizioGI system's ability to excite and detect PpIX fluorescence was demonstrated using *in vitro* cancer cells and *ex vivo* tissue in preceding sections of this chapter. Various groups have also reported on the fluorescence detection of PpIX at imaging time points between 2 and 5 hours post 5-ALA injection in rat models of ovarian cancer (Major *et al.*, 1997; Chan *et al.*, 2002; Regis *et al.*, 2007). Furthermore, a 250-mg/kg body weight 5-ALA dosage was used in our experiment - this was 2.5 times higher than these studies, implying that correspondingly stronger PpIX signals should be observed. One possible physiological explanation is our choice of the IGROV-1 cell line for tumour induction, whose tumours may not demonstrate effective conversion of 5-ALA to PpIX at high enough levels *in vivo* for detection by our FCE instrument; the three aforementioned groups all used the NuTu-19 human ovarian cancer cell line for tumour induction. Future work will include FCE-PDD imaging experiments using alternative cancer cell lines for further validation of the technique *in vivo*.

Most of the FCE-detected fluorescence came from normal murine tissues. The highest fluorescence signals were seen in kidney images (Figures 6.12C, F and J), due most likely to the excretion of 5-ALA induced PpIX, a large fraction of which is cleared via this organ (Kennedy, 2006). This is seen as a quantifiable increase in fluorescence signal in Figure 6.13 (red solid line), which rises from mean basal levels (about 320 a.u.) in the negative control mouse kidney to a high of 680 a.u. at 180 minutes after 5-ALA injection in the tumour mouse. No fluorescence was visible from the liver images (Figures 6.12D, G and K) of both tumour-bearing and naive animals although a small signal was quantified (Figure 6.13, green dashed-dotted line). This is an interesting result since the

liver was previously found to have five times the rate of PpIX build-up than tumour tissues (Jacques *et al.*, 1995). It could be that PpIX accumulation in the liver and tumours had already reached its peak before the first imaging time point at 90 minutes and was already in the process of being excreted from the animal. Faint signals were visible in the spleen (Figures 6.12B, E and I) - an observation that is corroborated by previous reports of minute PpIX accumulations found in the spleens of 5-ALA treated human patients and animals (van den Boogert *et al.*, 1998; Kennedy, 2006). This is visible as quantifiable PpIX signals from the splenic images, which increases slightly from basal levels at the 90 minute imaging time point and then returns to near-original levels again at 180 minutes (Figure 6.13, blue dashed line). Spleen and liver tissues exhibit lower levels of fluorescence signal intensities at the 180 time point than that recorded from the negative control mouse (refer to Figure 6.13). A likely explanation for this could be the different rates at which PpIX is processed in these organs between the different animals imaged.

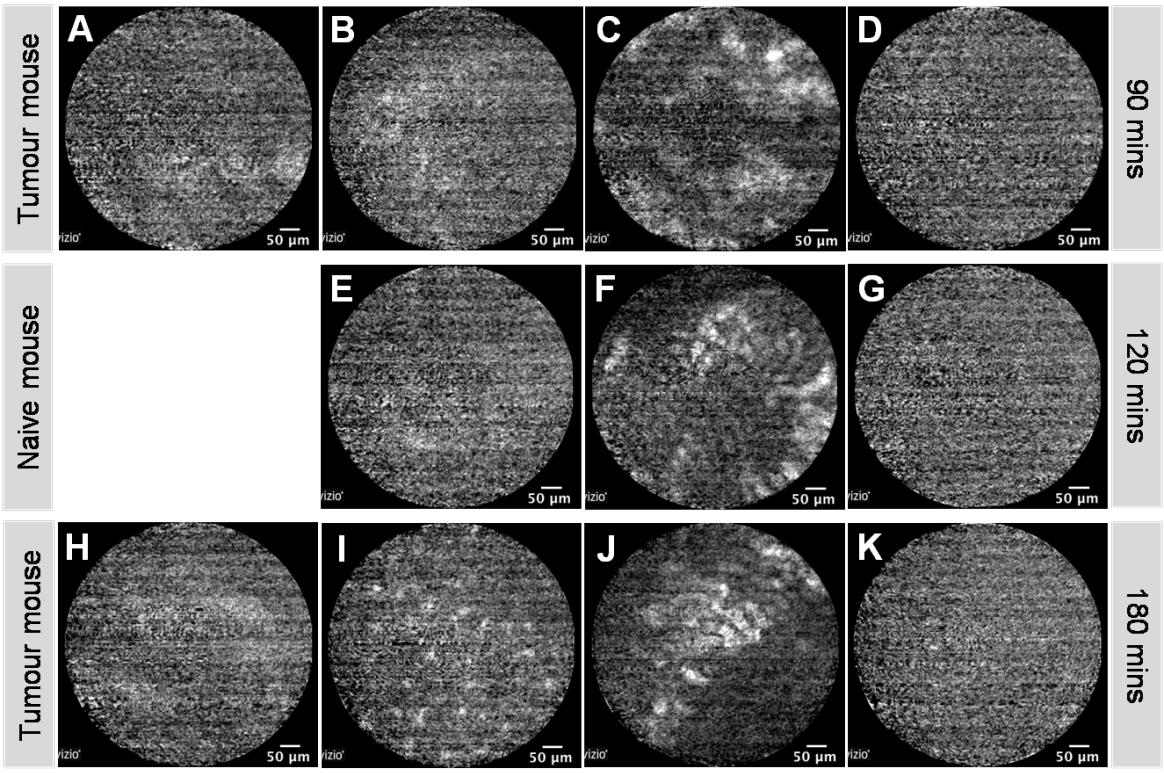


Figure 6.12. Example FCE images of murine healthy and IGROV-1 tumour tissues *in vivo* acquired at different time points after intravenous injection of 5-ALA (250 mg/kg body weight). Tumour mouse (post 90 minutes) – tumour (A), spleen (B), kidney (C), liver (D); Naive mouse (post 120 minutes) – spleen (E), kidney (F), liver (G); Tumour mouse (post 180 minutes) – tumour (H), spleen (I), kidney (J), liver (K).

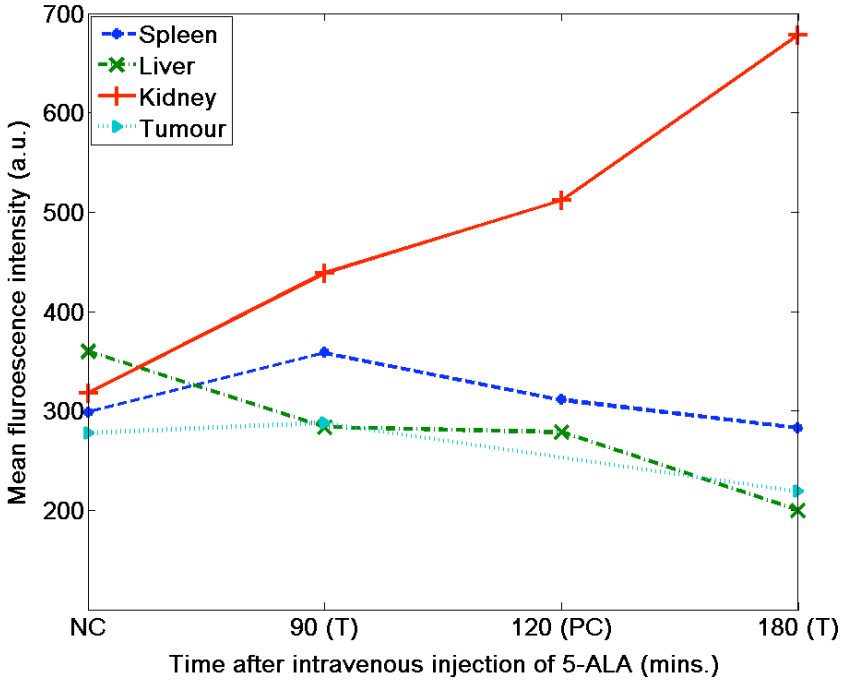


Figure 6.13. Mean fluorescence intensities obtained from FCE images of various photosensitised murine tissues *in vivo* at different time points after intravenous injection of 5-ALA (250 mg/kg body weight). NC: negative control mouse, T: tumour mouse, PC: positive control mouse.

6.4. Probing fluorescent signatures from a tumour-specific PET imaging optical analogue

The possibility of imaging across different resolution scales in conjunction with positron emission tomography (PET) imaging was later explored by applying fluorescence confocal endomicroscopy (FCE) for detection of the tumour-specific fluorescent optical biomarker 2-[*N*-(7-nitrobenz-2-oxa-1,3-diaxol-4-yl)amino]-2-deoxyglucose (2-NBDG). 2-NBDG is a fluorescently labelled deoxyglucose analogous to 2-deoxy-2 [^{18}F] fluoro-D-glucose (FDG), the widely used molecule during whole-body FDG-PET imaging procedures for cancer detection. The motivation behind FDG-PET is that tumours have a higher degree of glucose utilisation compared to normal tissues due to increased metabolic activity. This results in upregulation of cellular intermembrane glucose transporters like GLUT-1 and hexokinase in tumours, leading to an increased accumulation of detectable FDG specifically in these tissues (Gambhir, 2002).

One setback FDG-PET imaging suffers from however is poor spatial resolution (1 to 2 mm) (Weissleder and Pittet, 2008), posing a considerable limitation especially for the purposes of early cancer detection where morphological tissue changes occur at the microscopic levels. The recently developed radiolabeled 2-NBDG optical analogue by Yoshioka and colleagues (Yoshioka *et al.*, 1996) may offer a potential solution: besides being detectable by conventional PET imaging, its detection may also be extended to optical imaging methods such as confocal laser scanning microscopy and FCE. This results in several advantages such as no ionising radiation from the optical imaging procedure, high spatial and temporal resolution, and the possible translation of the technique to minimally invasive and intraoperative settings (Sheth *et al.*, 2009). We applied FCE imaging to determine if cellular level resolution could be achieved using the technique in both 2-NBDG-treated *in vitro* human ovarian cancer cells and a murine model of ovarian cancer *in vivo*.

6.4.1. Instrumentation and imaging procedure

As with previous sections of this chapter, imaging of 2-NBDG fluorescence from *in vitro* human ovarian cancer cell lines and *in vivo* murine tissue was performed with the CellvizioGI FCE system using the GastroFlex Type Z confocal miniprobe. 488 nm (blue light) excitation from the CellvizioGI laser system unit was sufficient to elicit fluorescence emissions from the fluorescent labelled 2-NBDG glucose analogue, which absorbs at 465 - 470 nm and emits fluorescence at around 540 nm (O'Neil *et al.*, 2005; Sheth *et al.*, 2009). Cells were imaged with the FCE confocal miniprobe in their culture dishes whilst placed on top of a fine-adjustment translational stage. The miniprobe was held firmly in place throughout the imaging procedure using a mini V-clamp as before. *In vivo* murine tissues were imaged by hand with the animal carcass secured horizontally on a Styrofoam board with the aid of metal pins.

6.4.2. *In vitro* imaging of fluorescent labelled human ovarian cancer cells

Human ovarian cancer cells used previously, namely OVCAR-5, SKOV-5 and IGROV-1, were incubated under standard conditions in 35 mm plastic cell-culture dishes containing sterile RPMI 1640 media, 10% foetal calf serum (FCS), penicillin-streptomycin antibiotics and the fluorescently labelled deoxyglucose analogue 2-NBDG

(500 nM). 30 minutes after the start of incubation, the growth media was carefully removed using a 1.0 mL pipette and the cells gently washed once with 1x PBS before FCE imaging was performed *in vitro*.

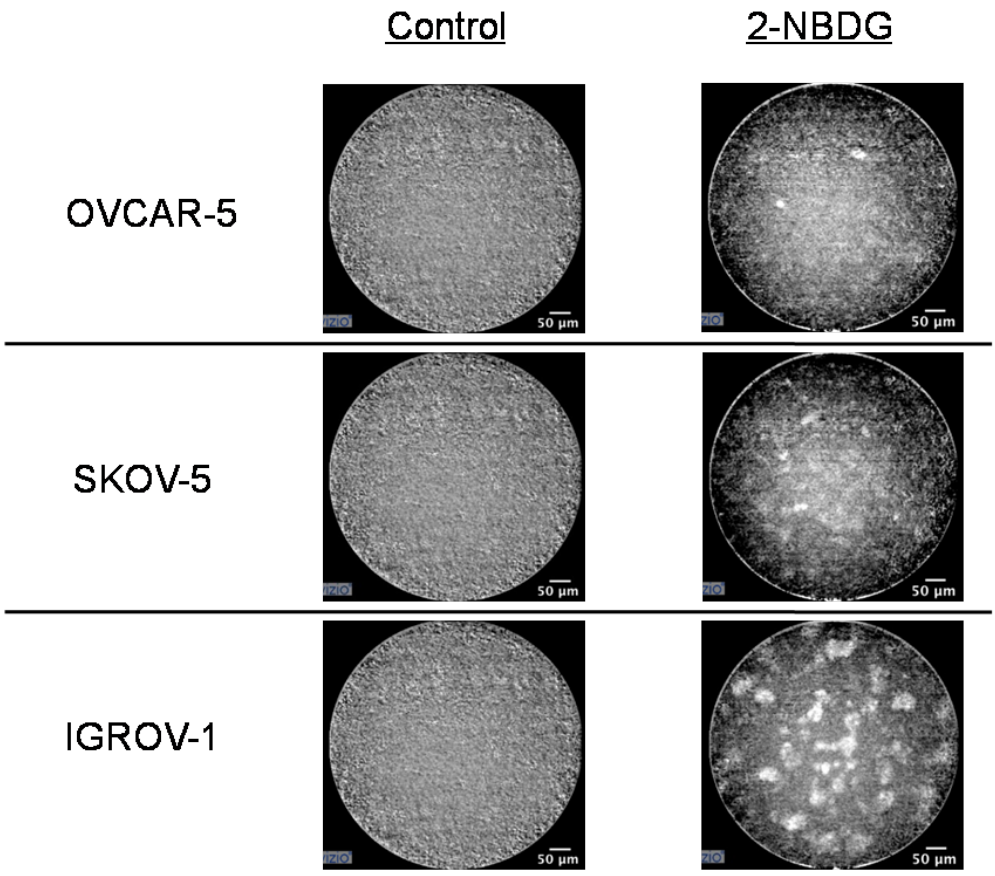


Figure 6.14. FCE images from 3 different human ovarian cancer cell cultures showing either control or fluorescent 2-NBDG-incubated populations incubated for 30 minutes prior to imaging. Uptake of 2-NBDG appears to be highest in IGROV-1 cells, which exhibit the brightest fluorescence out of the three different cell populations.

Results from this imaging experiment are shown in Figure 6.14, where differential uptake of 2-NBDG by the three ovarian cancer cell types is clearly evident. FCE images of 2-NBDG incubated cell lines show a much higher number of fluorescent cells in the IGROV-1 population as compared to the OVCAR-5 and SKOV-5 populations – an indication that 2-NBDG was uptaken the most by IGROV-1 cells. This observation is quantified by calculating the signal to background ratios (SBRs) for each of the three cell types using MatLab as described in section 5.3.1, with greater SBRs signifying higher fluorescence contrast and hence most likely greater 2-NBDG uptake. Results from this

analysis are presented as a bar chart in Figure 6.15, where IGROV-1 FCE images are seen to possess the highest SBRs (average of about 91) compared with OVCAR-5 and SKOV-5 images (average SBRs of about 14 and 24 respectively). Based on these findings, the IGROV-1 cell line was chosen for inducement of subcutaneous tumours in a murine model of ovarian cancer for *in vivo* FCE imaging experiments in the next sub-section.

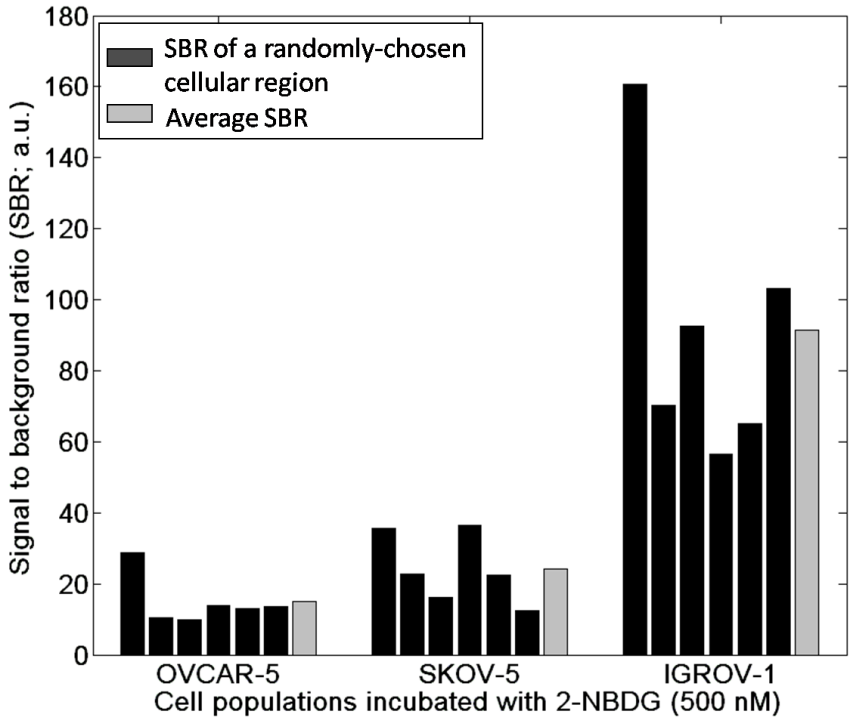


Figure 6.15. Bar chart representing the signal to background ratios (SBRs) from FCE images of three different human ovarian cancer cell populations incubated with 2-NBDG: OVCAR-5, SKOV-5 and IGROV-1.

6.4.3. *In vivo* imaging of tumour-specific fluorescent biomarkers from murine tumour tissue

The ability of FCE imaging to detect tumour-specific fluorescent signatures from biomarkers *in vivo* was investigated using a murine tumour model of ovarian cancer. Ethical approval for the study was granted by the UK Home Office under the Animals (Scientific Procedures) Act 1986 as stated in section 6.3.6. Tumours were induced by subcutaneous injection of IGROV-1 human ovarian cancer cells in anaesthetised SCID/beige mice, with imaging performed about ten days after tumour cell injection.

Before commencing FCE imaging, mice were anaesthetised by inhalation and injected intravenously via the tail vein with 2-NBDG (500 nM in 1x PBS). Three mice were used in this experiment – two tumour-bearing mice, with one serving as the negative control, and another naive non tumour-bearing mouse. All animals were starved for 18 hours prior to dye injection to allow for optimal uptake of the fluorescent 2-NBDG glucose analogue by actively metabolising cells. FCE imaging was performed 20 minutes after intravenous injection of 2-NBDG.

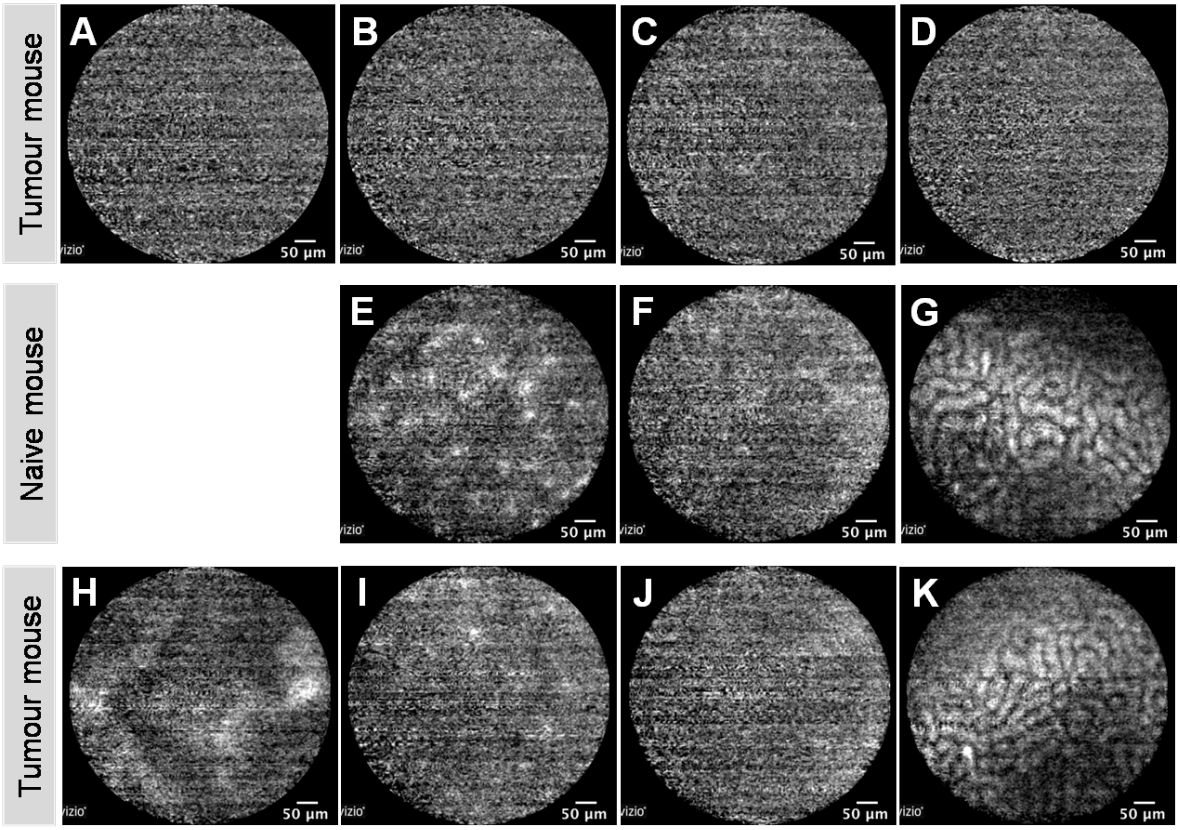


Figure 6.16. Example FCE images of healthy and IGROV-1 tumour murine tissues *in vivo* 20 minutes after intravenous injection of the fluorescent deoxyglucose analogue 2-NBDG. Negative control (NC) tumour mouse - tumour (A), spleen (B), liver (C), kidney (D); Naïve non tumour-bearing mouse – spleen (E), liver (F), kidney (G); Tumour mouse – tumour (H), spleen (I), liver (J), kidney (K).

Figure 6.16 shows FCE imaging results from tumour and normal tissues of 2-NBDG-exposed murine cancer models 20 minutes post-injection. As expected, no detected 2-NBDG fluorescence signals were visible in tissues of the negative control tumour mouse (Figure 6.16A-D) with mean basal fluorescence signals of between 280 to about 350 a.u.,

as quantified using the Cellvizio Viewer statistical histogram software (Figure 6.17). Fluorescence was observed in all other 2-NBDG treated tissues, both tumour and normal, with fluorescent regions seen in all images (Figure 6.16E-K). 2-NBDG treated murine tumour tissues displayed regions of weak fluorescence (Figure 6.16H), shown statistically to only be about 20% brighter than the untreated tumour tissue (336 vs 278 a.u.; Figure 6.17). Splenic tissue exposed to 2-NBDG also exhibited regions of weak fluorescence (Figures 6.16E and I); these appeared similar to the 2-NBDG tumour image in Figure 6.16H with mean fluorescence intensities of between 280 and 369 a.u.. Liver tissues of 2-NBDG treated mice displayed the least fluorescence (Figures 6.16F and J), with mean fluorescence intensities similar for both treated and untreated mice (mean intensity average of 334 a.u.; refer to Figure 6.17). The highest 2-NBDG fluorescent signals were seen in the kidneys (Figure 6.16G and K), which are one of the main sites for glucose clearance. Mean fluorescence intensity in the kidney tissues sampled had values of 671 and 655 a.u. for the naive and tumour mouse respectively (Figure 6.17).

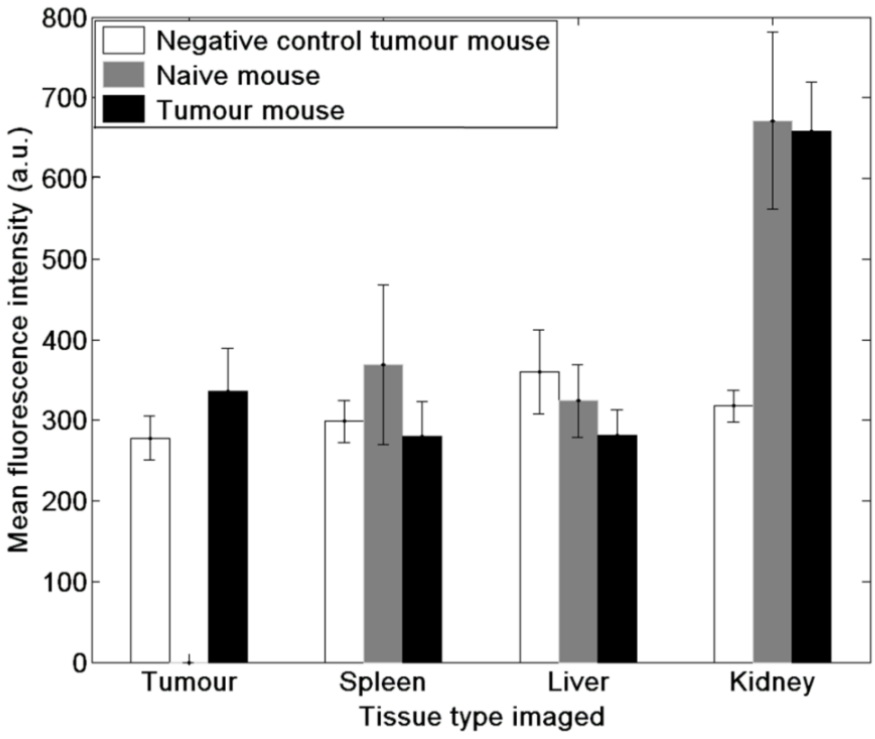


Figure 6.17. Bar chart representing mean fluorescence intensities from FCE images of various *in vivo* murine tissues obtained 20 minutes after intravenous injection of 2-NBDG (500 nM).

Various fluorescence studies have shown that tumour tissues display more rapid uptake of 2-NBDG as a result of higher metabolic activity compared to normal tissue, evidenced by increased DNA and protein synthesis and glycolysis (Warburg, 1956; Weber, 1977). This feature is widely exploited in FDG-PET imaging to distinguish between tumour and healthy tissues (O'Neil *et al.*, 2005; Nitin *et al.*, 2009). However, *in vivo* FCE imaging performed in this study on normal and tumour murine tissues demonstrated otherwise: 2-NBDG fluorescence was visible in both murine tumour tissue as well as in normal tissues of the spleen, liver and kidney. The non-specific 2-NBDG accumulation may have most likely occurred due to relatively similar levels of metabolic activity in both tumours and normal murine tissue types. Tumours exhibit different phases of growth, with exponential growth rates at the outset and more linear growth thereafter (Mackillop, 1990; Simeoni *et al.*, 2004). It was probable that the IGROV-1-induced murine tumour had already reached its linear growth phase ten days after initial cancer cell injection; this is the time-point when our FCE/2-NBDG experiment was performed. Barring further studies on IGROV-1 tumour growth kinetics and optimal 2-NBDG imaging time points, the low levels of detected fluorescence and poor image contrast seen in the FCE images (Figure 6.16) indicate that 2-NBDG is not an ideal tumour marker candidate for the purposes of cancer detection with FCE at this point.

6.5. Multimodal endoscopic viewfinder imaging technique

Imaging experiments performed up till this point in the thesis explored three different optical techniques for early cancer detection and diagnosis, namely multispectral fluorescence imaging (MFI), hyperspectral reflectance imaging (HRI) and fluorescence confocal endomicroscopy (FCE). To briefly recapitulate, MFI and HRI are both imaging-based spectroscopic approaches, allowing the sampling of fluorescence and diffuse reflectance signals respectively from larger regions of tissue compared with conventional methods. Since there is no direct tissue contact with the imaging probe positioned a few centimetres away from the interrogated region, probe-tissue contact pressure effects are also effectively eliminated. FCE is a point-based imaging modality that captures high resolution, cellular-level detail with image qualities approaching that of histology, permitting morphological and functional assessment of tissue disease states in real time. With the diagnostic effectiveness of each technique validated in earlier chapters

of this thesis, we next set out to apply them in concert to demonstrate a multimodal endoscopic viewfinder (MEV) imaging approach for the *in vivo* detection and diagnosis of tissue disease states.

Individually, each imaging technique has its limitations. Although MFI and HRI can effectively visualise the "big picture" through regional sampling of *in vivo* tissues, neither of these techniques have the spatial resolution to elucidate minute cellular-level tissue surface details where the earliest cancerous changes first occur. Conversely, FCE has high spatial resolving power and the ability to visualise tissues at the fine cellular level. Being a point imaging method however, it suffers from the inherent problems of such an approach e.g. the need to acquire data from multiple points to allow for sampling of a larger tissue area, hence leading to longer procedure times and also a high rate of sampling error due to the random nature of the data acquisition process. In combination therefore, these three techniques complement each other, resulting in a holistic and comprehensive imaging approach for early cancer detection and diagnosis without the need for tissue biopsies.

Figure 6.18 shows a series of images collected from separate imaging experiments to illustrate the proposed the MEV imaging technique. In line with routine practice, an endoscopist first employs conventional white-light endoscopic (WLE) imaging to survey the suspect diseased tissue region (Figure 6.18B). With the system in MFI/HRI mode, real-time image processing with the FR-IsoMap algorithm identifies a suspect cancerous lesion on the tissue mucosa (Figure 6.18C). The lesion appears a different colour in the FR-IsoMap colour image due to it possessing different spectral properties from the healthy surrounding tissue. For real-time histological confirmation, FCE imaging is next performed on the suspect lesion. This is done by inserting the FCE confocal miniprobe through the endoscope's accessory channel (Figure 6.18A) and placing it in gentle contact with the tissue surface. The resulting *in vivo* FCE images provide cellular-level morphological confirmation of the tissue disease state akin to a 'virtual histology' (see example in Figure 6.18D), thus allowing the clinician to swiftly decide upon the next course of therapeutic action.

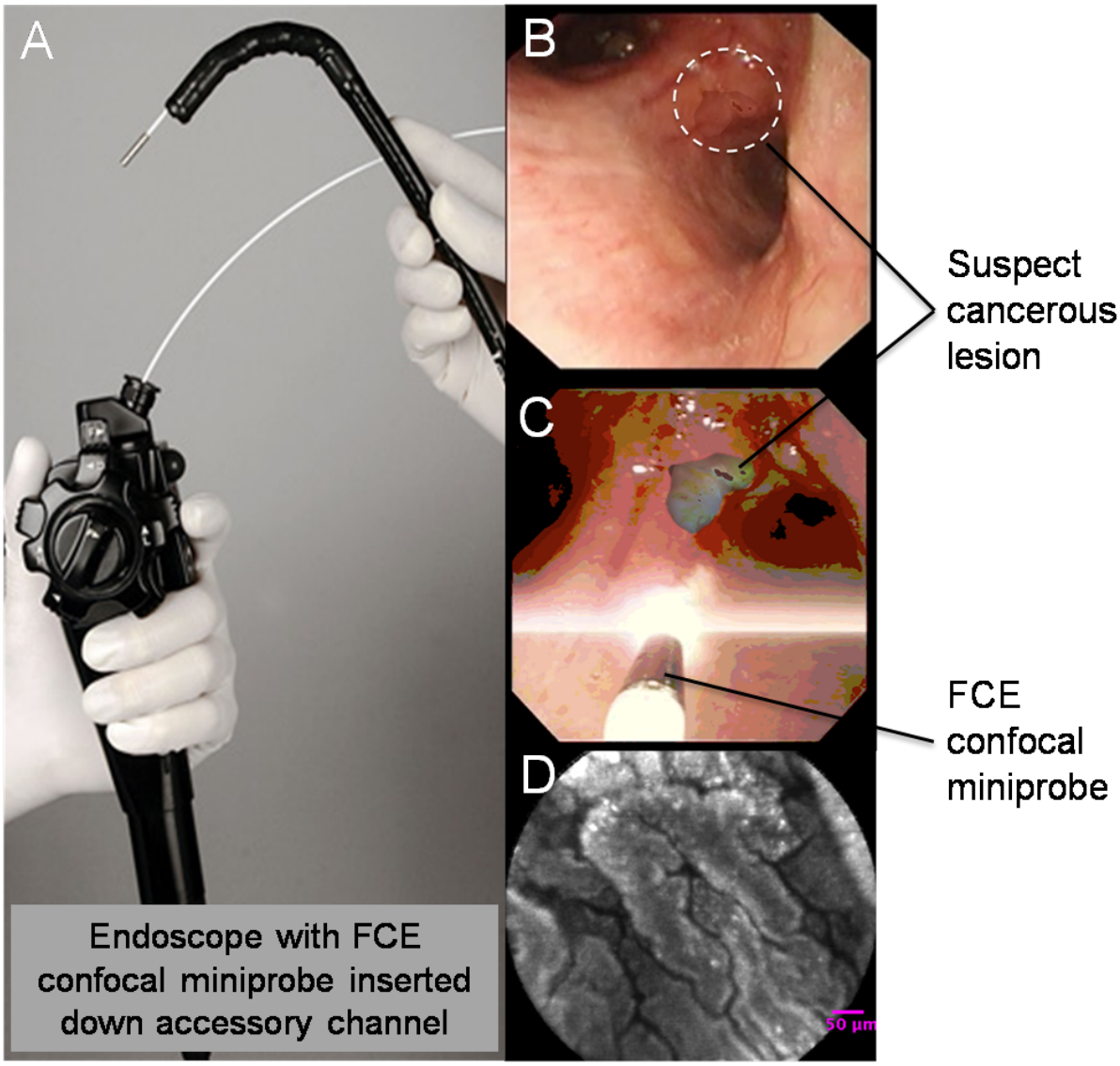


Figure 6.18. Images illustrating the proposed multimodal endoscopic viewfinder (MEV) imaging technique. The confocal miniprobe is inserted down the accessory channel of a flexible endoscope during *in vivo* FCE tissue imaging (A). Initial white light endoscopic (WLE) imaging shows a suspect cancerous lesion (dashed white circle) (B). This lesion appears in the FR-IsoMap image as a different colour from the surrounding healthy tissue due to differences in spectral properties; the tip of the FCE miniprobe is visible in the field of view as it approaches the lesion (C). Example FCE image of the interrogated cancerous lesion tissue providing real-time disease confirmation via a 'virtual histology' (D). Note that these images are compiled from different experiments and were not acquired from an actual MEV imaging procedure. (Figure 6.18A adapted from MedGadget.com; Figures 6.18B and C courtesy of Mr Richard Newton, Clinical Research Fellow, Imperial College London)

6.5.1. Instrumentation and imaging procedure

The MEV imaging approach employed two previously demonstrated systems for tissue diagnosis: 1) the supercontinuum fibre laser-based imaging system as described in section 4.2 of the thesis for MFI and HRI procedures, and 2) the CellvizioGI fluorescence confocal endomicroscope system detailed earlier in section 5.4 for FCE imaging. During the MEV imaging procedure, MFI and HRI were the first imaging techniques to be applied followed by FCE in this order. The rationale behind this two-part approach was that larger tissue regions measuring approximately 10 cm squared area are imaged first using MFI and HRI for the identification of suspect lesional areas, before zooming in to these lesions using FCE to allow for more finely detailed μm-scale histological assessment for disease confirmation.

MFI and HRI were performed using a rigid laparoscope with the supercontinuum laser emitting at 16 excitation wavelengths between 416 and 518 nm, each possessing bandwidths of about 4 to 8.5 nm (see Figure 6.19). For MFI, a 600 nm longpass filter was included to only allow transmission and recording of fluorescent signals above this emission wavelength; no longpass filter was used during HRI. FCE imaging was performed with the GastroFlex Type Z fibered confocal miniprobe, which transmitted 488 nm laser excitation from the laser system unit to the imaged tissue sample.

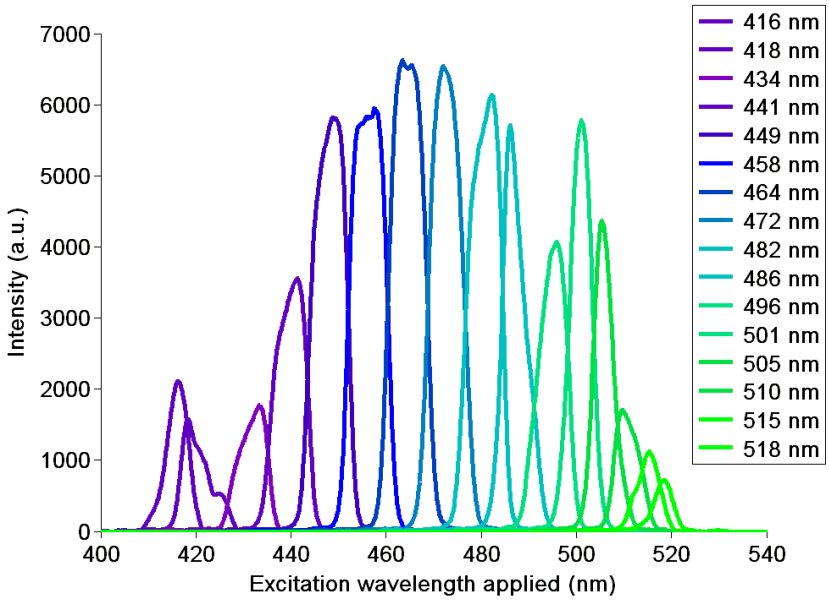


Figure 6.19. The 16 excitation wavelengths applied during MFI and HRI for eliciting respective fluorescence and diffuse reflectance signals from tissues during MEV imaging.

6.5.2. Viewfinder imaging of photosensitised *ex vivo* bladder cancer tissue

Ex vivo human bladder tissue samples imaged during the endoscopic viewfinder imaging procedure were excised via cold-cut biopsy from a patient undergoing a routine TURBT procedure for bladder cancer surveillance as in section 6.2.3.2. Informed consent was obtained before surgery and all imaging work was performed under ethical approval as before (REC Reference No. 08/H0719/37). A total of five bladder tissue samples with different disease conditions were imaged *ex vivo*: two healthy samples, two tumour samples and one necrotic tumour sample, each measuring approximately 0.5 to 1.5 cm in diameter. The tissues were incubated with Hartmann's solution containing 5-ALA (1.0 mM) at 37°C temperature and 5% CO_2 for 60 minutes, within half an hour of surgical removal from the patient.

For MFI and HRI experiments, *ex vivo* human bladder tissues were placed on top of a non-reflective black plastic tray with the tip of the laparoscope positioned about 70 mm above it during data acquisition. The laparoscope served the dual function of delivering the spectrally filtered excitation light to the tissue samples as well as for collection of emitted fluorescence and diffuse reflected signals. For FCE imaging experiments, the bladder tissues were imaged by hand with the confocal miniprobe in gentle contact with the tissue. As before, extra care had to be taken to ensure the right amount of contact pressure was applied by the confocal miniprobe tip on the surface of the tissue for obtaining optimal focus and image quality and contrast. The tissue sampling arrangement for MEV imaging is MFI and HRI first followed by FCE, with the ensuing imaging results presented in this order.

Results from MFI of the *ex vivo* bladder tissues are presented in Figure 6.20 as a graph of fluorescence spectra normalised by area under the curve against the corresponding excitation wavelengths applied. Between the excitation wavelengths of about 416 and 443 nm, 5-ALA-treated tumour and necrotic tumour tissues displayed the highest relative amounts of fluorescence. This is most likely due to the 5-ALA-induced production of protoporphyrin IX (PpIX; 400 to 450 nm absorption maxima), which has been previously shown to accumulate preferentially in tumour cells and tissues. Lower relative fluorescent signals were seen in the 5-ALA-treated healthy tissue and non-treated healthy and tumour tissues. This was possibly as a result of no to very little accumulation of the

fluorescent PpIX photosensitiser. Above 443 nm, tissue samples exhibited a higher relative amount of autofluorescence signals overall. However instead of 5-ALA-treated tissues showing higher relative levels of fluorescence, it was the untreated tissue samples this time round between the excitation wavelength range of 443 to 486 nm. A possible explanation for this is additional contributions to the overall detected fluorescence signal by endogenous tissue fluorophores present in bladder tissue such as flavin adenine dinucleotide (FAD), elastin and the lipopigments. Note that this is the case due to the normalisation of the spectra so that the areas under the curve are equal, and the actual amounts of fluorescence emitted by the samples is not comparable. Both healthy bladder tissue samples displayed higher relative fluorescence levels at around the 449 to 472 nm excitation range, most likely due to emission from FAD, which is characteristic of such actively metabolising healthy tissues. Conversely, tumour and necrotic tumour tissue exhibited lower relative fluorescence at this excitation range.

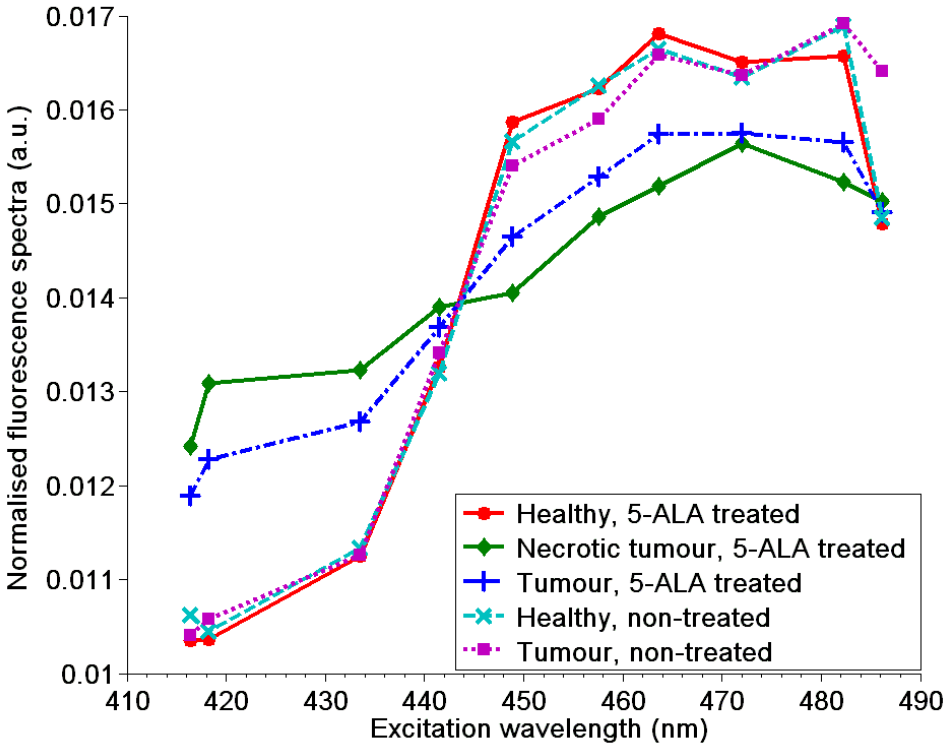


Figure 6.20. Graph of normalised fluorescence spectra plotted against excitation wavelength for respective 5-ALA- and non photosensitiser-treated *ex vivo* human bladder tissue samples with various disease conditions.

HRI results obtained from the *ex vivo* bladder tissues proved inconclusive, with no significant differences observed in terms of diffuse reflectance spectra between the

samples. Diffuse reflectance signals are affected to a considerable extent by the oxyhaemoglobin (HbO) and deoxyhaemoglobin (HbR) content of tissues, which serve as strong light absorbers especially in the visible range of the electromagnetic spectrum (400 to 700 nm). Changes in the relative concentrations of these chromophores often reflect changes in the physiological and pathological conditions of a particular organ or tissue region. Results from HRI consequently imply the need to image live tissues *in vivo*, i.e. ones with an active blood supply and circulation. This would allow detection of viable differences in the diffuse reflectance spectra between tumour and healthy tissues owing to variations in mucosal vasculature and associated haemoglobin content. As such, we expect to achieve effective discrimination between tumour and healthy tissues with our HRI approach *in vivo in situ*.

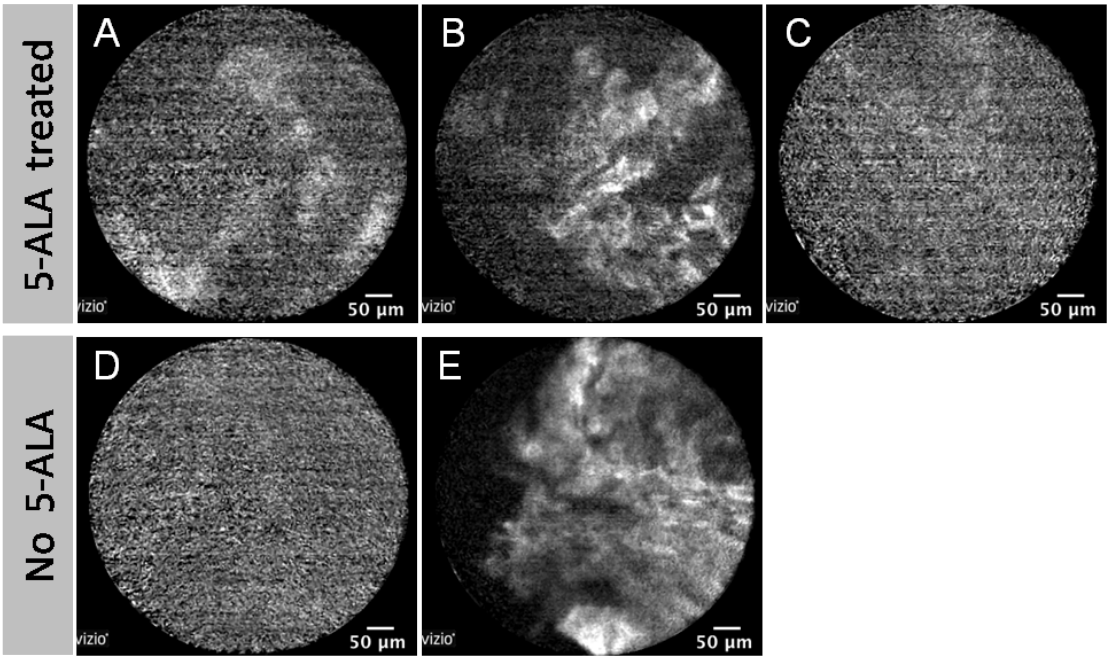


Figure 6.21. Example FCE images of 5-ALA treated and untreated *ex vivo* human bladder tissue after 60 minutes of incubation at 37°C temperature and 5% CO_2: 5-ALA treated tumour tissue (A); 5-ALA treated necrotic tumour tissue (B); 5-ALA treated healthy tissue (C); untreated normal tissue (D); untreated necrotic tumour tissue (E).

FCE images of 5-ALA-treated and untreated *ex vivo* bladder tissues in Figure 6.21 are included to demonstrate the cellular-level diagnostic information that can be obtained after follow-up FCE imaging in the second part of the MEV imaging approach. Regions of bright fluorescence are visible in the 5-ALA-treated *ex vivo* tumour and necrotic

tumour tissues (Figure 6.21A and B), implying the occurrence of PpIX synthesis in these tissues even under such less-than-optimal physiological conditions. We would therefore anticipate stronger PpIX fluorescence detected and hence achieve better imaging contrast during future *in vivo* FCE imaging procedures of a similar nature.

6.6. Summary

Initial experiments in this chapter have established AO as the optimal contrast agent for fluorescence confocal endomicroscopy (FCE) imaging using *ex vivo* porcine tissues. AO was subsequently applied to FCE imaging of *ex vivo* human ovarian cancer and bladder cancer tissues, which resulted in the successful characterisation of cancer tissue morphology. This demonstrated the possibility of performing FCE imaging for real-time intrasurgical histopathology.

FCE was next explored as a photodynamic diagnostic (PDD) modality during FCE-PDD imaging of 5-ALA photosensitised *in vitro* human ovarian cancer cell lines, *ex vivo* human pharyngeal, bladder and small-cell lung cancer tissues and *in vivo* murine tumour tissues. From time-lapse FCE-PDD experiments of *in vitro* cell lines and *ex vivo* tissues, the possibility of detecting PpIX fluorescence by the system was demonstrated and the optimal imaging time window of highest PpIX fluorescence was established for each imaging sample. *In vivo* murine FCE-PDD imaging results were not a good reflection of that obtained *in vitro* and *ex vivo* however. This was possibly due to the use of a different cell line for tumour inducement, IGROV-1, compared to other similar successful studies in the literature.

The use of FCE as a complementary technique to FDG-PET imaging was investigated using the fluorescent 2-NBDG glucose molecule analogous to FDG. IGROV-1 ovarian cancer cells showed good uptake of 2-NBDG *in vitro* and were subsequently used for *in vivo* tumour inducement in a murine model. *In vivo* imaging results however showed non-specific accumulation of 2-NBDG in both normal and tumour tissues, possibly due to similar metabolic activity in the two tissue types. With better understanding of tumour growth kinetics and optimal imaging time points, we expect the utility of FCE/2-NBDG imaging to be fully realised as an effective means of cancer detection *in vivo*.

As a conclusion to the chapter, the combined application of multispectral fluorescence imaging (MFI), hyperspectral reflectance imaging (HRI) and FCE as a multimodal endoscopic viewfinder (MEV) imaging approach was proposed. This novel imaging concept was demonstrated on 5-ALA photosensitiser-treated healthy and cancerous human bladder tissue as a possible technique for early cancer diagnosis.

6.7. References

Bartošová J, Hrkal Z. Accumulation of protoporphyrin-IX (PpIX) in leukemic cell lines following induction by 5-aminolevulinic acid (ALA). *Comparative Biochemistry and Physiology - Part C: Toxicology and Pharmacology* 2000;**126(3)**:245-252.

van den Boogert J, van Hillegersberg R, de Rooij FWM, de Bruin RWF, Edixhoven-Bosdijk A, Houtsmuller AB, Sierseme PD, Wilson JHP, Tilanus HW. 5-Aminolaevulinic acid-induced protoporphyrin IX accumulation in tissues: pharmacokinetics after oral or intravenous administration. *Journal of Photochemistry and Photobiology B: Biology* 1998;**44(1)**:29-38.

Bordier B, Mazerolles C, Malavaud B. Photodynamic diagnosis in non-muscle-invasive bladder cancer. *European Urology Supplements* 2010;**9(3)**:411-418.

Chan JK, Monk BJ, Cuccia D, Pham H, Kimel S, Gu M, Hammer-Wilson MJ, Liaw LH, Osann K, DiSaia PJ, Berns M, Tromberg B, Tadir Y. Laparoscopic photodynamic diagnosis of ovarian cancer using 5-aminolevulinic acid in a rat model. *Gynecologic Oncology* 2002;**87(1)**:64-70.

Claydon PE, Ackroyd R. 5-Aminolaevulinic acid-induced photodynamic therapy and photodetection in Barrett's esophagus. *Diseases of the Esophagus* 2004;**17(3)**:205-212.

Csanády M, Kiss JG, Iván L, Jóri J, Czigner J. ALA (5-aminolevulinic acid)-induced protoporphyrin IX fluorescence in the endoscopic diagnostic and control of pharyngo-laryngeal cancer. *European Archives of Otorhinolaryngology* 2004;**261(5)**:262-266.

Denzinger S, Burger M. Photodynamic diagnostics of bladder tumors. *Current Urology Reports* 2008;**9(2):**101-105.

D'Hallewin MA, Kamuhabwa AR, Roskams T, De Witte PA, Baert L. Hypericin-based fluorescence diagnosis of bladder carcinoma. *BJU International* 2002;**89(7)**:760-763.

Dougherty TJ, Henderson BW, Gomer CJ, Jori G, Kessel D, Korbelik M, Moan J, Peng Q. Photodynamic therapy. *Journal of the National Cancer Institute* 1998;**90(12)**:889-905.

El-Sharabasy MMH, El-Waseef AM, Hafez MM, Salim SA. Porphyrin metabolism in some malignant diseases. *British Journal of Cancer* 1992;**65**:409–412.

Endlicher E, Messmann H. Photodynamic diagnosis in the gastrointestinal tract. *Gastrointestinal Endoscopy Clinics of North America* 2004;**14**:475-485.

Frei KA, Bonel HM, Frick H, Walt H, Steiner RA. Photodynamic detection of diseased axillary sentinel lymph node after oral application of aminolevulinic acid in patients with breast cancer. *British Journal of Cancer* 2004;**90(4)**:805-809.

Gambhir SS. Molecular imaging of cancer with positron emission tomography. *Nature Reviews Cancer* 2002;**2**:683-693.

Hamad LO, Vervoorts A, Hennig T, Bayer R. Ex vivo photodynamic diagnosis to detect malignant cells in oral brush biopsies. *Lasers in Medical Science* 2010;**25(2)**:293-301.

Henderson BW, Gollnick SO. Mechanistic principles of photodynamic therapy. In: *Biomedical Photonics Handbook* (Vo-Dinh T, ed). Boca Raton: CRC Press. 2003:**36**.

van Hillegersberg R, Van den Berg JW, Kort WJ, Terpstra OT, Wilson JH. Selective accumulation of endogenously produced porphyrins in a liver metastasis model in rats. *Gastroenterology* 1992;**103(2)**:647-651.

Jacques SL, Rodriguez T, Schwartz J. Kinetics of ALA-induced protoporphyrin IX accumulation in the liver, skin, and tumor of a rat model. *Proceedings of SPIE* 1995; **2392**:1–8.

Karrer S, Abels C, Szeimies RM, Bäumler W, Dellian M, Hohenleutner U, Goetz AE, Landthaler M. Topical application of a first porphycene dye for photodynamic therapy - penetration studies in human perilesional skin and basal cell carcinoma. *Archives of Dermatology Research* 1997;**289(3)**:132-137.

Kelty CJ, Brown NJ, Reed MWR, Ackroyd R. The use of 5-aminolaevulinic acid as a photosensitiser in photodynamic therapy and photodiagnosis. *Photochemical and Photobiological Sciences* 2002;**1**:158–168.

Kennedy JC. Introduction. In: *Photodynamic Therapy with ALA – A Clinical Handbook* (Pottier R, Krammer B, Stepp H, Baumgartner R, eds). Cambridge: The Royal Society of Chemistry. 2006;**1**:1-13.

Kennedy JC, Pottier RH. Endogenous protoporphyrin IX, a clinically useful photosensitizer for photodynamic therapy. *Journal of Photochemistry and Photobiology B* 1992;**14(4)**:275-292.

Kim SM, McCulloch T, Rim K. Evaluation of the viscoelastic properties of pharyngeal tissue. *Tissue Engineering* 1998;**4(4)**:389-401.

Kondo M, Hirota N, Takaoka T, Kajiwara M. Heme-biosynthetic enzyme activities and porphyrin accumulation in normal liver and hepatoma cell lines of rat. *Cell Biology and Toxicology* 1993;**1**:95-105.

Ladner DP, Steiner RA, Allemann J, Haller U, Walt H. Photodynamic diagnosis of breast tumours after oral application of aminolevulinic acid. *British Journal of Cancer* 2001;**84(1)**: 33–37.

Lin MG, Yang TL, Chiang CT, Kao HC, Lee JN, Lo W, Jee SH, Chen YF, Dong CY, Lin SJ. Evaluation of dermal thermal damage by multiphoton autofluorescence and second-harmonic-generation microscopy. *Journal of Biomedical Optics* 2006;**11(6)**:064006.

Löning M, Diddens H, Küpker W, Diedrich K, Hüttmann G. Laparoscopic fluorescence detection of ovarian carcinoma metastases using 5-aminolevulinic acid-induced protoporphyrin IX. *Cancer* 2004;**100(8)**:1650-1656.

Mackillop WJ. The growth kinetics of human tumours. *Clinical Physics and Physiological Measurement* 1990;**11 Suppl. A**:121- 123.

Maisch T, Santarelli F, Schreml S, Babilas P, Szeimies RM. Fluorescence induction of protoporphyrin IX by a new 5-aminolevulinic acid nanoemulsion used for photodynamic therapy in a full-thickness ex vivo skin model. *Experimental Dermatology* 2010;**19**:e302-e305.

Major AL, Rose GS, Chapman CF, Hiserodt JC, Tromberg BJ, Krasieva TB, Tadir Y, Haller U, DiSaia PJ, Berns MW. In vivo fluorescence detection of ovarian cancer in the NuTu-19 epithelial ovarian cancer animal model using 5-aminolevulinic acid (ALA). *Gynecologic Oncology* 1997;**66(1)**:122-132.

Mayinger B, Neidhardt S, Reh H, Martus P, Hahn EG. Fluorescence induced with 5-aminolevulinic acid for the endoscopic detection and follow-up of esophageal lesions. *Gastrointestinal Endoscopy* 2001;**54(5)**:572-578.

Mayinger B, Reh H, Hochberger J, Hahn EG. Endoscopic photodynamic diagnosis: oral aminolevulinic acid is a marker of GI cancer and dysplastic lesions. *Gastrointestinal Endoscopy* 1999;**50(2)**:242-246.

Nitin N, Carlson AL, Muldoon T, El-Naggar AK, Gillenwater A, Richards-Kortum R. Molecular imaging of glucose uptake in oral neoplasia following topical application of fluorescently labelled deoxy-glucose. *International Journal of Cancer* 2009;**124**:2634-2642.

O'Neil RG, Wu L, Mullani N. Uptake of a fluorescent deoxyglucose analog (2-NBDG) in tumour cells. *Molecular Imaging and Biology* 2005;**7**:388-392.

Peng Q, Berg K, Moan J, Kongshaug M, Nesland JM. 5-aminolevulinic acid-based photodynamic therapy: principles and experimental research. *Photochemistry and Photobiology* 1997;**65(2)**:235-251.

Regis C, Collinet P, Farine MO, Mordon S. Comparison of aminolevulinic acid- and hexylester aminolevulinate-induced protoporphyrin IX fluorescence for the detection of ovarian cancer in a rat model. *Photomedical Laser Surgery* 2007;**25(4)**:304-311.

Rubino GF, Rasetti L. Porphyrin metabolism in human neoplastic tissues. *Panminerva Medica* 1966;**8**:290-292.

Schoenfeld N, Mamet R, Leibovici L, Epstein O, Teitz Y, Atsmon A. Growth rate determines activity of porphobilinogen deaminase both in nonmalignant and malignant cell lines. *Biochemical Medicine and Metabolic Biology* 1988;**40(2)**:213-217.

Sheth RA, Josephson L, Mahmood U. Evaluation and clinically relevant applications of a fluorescent imaging analog to fluorodeoxyglucose positron emission tomography. *Journal of Biomedical Optics* 2009;**14(6)**:064014.

Simeoni M, Magni P, Cammia C, De Nicolao G, Croci V, Pesenti E, Germani M, Poggesi I, Rocchetti M. Predictive pharmacokinetic-pharmacodynamic modeling of tumor growth kinetics in xenograft models after administration of anticancer agents. *Cancer Research* 2004;**64(3)**:1094-1101.

Starcher BC. Elastin and the lung. *Thorax* 1986;**41**:577-585.

Vo LT, Anikijenko P, McLaren WJ, Delaney PM, Barkla DH, King RG. Autofluorescence of skin burns detected by fiber-optic confocal imaging: evidence that cool water treatment limits progressive thermal damage in anesthetized hairless mice. *Journal of Trauma* 2001;**51(1)**:98-104.

Vrouenraets MB, Visser GW, Snow GB, van Dongen GA. Basic principles, applications in oncology and improved selectivity of photodynamic therapy. *Anticancer Research* 2003;**23(1B)**:505-522.

Warburg O. On the origin of cancer cells. *Science* 1956;**125**:309-314.

Weber G. Enzymology of cancer cells. *New England Journal of Medicine* 1977;**296**:541-555.

Weir MM, Vernon DI, Brown SB. Influence of serum proteins on the accumulation of aminolaevulinic acid-induced protoporphyrin IX in cells in culture. *Proceedings of SPIE* 1995;**2371**:40-44.

Weissleder R, MJ Pitett. Imaging in the era of molecular oncology. *Nature* 2008;**452**:580-589.

Wilson BC. Photodynamic therapy for cancer: principles. *Canadian Journal of Gastroenterology* 2002;**16(6)**:393–396.

Yoshioka K, Takahashi H, Homma T, Saito M, Oh KB, Nemoto Y, Matsuoka H. A novel fluorescent derivative of glucose applicable to the assessment of glucose uptake activity of Escherichia coli. *Biochimica et Biophysica Acta* 1996;**1289(1)**:5-9.

Zeisser-Labouèbe M, Lange N, Gurny R, Delie F. Hypericin-loaded nanoparticles for the photodynamic treatment of ovarian cancer. *International Journal of Pharmaceutics* 2006;**326(1-2)**:174-181.

Zheng W, Olivo M, Soo KC. The use of digitized endoscopic imaging of 5-ALA-induced PPIX fluorescence to detect and diagnose oral premalignant and malignant lesions in vivo. *International Journal of Cancer* 2004;**110(2)**:295-300.

Zhong W, Celli JP, Rizvi I, Mai Z, Spring BQ, Yun SH, Hasan T. In vivo high-resolution fluorescence microendoscopy for ovarian cancer detection and treatment monitoring. *British Journal of Cancer* 2009;**101(12)**:2015-2022.

7

Conclusions and Future Outlook

The work discussed in this thesis spans three different optical imaging modalities – multispectral fluorescence imaging (MFI), hyperspectral reflectance imaging (HRI) and fluorescence confocal endomicroscopy (FCE) – with accompanying experiments performed within the contexts of early cancer detection and diagnosis. Samples under investigation ranged from fluorescent dye solutions and tissue phantoms to *ex vivo* tissue specimens, finally culminating with *in vivo* work in animal tumour models. Our aim was to establish the clinical utility of these optical imaging techniques as potential 'red flag' and 'optical biopsy' methods for minimally invasive *in vivo in situ* disease monitoring.

The MFI and HRI techniques surveyed in chapters 3 and 4 utilised a custom-built supercontinuum fibre laser system. The system, incorporating either a motor-controlled slit or digital multimirror device (DMD), allows for laparoscopic acquisition of diagnostic images based on the principles of conventional fluorescence spectroscopy (FS) and diffuse reflectance spectroscopy (DRS). Further image processing with the FR-IsoMap data dimensionality reduction technique allowed for selection of the most meaningful data parameters for generation of an RGB colour map of the imaged region. We note that MFI of unstained colorectal tissue samples in chapter 4 did not produce conclusive FR-IsoMap results, possibly as a result of low tissue autofluorescence emissions that were not efficiently captured by our imaging system. This highlights one of the particular difficulties in performing MFI on tissues both *ex vivo* and *in vivo*, a challenge that we believe will be addressed in the near future given more sophisticated detection optics and image processing algorithms.

By spanning the fields of both wide-field macroscopic imaging and localised point-based techniques, our unique MFI and HRI approach allows for the generation of macroscopic 'regional' images whilst taking into account fluorescence and diffuse reflectance signals acquired from the respective tissue regions. Hence, diagnostic information incorporating

spectral properties of each sampled area is relayed to the operator in terms of a more intuitive and qualitative image-based format. Possible correlation of imaging results in the form of FR-IsoMap colour maps with established cancer classification systems such as the Dukes' grading or TNM systems will also potentially allow for greater effectiveness of disease discrimination *in vivo in situ*. We anticipate that our easily-accessible MFI and HRI diagnostic approach to find many applications in the clinic, either as a stand-alone or complementary technique to currently-established clinical imaging modalities such as MRI, PET and CT imaging.

One key challenge we foresee during further development and future implementation of our dual MFI/HRI technique is the difficulty in acquiring large amounts of spectral information *in vivo* for a comprehensive diagnosis. When imaging inside a living patient, it is also inevitable that various image artefacts may arise due to respiratory movements and tissue deformation. For the method to be viable, it is therefore necessary to not only speed up the entire image acquisition process but to also ensure that only the most meaningful and accurate diagnostic data is collected. This can be addressed in the following ways:

i. Complete characterisation of various cancerous tissues with the imaging techniques *ex vivo* before *in vivo* implementation. This would allow for further validation of the techniques and better understanding of signals that would be acquired *in vivo* as well as generation of a comprehensive training set for effective discrimination of tissue states by the FR-IsoMap algorithm;
ii. Using a spectral selection method for choosing only the most diagnostically meaningful spectra to be applied during imaging. An example of this would a Bayesian framework for feature selection (BFFS) previously demonstrated by our group on MFI data (Wood *et al.*, 2008). The method uses receiver operating characteristic (ROC) curves for determining the optimal combination of excitation wavelengths to be applied. This would consequently result in faster acquisition of a smaller *in vivo* image data set yielding the most pertinent data for a more comprehensive diagnosis; and
iii. Performing image registration to allow correct alignment of images from a moving surface. This method is currently being investigated by our group using a customised trinocular (three-channel) rigid endoscope. The unique

approach allows for combined stereoscopic visualisation and multispectral imaging, thereby resulting in simplified navigation and more straightforward 3D identification of tissue regions of interest (Clancy *et al.*, 2010).

Apart from performing additional *ex vivo* tissue characterisation with our dual MFI and HRI technique, future work will also include *in vivo* tissue imaging in animal models of cancer. This is to familiarise ourselves with the detected signals in preparation for future *in vivo in situ* MFI/HRI procedures in patients. Possible modifications to the supercontinuum laser system may also be performed to allow additional modalities such as multispectral polarised light imaging to be carried out. In addition, various parts of the system may be upgraded: e.g. the laser system could be changed to one of a higher power for a greater excitation signal and also a newer, more sensitive camera could be included with the ability to detect lower fluorescence signals than at present.

FCE experiments presented in chapters 5 and 6 have utilised the commercial CellvizioGI system. Previous studies in the literature have applied the technique for 'virtual histology' in a range of different tissue types (refer to section 2.5.4 for more details). Besides characterising the morphology of healthy and cancerous tissues both *ex vivo* and *in vivo*, we have further extended the facility of the technique towards more novel functional imaging applications.

With FCE, we have successfully demonstrated the technique's potential to assess chemotherapy response at the cellular level *in vitro* over a short five-day period. This has implications for ovarian cancer screening, enabling faster knowledge of treatment outcomes than currently employed methods e.g. MRI and the CA-125 tumour marker. Of slight concern however is the application of acridine orange (AO) dye for attaining optimal image contrast during imaging. Although approved by the FDA for use in an endobag (see section 5.4.2 and Tanbakuchi *et al.*, 2010), its recognised cytotoxic properties will still hinder widespread application in patients. As such, additional work has to be carried out to uncover a suitable and less/non-toxic dye substitute, or to evaluate situations where the use of such a mildly toxic agent may still be appropriate *in vivo*.

The use of FCE as a photodynamic diagnostic (PDD) tool was also effectively demonstrated. In line with various reports in the literature, we have managed to observe 5-aminolevulinic (5-ALA)-induced protoporphyrin IX (PpIX) fluorescence from both cells (as previously reported by Bartošová and Hrkal, 2000; Betz *et al.*, 2002) and *ex vivo* tissues (see section 6.3.5 and Karrer *et al.*, 1997; Maisch *et al.*, 2009). Apart from the two *ex vivo* studies mentioned, we have yet to find others in the literature where PpIX was induced *ex vivo* following 5-ALA application. We believe our work on 5-ALA-treated human small cell lung cancer (SCLC) and pharyngeal cancer tissues to be the first example of *ex vivo*-induced PpIX fluorescence detected in cancerous tissues by FCE-PDD. In the process, we have also established a protocol for incubation of *ex vivo* tissues with 5-ALA, which could be extended for the characterisation of other photosensitisers in *ex vivo* tissue.

FCE-PDD results obtained from 5-ALA-treated *in vivo* murine ovarian cancer models were unexpected, with no to very little PpIX signals observed from tumours. We hope to address this in future work by looking at different parameters that may result in a positive PpIX signal, for example:

i. Ensuring tumours are at their most active stage of growth during the time of imaging i.e. the exponential or log phase, for optimal 5-ALA intracellular conversion;
ii. Imaging at different time points below 90 minutes from the start of intravenous injection of 5-ALA. Strong PpIX signals were observed in the healthy kidneys and spleen of the sacrificed animals from 90 minutes after 5-ALA injection, indicating that PpIX accumulation in tumours may already have reached its peak and was being processed and excreted from the animal; and
iii. Using an alternative cell line for *in vivo* tumour induction such as the NuTu-19 ovarian carcinoma cell line, whose tumours have exhibited positive 5-ALA-induced PpIX signals *in vivo* (refer to section 6.3.6 and Major *et al.*, 1997; Chan *et al.*, 2002; Regis *et al.*, 2007).

FCE imaging of the tumour-specific fluorescent-labeled 2-NBDG optical biomarker in *in vivo* murine tissues produced results conflicting with that in the literature. Previous

studies have demonstrated more rapid and greater uptake of 2-NBDG in tumours compared to normal tissues as a result of higher metabolic activity (O'Neil *et al.*, 2005; Nitin *et al.*, 2009). FCE images from our study however displayed visible 2-NBDG fluorescence in both murine tumours and normal tissues such as that from the spleen, liver and kidney. We have attributed this observation to similar metabolic activity in both tumour and normal tissues. Further tests on tumour growth kinetics are required so as to determine a more optimal imaging time-point for better exploitation of the technique *in vivo*.

On the whole, we have shown the possibility of detecting fluorescence originating from photosensitisers and fluorescently labelled biomarkers *in vivo* with FCE. It would be difficult however to further validate the full effectiveness of these different functional FCE imaging approaches given the spatially limited point-imaging nature of the procedure. Hence, a macroscopic optical viewfinder method is first needed to visualise larger tissues regions *in vivo* before subsequently applying FCE for more microscopic detection.

One particular challenge when imaging with the FCE confocal miniprobe was the precise amount of pressure that had to be applied for obtaining optimal image quality and contrast. This could possibly have arisen due to the requirement of a minimum working distance between the miniprobe and the target surface, or to prevent deformation of the imaged surface. We have managed to avoid the problem during *in vitro* cellular imaging by holding the miniprobe in place with a miniature V-clamp and translating the cell samples with a moveable mechanical stage. With *ex vivo* and *in vivo* tissues however, imaging had to be performed by hand, making the application of a constant probe pressure a delicate and at times frustrating process. Future *in vivo* FCE imaging procedures with the confocal miniprobe inserted down an endoscope port would be an even greater challenge since the operator would receive possibly no haptic feedback throughout. A solution to this would be to perform FCE imaging *in vivo* with the aid of a force sensor such as that employed by Noonan and colleagues: the group incorporated a force/torque sensor at the tip of a robotic endoscope to maintain an optimal force applied by their fluorescent imaging probe (Noonan *et al.*, 2010). In this manner, it would therefore be possible to maintain a constant pressure with the probe on tissue surfaces *in vivo*, hence allowing for the acquisition of FCE images with consistent quality and contrast.

FCE is still in its infancy, with first demonstration of the technique on colorectal cancer tissues *in vivo* published only in late 2004 by Kiesslich and colleagues (Kiesslich *et al.*, 2004). Rising interest in the technique will see further system improvements, more tumour-specific molecular contrast agents developed and a possible standardisation of FCE image interpretation through both preclinical and clinical trials (Bisschops and Bergman, 2010). Though FCE will not entirely replace standard histology, this will eventually result in greater adoption of the technique in routine clinical practice.

Some limitations of our imaging studies included:

i. The poor availability of *ex vivo* tissue samples for proper validation of our imaging techniques.

   Initial MFI and HRI experiments were performed on frozen colorectal tissue obtained from an NHS-approved tissue bank. Though not a good reflection of *in vivo* imaging conditions, imaging work was carried out on these frozen tissues because ethical approval had not been granted at that point for the use of freshly resectioned *ex vivo* samples. Once approval was granted, we proceeded to image fresh surplus *ex vivo* tissues obtained from routine surgical resections; these were sourced from our clinical collaborators and consisted of cancerous tissues from the pharynx, lung, bladder and ovaries. We note that tissues from these organs may not be in line with our end goal of imaging more easily accessible hollow organs minimally invasively. Due to the constraint of tissue availability however, a compromise had to be made to use these tissue samples at hand. Future work would therefore involve expanding our base of clinical collaborators to ensure that fresh tissues from more relevant organs are obtained for imaging studies.

ii. The quantification of cell numbers with FCE during *in vitro* characterisation of cell function and morphology.

   FCE was performed with the main purpose of characterising morphological response of *in vitro* cancer cells to cisplatin-based chemotherapy. As an added parameter for assessing drug response, tracking of cellular attrition rates was also decided upon. We note that this is not the gold standard

approach to quantifying cells *in vitro*. Should the need arise in the future, a more proper technique will be employed such as using a haemocytometer and the Trypan blue stain.

The last ten years has seen enormous strides made in biomedical engineering with concomitant advances in the imaging sciences. Buzzwords such as 'optical biopsy' and 'virtual histology' are fast becoming commonplace in every a clinician's daily vocabulary. Helped along by excellent results from preclinical imaging trials involving animal models of disease, it is without doubt that optical imaging techniques will play a pivotal role in medicine. Apart from disease classification, such techniques will also provide greater insight into the molecular basis of disease in model organisms as well as aid in the development of novel cancer therapies (Contag, 2007).

Just as we have suggested a multimodal endoscopic viewfinder (MEV) imaging approach, so will the manner in which cancer is detected and diagnosed. We envision the likely combination of two complementary techniques for early cancer detection: a wide-field optical imaging approach such as MFI or narrow-band imaging (NBI) as the initial 'red flag' technique, followed closely by a localised point-based method like FCE or endocytoscopy for more accurate disease confirmation based on cellular morphology (Anandasabapathy, 2008). Coupled with the development of more tumour-specific tracking agents such as dye-peptide conjugates (Ye *et al.*, 2006), nanoparticles (Achilefu, 2004) and fluorescent-labeled dendrimers (Backer *et al.*, 2005), optical imaging approaches are set to become the modalities of choice for routine cancer screening and surveillance in the near future.

References

Achilefu S. Lighting up tumors with receptor-specific optical molecular probes. *Technology in Cancer Research & Treatment* 2004;**3(4)**:393-409.

Anandasabapathy S. Endoscopic imaging: emerging optical techniques for the detection of colorectal nelplasia. *Current Opinion in Gastroenterology* 2008;**24**:64-69.

Backer MV, Gaynutdinov TI, Patel V, Bandyopadhyaya AK, Thirumamagal BT, Tjarks W, Barth RF, Claffey K, Backer JM. Vascular endothelial growth factor selectively targets boronated dendrimers to tumor vasculature. Molecular Cancer Therapeutics 2005;**4(9)**:1423-1429.

Bartošová J, Hrkal Z. Accumulation of protoporphyrin-IX (PpIX) in leukemic cell lines following induction by 5-aminolevulinic acid (ALA). *Comparative Biochemistry and Physiology - Part C: Toxicology and Pharmacology* 2000;**126(3)**:245-252.

Betz CS, Lai JP, Xiang W, Janda P, Heinrich P, Stepp H, Baumgartner R, Leunig A. In vitro photodynamic therapy of nasopharyngeal carcinoma using 5-aminolevulinic acid. *Photochemical and Photobiological Sciences* 2002;**1(5)**:315-319.

Bisschops R, Bergman J. Probe-based confocal laser endomicroscopy: scientific toy or clinical tool? *Endoscopy* 2010;**42**:487-489.

Chan JK, Monk BJ, Cuccia D, Pham H, Kimel S, Gu M, Hammer-Wilson MJ, Liaw LH, Osann K, DiSaia PJ, Berns M, Tromberg B, Tadir Y. Laparoscopic photodynamic diagnosis of ovarian cancer using 5-aminolevulinic acid in a rat model. *Gynecologic Oncology* 2002;**87(1)**:64-70.

Clancy NT, Stoyanov D, Sauvage V, James DRC, Yang G-Z, Elson DS. A triple endoscope system for alignment of multispectral images of moving tissue. *Biomedical Optics (BIOMED),* OSA Technical Digest (CD) (Optical Society of America 2010), paper BTuD27.

Contag CH. In vivo pathology: seeing with molecular specificity and cellular resolution in the living body. *Annual Review of Pathology: Mechanisms of Disease* 2007;**2**:277-305.

Kiesslich R, Burg J, Vieth M, Gnaendiger J, Enders M, Delaney P, Polglase A, McLaren W, Janell D, Thomas S, Nafe B, Galle PR, Neurath MF. Confocal laser endoscopy for diagnosing intraepithelial neoplasias and colorectal cancer in vivo. *Gastroenterology* 2004;**127(3)**:706-713.

Major AL, Rose GS, Chapman CF, Hiserodt JC, Tromberg BJ, Krasieva TB, Tadir Y, Haller U, DiSaia PJ, Berns MW. In vivo fluorescence detection of ovarian cancer in the NuTu-19 epithelial ovarian cancer animal model using 5-aminolevulinic acid (ALA). *Gynecologic Oncology* 1997;**66(1)**:122-132.

Nitin N, Carlson AL, Muldoon T, El-Naggar AK, Gillenwater A, Richards-Kortum R. Molecular imaging of glucose uptake in oral neoplasia following topical application of fluorescently labelled deoxy-glucose. *International Journal of Cancer* 2009;**124**:2634-2642.

Noonan D, Payne C, Shang J, Sauvage V, Newton R, Elson D, Darzi A, Yang G. Force adaptive multi-spectral imaging with an articulated robotic endoscope. *Medical Image Computing and Computer Assisted Intervention MICCAI* 2010;**6363**:245-252.

O'Neil RG, Wu L, Mullani N. Uptake of a fluorescent deoxyglucose analog (2-NBDG) in tumour cells. *Molecular Imaging and Biology* 2005;**7**:388-392.

Regis C, Collinet P, Farine MO, Mordon S. Comparison of aminolevulinic acid- and hexylester aminolevulinate-induced protoporphyrin IX fluorescence for the detection of ovarian cancer in a rat model. *Photomedical Laser Surgery* 2007;**25(4)**:304-311.

Tanbakuchi AA, Udovich JA, Rouse AR, Hatch KD, Gmitro AF. In vivo imaging of ovarian tissue using a novel confocal microlaparoscope. *American Journal of Obstetrics and Gynecology* 2010;**202(1)**:90.e1-9.

Wood TC, Thiemjarus S, Koh KR, Elson DS, Yang GZ. Optimal feature selection applied to multispectral fluorescence imaging. *Medical Image Computing and Computer Assisted Intervention MICCAI* 2008;**11(2)**:222-229.

Ye Y, Bloch S, Xu B, Achilefu S. Design, synthesis and evaluation of near infrared fluorescent multimeric RGD peptides for targeting tumors. *Journal of Medicinal Chemistry* 2006;**49**:2268-2275.

Publications and Conferences

Koh KR, Newton RC, Ghaem-Maghami S, Yang GZ and Elson DS. Characterising ovarian cancer morphology and response to chemotherapy using fluorescence confocal endomicroscopy. *Proceedings of IEEE Photonics Society Winter Topical Meeting on Advanced Imaging in Bio-Photonics* 2010;**WB3.3**.

Wood TC, Koh KR, Elson DS. Challenges in multimodal (fluorescence, reflectance, polarisation) tissue imaging using rigid endoscopes. *IEEE Photonics Society Winter Topical Meeting on Advanced Imaging in Bio-Photonics* 2010;**WB3.1**.

Wood TC, Sauvage V, Koh KR, Elson DS. Development and analysis of a polarised endoscopic hyperspectral reflection and fluorescence imaging system. *SPIE Design and Quality for Biomedical Technologies III* 2010, San Francisco, CA, USA.

Sauvage V, James DRC, Wood TC, Koh KR, Elson DS. Development of a hyperspectral laparoscope system for intraoperative diagnosis of intestinal ischemia. *SPIE BiOS Conference 7555*, *Advanced Biomedical and Clinical Diagnostic Systems VIII* 2010*,* San Francisco, CA, USA.

Koh KR, Wood TC, Goldin RD, Yang GZ and Elson DS. Visible and near infrared autofluorescence and hyperspectral imaging spectroscopy for the investigation of colorectal lesions and detection of exogenous fluorophores. *Proceedings of SPIE Vol. 7169, Advanced Biomedical and Clinical Diagnostic Systems VII* 2009;**71691E**.

Wood TC, Sauvage V, Koh KR, Elson DS. Development and analysis of a polarised endoscopic hyperspectral reflection and fluorescence imaging system. *SPIE International Conference on Optical Instrument and Technology (Optical Trapping and Microscopy)* 2009, Shanghai, China.

Wood TC, Sauvage V, Koh KR, Elson DS. Development and analysis of a polarised endoscopic hyperspectral reflection and fluorescence imaging system. *SPIE/OSA European Conferences on Biomedical Optics* 2009, Munich, Germany.

Wood TC, Koh KR, Sauvage V, Yang GZ, Elson DS. Analysis of multi-modal multi-spectral laparoscopic images. *SPIE/OSA European Conferences on Biomedical Optics* 2009, Munich, Germany.

Zhang H, Koh KR, Wood TC, Yang GZ, Elson DS. A fluorescence imaging system based on optimal excitation spectrum control using a photonic crystal fibre supercontinuum laser and digital multimirror. *Photonics Europe* 2008, Biophotonics: Photonic Solutions for Better Health Care, SPIE, Strasbourg, France.

Wood TC, Koh KR, Sauvage V, Yang GZ, Elson DS. Analysis of multi-modal multi-spectral laparoscopic images. *Photonics* 2008, Institute of Physics, Edinburgh, Scotland.

Koh KR, Wood TC, Zhang H, Lekadir K, Elson DS and Yang GZ. Fluorescence excitation spectroscopic imaging with a tuneable light source and dimensionality reduction using FR-IsoMap. *Proceedings of SPIE Vol. 6848, Advanced Biomedical and Clinical Diagnostic Systems VI* 2008;**68480Z**.

Wood TC, Thiemjarus S, Koh KR, Elson DS, Yang GZ. Optimal feature selection applied to multispectral fluorescence imaging. *Medical Image Computing and Computer Assisted Intervention* 2008;**11(2)**:222-229.

Koh KR, Lekadir K, Elson DS and Yang GZ. Excitation/Emission resolved fluorescence imaging with FR-IsopMap. *Proceedings of Medical Image Understanding and Analysis – MIUA* 2007, University of Wales, Aberystwyth.